



UNIVERSITAT DE  
BARCELONA

## Complex Oxide Heterostructures for Spin Electronics

Sergi Martín Ríó



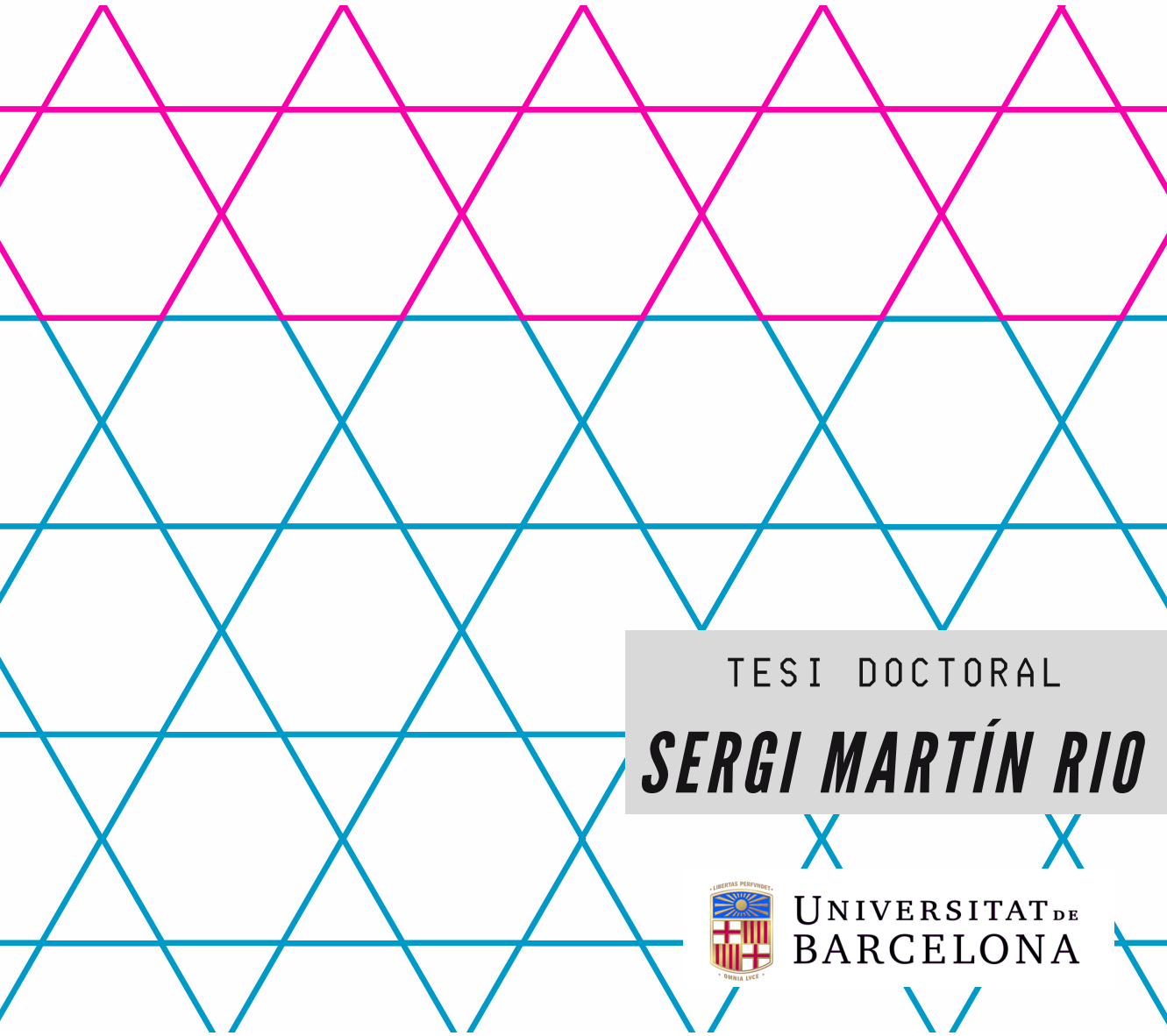
Aquesta tesi doctoral està subjecta a la llicència **Reconeixement- NoComercial – SenseObraDerivada 4.0. Espanya de Creative Commons.**

Esta tesis doctoral está sujeta a la licencia **Reconocimiento - NoComercial – SinObraDerivada 4.0. España de Creative Commons.**

This doctoral thesis is licensed under the **Creative Commons Attribution-NonCommercial-NoDerivs 4.0. Spain License.**



# *Complex Oxide Heterostructures for Spin Electronics*



TESI DOCTORAL

***SERGI MARTÍN RIO***

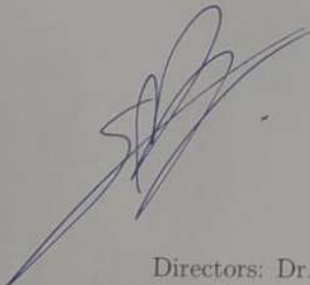


UNIVERSITAT DE  
BARCELONA

# Complex Oxide Heterostructures for Spin Electronics

Memòria presentada per optar al grau de doctor per la

Universitat de Barcelona



Programa de doctorat en Física

Autor: Sergi Martín Rio

Directors: Dr. Benjamín Martínez Perea i Dr. Carlos Frontera Beccaria

Tutor: Dr. Giancarlo Franzese

Institut de Ciència de Materials de Barcelona (ICMAB-CSIC)



UNIVERSITAT<sup>DE</sup>  
BARCELONA

*All science would be superfluous if the outward  
appearance and the essence of things directly  
coincided*

— Karl Marx



# Agraïments

D'entrada, voldria agrair als membres del tribunal, Jacobo Santamaría, Amílcar Labarta, Fèlix Casanova, Luís Hueso, Ferran Macià i Jordi Sort, per haver accedit a l'avaluació d'aquesta tesi. També m'agradaria donar les gràcies als meus directors, Carlos Frontera i Benjamín Martínez, per haver-me donat l'oportunitat de realitzar-la, i a totes les persones que formen part del nostre grup, sense les quals aquesta feina no hagués tirat endavant. En l'àmbit institucional, voldria donar les gràcies a l'Institut de Ciència de Materials de Barcelona (ICMAB-CSIC) i a la Universitat de Barcelona (UB) per haver-me permès dur a terme aquest doctorat. A més, voldria agrair al Ministerio de Ciencia e Innovación pel finançament d'aquesta tesi a través del projecte HETEROCS (MAT2015-71664-R), així com al programa Horizon 2020 d'Investigació i Innovació de la Unió Europea, que ha finançat algunes estades a l'estranger realitzades durant el doctorat mitjançant la beca Marie Skłodowska-Curie No. 645658 (DAFNEOX Project). En aquest punt, voldria aprofitar per a adreçar-me individualment a les persones amb qui he conviscut tots aquests anys.

Als meus directors de tesi, Carlos i Benja, per tot el suport i esforç perquè aquesta tesi anés a bon port. Gràcies per totes les hores dedicades a la discussió de resultats, lectura, revisió i correcció del text. A en Carlos, per ajudar-me a comprendre amb més profunditat aquest món estrany dels espins. Per tenir sempre oberta la porta del teu despatx i ajudar-me amb el calgués – discutir articles, especular a la pissarra o parlar de la vida –, amb un somriure, encara que estiguessis ficat en *mil fregaos*. Aquesta tesi no seria ni la meitat del que és sense la teva contribució i ajuda. A Benja, per tu carisma, pragmatismo, pedagogía y sentido del humor. Por enseñarme cómo funciona este oficio, por confiar en mi desde el principio, poniéndome a cargo del primer espectroscopio FMR del grupo, y echarme una mano en todo cuanto necesitaba, gracias.

A en Lluís, que has sigut com un tercer director en aquesta tesi. Pel teu optimisme i esperit curiós, que desborda i es contagia, i per demostrar-me amb l'exemple la (molta!) paciència i fortalesa que es requereixen per a ser físic experimental. A Alberto, por tu paciencia, curiosidad y sentido pedagógico, por ayudarme con el manejo del FMR y explicarme conceptos complejos de forma sencilla. A Zorica, por tus consejos y ayuda: sin tu empuje final hubiera sido imposible crecer las capas de manganitas con iridatos. A en Bernat, per la teva ajuda i paper clau al muntatge

definitiu de l'FMR i per fer més agradables les llargues sessions de mesura al laboratori. A en Narcís, pel teu sentit de l'humor, ajuda i suport durant la tesi. Por último, no me podría olvidar de mis inseparables compañeros de doctorado: el doctor Víctor Fuentes y la doctora Mónica Bernal, por haber hecho más agradable y fácil esta etapa, por haberme ayudado al inicio del doctorado. Por compartir frustraciones (¡demasiadas a veces!) pero también para celebrar las cosas buenas. En general, gràcies a tothom per tots per aquests anys, que han estat plens d'alts i baixos – amb pràcticament un any sencer aturats per la pandèmia – per haver-m'ho posat tot tan fàcil.

Aquest doctorat m'ha permès viatjar mitjançant diferents congressos i estades. Voldria agrair a les persones de la Universidad Técnica Federico Santa María de Valparaíso, Carlos García, Claudio, Luís, Cristian, Mariam, Ignacio, Igor, y muchos más, por darme la oportunidad de trabajar con vosotros y acogerlos, a Víctor y a mí, como a dos más del grupo (asados, pisco, empanadas y chorrillanas mediante). També m'agradaria donar les gràcies a en Fèlix Casanova i en Luís Hueso per acollir-me al seu grup de Donostia-San Sebastián, i a totes les persones que em va ajudar durant i després de l'estada i per totes les coses que em van ensenyar: Juanma, Montse, Sara, Roger, i molts més, gràcies.

En general, agrair la feina i ajuda rebuda per part de tots els tècnics i personal de l'ICMAB. A en Luigi, la Neus i la Marta, de la sala blanca; a l'Anna, en Joan i en Xavi del servei de raigs X; l'Anna i la Judith, del SEM; a en Bernat i en Ferran, del laboratori de baixes temperatures; i a en Guillaume, de l'ICN2, per les mesures d'XPS. També voldria agrair a Cesar Magén i Ramón Manzorro de la Universidad de Zaragoza i Jaume Gázquez, de l'ICMAB, per les imatges i anàlisis d'STEM.

Personalment, voldria donar les gràcies a en David per ajudar-me a no defallir mai, pel seu suport i la seva paciència. Gràcies per estar sempre al meu costat i fer la vida més bonica. Tambien me gustaría dar las gracias a mi familia, especialmente a mis padres, Carmen y Carlos, por haberme enseñado con su ejemplo todo lo que se puede conseguir a base de esfuerzo y sacrificio. Gracias por vuestro amor, cariño y apoyo infinitos.

# Abstract

The discovery in 1988 of giant magnetoresistance (GMR) set the starting point of the spintronics revolution. In GMR-related phenomena the spin degree of freedom of electrons is crucial, but it is still linked to the presence of charge carriers in the system. On the other hand, since the experimental detection of the spin Hall effect at the beginning of this century, the direct manipulation of spin currents with no charges involved became a very hot topic. In this way, the delicate interplay between charge, spin and orbital degrees of freedom in materials and structures has attracted a renewed interest in the last few years. Technologically speaking, one of the most attractive features of pure spin currents is the disappearance of Joule heating, which is directly linked to the amazing problem of heat dissipation in today's microelectronic devices. As such, the generation, manipulation, and detection of pure spin currents is still one of the major challenges in spintronics nowadays. In this regard, the charge-to-spin currents interconversion processes play a very relevant role and having the set of materials and structures that maximize these processes is of paramount importance.

In this Thesis, the generation, manipulation, and detection of pure spin currents in ferromagnetic/normal metal bilayers is addressed. The use of manganese-based complex oxide perovskites is especially relevant in the context of this Thesis. In general, complex oxide materials are very appealing from the technological viewpoint due to their inherent multifunctional nature. The first experimental block of this Thesis (Chapters 4 and 5) concentrates on the generation of microwave-mediated pure spin currents *via* spin pumping and their subsequent detection by means of inverse spin Hall effect (ISHE) voltage measurements. Conversely, the second block (Chapter 6) focuses on spin Hall magnetoresistance (SMR) measurements.

The archetypal bilayer composed by  $\text{Ni}_{80}\text{Fe}_{20}$  (Permalloy or Py)/Pt is studied in Chapter 4. This chapter is fundamental for it allows us to foreseen the capabilities and versatility of ferromagnetic resonance (FMR) spectroscopy for disclosing the crucial magnetodynamical parameters of the system. Simultaneously, the generation of pure spin currents by means of spin pumping is also triggered by microwave absorption during FMR. The effective generation of a pure spin current is demonstrated *via* ISHE in FM/NM bilayers. The generated pure spin current is converted to a transverse charge current (*via* ISHE) in the high spin-orbit coupling Pt capping layer and detected as a transverse voltage difference across the film. In this Chapter, the

dual nature of FMR spectroscopy is highlighted and a novel method for suppressing parasitic voltage contributions to the overall ISHE voltage signal is presented. Finally, in order to gain insight into the behavior of these parasitic effects, a numerical study based on our actual experimental system is performed.

In Chapter 5, the suitability as spin current injectors/detectors of three different complex oxide heterostructures is investigated, namely:  $\text{La}_{0.92}\text{MnO}_3$  (LMO)/Pt,  $\text{La}_{2/3}\text{Sr}_{1/3}\text{MnO}_3$  (LSMO)/Pt and LSMO/SrIrO<sub>3</sub> (SIO). The latter is especially relevant in the context of this Thesis for it is the only all-oxide complex structure evaluated. All measurements contained in this Chapter are analogous to those shown in Chapter 4, i.e., generation of pure spin currents by means of FMR-mediated spin pumping and their subsequent detection *via* ISHE voltage signals measurement. Unlike any other film in this Thesis, LMO films have been prepared by chemical methods. In the last few years, however, there has been some concerns regarding the suitability of chemically deposited thin films for challenging applications which require microstructural quality and sharp interfaces, as in spintronics. In this regard, it is demonstrated the structural high-quality and efficient spin injection capabilities of chemically deposited LMO films for a wide range of temperatures. Similarly, in the second part of this Chapter, the spin injection performance of LSMO films in LSMO/Pt bilayer systems is shown. In a second step, a material with presumably large spin-orbit interaction, such as SIO, is introduced as spin detector, and the spin injection/detection processes in the all-oxide heterostructure LSMO/SIO are addressed. In this case, it is demonstrated the promising role of SIO as an efficient spin-to-charge converter, thus opening the door to the development of high-quality spin-to-charge conversion devices based on all-oxide heterostructures.

Finally, the last Chapter of this Thesis focuses on the measurement of a rather different spintronic effect: spin Hall magnetoresistance (SMR). In this magnetoresistive effect, a pure spin current is generated *via* spin Hall effect (SHE) in a high spin-orbit coupling capping film (Pt in this case) and directed towards the  $\text{La}_2\text{CoMnO}_6$  (LCMO)/Pt interface. The interaction between this spin current and the magnetization of the ferromagnetic insulating thin LCMO film is at the heart of SMR. The experimental results found in this Chapter exemplify the exceptional role played by the interface. Additionally, a theoretical model is employed for interpreting the results obtained and it is seen that the magnetic state of the uppermost layers of the LCMO film are actually magnetically decoupled from the rest of the film, exhibiting a behavior compatible with a 2D Heisenberg ferromagnet, with no long-range magnetic order nor transition temperature.

# Resum

El descobriment l'any 1988 de la magnetoresistència gegant (GMR) va marcar l'inici de la revolució espintrònica. El grau de llibertat d'espí dels electrons és essencial per als fenòmens relacionats amb la GMR. Així i tot, aquests sistemes encara depenen de la presència de portadors de càrrega. Així mateix, des de la detecció experimental de l'efecte Hall d'espí al començament d'aquest segle, la manipulació directa de corrents d'espí sense necessitat de càrregues va esdevenir un tema de gran interès. D'aquesta manera, els darrers anys l'entrelligament entre els diferents graus de llibertat – de càrrega, d'espí i orbital – en materials i estructures ha viscut un renovat interès. Des del punt de vista tecnològic, una de les característiques més atractives dels corrents purs d'espí és la desaparició de l'escalfament per efecte Joule, el qual està directament connectat al gran problema de la dissipació de calor present als aparells electrònics actuals. Com a resultat, la generació, manipulació i detecció de corrents purs d'espí és encara un dels grans reptes de l'espintrònica. En aquest aspecte, els processos d'interconversió entre càrregues i espins juguen un paper molt rellevant, i el fet de tenir els materials i les estructures que maximitzen aquests processos és del tot important.

En aquesta tesi, la generació, manipulació i detecció de corrents purs d'espí a bicapes ferromagnet/metall normal (FM/NM) és discutida. L'ús d'òxids complexos basats en manganès amb estructura de perovskita és especialment rellevant. En general, els materials formats per òxids complexos són molt atractius des del punt de vista tecnològic a causa de la seva inherent natura multifuncional. El primer bloc experimental (capítols 4 i 5) es concentra en l'ús de microones per a la generació de corrents purs d'espí per mitjà del bombeig d'espins. Seguidament, aquests corrents són detectats mesurant el voltatge induït per l'efecte Hall d'espí invers (ISHE). Així mateix, el segon bloc (capítol 6) se centra en mesures de magnetoresistència Hall d'espí (SMR).

La bicapa arquetípica composta per  $\text{Ni}_{80}\text{Fe}_{20}$  (Permalloy o Py)/Pt és estudiada al capítol 4. Aquest capítol és fonamental perquè ens permet preveure les capacitats i la versatilitat de l'espectroscòpia de ressonància ferromagnètica (FMR) per a revelar les variables magnetodinàmiques clau del sistema. A la vegada, la generació de corrents purs d'espí per mitjà del bombeig d'espins és també activada gràcies a l'absorció de microones durant la ressonància ferromagnètica. La generació efectiva de corrents purs d'espí sota condicions de ressonància és demostrada a través de

l'ISHE a les bicapes FM/NM. El corrent d'espí generat és transformat en un corrent de càrrega transversal (per mitjà d'ISHE) a la capa de Pt d'alt acoblament espí-òrbita, i aquesta és detectada com una diferència de potencial transversal a la capa. En aquest capítol, la natura dual de l'espectroscòpia d'FMR és clarament mostrada i un nou mètode per a eliminar les contribucions paràsites al voltatge total mesurat és presentat. Finalment, per tal d'aprofundir en el coneixement relacionat amb el comportament d'aquests efectes paràsits, un estudi numèric basat en el nostre propi sistema experimental és dut a terme.

Al capítol 5, la idoneïtat com a injectors o detectors de corrents d'espí de tres heteroestructures formades per òxids complexos és investigada, específicament:  $\text{La}_{0.92}\text{MnO}_3$  (LMO)/Pt,  $\text{La}_{2/3}\text{Sr}_{1/3}\text{MnO}_3$  (LSMO)/Pt i LSMO/SrIrO<sub>3</sub> (SIO). Aquesta última és especialment rellevant en el context d'aquesta tesi, ja que és l'única heteroestructura estudiada en què tots els components són òxids complexos. Totes les mesures contingudes en aquest capítol són anàlogues a aquelles mostrades al capítol 4, és a dir, la generació de corrents purs d'espí per mitjà d'FMR (que facilita el bombeig d'espins) i la posterior detecció a través de la mesura del senyal de voltatge d'ISHE. A diferència de cap altra mostra estudiada a aquesta tesi, les capes d'LMO han sigut crescudes per mètodes químics. Als últims anys, però, hi ha hagut certa preocupació relacionada amb la idoneïtat de les capes primes crescudes per mètodes químics per a ser utilitzades en aplicacions puntals, les quals requereixen qualitat microestructural i interfícies planes, com a l'espintrònica. En aquest aspecte, s'han demostrat l'alta qualitat estructural i la capacitat d'injectar eficientment corrents d'espí de les capes d'LMO crescudes químicament per un ample ventall de temperatures. De manera similar, a la segona part d'aquest capítol el rendiment de les capes d'LSMO com a injectores d'espí en bicapes LSMO/Pt és discutit. En un pas posterior, un material amb acoblament espí-òrbita presumiblement alt, com és el SIO, és introduït com a detector d'espí, i els processos d'injecció/detecció d'espí a l'heteroestructura LSMO/SIO és adreçat. En aquest cas, és demostrat el paper prometedor del SIO com a material convertidor d'espins a càrregues, fet que obre la porta al desenvolupament d'aparells convertidors d'espins a càrregues d'alta qualitat basats en heteroestructures en les quals tots els components són òxids complexos.

Finalment, l'últim capítol d'aquesta tesi se centra en la mesura un efecte espintrònic prou diferent: la magnetoresistència Hall d'espí (SMR). En aquest efecte magnetoresistiu, un corrent pur d'espí és generat per mitjà de l'efecte Hall d'espí (SHE) a la capa d'alt acoblament espí-òrbita NM (Pt en aquest cas) i dirigida a la interfície formada pel  $\text{La}_2\text{CoMnO}_6$  (LCMO) i el Pt. La interacció entre aquest corrent d'espí i la magnetització de la capa prima ferromagnètica aïllant LCMO és al cor de la SMR. Els resultats experimentals trobats en aquest capítol exemplifiquen el paper excepcional jugat per la interfície. A més a més, un model teòric és emprat per a la interpretació dels resultats obtinguts i s'observa que l'estat magnètic de les últimes

filers superiors del LCMO estan desacoblades magnèticament respecte de la resta de la capa. Aquestes exhibeixen un comportament compatible amb un ferromagnet bidimensional de Heisenberg, el qual no presenta ordre magnètic de llarg abast ni temperatura de transició.





# Contents

<b>Agraïments</b> . . . . .	i
<b>Abstract</b> . . . . .	iii
<b>Resum</b> . . . . .	v
<b>1 Introduction</b> . . . . .	<b>1</b>
1.1 Historical Background and Current Trends . . . . .	2
1.2 Future Perspectives . . . . .	4
1.3 Why Complex Oxides? . . . . .	6
1.4 This Thesis . . . . .	7
<b>2 Spin Currents</b> . . . . .	<b>9</b>
2.1 Micromagnetics . . . . .	9
2.2 Transport Properties of <i>3d</i> Metals and Definition of Spin Current . . . . .	12
2.3 Conservation Laws . . . . .	15
2.4 Spin-Orbit Coupling . . . . .	17
2.5 Spin Hall Effect . . . . .	19
<b>3 Magnetization Dynamics and Spin Pumping</b> . . . . .	<b>23</b>
3.1 Landau-Lifshitz-Gilbert Equation . . . . .	24
3.2 Theory of Ferromagnetic Resonance . . . . .	27

3.3	Spin Currents at the Interface Between a Ferromagnet and a Normal Metal . . . . .	32
3.3.1	Spin Hall Magnetoresistance . . . . .	36
3.4	Spin Pumping . . . . .	37
3.4.1	Detection of Spin Pumping . . . . .	40
<b>4</b>	<b>Spin Pumping and Inverse Spin Hall Effect in Permalloy/Pt Bilayers</b>	<b>43</b>
4.1	FMR Characterization and Spin Pumping in Py and Py/Pt Systems . . . . .	44
4.1.1	Samples Characterization and Growth Conditions . . . . .	44
4.1.2	Room Temperature FMR and Spin Pumping Characterization of Py and Py/Pt Bilayers . . . . .	46
4.1.3	Temperature Dependence of FMR and Spin Pumping . . . . .	50
4.2	Inverse Spin Hall Effect in Py and Py/Pt Systems . . . . .	57
4.2.1	Description of the Experiment and Experimental Setup . . . . .	57
4.2.2	Samples Preparation and Characterization . . . . .	60
4.2.3	Voltage Measurements for the $L = 5$ mm Samples . . . . .	63
4.2.4	Voltage Measurements as a Function of $L$ . . . . .	66
4.2.5	Numerical Study of the SRE in the Si// Py/Pt System . . . . .	79
<b>5</b>	<b>Spin Pumping and Inverse Spin Hall Effect in Complex Oxide Heterostructures</b>	<b>95</b>
5.1	Inverse Spin Hall Effect Measurements in $\text{La}_{0.92}\text{MnO}_3/\text{Pt}$ Bilayers . . . . .	95
5.1.1	Samples Characterization and Growth Conditions . . . . .	95
5.1.2	Spin to Charge Conversion in $\text{La}_{0.92}\text{MnO}_3/\text{Pt}$ Bilayers . . . . .	106
5.1.3	Temperature Dependence of Inverse Spin Hall Effect in $\text{La}_{0.92}\text{MnO}_3/\text{Pt}$ Bilayers . . . . .	112

5.2	Inverse Spin Hall Effect Measurements in $\text{La}_{2/3}\text{Sr}_{1/3}\text{MnO}_3/\text{SrIrO}_3$ Bilayers . . . . .	126
5.2.1	Samples Preparation and Description of the Experiment . . . . .	126
5.2.2	Magnetodynamical Properties of $\text{La}_{2/3}\text{Sr}_{1/3}\text{MnO}_3/\text{Pt}$ . . . . .	129
5.2.3	Spin to Charge Conversion in $\text{La}_{2/3}\text{Sr}_{1/3}\text{MnO}_3/\text{SrIrO}_3$ Bilayers . . . . .	133
<b>6</b>	<b>Spin Hall Magnetoresistance in <math>\text{La}_2\text{CoMnO}_6/\text{Pt}</math> bilayers</b>	<b>147</b>
6.1	Description of the Experiment . . . . .	147
6.2	Samples Preparation . . . . .	151
6.3	Spin Hall Magnetoresistance Measurements and Results . . . . .	154
6.4	Surface Magnetic State of the $\text{La}_2\text{CoMnO}_6$ Film . . . . .	162
<b>7</b>	<b>Summary and Conclusions</b>	<b>175</b>
<b>A</b>	<b>Experimental Techniques</b>	<b>183</b>
A.1	Preparation of Films . . . . .	183
A.1.1	Magnetron Sputtering Deposition . . . . .	183
A.1.2	Photolithography and Ion Milling . . . . .	185
A.2	Magnetic and Transport Characterization Techniques . . . . .	187
A.2.1	SQUID Magnetometry . . . . .	187
A.2.2	Ferromagnetic Resonance Spectroscopy . . . . .	188
A.2.3	Transport Measurements . . . . .	193
A.3	Structural and Surface Characterization Techniques . . . . .	194
A.3.1	X-ray Diffraction and Reciprocal Space Maps . . . . .	194
A.3.2	X-ray Reflectivity . . . . .	195

A.3.3	Scanning Electron Microscopy . . . . .	196
A.3.4	Scanning Transmission Electron Microscopy . . . . .	197
<b>B</b>	<b>Voltage Measurements Using Single-Stripe and Fringed Patterns: a Comparison</b>	<b>199</b>
<b>C</b>	<b>ADMR and FDMR Measurements in Additional <math>\text{La}_2\text{CoMnO}_6/\text{Pt}</math> Bilayers Using Different Pt Deposition Conditions</b>	<b>203</b>
C.1	Samples Preparation and Characterization . . . . .	203
C.2	ADMR and FDMR Measurements . . . . .	205
C.3	SMR Measurements on $\text{La}_2\text{CoMnO}_3/\text{Pt}$ Bilayer Under Tensile Strain .	209
	<b>Bibliography</b> . . . . .	<b>212</b>

## Introduction

---

If the 20th century was the century of electronics, the 21st century could as well be the century of spintronics. In conventional electronics, the fundamental parameter is the charge of electrons in motion, while in the emerging field of spintronics the spin degree of freedom of electrons has a central role. Sinova and Žutić [1] wonderfully defined spintronics as the “field where traditional solid-state physics and materials research have created their strongest bond, with each taking alternate leading roles in a unique, fast paced, technological tango” [1, p. 368]. But when did it all started?

Spintronics gained popularity in the end of the 20th century due to its implementation in read heads of hard disk drive (HDD) technology. Read heads are based on the so-called giant magnetoresistance (GMR) effect, discovered in 1988. This effect makes use of the relative orientation of the magnetization of two conducting ferromagnetic layers separated by a thin, metallic film. The electrons traveling across the layers are scattered differently depending on their spin orientation, resulting in a difference of resistance if the ferromagnetic layers have the same magnetization orientation (parallel, P, or low resistance state) or opposite orientation (antiparallel, AP, or high resistance state) (see Fig. 1.1). Since then, the increased research activity in this field has led to the discovery of new exciting effects such as spin transfer torque, spin Seebeck effect, or spin Hall effect, which are based entirely on the *direct manipulation* of the spin degree of freedom, unlike the classical GMR, which still depends on charge carriers. Technologically speaking, the research of new devices such as magnetic random access memories (MRAM) [2] or spin solar cells, for instance, is increasing over time.

This chapter is divided in four sections. Section 1.1 focuses on the historical background of spintronics through the 20th century and its development and

evolution until our days. Section 1.2 overviews some of the most recent technological applications in the field and points to its future perspectives. Section 1.3 presents the main properties of complex oxide perovskites, which constitute the basic compounds studied in this Thesis. Finally, in Section 1.4, a general overview of the organization of this Thesis and the content of each Chapter is addressed.

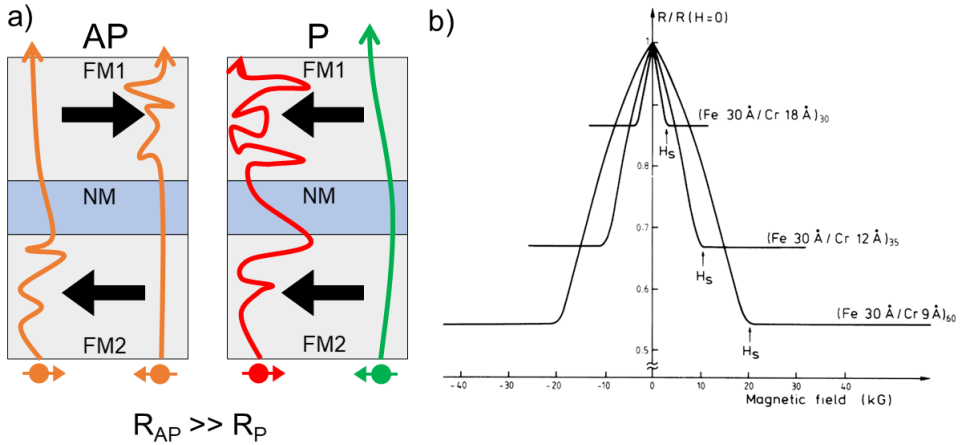


Figure 1.1: (a) Schematic diagram of the GMR spin-dependent scattering mechanism in a ferromagnetic/normal metal/ferromagnetic (FM1/NM/FM2) structure for the parallel (P) and antiparallel (AP) configurations. (b) First experimental observation of GMR in  $(Fe/Cr)_n$  multilayers [3]. In this case, however, the electric current is applied parallel to the plane of the films, and not perpendicular to it as in (a). Still, the physical principles exposed are the same.

## 1.1 Historical Background and Current Trends

The discovery in 1988 of GMR [3, 4] set the starting point of the spintronics revolution. Albert Fert, who shared the Nobel Prize in Physics with Peter Grünberg in 2007 for the independent discovery of GMR, stated that since then “[the] papers reporting the discovery of GMR attracted attention for their fundamental interest as well as for the many possibilities of applications, and the research on magnetic multilayers and GMR became a very hot topic” [5, p. 1519]. The effects regarding the mutual dependency of magnetization and electric current were known long before 1988. Anisotropic magnetoresistance (AMR), for instance, was discovered in 1857 by William Thomson (Lord Kelvin), and N. Mott [6] theorized the spin-dependent scattering of conduction carriers in ferromagnetic materials back in 1936. However, it was not until the technological development of thin films and multilayers growth

techniques and the advances in fabrication of nanostructures during the 1970s that these ideas regained interest. Complex multilayered nanostructures called spin-valve sensors based on GMR were implemented in the read heads of HDD in 1997 by IBM in substitution of AMR sensors [7]. Between 1991 and 2003 the recording areal density for spin-valve sensors was about 100 GBit/in<sup>2</sup> [7]. In 2005, a new giant tunneling magnetoresistance (TMR) sensor was introduced by Seagate, increasing the areal density up to 600 GBit/in<sup>2</sup> [8]. In 2019, the areal density was already above the TBit/in<sup>2</sup> [9].

At the same time, at the turn of the century, Hirsch [10] revived a topic theorized by Dyakonov and Perel already in 1971 [11]: The generation of a transverse *pure spin current* from a charge current flowing in a non-magnetic metal due to spin-orbit coupling (spin Hall effect) and its opposite effect (inverse spin Hall effect). At this point, the generation, manipulation and detection of pure spin currents gathered a lot of interest. If the first generation of spintronics is characterized by the manipulation of spin-dependent charge carriers in systems such as GMR spin-valves, the second generation is focused entirely on the manipulation of pure spin currents, regardless of charge. An essential property of spin currents is the suppression of Joule heating effects, since there is no net flow of charge. Technologically speaking, this feature is very relevant because it allows to solve the amazing problem of heat dissipation in microelectronic devices, thus contributing to the development of more sustainable and greener technology.

Led by these exciting perspectives, important breakthroughs were made and new physical effects were discovered. Spin transfer torque, for instance, was independently theorized by Berger [12] and Slonczewski et al. [13] in 1996. In spin transfer torque, the magnetization of a ferromagnet is driven to a dynamic state due to the interaction with a spin-polarized electric current (or a pure spin current), which exerts a torque on it, with no magnetic fields involved. Above a certain current threshold, magnetization reversal can be induced, opening the door to new promising technological applications such as spin transfer torque-based RAM, for example [8]. In addition, new magnetoresistive phenomena based on this effect, such as spin Hall magnetoresistance, have been discovered within this very last decade [14]. Following the discovery of spin transfer torque, Tserkovnyak, Brataas, and Bauer [15] experimentally generated pure spin currents by means of microwave-mediated magnetization precession in ferromagnetic/normal metal bilayers and called this process spin pumping. It was proved a bit later [16] that spin transfer torque and spin pumping are actually two sides of the same coin. Moreover, for the first time, an experiment conducted by Saitoh et al. in 2006 [17] measured the voltage signal generated by the conversion of a pure spin current into a charge current due to inverse spin Hall effect in Ni<sub>80</sub>Fe<sub>20</sub> (Permalloy or Py)/Pt bilayers. Additionally, it was found that the classical Seebeck and Peltier effects, whereby a thermal gradient induces an electric current and vice

versa, respectively, had their spintronic counterpart in the spin Seebeck and Peltier effects, paving the way for a new field of research called spin caloritronics [18]. On top of this, the spin solar cell already converts light to spin currents using a ferromagnetic/semiconductor junction [19], broadening the path to more sustainable forms of energy generation and harvesting. In Fig. 1.2, some of the main spin current generation methods are shown.

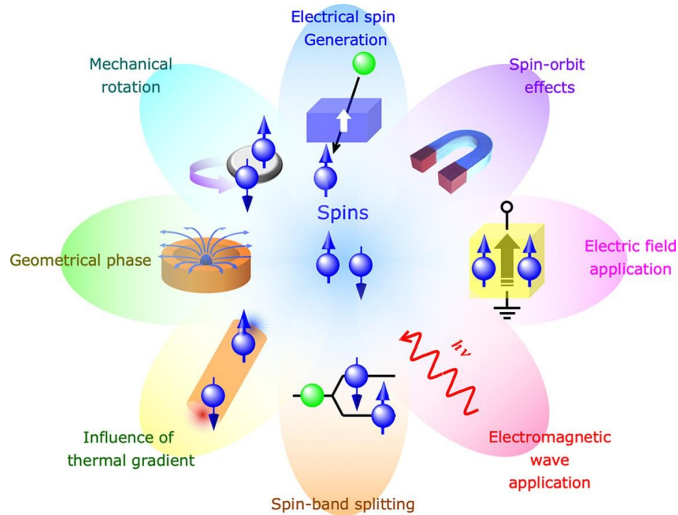


Figure 1.2: Schematic diagram compiling the major methods for generating spin-polarized and pure spin currents. Image reproduced from Ref. [8].

## 1.2 Future Perspectives

As reviewed in the previous section, the history of spintronics is the history of an ever-increasing field of research which, in no more than 30 years of existence, has shown an enormous potential in both technological transferability and fundamental physics research [20]. One of the main goals is to achieve the integration of spintronic devices into modern semiconductor electronics industry (CMOS technology), or even more: their full replacement.

A common topic in CMOS technology think tanks is the end of Moore’s law, which is the self-fulfilling prophecy that has set the roadmap for the technological progress in electronics for more than half a century. Moore’s law states that the density of transistors in a processor doubles every two years, and even though the progress in the field has been outstanding since the 1960s, now a dead end is about to be reached [21] due to the confluence of problems associated to the continuous shrinking of device’s



size, that promotes unwanted quantum effects, and the increase in power consumption, complicating the dissipation of heat, thereby affecting the overall efficiency of the device [22]. These kinds of problems cannot cope with an ever-increasing demand of high-density, high-speed, and low-power consumption in technological devices in the mid and long term. In addition, in the context of today's climate emergency, it is also necessary to take into account the environmental cost of large-scale production, fabrication, and distribution of technology-related commodities worldwide [23, 24]. In fact, we could also go further and ask ourselves if the improvement of technology and the quest for more efficient energy sources and devices by itself is enough to overcome the current climate crisis [25].

In this context, spintronics acts as a prominent candidate to cope with these issues [26, 27, 28]. Major semiconductor companies such as Intel or Samsung have already announced the implementation of MRAM and spin transfer torque-MRAM as a replacement for eFlash technology, although the main inconveniences are down-size scalability, thermal instability and high current density [29, 30]. IBM, on the other hand, is also behind a new kind of magnetic memory called racetrack memory, which stores information in domain walls and the read-and-write mechanisms are based on domain wall motion induced by pulses of spin-polarized currents. A racetrack memory “potentially extends a device structure in a 3D configuration” [8, p. 21] and thus treats the increase of density problem on a whole new level.

With regard to logic devices, in the long term, it is envisioned that spin-based devices will be more suitable than their CMOS counterparts for enabling beyond-Boolean logic devices, as suggested by recent experiments related to neuromorphic computing [31]. For the moment, the most probable mid-term application is that of a hybrid system which combines conventional CMOS technology and spintronic components, taking advantage of the interconversion between spin and charge currents mentioned before. The efficiency of these devices would depend on how fast this interconversion is and the number of interconversions before a computation is made. Therefore, one of the pressing challenges in the field is to find the set of materials and structures which maximize spin-to-charge conversion efficiency [8, 29, 32].

In this Thesis, the main focus is put on the spin generation and spin-to-charge conversion capabilities of complex oxide materials and heterostructures, specifically manganites. The observation in 1993 of so-called *colossal* magnetoresistance (CMR) in  $\text{La}_{0.67}\text{Ca}_{0.33}\text{MnO}_x$  [33] and  $\text{La}_{0.67}\text{Ba}_{0.33}\text{MnO}_x$  [34] thin films triggered the study of these compounds as electrodes for magnetic tunnel junctions (MTJs) but also paved the way for the development of oxide spintronics [35]. In the next section we review the main properties of complex oxide perovskites and relate them with the compounds studied in this Thesis.

### 1.3 Why Complex Oxides?

Oxygen is the most abundant chemical element on Earth's crust, constituting roughly 50 % by forming various types of oxide minerals [35]. As a result, one of the most attractive features of oxide compounds is their natural ubiquity and abundance [36]. On the other hand, their functional versatility and variability, ranging from ferromagnetism, ferroelectricity, or superconductivity, is unparalleled [36, 37, 38]. Of particular importance to this Thesis are the family of complex oxide perovskites. These compounds have the chemical composition  $ABO_3$ , and their structure consists of corner-sharing octahedras  $BO_6$  with a twelve-fold coordinated A cation at its body center [35]. Moreover, the combination of two alternating  $ABO_3$  perovskites can give rise to stable double-perovskite structures with chemical composition  $A_2BB'O_6$ . These two kinds of perovskite crystal structures are shown in Fig. 1.3.

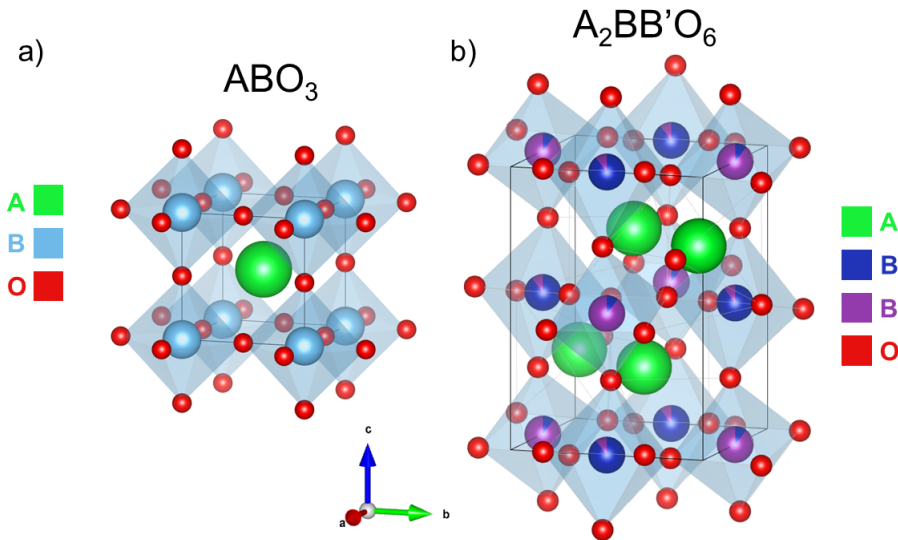


Figure 1.3: (a) Single perovskite structure of the form  $ABO_3$ . b) Double perovskite structure of the form  $A_2BB'O_6$ . These drawings have been made using the scientific 3D visualization software *VESTA* [39].

The major technological advantage of these materials is that different combinations of the A and B elements in the structure give rise to an array of the most diverse functionalities and behaviours [35, 36], as is exemplified in Fig. 1.4. As can be observed from the figure, lanthanum manganese-based perovskites are commonly associated with magnetic compounds. This feature comes from the delicate balance between charge, spin, and orbital degrees of freedom existing in these systems [36]. As such, epitaxial heterostructures of complex oxides may result in novel electronic phases and

physical phenomena due to, e.g., the inherent symmetry-breaking of interfaces, stress, charge transfer or ionic interdiffusion [36, 37, 40]. One of the most characteristic examples of this kind is that of the formation of a 2D electron gas between  $\text{LaAlO}_3$  and  $\text{SrTiO}_3$ , which are robust insulators [41]. This easy tuning of functionalities makes oxide perovskites even more interesting from the technological viewpoint.

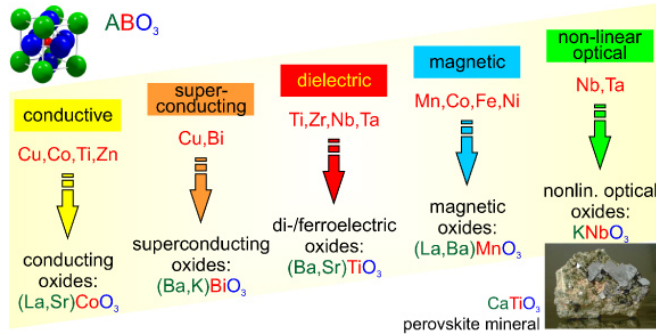


Figure 1.4: Schematic diagram showing the multifunctional nature of complex oxide perovskites. Depending on the combination of A and B elements in the structure, different physical properties arise. This family of materials earned its name from the mineral *perovskite*, which is shown at the bottom right side of the image. This image has been retrieved from Ref. [35].

In the field of spintronics, the spin current transport across different films demands high-quality interfaces. Even though there are many works focusing on the generation and detection of spin currents in bilayer and multilayer systems, the study of this kind of phenomena in all-oxide heterostructures is still rather scarce. Regarding to this, in Chapter 5 we study the ability of  $\text{La}_{0.92}\text{MnO}_3$  and  $\text{La}_{2/3}\text{Sr}_{1/3}\text{MnO}_3$  complex oxides for the dynamical generation and injection of spin currents into Pt and, within that Chapter, in Section 5.2, the spin-to-charge conversion efficiency of  $\text{SrIrO}_3$  is tested using  $\text{La}_{2/3}\text{Sr}_{1/3}\text{MnO}_3/\text{SrIrO}_3$  bilayers. In addition, in Chapter 6, the double-perovskite  $\text{La}_2\text{CoMnO}_6$  is used for measuring spin Hall magnetoresistance, which is a magnetoresistive effect entirely based on the interaction between the magnetization of the ferromagnet and spin currents at the interface.

## 1.4 This Thesis

This Thesis can be divided in two parts. The first part, comprising Chapters 1–3, is a general introduction to the field of spintronics, including its historical and theoretical backgrounds. The second part includes the main experimental results of this Thesis and occupies Chapters 4–6. The experimental techniques employed throughout this work are included in Appendix A. A brief review of each Chapter separately is

included here for clarity:

**Chapter 1** comprises a general introduction to spintronics, including a historical background of the field as well as its future perspectives. Moreover, it also overviews the basic properties of perovskites and the complex oxides studied in this Thesis.

**Chapter 2** is a bottom-up approach to the concept and general properties of spin currents. It also emphasises on the similarities and differences between spin and charge currents and under which circumstances and materials these currents can be coupled.

In **Chapter 3**, due to the relevance in most of the effects studied in this Thesis, magnetization dynamics is addressed and the theory of ferromagnetic resonance is introduced. In addition, the spin current transport phenomena across ferromagnetic/normal metal interfaces is studied with special emphasis on spin transfer torque and spin pumping effects, which are bonded by the same physical mechanisms.

**Chapter 4** focuses on the generation of spin currents by means of spin pumping in Py/Pt bilayers. The electrical detection of these spin currents *via* inverse spin Hall effect is also shown. This Chapter is fundamental because sets an experimental precedent for detecting spin currents in the Thesis.

In **Chapter 5** the focus is two-fold. On one hand, we test the capability for generating pure spin currents in chemically deposited  $\text{La}_{0.92}\text{MnO}_3$  thin films by means of spin pumping (Section 5.1). On the other hand, in Section 5.2, the generation and detection of pure spin currents in the complex oxide heterostructure  $\text{La}_{2/3}\text{Sr}_{1/3}\text{MnO}_3/\text{SrIrO}_3$  is shown.

Finally, **Chapter 6** deals with the measurement of spin Hall magnetoresistance in  $\text{La}_2\text{CoMnO}_6/\text{Pt}$  bilayer systems. It will become clear the crucial role played by the interface for the detection of these kind of effects.

## Spin Currents

The concept of spin current is extensively used in the specialized community. However, its precise definition and detection can be challenging. In this Chapter we trace back the idea behind it and present its similarities with ordinary charge current as well as its unique features. This Chapter is structured in the following way: Section 2.1 introduces the concept of magnetization field vector, which is very useful for characterizing the magnetic energy terms in mesoscopic systems. In section 2.2, Mott's two channels model is discussed and a first definition of spin current is presented. Then, in Section 2.3, the conservation laws of charge and spin currents are compared and the spin diffusion equation introduced. At the end of this Section, a general definition of spin current is presented. The last two Sections deal with the interrelation between charge and spin currents, being spin-orbit coupling the fundamental property connecting them. In Section 2.4, spin-orbit coupling is presented, whereas in Section 2.5 the physics of the spin Hall effect is outlined.

### 2.1 Micromagnetics

The theoretical description of magnetism in mesoscopic systems is called *micromagnetism*. This semi-classical model integrates the crucial quantum mechanical effects that give rise to ferromagnetism, such as exchange interaction, with a continuous field description of the magnetization [42]. We can define a slow-varying magnetization field vector  $\mathbf{M}(\mathbf{r})$  for characterizing the average magnetic moments in a given magnetic specimen of volume  $V$  as

$$\mathbf{M}(\mathbf{r}) = \frac{1}{V} \sum_i \mathcal{M}_i, \quad (2.1)$$

where  $\mathcal{M}_i$  is the magnetic moment of an atom at the  $i$ -th site. Moreover, within this model, the length of the magnetization vector does not change [43]. This assumption restricts the theory to temperatures well below the Curie point  $T_c$ . In a ferromagnetic material, the magnitude of  $\mathbf{M}(\mathbf{r})$  is equal to the *saturation* magnetization or  $M_s$ . The goal of this Section is to define the different energy terms that give rise to the overall magnetic energy in terms of the magnetization field vector  $\mathbf{M}(\mathbf{r})$ . In this way, we will start by introducing the exchange energy  $\mathcal{E}_{\text{ex}}$ , which can be written as [44, 45]

$$\mathcal{E}_{\text{ex}} = \mu_0 A \int d^3r \left( \frac{\nabla \mathbf{M}(\mathbf{r})}{M_s} \right)^2, \quad (2.2)$$

where  $A$  is the exchange stiffness constant and  $\mu_0$  the magnetic permeability in free space. In addition, the exchange stiffness constant can be defined in terms of the so-called exchange length  $\delta_{\text{ex}}$  as [45]

$$A = 2\pi (\delta_{\text{ex}} M_s)^2. \quad (2.3)$$

For most of  $3d$  transition metals, this length is generally small ( $\approx 2 - 8$  nm) [46, 47], which means that for macroscopic magnetic samples, exchange is a small fraction of the total magnetic energy of the system. Therefore, it is important to define and characterize the different energy terms besides exchange energy.

An important source of magnetic energy in ferromagnetic materials is magnetic anisotropy. In a broad sense it is the dependence of the magnetic properties of a system on the crystallographic directions. Magnetic anisotropy has both intrinsic and extrinsic contributions. Magnetocrystalline anisotropy is the main form of intrinsic anisotropy and it arises from spin-orbit coupling, as is seen in more detail in Section 2.4. The main effect of this anisotropy term is the alignment of the magnetization vector with the symmetry axis of the crystal lattice. The simplest anisotropy term of this kind is that of uniaxial anisotropy, which can be expressed as [47]

$$\mathcal{E}_k(\text{uniaxial}) = \mu_0 K_1 V \sin^2(\theta), \quad (2.4)$$

where  $K_1$  is a scalar anisotropy constant,  $V$  the volume of the specimen, and  $\theta$  the angle between the magnetization vector and the crystallographic easy axis direction.

It is referred to as *easy* axis to the crystallographic axis by which the anisotropy energy is minimized and *hard* axis otherwise.

In addition to the intrinsic anisotropy contributions, extrinsic terms do also contribute to the total anisotropy. Regarding this, a common source of anisotropy is strain [48]. The lattice parameter mismatch between the substrate and the film changes the distance between neighbouring ions, thus affecting the overall electronic and magnetic properties of the film, giving rise to second-order contributions to the magnetic anisotropy energy. Likewise, the intrinsic translational symmetry-breaking of film surfaces induces an additional contribution to the total anisotropy: the surface anisotropy energy reads [49]

$$\mathcal{E}_{\text{k(surface)}} = \frac{\mu_0 K_2}{2} \int d^3r \left( \mathbf{n} \cdot \frac{\mathbf{M}(\mathbf{r})}{M_s} \right)^2, \quad (2.5)$$

where  $\mathbf{n}$  is a unit vector normal to the surface of the film and  $K_2$  an interface/surface anisotropy constant.

In the presence of an external source, such as a magnetic field  $\mathbf{H}_{\text{ext}}$ , the coupling between  $\mathbf{H}_{\text{ext}}$  and the magnetization is the well-known Zeeman interaction, which in terms of energy reads

$$\mathcal{E}_{\text{Zee}} = -\mu_0 \int d^3r \mathbf{M}(\mathbf{r}) \cdot \mathbf{H}_{\text{ext}}. \quad (2.6)$$

The last two most important magnetic energy contributions are the magnetostatic interaction and the demagnetizing field interaction. The magnetostatic interaction mediates the coupling between the magnetization and the magnetic dipolar field  $\mathbf{H}_{\text{dip}}$  created by the magnetization distribution itself [45]. In macroscopic ferromagnetic materials, the formation of separate regions with different magnetization directions (magnetic domains) occurs in order to reduce the magnetostatic energy of the system. Formally, its energy can be expressed as [49]

$$\mathcal{E}_{\text{ms}} = -\frac{\mu_0}{2} \int d^3r \mathbf{H}_{\text{dip}} \cdot \mathbf{M}(\mathbf{r}). \quad (2.7)$$

In the absence of electric current,  $\nabla \times \mathbf{H}_{\text{dip}} = 0$ , therefore  $\mathbf{H}_{\text{dip}} = -\nabla\phi$ , where  $\phi$  is a scalar potential analogous to the electrostatic potential, which can be expressed as [49]

$$\phi = - \int d^3r' \frac{\nabla \mathbf{M}(\mathbf{r}')}{|\mathbf{r} - \mathbf{r}'|}. \quad (2.8)$$

Moreover, if the system is uniformly magnetized,  $\nabla \mathbf{M}(\mathbf{r}) = 0$  and Eq. 2.8 vanishes. Despite that, the magnetostatic interaction gives rise to the so-called stray or demagnetizing field, which depends entirely on the shape of the sample and becomes important in mesoscopic systems such as ultrathin films. The demagnetizing field can be expressed as

$$\mathbf{H}_d = -N\mathbf{M}(\mathbf{r}), \quad (2.9)$$

where  $N$  is the demagnetizing factor, which in general is a tensor of trace 1. For example, in the case of an ultrathin film, where the  $x$  and  $y$  directions are infinite with respect to the  $z$  direction, the demagnetizing factors are  $N_x = N_y = 0$  and  $N_z = 1$ , with no off-diagonal components. In general,  $N_x + N_y + N_z = 1$  should hold. The effect of the demagnetizing field is usually regarded as *shape* anisotropy, and the easy axis of magnetization is normally a trade-off between shape and magnetocrystalline anisotropies. We can express the demagnetizing field energy  $\mathcal{E}_d$  just like the magnetostatic energy (Eq. 2.7) but using  $\mathbf{H}_d$  instead of  $\mathbf{H}_{\text{dip}}$ .

Finally, the overall magnetic properties of the magnetic system can be characterized by the magnetic free energy functional  $\mathcal{E}[\mathbf{M}(\mathbf{r})]$ , which is defined as the sum of all of the above mentioned energy terms, i.e.,

$$\mathcal{E}[\mathbf{M}(\mathbf{r})] = \mathcal{E}_{\text{ex}} + \mathcal{E}_{\text{k}} + \mathcal{E}_{\text{Zee}} + \mathcal{E}_{\text{ms}} + \mathcal{E}_d, \quad (2.10)$$

where  $\mathcal{E}_{\text{k}}$  includes any source of magnetic anisotropy present in the system.

## 2.2 Transport Properties of 3d Metals and Definition of Spin Current

Most of the materials studied in this Thesis belong to the ferromagnetic 3d transition metals. In this Section we review their basic transport properties, which are best described using Mott's two channels model [50]. The two basic features of this model are:



1. An electrical conductivity divided into two, independent spin-channels: one for spin-up electrons ( $\sigma_{\uparrow}$ ) and the other for spin-down electrons ( $\sigma_{\downarrow}$ )<sup>1</sup>. This occurs because spin-flip scattering in ferromagnetic metals is low.
2. In  $3d$  transition metals the electric current is mostly carried by  $sp$ -band electrons. Particularly, in ferromagnets, the  $d$ -band electrons are exchange split, meaning that the density of states for spin-up and spin-down electrons are different. Then, since the probability of scattering is proportional to the density of states, the scattering rates are spin-dependent, i.e., different for the two conduction channels.

Mott's two channels model gained popularity throughout the 1970s when A. Fert and I. A. Campbell applied it to nickel and nickel-iron alloys in order to explain the peculiar, giant magnetoresistance effect that was being observed in these materials [51, 52]. Formally, the conductivity of a metal in terms of Mott's arguments is expressed as

$$\sigma = \sigma_{\uparrow} + \sigma_{\downarrow}, \quad (2.11)$$

and according to Drude's conductivity model, each spin-dependent conductivity can be written as [47]

$$\sigma = \frac{e^2}{3\pi^2\hbar} \lambda k_F^2, \quad (2.12)$$

where  $e$  is the elementary charge,  $\hbar$  is Planck's constant,  $k_F$  is the Fermi momentum and  $\lambda$  the mean free path, which is defined as the product of the electron relaxation time  $\tau$  and the Fermi velocity  $v_F$ . The relaxation time can be estimated using Fermi's Golden Rule:

$$\tau^{-1} = \frac{2\pi}{\hbar} \langle V_{\text{scatt}}^2 \rangle \nu_F, \quad (2.13)$$

where  $\langle V_{\text{scatt}}^2 \rangle$  is the average value of the scattering potential and  $\nu_F$  is the density of states at the Fermi level. The scattering potential is in general an extrinsic property of the material, since it has contributions from defects, impurities, or lattice vibrations. It is important to note that each quantity in Eqs. 2.12 and 2.13 is spin-dependent but the spin index has not been included for clarity.

---

<sup>1</sup>The *up* and *down* terminology refers to the projection of the spin with respect to the quantization axis.

Now we move on to understand how spin (i.e., spin angular momentum) diffuses and in which manner it can be understood as a current analogous to a that of charges. We start by addressing the basic properties and equations that govern charge currents. Generally, charge current density  $\mathbf{j}$  can be expressed as a combination of both drift and diffusion currents [53],

$$\mathbf{j} = \sigma \mathbf{E} + eD \nabla n, \quad (2.14)$$

where the first term corresponds to the drift current induced by an electric field  $\mathbf{E}$  ( $\sigma$  is the conductivity of the material) and the second term is the diffusion current due to a gradient in carrier density  $n$  ( $D$  being the diffusion constant). Additionally,  $\nabla n = \nu_F \nabla \mu^c$ , being  $\mu^c$  the *chemical* potential, which by definition is equal to the Fermi energy at  $T = 0$ . The gradient of the *electrochemical* potential  $\mu = \mu^c - e\phi$  is

$$\nabla \mu = e\mathbf{E} + \frac{\nabla n}{\nu_F}, \quad (2.15)$$

being  $\phi$  the scalar potential. Thus, combining equations 2.14 and 2.15 one finds that

$$\mathbf{j} = \frac{\sigma}{e} \nabla \mu, \quad (2.16)$$

which identifies the electrochemical potential gradient as a source of electric current. Now, according to Mott's two channels model, the electrochemical potential can be expressed as a spin-dependent quantity, for it depends on the density of states at the Fermi level. Therefore, the *spin-dependent* current density is given by

$$\mathbf{j}_\sigma = \frac{\sigma_\sigma}{e} \nabla \mu_\sigma, \quad (2.17)$$

where the subscript  $\sigma$  stands for spin-up ( $\sigma = \uparrow$ ) or spin-down ( $\sigma = \downarrow$ ) spin states, and the spin-dependent electrochemical potential is  $\mu_\sigma = \mu_\sigma^c - e\phi$ . Now, the charge and spin currents are obtained as the sum and difference of spin-up and spin-down current density contributions, respectively, i.e.,

$$\mathbf{j}_c \equiv \mathbf{j}_\uparrow + \mathbf{j}_\downarrow = \frac{1}{e} \nabla (\sigma_\uparrow \mu_\uparrow + \sigma_\downarrow \mu_\downarrow), \quad (2.18)$$

$$\mathbf{j}_s \equiv \mathbf{j}_\uparrow - \mathbf{j}_\downarrow = \frac{1}{e} \nabla (\sigma_\uparrow \mu_\uparrow - \sigma_\downarrow \mu_\downarrow). \quad (2.19)$$

It should be noted from these equations that charge and spin currents have the same units ( $\text{A} \cdot \text{m}^{-2}$ ). For simplicity, this convention is used throughout this Thesis. However, in order to get the *natural* units of spin current one should multiply  $\mathbf{j}_s$  by  $\hbar/2e$ . In ferromagnetic metals, the conductivities for spin-up and spin-down electrons are usually different ( $\sigma_\uparrow \neq \sigma_\downarrow$ ). On the other hand, in non-magnetic (or normal) metals the conductivity is spin-independent ( $\sigma_\uparrow = \sigma_\downarrow \equiv \sigma$ ), thus the spin current in a normal metal would simply be  $\mathbf{j}_s = \sigma \nabla(\mu_\uparrow - \mu_\downarrow)/e$ , which means that a spin current can be induced in a normal metal when there is a gradient in the electrochemical potential difference for spin-up and spin-down electrons. This electrochemical potential difference is called *spin accumulation*  $\mu_s = \mu_\uparrow - \mu_\downarrow$  [54, 55], and is a fundamental quantity in spintronics. In Chapter 3, we focus our attention on the spin transport through ferromagnetic/normal metal interfaces, whereby the crucial role spin accumulation played in these systems is evidenced.

## 2.3 Conservation Laws

One of the fundamental and defining properties of charge currents is charge conservation, which is mathematically described by the continuity equation

$$\frac{\partial \rho}{\partial t} + \nabla \cdot \mathbf{j}_c = 0, \quad (2.20)$$

being  $\rho$  the charge density. On the other hand, due to spin-flip relaxation processes, the spin current is not generally conserved. In this way, a similar continuity equation can be used to describe spin currents [56, 57]

$$\frac{\partial \mu_s}{\partial t} + \frac{1}{e\nu_F} \nabla \cdot \mathbf{j}_s = \frac{\mu_s}{\tau_s}, \quad (2.21)$$

where the extra term at the right hand-side of Eq. 2.21 reflects spin relaxation, being  $1/\tau_s = 1/\tau_{\uparrow\downarrow} + 1/\tau_{\downarrow\uparrow}$  the spin-flip relaxation rate [53, 54]. The terms  $1/\tau_{\uparrow\downarrow}$  and  $1/\tau_{\downarrow\uparrow}$  are defined as the scattering rate of flipping an electron spin from the up to down state and vice versa, respectively. The spin relaxation time  $\tau_s$  should not be confused with the electron relaxation time  $\tau$  defined in Eq. 2.13. In fact, in 3d transition metals the rate of scattering events without spin flip is much larger than  $\tau_s^{-1}$  [54, 55].

The equation describing spin diffusion in a normal metal can be easily obtained from Eqs. 2.21. In the steady state,  $\partial \mu_s / \partial t = 0$ , and Eq. 2.21 reads  $\nabla \cdot \mathbf{j}_s = (e\nu_F / \tau_s) \mu_s$ .

Therefore, by combining this result with Eq. 2.19 one gets the spin diffusion equation [53, 54, 55, 56, 58],

$$\nabla^2 \mu_s = \frac{1}{\lambda_{sd}^2} \mu_s, \quad (2.22)$$

where  $(1/\lambda_{sd}^2) \equiv e^2 \nu_F / (\sigma \tau_s)$  is the *spin diffusion length*. The spin diffusion length is a material-dependent phenomenological quantity that accounts for the decay of a spin current along its propagation direction [59]. Hence, it is one of the most valuable figures of merit in spintronics.

It is worth noting that the spin continuity equation presented above is only valid for a given spin polarization direction (i.e., up- and down-spin states in relation to a given quantization axis). In general, the flow of spin current is best described as a second rank tensor  $\mathcal{J}_{s,\alpha}^\sigma$  instead of a vector such as ordinary charge current.  $\mathcal{J}_{s,\alpha}^\sigma$  describes a spin current density propagating along the  $\alpha$  spatial direction and with spin polarization along  $\sigma$ . In this picture, Eq. 2.21 becomes

$$\frac{\partial \mu_s^\sigma}{\partial t} + \frac{1}{e \nu_F} \partial_\alpha \mathcal{J}_{s,\alpha}^\sigma = \Gamma_{\sigma\gamma} \mu_s^\gamma, \quad (2.23)$$

which is the spin continuity equation for an arbitrary spin polarization direction. Here,  $\Gamma_{\sigma\gamma}$  is the spin-flip relaxation tensor [57] and  $\boldsymbol{\mu}_s$  is the spin accumulation vector.

As a final remark, it should be mentioned that the spin current tensor that appears in Eq. 2.23 is not limited to the picture of two spin-polarized charge currents with opposing directions, as described in Eq. 2.19. In fact, spin current is just a fancy name for describing the coherent propagation of spin angular momentum. In solids, this spin current can be carried by conduction electrons, but it may as well be carried by so-called *spin waves*, which can be defined as the collective motion of spins coupled by the exchange interaction [60]. The quantization of spin waves is called a *magnon* and sometimes these two terms are used on an equal basis. It has been observed that spin wave spin currents persist over longer distances compared to their charge-mediated counterparts. Actually, the transmission of spin wave spin current signals over macroscopic distances ( $\approx 1$  mm) has been reported [60]. In Fig. 2.1, a schematic diagram of these two types of spin currents is shown. Finally, a third, yet obvious kind of spin current is that of spin-polarized charge current: since electrons have spins, the motion of an electron entails the transmission of spins.

In the next Section, the spin-charge coupling of currents is addressed, with special

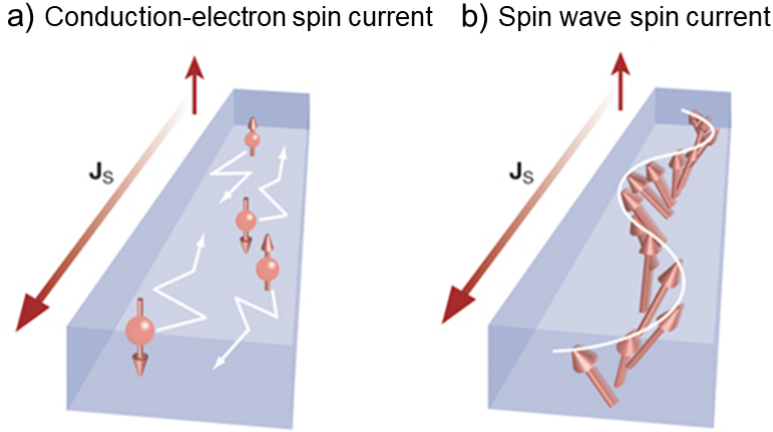


Figure 2.1: Schematic diagram of a spin current carried by opposing spin polarized charge currents (a), and carried by spin waves (b). This image has been adapted from Ref. [60].

emphasis on spin-orbit coupling and spin-dependent Hall effects.

## 2.4 Spin-Orbit Coupling

A key feature of spintronics is the easy interconversion between charge and spin currents. The underlying mechanism behind this phenomenon is the so-called spin Hall effect, which has its origin in spin-orbit coupling (SOC) and is closely related to the physics of the anomalous Hall effect. In order to illustrate the basic features of SOC, let's suppose that an electron is moving through an electric field  $\mathbf{E} = -\nabla\phi$ . In its frame of reference it experiences a magnetic field  $\mathbf{B}$  equal to [61]

$$\mathbf{B} = -\frac{\mathbf{v} \times \mathbf{E}}{c^2}, \quad (2.24)$$

where  $\mathbf{v}$  is the electron velocity and  $c$  the speed of light in vacuum. The (Zeeman) interaction between this magnetic field and the electron spin  $\hat{\sigma}$  is SOC. If  $\xi$  is the SOC strength constant, the SOC Hamiltonian is given by [61, 62]

$$\mathcal{H}_{SO} = \frac{\xi}{\hbar} \hat{\sigma} (\nabla\phi \times \mathbf{p}), \quad (2.25)$$

where  $\nabla\phi$  is the gradient of the scalar potential,  $\mathbf{p}$  the linear momentum operator, and  $\hat{\boldsymbol{\sigma}}$  is a vector of Pauli matrices. In a solid, for instance,  $\phi$  would be the potential arising from the crystal structure, impurities, or defects [61]. This ultimately means that the electron spin is absolutely bounded to its environment. In fact, SOC is the primary reason of why spin currents are not conserved, or as S. Maekawa puts it: “In the presence of spin-orbit interaction [...] the non-conservation of spin is due to the angular momentum transfer of spin to the orbit and eventually into macroscopic degrees of freedom such as the lattice system” [53, p. 14]. In order to have a clearer picture of this interaction, let’s use the central potential approximation for a hydrogen atom, i.e.,  $\phi(\mathbf{r}) = \phi(r) \Rightarrow \nabla\phi = (\partial_r\phi/r)\hat{\mathbf{r}}$ , where  $\hat{\mathbf{r}}$  is the unit vector of the radial direction  $r$ . In this case, it is easy to see that

$$\mathcal{H}_{SO} = \frac{2\xi}{\hbar^2} (\partial_r\phi/r) \mathbf{s} \cdot \mathbf{l}, \quad (2.26)$$

where  $\mathbf{l} = \mathbf{r} \times \mathbf{p}$  and  $\mathbf{s} = (\hbar/2)\hat{\boldsymbol{\sigma}}$  are the orbital and spin angular momentum operators, respectively. While equation 2.26 is only an approximation for a hydrogen atom, we can glimpse what it means. Assuming that the orbital angular momentum  $\mathbf{l}$  is connected to the crystal lattice, the spin-orbit interaction would couple the spin to the crystal lattice symmetry, giving rise to magnetocrystalline anisotropy [63], as mentioned in Section 2.1.

Hitherto, SOC is viewed as an interaction that connects the spin of the electrons with its environment, but how strong is this interaction and which materials have the highest SOC? To answer this requires the solving of the Schrödinger equation with the spin-orbit Hamiltonian (Eq. 2.26). The solution evidences that the spin-orbit coupling energy scales as  $\sim Z^4$  and  $n^{-3}$  [64], being  $Z$  the atomic number and  $n$  the principal quantum number. However, it should be bore in mind that this is only an approximation and, thus, it has limited validity. In Fig. 2.2 the calculated SOC strength  $\lambda_{nl}$ <sup>2</sup> (from Ref. [65]) as a function of the atomic number  $Z$  is shown. It is inferred from it that the  $Z^4$  dependence expected for the hydrogen atoms is just an approximation. Moreover, it is observed that 5d transition heavy metals such as Pt, W, Ta, or Ir present a higher spin-orbit coupling than 3d transition metals and therefore should be very suited for spintronic applications. Particularly, Pt is chosen

---

<sup>2</sup>The SOC strength for individual electron orbitals  $\lambda_{nl}$  is defined in Ref. [65] and is related to  $\xi$  from Eq. 2.25 by

$$\lambda_{nl} = \frac{l}{2}\xi \int_0^\infty dr \varphi_{nl}^2(r) \frac{1}{r} \frac{\partial\phi}{\partial r}, \quad (2.27)$$

where the radial wavefunction of the orbitals with quantum numbers  $n$  and  $l$  is denoted by  $\varphi_{nl}$ , and  $\xi \equiv g\hbar^2 e / (m^2 c^2)$  is the SOC strength defined in Eq. 2.25, with  $g$ ,  $m$ , and  $c$  being the  $g$ -factor, the electron’s rest mass, and the speed of light in vacuum, respectively.

as the high-SOC element of all the systems presented in this Thesis, while Ir (from  $\text{SrIrO}_3$ ) is used in Chapter 5.

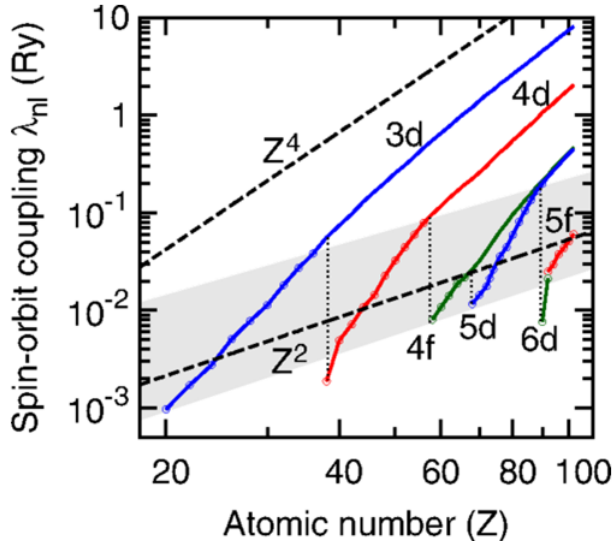


Figure 2.2: Dependence of the individual SOC strength  $\lambda_{nl}$  for atoms as a function of their atomic number  $Z$ . This figure has been retrieved from Ref. [65].

Technologically speaking, the fact that SOC connects the spin degree of freedom with other degrees of freedom of a given system makes it a very attractive property. Moreover, due to its prominent role on a variety of phenomena such as spin Hall effects, spin-orbit torques, or topological insulators, a new field of research called spin-orbitronics is emerging, and novel applications and phenomena are being addressed [66]. In this Thesis we fundamentally focus on the spin Hall effect, in which SOC plays a fundamental role by mediating the interconversion between spin and charge currents.

## 2.5 Spin Hall Effect

The spin Hall effects are the set of mechanisms that allow the interconversion between spin and charge currents. The underlying physical picture is analogous to that of the anomalous Hall effect (AHE) present in ferromagnetic materials, by which SOC makes spin-up and spin-down electrons to be scattered differently when flowing in a conductor. As in the case of the AHE, the spin Hall effect (SHE) can originate from three distinct microscopic mechanisms [67, 68]: intrinsic, skew scattering, and

side-jump. The intrinsic mechanism, as its name implies, depends entirely on the electronic band structure and it exists even in perfect crystals with no impurities nor disorder. Skew scattering and side-jump are regarded as extrinsic effects. In a broad sense, skew scattering and side-jump mechanisms are considered to arise from the SOC in the disorder potential and impurities, respectively [67].

SHE converts unpolarized charge currents into transverse pure spin currents. On the contrary, the inverse SHE (ISHE) converts pure spin currents into transverse charge currents. In Fig. 2.3 both SHE and ISHE mechanisms are illustrated. Although these effects were theoretically predicted over five decades ago by Dyakonov and Perel [11], it was not until the beginning of this century that they could be experimentally tested [10, 17, 69, 70, 71]. Both SHE and ISHE are very attractive from the technological point of view. In logic devices, for example, a new kind of all-semiconductor transistor based in SHE and ISHE has already been developed [72].

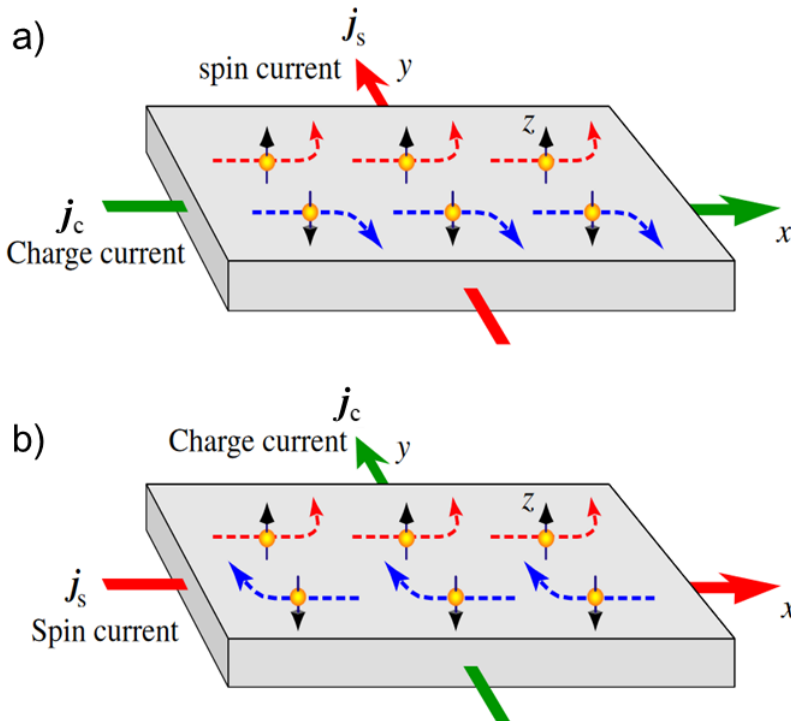


Figure 2.3: Schematic diagrams of SHE and ISHE mechanisms. In the SHE (a), a charge current  $j_c$  generates a transverse pure spin current  $j_s$ . Whereas in the ISHE (b), a pure spin current  $j_s$  is converted into a transverse charge current  $j_c$ . Image adapted from Ref. [73].



In order to mathematically express the interconnection between spin and charge currents in high-SOC systems, it is useful to follow the argument proposed by Dyakonov [74, 56], i.e., the spin-charge coupling is mediated by a single, SOC-dependent, phenomenological parameter: the spin Hall angle  $\Theta_{\text{SH}}$ . The drift-diffusion equation for charge and spin currents in systems *without* considering SOC is given by,

$$\mathbf{j}_c^{(0)} = \sigma \mathbf{E} + eD \nabla n, \quad (2.28)$$

$$\mathcal{J}_{s,\alpha}^{\sigma(0)} = \mu e \nu_{\text{F}} E_{\alpha} \mu_s^{\sigma} + e \nu_{\text{F}} D \frac{\partial \mu_s^{\sigma}}{\partial x_{\alpha}}, \quad (2.29)$$

where the superscript  $(0)$  denotes the charge and spin current densities without SOC. The index  $\alpha$  denotes the spatial propagation direction, while the index  $\sigma$  the spin polarization direction. The quantity  $\mu = en\sigma$  is the electron mobility. Furthermore, in order to account for SOC, the interconnection between spin and charge currents can be obtained by extending the usual drift-diffusion equation for charge transport to the spin-charge drift-diffusion equation. According to this [56, 67, 74, 75]:

$$j_{c,\alpha} = \sigma E_{\alpha} + eD \frac{\partial n}{\partial x_{\alpha}} + \Theta_{\text{SH}} \epsilon_{\alpha\beta\gamma} \left( \mu e \nu_{\text{F}} E_{\beta} \mu_s^{\gamma} + e \nu_{\text{F}} D \frac{\partial \mu_s^{\gamma}}{\partial x_{\beta}} \right), \quad (2.30)$$

$$\mathcal{J}_{s,\alpha}^{\sigma} = \mu e \nu_{\text{F}} E_{\alpha} \mu_s^{\sigma} + e \nu_{\text{F}} D \frac{\partial \mu_s^{\sigma}}{\partial x_{\alpha}} - \Theta_{\text{SH}} \epsilon_{\alpha\sigma\gamma} \left( \sigma E_{\gamma} + eD \frac{\partial n}{\partial x_{\gamma}} \right), \quad (2.31)$$

where  $\epsilon_{\alpha\sigma\gamma}$  is the Levi-Civita tensor, and the summation is made over repeated indices. Eqs. 2.30 and 2.31 cover the entire spin-charge coupling phenomena, and thermal effects can simply be added when required. Now, let's take a look in more detail at equations 2.30 and 2.31. The third term in the right hand side of Eq. 2.30 represents the AHE, while the fourth term, which expresses the charge current induced by an inhomogeneous spin accumulation, corresponds to ISHE. Regarding to Eq. 2.31, the third term in the right hand side represents the SHE originated from an electric field, while the fourth term represents the SHE from a diffusive current.

The interrelation between charge and spin currents can be expressed in a more familiar form. Note that Eqs. 2.30 and 2.31 can be rewritten as

$$j_{c,\alpha} = j_{c,\alpha}^{(0)} + \Theta_{\text{SH}} \epsilon_{\alpha\beta\gamma} \mathcal{J}_{s,\beta}^{\gamma(0)}, \quad (2.32)$$

$$\mathcal{J}_{s,\alpha}^{\sigma} = \mathcal{J}_{s,\alpha}^{\sigma(0)} - \Theta_{\text{SH}} \epsilon_{\alpha\sigma\gamma} j_{c,\gamma}^{(0)}. \quad (2.33)$$

Now, considering that  $\mathcal{J}_{s,\alpha}^{\sigma(0)} = 0$  (i.e.,  $\boldsymbol{\mu}_s = 0$ ), we get

$$\mathcal{J}_{s,\alpha}^{\sigma} = -\Theta_{\text{SH}}\epsilon_{\alpha\sigma\gamma}j_{c,\gamma}, \quad (2.34)$$

which corresponds to the spin current generated from a charge current due to the SHE. We can postulate that the spin current density tensor  $\mathcal{J}_{s,\alpha}^{\sigma}$  is expressed as the tensor product between  $\boldsymbol{j}_s$  and  $\hat{\boldsymbol{\sigma}}$ :  $\mathcal{J}_{s,\alpha}^{\sigma} = j_{s,\alpha}\hat{\sigma}_{\sigma}$ , being the latter a vector of Pauli matrices, and  $\boldsymbol{j}_s$  a vector along the spin current propagation direction. Thus, introducing this definition and multiplying both sides by  $\hat{\sigma}_{\sigma}$  one obtains

$$j_{s,\alpha}\hat{\sigma}_{\sigma}^2 = -\Theta_{\text{SH}}\epsilon_{\alpha\sigma\gamma}\sigma_{\sigma}j_{c,\gamma}, \quad (2.35)$$

which finally reduces to the more customary expression [17]

$$\boldsymbol{j}_s = \Theta_{\text{SH}}\boldsymbol{j}_c \times \hat{\boldsymbol{\sigma}}, \quad (2.36)$$

Likewise, following the same approach a simplified expression for the charge current generated by a spin current (ISHE) can be analogously found:

$$\boldsymbol{j}_c = \Theta_{\text{SH}}\boldsymbol{j}_s \times \hat{\boldsymbol{\sigma}}. \quad (2.37)$$

Experimentally, the SHE has been measured in several ways (see Ref. [76] and references therein), including both optical and electrical detection methods and different sample geometries and structures, being the most usual the non-local geometries, by which the injection of the charge current and the detection of the spin current are spatially separated. Due to the fact that SHE results in an spin imbalance, the electrical detection of this effect is trickier than in the case of ISHE, whereby the resulting charge current implies an electric voltage that can be detected by conventional means [17] (e.g., a voltmeter). Owing to the relative simplicity of detecting ISHE, it has become a popular method for detecting spin currents. Particularly, in this Thesis, we make use of Pt and SrIrO<sub>3</sub> thin films to electrically detect the spin current generated by spin pumping from a set of different adjacent ferromagnetic layers (Py, La<sub>0.92</sub>MnO<sub>3</sub>, and La<sub>2/3</sub>Sr<sub>1/3</sub>MnO<sub>3</sub>), as detailed later on.

## Magnetization Dynamics and Spin Pumping

So far, the magnetization and the magnetic degrees of freedom such as spin and spin polarization have been presented as static quantities or, at least, its dynamic behaviour has not been addressed. Due to the different physical phenomena covered in this Thesis and the experimental techniques involved, the understanding of magnetization dynamics is of paramount importance. Magnetization dynamics is central to areas such as magnetization reversal due to spin transfer torque, the generation of pure spin currents from magnetic precession (spin pumping), or magnon diffusion in ferromagnetic insulators. It is also worth mentioning the close relation between magnetization dynamics and energy dissipation and out-of-equilibrium processes. Therefore, the functionality and efficiency of spintronic devices involving some sort of dynamic magnetic regime are limited by these features. This Chapter is devoted to the introduction of the main features of this field. Section 3.1 introduces the main general principles and equations that govern magnetization dynamics in ferromagnetic systems and the magnetic relaxation mechanisms involved. Then, in Section 3.2, the theoretical principles of ferromagnetic resonance are outlined. The last two Sections of this Chapter cover the fundamental physical principles behind spin current transport across ferromagnetic/normal metal interfaces (Section 3.3) and the spin pumping effect (Section 3.4).

### 3.1 Landau-Lifshitz-Gilbert Equation

In the previous Chapter, the concept of magnetization field vector  $\mathbf{M}(\mathbf{r})$  was introduced. This quantity represents the local magnetization at every point of the ferromagnetic material and, therefore, determines its (equilibrium) state. However, dynamic and non-equilibrium states are also very important for a different set of phenomena. Hence, it is necessary to extend the concept of static magnetization  $\mathbf{M}(\mathbf{r})$  to the general, time-varying vector field  $\mathbf{M}(\mathbf{r}, t)$ . The time evolution of  $\mathbf{M}(\mathbf{r}, t)$  is the topic of magnetization dynamics. In order to construct a dynamical equation for magnetic phenomena, two main constraints should be taken into consideration [77]:

1. The magnitude of the local magnetization vector at each point is equal to the saturation magnetization  $M_s$  for a given temperature,

$$|\mathbf{M}(\mathbf{r}, t)| = M_s. \quad (3.1)$$

This is commonly known as the *macrospin* approximation. It is a fairly good approximation in ultrathin films of the order of exchange length (see Eq. 2.3), in which the collective magnetic moments are locked in the same direction.

2. The effective magnetic field  $\mathbf{H}_{\text{eff}}(\mathbf{r}, t)$  comprises all internal and external sources of magnetic field in the system. It can be mathematically defined as

$$\mu_0 \mathbf{H}_{\text{eff}}(\mathbf{r}, t) = -\frac{1}{V} \frac{\delta \mathcal{E}[\mathbf{M}(\mathbf{r}, t)]}{\delta \mathbf{M}(\mathbf{r}, t)}, \quad (3.2)$$

where  $\mathcal{E}[\mathbf{M}(\mathbf{r}, t)]$  is the magnetic free energy defined in the previous Chapter (see Eq. 2.10) and  $V$  the volume of the ferromagnetic specimen. Thus, the second constraint states that the magnetization vector in equilibrium is aligned with  $\mathbf{H}_{\text{eff}}(\mathbf{r}, t)$ , i.e., that  $\mathbf{M}(\mathbf{r}, t) \times \mathbf{H}_{\text{eff}}(\mathbf{r}, t) = 0$ .

Consequently, when the system is not at equilibrium,  $\mathbf{M}(\mathbf{r}, t) \times \mathbf{H}_{\text{eff}}(\mathbf{r}, t) \neq 0$ . In this case, the magnetization will evolve according to some sort of dynamic equation to restore equilibrium. The simplest form of this equation is that of the magnetization precessing around the effective field, which can be mathematically written as

$$\frac{\partial \mathbf{M}(\mathbf{r}, t)}{\partial t} = -\gamma \mathbf{M}(\mathbf{r}, t) \times \mathbf{H}_{\text{eff}}(\mathbf{r}, t), \quad (3.3)$$

where  $\gamma = g\mu_B/\hbar > 0$  is the gyromagnetic ratio, which determines the direction and rate of precession of the magnetization around the effective field,  $g$  is the  $g$ -factor, which quantifies the ratio between orbital and spin angular momenta and is

approximately 2 for free electrons, and  $\mu_B$  is Bohr's magneton. This equation was originally proposed by Landau and Lifshitz [78] and satisfies the two fundamental constraints mentioned above. Nevertheless, it describes a magnetization indefinitely precessing around the effective magnetic field, when in reality the magnetization vector relaxes and eventually aligns with the effective field direction. In general, magnetic relaxation or damping processes involve the transfer of energy from the magnetization field to microscopic thermal motion within the lattice of the magnetic system [79, 80]. The details on the specific mechanisms that allow this energy transfer are too complex to be taken into account explicitly in a single field equation [80]. Therefore, it is convenient to treat magnetic relaxation in a phenomenological way, i.e., introducing a damping parameter which can be determined experimentally but without knowing the details of the energy transfer mechanisms. The dependence of this damping parameter on the material properties and experimental setup may allow us to identify the different relaxation processes that comprise it [80]. The most common description of magnetization dynamics including relaxation is based on the Landau-Lifshitz-Gilbert (LLG) equation [80], which reads

$$\frac{\partial \mathbf{M}(\mathbf{r}, t)}{\partial t} = -\gamma \mathbf{M}(\mathbf{r}, t) \times \mathbf{H}_{\text{eff}}(\mathbf{r}, t) + \frac{\alpha}{M_s} \mathbf{M}(\mathbf{r}, t) \times \frac{\partial \mathbf{M}(\mathbf{r}, t)}{\partial t}, \quad (3.4)$$

and includes the dimensionless Gilbert damping parameter  $\alpha$ . As can be observed, the right hand side of Eq. 3.4 is composed of two terms that induce a torque on the magnetization: (i) a field-like torque (first term) and (ii) a damping-like torque (second term). This fundamental equation describes the damped precessional motion of the magnetization around the effective field. In Fig. 3.1, a schematic diagram of the magnetization dynamics according to the LLG equation is shown.

In general, the physical mechanisms behind the Gilbert damping parameter  $\alpha$  can be divided into two main categories: intrinsic and extrinsic. The intrinsic damping mechanisms are inherent to the fundamental physical state of the ferromagnetic system and are commonly related to SOC [79]. On the other hand, an array of different phenomena can result in extrinsic damping contributions. For instance [79, 81]: magnetic inhomogeneities across the film, magnetic impurities, grain boundaries, structural defects, granular structures, doping, strain due to lattice mismatch, local anisotropies, or eddy currents [82]. The usual physical picture behind extrinsic mechanisms is that of two-magnon scattering, i.e., the relaxation of the uniform precessional mode into different non-uniform secondary modes [79, 81, 83]. In Fig. 3.2, a diagram of the different precessional dissipation channels and the pathways of energy transfer between them is shown. It is worth noticing that in Fig. 3.2 magnetic precession is induced by a radiofrequency (rf) magnetic field. The absorption of transverse rf magnetic fields by ferromagnetic specimens is known as ferromagnetic

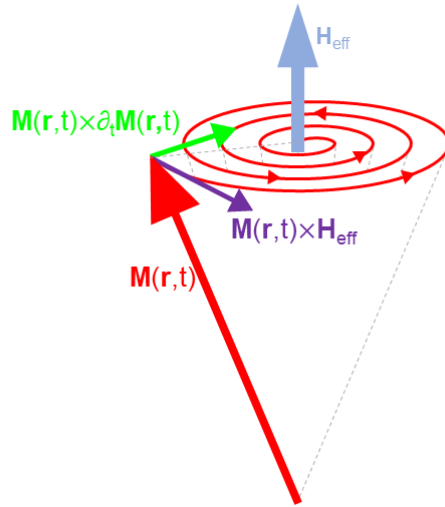


Figure 3.1: Schematic diagram of magnetization dynamics around an effective magnetic field according to the LLG equation (Eq. 3.4).

resonance, which is discussed in the next Section.

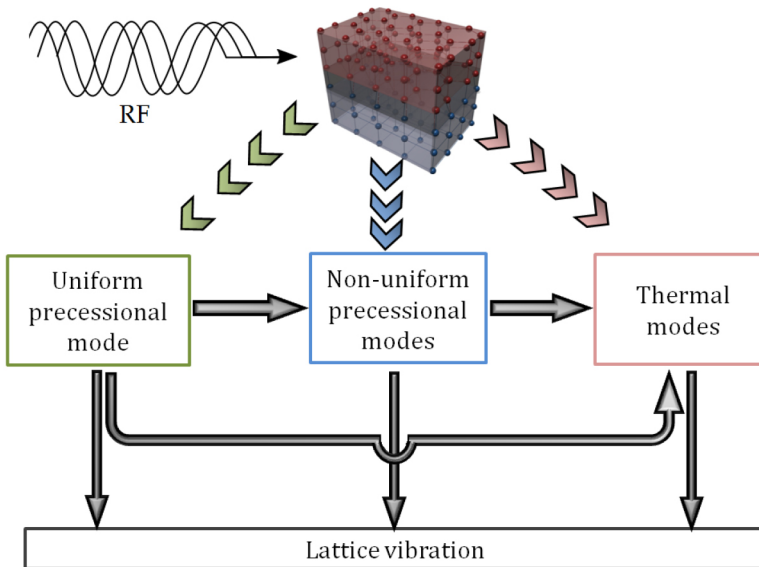


Figure 3.2: Precessional dissipation channels of ferromagnetic resonance.. We can see three precessional modes (uniform, non-uniform, and thermal) and the pathways of energy transfer between them. All three end up in the phonon bath of the lattice. Image retrieved from Ref. [79].

Owing to the inherent link between Gilbert damping and energy dissipation mechanisms, it has become one of the most important parameters for the development of energy efficient, low-consuming spin-based devices [84]. For instance, the transmission of spin waves in the context of magnonic devices requires the use of materials with ultra-low magnetic damping [60, 84, 85]. Moreover, ferromagnetic materials with very low Gilbert damping are also desired for applications related to spin transfer torque-induced magnetization reversal, since the threshold current needed would be lower [86, 87, 88]. While in spin pumping experiments the injection of spin currents from a precessing ferromagnet into a high-SOC non-magnetic metal entails an enhancement of  $\alpha$  [15]. Spin pumping is specially relevant in the context of this Thesis, as it is studied in four different bilayer systems. As such, a complete account of this effect and its relation to magnetization dynamics is found in Section 3.4. Before that, however, it is necessary to introduce the phenomenon of ferromagnetic resonance (Section 3.2), since it is at the core of the spin pumping effect and the bridge between it and magnetization dynamics, as well as the fundamentals of spin current transport at ferromagnetic/normal metal interfaces (Section 3.3).

## 3.2 Theory of Ferromagnetic Resonance

Ferromagnetic resonance (FMR) describes the absorption of transverse rf magnetic fields by ferromagnetic materials. It was independently discovered by Griffiths [89] and Zavoisky [90] in 1946 and its theoretical foundations were introduced by Kittel between 1947 and 1951 [91]. In Appendix A.2.2, the details of FMR spectroscopy are outlined. Nevertheless, in this Section, the theoretical principles of FMR as well as its main results are presented.

Let  $\mathbf{M}(\mathbf{r})$  be the magnetization vector in equilibrium and aligned with the effective magnetic field of the system  $\mathbf{H}_{\text{eff}}(\mathbf{r}) = \mathbf{H} + \mathbf{H}_{\text{eff}}^0(\mathbf{r})$ , where  $\mathbf{H}$  is an externally applied static magnetic field, and  $\mathbf{H}_{\text{eff}}^0(\mathbf{r})$  comprises all internal magnetic field contributions such as anisotropy fields. In the presence of a small transverse rf magnetic field  $\mathbf{h}(t)$ , the magnetization vector will precess around  $\mathbf{H}_{\text{eff}}(\mathbf{r})$  according to the LLG equation (Eq. 3.4). In most experiments, FMR absorption measurements are performed by fixing the frequency  $\omega$  of this incoming rf magnetic field  $\mathbf{h}(t)$  while sweeping the magnitude of the static magnetic field  $\mathbf{H}$ . The maximum of absorption (resonance) will occur when the Larmor frequency of the ferromagnetic system  $\omega_L = \gamma H_{\text{eff}}$  matches that of the incoming microwave. The two most important parameters in FMR experiments are the resonance field  $H_{\text{res}}$  and the resonance linewidth  $\Delta H$ . The former corresponds to the static field  $H$  at which the FMR absorption is maximum, whereas  $\Delta H$  is a signature of magnetic relaxation phenomena. The fitting of the respective curves relating the resonance frequency of the system with  $H_{\text{res}}$  and  $\Delta H$  allow us to

obtain the fundamental magnetodynamical properties of the system, i.e., saturation magnetization, gyromagnetic ratio (and  $g$ -factor), anisotropy contributions, Gilbert damping, and inhomogeneous damping. In this Section, an expression for the FMR microwave absorption of a ferromagnetic thin film as a function of the applied static field is calculated. This calculation will allow us to foresee the capabilities and power of FMR spectroscopy for the magnetic characterization of ferromagnetic specimens.

A general solution to the problem of finding the FMR absorption involves the combination of Maxwell's equations for the rf electric and magnetic fields in the film and the LLG equation to account for the magnetization dynamics [92]. This approach is actually followed in Chapter 4 to account for the variation of the rf fields across Py/Pt bilayers. However, this calculation can be substantially simplified if one considers that the magnitude of the rf magnetic field across the film is constant and that all magnetic moments are perfectly aligned with each other [92]. It is also important to mention that in the case of large extrinsic damping contributions this approach crumbles. However, *within* this limiting case, the LLG equation can be solved and analytic expressions of the FMR absorption can be obtained. Lastly, it is also assumed that the dominant contribution to the effective field is the applied static field, ensuring that the static component of the magnetization is aligned with it. In Fig. 3.3, a schematic diagram of the system and the main quantities involved in the calculation are shown. According to the diagram, the static magnetic field direction is along the  $z$  axis, while the dynamic magnetic field has components in the transverse directions,  $\mathbf{h}(t) = h_x e^{i\omega t} \hat{\mathbf{x}} + h_y e^{i\omega t} \hat{\mathbf{y}} + c.c.$ , where  $\omega = 2\pi f$  is the frequency of the rf field. On the other hand, the magnetization vector has both dynamic and static components,  $\mathbf{M}(\mathbf{r}, t) = M_s \hat{\mathbf{k}} + \mathbf{m}(t)$ , where  $\mathbf{m}(t) = m_x e^{i\omega t} \hat{\mathbf{x}} + m_y e^{i\omega t} \hat{\mathbf{y}} + c.c.$ . It should be mentioned that the quantities  $h_x$ ,  $h_y$ ,  $m_x$ , and  $m_y$  are complex numbers, i.e., have an amplitude and a phase. Moreover, since the magnitude of  $\mathbf{h}(t)$  is much lower than that of  $\mathbf{H}$ , it is reasonable to assume that the dynamic components of  $\mathbf{M}(\mathbf{r}, t)$  are also significantly smaller than  $M_s$ . Hence, we further assume that the length of the magnetization vector does not change,  $|\mathbf{M}(\mathbf{r}, t)| = \sqrt{M_z^2 + m_x^2 + m_y^2} = M_s$ , with  $M_z \gg m_x, m_y$ . Finally, due to the ultrathin thickness of the film, it is sound to consider that the main sources of anisotropy in the system are i) a second-order interface/surface anisotropy ( $K_2$ ), ii) shape anisotropy (through the demagnetizing field  $H_{d,i} = -4\pi N_i M_i$ , being  $i = x, y, z$ ), and iii) a fourth-order uniaxial anisotropy term ( $K_4$ ) related to the intrinsic properties of the film.

Now, taking into consideration all these ingredients, the LLG equation results in the following system of equations for  $m_x$  and  $m_y$ ,



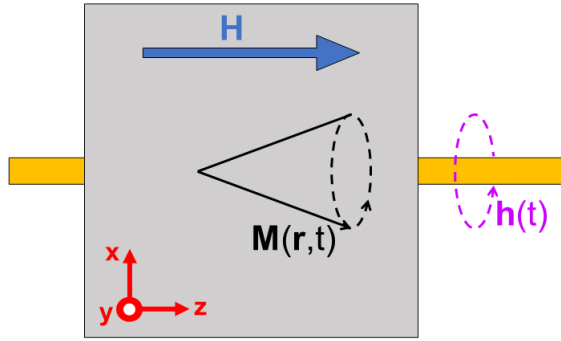


Figure 3.3: Schematic diagram of the FMR experimental setup with the main quantities involved. The rf magnetic field is supplied by a coplanar waveguide in our system (represented as a yellow stripe under the film).

$$m_x = \frac{i\gamma}{\omega} \left[ \mathfrak{B} + i\frac{\alpha}{\gamma}\omega \right] m_y - \frac{i\gamma}{\omega} M_{\text{eff}} h_y, \quad (3.5)$$

$$m_y = -\frac{i\gamma}{\omega} \left[ \mathfrak{H} + i\frac{\alpha}{\gamma}\omega \right] m_x + \frac{i\gamma}{\omega} M_{\text{eff}} h_x, \quad (3.6)$$

where  $4\pi M_{\text{eff}} = 4\pi M_s - 2K_2/M_s$  is the effective magnetization<sup>1</sup>,  $\mathfrak{B} = \mathfrak{H} + 4\pi M_{\text{eff}}$  is the magnetic induction, and  $\mathfrak{H} = H + 2K_4/M_s$ . Now, Eqs. 3.5 and 3.6 can be easily rearranged in order to express the dynamic components of the magnetization in terms of  $h_x$  and  $h_y$ . These quantities are related to each other through the dynamic susceptibility tensor  $\tilde{\chi}$  [93, 94, 95], i.e.,

$$\begin{pmatrix} m_x \\ m_y \\ 0 \end{pmatrix} = \begin{pmatrix} \chi_{xx} & i\chi_{xy} & 0 \\ -i\chi_{xy} & \chi_{yy} & 0 \\ 0 & 0 & 0 \end{pmatrix} \begin{pmatrix} h_x \\ h_y \\ 0 \end{pmatrix}. \quad (3.7)$$

Thus, combining Eqs. 3.5, 3.6, and 3.7 it can be shown that the elements of  $\tilde{\chi}$  are

<sup>1</sup>In order to obtain Eqs. 3.5 and 3.6 it has been assumed that the interface/surface anisotropy term  $K_2$  is very small compared to  $M_s$ . In this case,  $4\pi M_{\text{eff}} \approx 4\pi M_s$ . However, this is not always true, as is observed in Chapter 5 when studying the magnetodynamical properties of  $\text{La}_{0.92}\text{MnO}_3$  and  $\text{La}_{2/3}\text{Sr}_{1/3}\text{MnO}_3$ .

$$\chi_{xx} = \frac{-\gamma^2 \left( \mathfrak{B} + i\frac{\alpha}{\gamma}\omega \right) M_{\text{eff}}}{\omega^2 - \gamma^2 \left( \mathfrak{B} + i\frac{\alpha}{\gamma}\omega \right) \left( \mathfrak{H} + i\frac{\alpha}{\gamma}\omega \right)}, \quad (3.8)$$

$$\chi_{xy} = \frac{-\gamma\omega M_{\text{eff}}}{\omega^2 - \gamma^2 \left( \mathfrak{B} + i\frac{\alpha}{\gamma}\omega \right) \left( \mathfrak{H} + i\frac{\alpha}{\gamma}\omega \right)}, \quad (3.9)$$

$$\chi_{yy} = \frac{-\gamma^2 \left( \mathfrak{H} + i\frac{\alpha}{\gamma}\omega \right) M_{\text{eff}}}{\omega^2 - \gamma^2 \left( \mathfrak{B} + i\frac{\alpha}{\gamma}\omega \right) \left( \mathfrak{H} + i\frac{\alpha}{\gamma}\omega \right)}. \quad (3.10)$$

It should be noted that all the components of  $\tilde{\chi}$  have the same denominator. In this way, each susceptibility component becomes maximal (i.e., resonant) when  $\omega^2 = \gamma^2(\mathfrak{B} + i\alpha\omega/\gamma)(\mathfrak{H} + i\alpha\omega/\gamma)$  [92, 95, 94]. Consequently, taking  $\alpha = 0$  we find that the resonance frequency of the system corresponds to  $\omega = \gamma\sqrt{\mathfrak{B}_{\text{res}}\mathfrak{H}_{\text{res}}}$ , and taking into account the definitions of  $\mathfrak{B}$  and  $\mathfrak{H}$  it becomes

$$\omega = \gamma \left( H_{\text{res}} + \frac{2K_4}{M_s} \right)^{1/2} \times \left( H_{\text{res}} + \frac{2K_4}{M_s} + 4\pi M_{\text{eff}} \right)^{1/2}. \quad (3.11)$$

This result is the well-known Kittel Equation [91] and it is one of the primary results of FMR. As can be observed, the main magnetodynamical parameters of the system can be effectively obtained from the fitting of the curves relating the resonance frequencies with the corresponding resonance fields. Kittel equation is of the utmost importance in this Thesis since it is consistently employed for the magnetic characterization of the ferromagnetic films studied.

As is mentioned at the beginning of this Section, the two key parameters in FMR absorption curves are the resonance field  $H_{\text{res}}$  and resonance linewidth  $\Delta H$ . Kittel equation relates the resonance field with the resonance frequency, but how is  $\Delta H$  related to it? An answer to this question can be obtained by analysing the lineshape of FMR absorption curves derived from this approach. For doing so, we can re-write the static magnetic field  $H$  as  $H_{\text{res}} + (H - H_{\text{res}})$ . Then, keeping only terms linear with  $(H - H_{\text{res}}) + i\alpha\omega/\gamma$ , the susceptibility tensor elements (Eqs. 3.8, 3.9, and 3.10) become

$$\chi_{xx} = \frac{M_{\text{eff}}(\mathfrak{B}_{\text{res}} + H - H_{\text{res}} + i\frac{\alpha}{\gamma}\omega)}{(\mathfrak{B}_{\text{res}} + \mathfrak{H}_{\text{res}}) \left[ (H - H_{\text{res}}) + i\frac{\alpha}{\gamma}\omega \right]}, \quad (3.12)$$

$$\chi_{xy} = \frac{\omega M_{\text{eff}}}{\gamma(\mathfrak{B}_{\text{res}} + \mathfrak{H}_{\text{res}}) \left[ (H - H_{\text{res}}) + i\frac{\alpha}{\gamma}\omega \right]}, \quad (3.13)$$

$$\chi_{yy} = \frac{M_{\text{eff}}(\mathfrak{H}_{\text{res}} + H - H_{\text{res}} + i\frac{\alpha}{\gamma}\omega)}{(\mathfrak{B}_{\text{res}} + \mathfrak{H}_{\text{res}}) \left[ (H - H_{\text{res}}) + i\frac{\alpha}{\gamma}\omega \right]}. \quad (3.14)$$

Where  $\mathfrak{B}_{\text{res}}$  and  $\mathfrak{H}_{\text{res}}$  are the magnetic induction and magnetic field defined before but evaluated at  $H = H_{\text{res}}$ . Then, considering that near resonance  $|H - H_{\text{res}}| \ll H$ , that terms proportional to  $\alpha^2$  are very small in front  $\mathfrak{H}_{\text{res}}$ , and by separating the real and imaginary parts of each term, one finally obtains

$$(\chi_{xx}, \chi_{xy}, \chi_{yy}) = (A_{xx}, A_{xy}, A_{yy}) (\mathcal{D} - i\mathcal{L}), \quad (3.15)$$

where

$$A_{xx} \approx \frac{M_{\text{eff}}\mathfrak{B}_{\text{res}}}{\Delta H(\mathfrak{B}_{\text{res}} + \mathfrak{H}_{\text{res}})}, \quad (3.16)$$

$$A_{xy} \approx \frac{\omega M_{\text{eff}}}{\gamma\Delta H(\mathfrak{B}_{\text{res}} + \mathfrak{H}_{\text{res}})}, \quad (3.17)$$

$$A_{yy} \approx \frac{M_{\text{eff}}\mathfrak{H}_{\text{res}}}{\Delta H(\mathfrak{B}_{\text{res}} + \mathfrak{H}_{\text{res}})}, \quad (3.18)$$

$$(3.19)$$

and

$$\mathcal{D} = \frac{\Delta H(H - H_{\text{res}})}{(H - H_{\text{res}})^2 + \Delta H^2}, \quad (3.20)$$

$$\mathcal{L} = \frac{\Delta H^2}{(H - H_{\text{res}})^2 + \Delta H^2}, \quad (3.21)$$

being the resonance linewidth defined as  $\Delta H = \alpha\omega/\gamma$ , which means that it depends linearly on the resonance frequency. In experiments, in order to account for possible

contributions arising from small magnetic inhomogeneities present in the films, a frequency-independent (small) inhomogeneous damping term  $\Delta H(0)$  is also included, thus giving

$$\Delta H = \Delta H(0) + \frac{\alpha}{\gamma}\omega. \quad (3.22)$$

Kittel equation (Eq. 3.11) and Eq. 3.22 are the primary results on which FMR spectroscopy is based. By using Eqs. 3.20 and 3.21 one can define the spin resonance phase  $\phi$  as  $\tan \phi = \Delta H / (H - H_{\text{res}}) = \mathcal{L} / \mathcal{D}$ . This phase corresponds to the phase shift between the rf driving field and the dynamic magnetization response [93]. Near FMR,  $\phi$  changes sign over a field range close to  $\Delta H$  from  $180^\circ$  below  $H_{\text{res}}$  to  $0^\circ$  above  $H_{\text{res}}$  [93]. The terms  $\mathcal{D}$  and  $\mathcal{L}$  are, respectively, the dispersive (antisymmetric) and lorentzian (symmetric) contributions to the overall FMR absorption lineshape.

As a final remark, it is important to recall that the results presented in this Section were obtained under a series of approximations: i) ultrathin films of the order of exchange length (macrospin approximation) and thinner than the rf skin depth; ii) low anisotropy; and iii) intrinsic Gilbert damping mechanisms dominating over extrinsic contributions. Far from these approximations, the results outlined in this Section may not be true. This question is deeply discussed in Chapter 4 for the case of Py/Pt bilayers. In this system, it is suggested that extrinsic relaxation mechanisms may play a major role at low temperatures. Moreover, in Chapter 5, the presence of large interfacial anisotropy contributions hampers the linear relation between  $\Delta H$  and  $\omega$  outlined in Eq. 3.22. In either way, FMR not only allows us to characterize the magnetization dynamics of our films. Instead, FMR is also used for dynamically injecting spin currents from a precessing ferromagnet into an adjacent normal metal *via* spin pumping.

### 3.3 Spin Currents at the Interface Between a Ferromagnet and a Normal Metal

In Chapter 2, Mott's two channels model is introduced for describing and defining the charge and spin transport properties of ferromagnetic metals. As mentioned, Mott's model gained popularity throughout the 1970s in order to explain the novel GMR effect observed in spin-valve structures made of nickel and nickel-iron alloys [50, 51, 52]. In its simpler form, spin-valves are trilayer structures composed of two ferromagnetic films (FM1 and FM2) separated by a thin non-magnetic (NM) spacer. The large difference in resistance observed when the magnetizations of the

ferromagnets are parallel or antiparallel to each other is the GMR effect. In Fig. 3.4a a schematic diagram of a spin-valve structure for GMR is shown. It is known that an unpolarized charge current becomes polarized upon passing through a ferromagnet. In Fig. 3.4a, the current flowing from FM1 to the NM spacer creates a spin accumulation  $\mu_s$  in the NM film. If the spin coherence is maintained across the NM thickness, this current will flow and pass FM2 up to the other end of the system. It is important to notice that the build-up spin accumulation  $\mu_s$  at the NM spacer is simply a scalar quantity denoting the difference in electrochemical potential of up- and down-spin states. In this particular case and using Mott's arguments, an equivalent circuit can be used to represent the spin-valve trilayer system. This circuit is sketched in Fig. 3.4b and, as can be observed, the resistance of the NM film is considered to be negligible compared to the resistance of the ferromagnetic films. In a similar way, by combining conventional circuit theory with Mott's two channels model more complex structures can be studied.

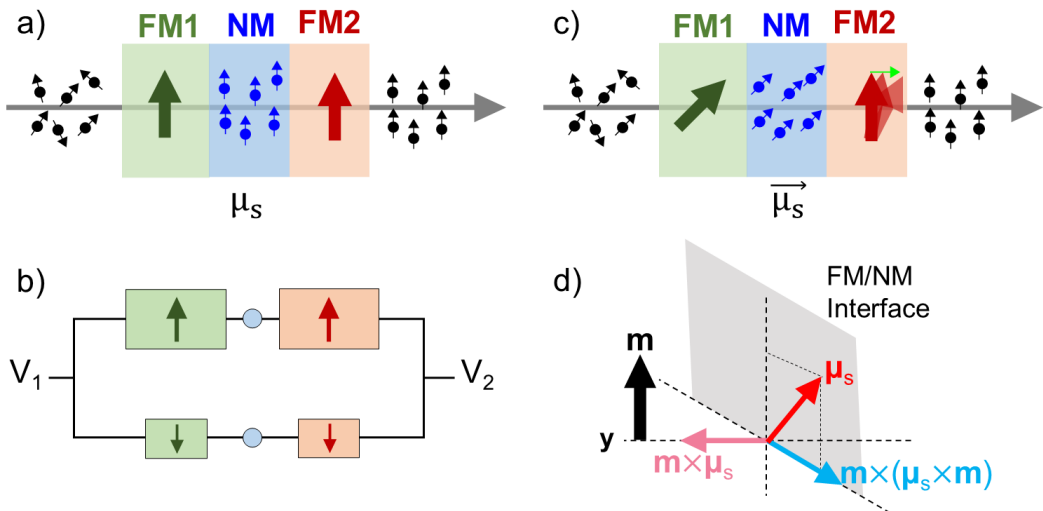


Figure 3.4: a) Schematic diagram of the typical spin-valve structure with a non-magnetic metallic layer sandwiched between two ferromagnetic films with collinear magnetizations. b) Electronic circuit interpretation of the system in (a), in which Mott's two channels model is applied. c) Spin-valve structure with a configuration in which the magnetizations are non-collinear. In this case, the two channel model cannot be applied and the vectorial nature of the spin accumulation  $\vec{\mu}_s$  must be fully taken into account. d) Vector representation of the transverse spin current components at the interface between a ferromagnet and a non-magnetic metal.

Moreover, at the beginning of this century, A. Brataas and co-workers developed *magneto-electronic* circuit theory (MCT) [96, 97, 98] with the object of studying charge and spin transport in spin-valve-like systems with non-collinear magnetizations using the framework of scattering theory. Contrary to GMR-like systems in which

the relative orientation between magnetizations is either parallel or antiparallel (i.e., collinear), in non-collinear systems the direction of the magnetizations is arbitrary by definition (see Fig. 3.4c). In this situation, the current flowing from the NM spacer into the FM2 film has spin components which are not eigenstates of the ferromagnet, but a coherent linear combination of up- and down-spin states. Thus, in non-collinear structures, the vectorial nature of spin accumulation  $\boldsymbol{\mu}_s$  in the NM must be fully taken into consideration [97, 98]. Moreover, it is obvious that the two channel model by which the conductivity of the ferromagnet is separated into two independent spin channels is no longer valid. Instead of that, a  $2 \times 2$  matrix representation in Pauli spin-space must be used [98]. In this model, the conductivity is best expressed as a  $2 \times 2$  matrix in which the diagonal, isotropic terms represent the usual spin-dependent conductances ( $G^\uparrow$  and  $G^\downarrow$ ), while the off-diagonal components are the so-called *spin-mixing* conductances ( $G^{\uparrow\downarrow}$ ) [98, 97]. The spin-mixing conductance is a parameter that depends on the properties of the FM/NM interface, and it is called *mixing* because it connects the two independent spin channels [99]. Within scattering theory, it depends on the reflection and transmission coefficients of the scattering matrix at the interface [98].

In non-collinear structures, the spin current at the FM/NM interface is composed of three different components: i) a *longitudinal* component parallel to the magnetization direction  $\mathbf{m} = \mathbf{M}/M_s$ , which is basically a spin polarized charge current; ii) a *transverse* component in the plane with  $\mathbf{m}$  and the spin accumulation  $\boldsymbol{\mu}_s$  in the NM; and iii) a transverse component normal to that plane. These transverse components are sketched in Fig. 3.4d. A thorough derivation of the general expression for the transverse spin current at the FM/NM interface can be found in the long article by Brataas, Bauer, and Kelly [98] and the final result is presented here for clarity. Supposing that the spin current propagates in the  $y$  direction and that the interface between the FM and the NM is at  $y = 0$  (see Fig. 3.4d), one gets [57, 98]

$$-ej_{s,y}\hat{\boldsymbol{\sigma}}(0) = G_s\boldsymbol{\mu}_s + G_r\mathbf{m} \times (\boldsymbol{\mu}_s \times \mathbf{m}) + G_i\mathbf{m} \times \boldsymbol{\mu}_s, \quad (3.23)$$

where  $\hat{\boldsymbol{\sigma}}$  is a vector of Pauli matrices denoting the spin current polarization direction,  $G_r$  and  $G_i$  are the real and imaginary parts of the spin-mixing conductance  $G^{\uparrow\downarrow}$ , and  $G_s$  is the spin-sink or effective conductance, which is independent of the relative orientation between  $\mathbf{m}$  and  $\boldsymbol{\mu}_s$  and is entirely related to spin-flip absorption processes at the interface [100].  $G_s$  is usually eluded in experiments describing spin transport across ferromagnetic/normal metal interfaces [101] but it becomes important when other magnetic textures are involved [57]. It is thus included here for completeness. In the remaining of this Chapter, however, it is dismissed, but its precise definition and role will become clear in Chapter 6 when studying spin Hall magnetoresistance in  $\text{La}_2\text{CoMnO}_6/\text{Pt}$  bilayers. It should be noted that  $G_s$ ,  $G_r$ , and  $G_i$  in Eq. 3.23 have

units of conductance per unit area ( $\Omega^{-1} \cdot \text{m}^{-2}$ ) since the spin current has units of current density ( $\text{A} \cdot \text{m}^{-2}$ ). In modern literature, however, these quantities are usually expressed in units of  $\text{m}^{-2}$ . This can be accomplished by simply dividing each term by  $e^2/\hbar$ , where  $e$  is the fundamental charge and  $\hbar$  the reduced Planck's constant. In this Thesis we will always express the spin-mixing conductance in units of  $\text{m}^{-2}$  unless otherwise indicated.

The transverse spin current components are very relevant for a different set of phenomena since they entail spin angular momentum transfer upon interaction with the ferromagnetic order parameter. Specifically, in a ferromagnet, the spin *decoherence* length  $\lambda_c$  characterizes the length over which the transverse spin current is *absorbed* by the ferromagnet. In 3d transition metals, it has been found that  $\lambda_c$  is comprised between the lattice parameter [98] and  $\approx 3 \text{ nm}$  [102, 103], although some authors argue that it should be much larger [104]. This means that most of the transverse spin current is lost at the first layers of the FM or at the interface between the FM and the NM. This destruction of angular momentum is per definition equal to a torque on the magnetization [53] (exemplified in Fig. 3.4c as a green arrow in the FM2 magnetization). In fact, the spin transfer torque (STT) independently discovered by Slonczewski et al. [13] and Berger [12] in 1996 is equivalent to the absorption of a spin current at the interface between a NM and a FM whose magnetization is transverse to the spin current polarization (or spin accumulation direction) [53, 105]. In general, this torque is proportional to  $-\mathbf{m} \times j_s \hat{\sigma} \times \mathbf{m}$ , and becomes proportional to the spin current  $-j_s \hat{\sigma}$  when  $\hat{\sigma} \perp \mathbf{m}$ . STT is the physical principle behind spin current-driven magnetization dynamics, since the torque  $\boldsymbol{\tau}$  is equal to the rate of change of magnetization, [53]

$$\boldsymbol{\tau} \equiv \frac{\partial \mathbf{m}}{\partial t} = -\frac{\gamma}{M_s t_{\text{FM}}} [G_r \mathbf{m} \times (\boldsymbol{\mu}_s \times \mathbf{m}) + G_i \mathbf{m} \times \boldsymbol{\mu}_s]. \quad (3.24)$$

Here,  $\gamma$  is the gyromagnetic ratio,  $M_s$  the saturation magnetization, and  $t_{\text{FM}}$  the thickness of the ferromagnetic film. It should also be noted that the strength of  $\boldsymbol{\tau}$  is proportional to the magnitude of the spin current at the FM/NM interface (see Eq. 3.23). In order to understand STT-driven magnetization dynamics,  $\boldsymbol{\tau}$  can be simply added as extra term to the LLG equation (Eq. 3.4). By doing so, it can be seen that the first term on the right hand side of Eq. 3.24 is parallel to the Gilbert damping-like torque term in the LLG equation. In this way, when both terms point in the same direction, the magnetization vector will reach equilibrium faster. Conversely, when STT opposes damping-like torque, magnetization reversal may take place [13, 106, 2]. As a result, ultralow damping materials are very suited for STT-driven magnetization reversal processes due to the larger impact of  $\boldsymbol{\tau}$  on their dynamics. In Fig. 3.5, a schematic diagram of magnetization reversal considering the magnitude

of the applied spin current is shown. Additionally, the second term on the right hand side of Eq. 3.24 can be understood as the precession of spin accumulation around the magnetization field, and modifies the field-like torque term in the LLG equation and precession frequency [53].

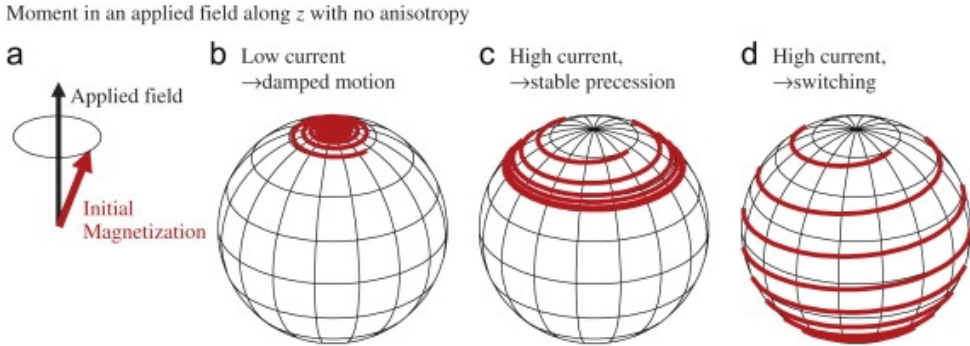


Figure 3.5: a) Initial magnetic configuration with the magnetization vector at an angle with the applied magnetic field, for instance due to a thermal fluctuation. b) For spin currents below the critical current, the magnetization vector spirals back to equilibrium position, i.e., aligned with the magnetic field. c) For currents higher than the critical value, the damping-like torque term becomes negative and the magnetization vector spirals away from the magnetic field. In this case, the final configuration might be that of an steady precession state with large precession angle (c) or full magnetization reversal (d). Image adapted from Ref. [106].

### 3.3.1 Spin Hall Magnetoresistance

In a FMI/NM bilayer system (where FMI stands for FM insulator) a charge current flowing through the high-SOC NM film may be converted to a transverse spin current due to the SHE. This spin current is directed towards the FMI/NM interface and depending on the relative orientation between its spin polarization direction  $\hat{\sigma}$  and the magnetization direction  $\mathbf{M}$  of the FMI it may be absorbed *via* STT or reflected back to the NM layer. It turns out that the resistance measured when  $\hat{\sigma} \parallel \mathbf{M}$  or  $\hat{\sigma} \perp \mathbf{M}$  is different. This difference in resistance is the so-called spin Hall magnetoresistance effect. An exhaustive account on this effect is found in Chapter 6 for describing the spin Hall magnetoresistance measurements performed in the bilayer system composed by the ferromagnetic insulator  $\text{La}_2\text{CoMnO}_6$  and Pt.

In this Section, it was shown how magnetization dynamics can be induced due to the action of transverse spin currents in terms of spin transfer torque, with no magnetic fields involved. Consequently, it is natural to ask if the opposite is true, i.e., if magnetization dynamics can result in the emission of spin currents. Naturally, the answer to that question is affirmative: Magnetization dynamics can effectively emit



spin currents by means of an effect called *spin pumping*.

### 3.4 Spin Pumping

Spin current-induced magnetization dynamics is just one side of the coin. The reciprocal effect, known as spin pumping, entails that a moving magnetization in a FM can emit (*pump*) a spin current into an adjacent NM [107]. The scattering theory for spin currents induced by magnetization dynamics was developed by Tserkovnyak et al. [107] at the beginning of this century. However, the experimental realization of spin pumping can be traced back to the 1970s in the pioneering works of Silsbee, Jánossy, and Monod [108, 109], which postulated a coupling between the dynamic ferromagnetic magnetization and the spin accumulation in adjacent normal metals in order to explain the enhancement of microwave transmission through normal metal foils when coated by a ferromagnetic layer [53]. Spin pumping is of paramount importance for the development of this Thesis due to its intimate connection with magnetization dynamics, FMR, and spin current generation.

It was shown by Tserkovnyak et al. [107] that the pumped spin current out of the ferromagnetic material has the form

$$j_{s,y}^{\text{pump}} \hat{\sigma} = \frac{e}{4\pi} \left[ G_r \mathbf{m} \times \frac{\partial \mathbf{m}}{\partial t} + G_i \frac{\partial \mathbf{m}}{\partial t} \right], \quad (3.25)$$

which describes a spin current propagating in the  $y$  direction (i.e., normal to the FM/NM interface) with a time-dependent spin polarization oriented perpendicular to  $\mathbf{m} = \mathbf{M}(\mathbf{r}, t)/M_s$ . A schematic diagram of the spin pumping effect is shown in Fig. 3.6. The dc and ac components of the spin current are explicitly shown in the figure. It should be noted that, due to the small precession angles found in FMR experiments, the ac contribution is significantly larger than its dc counterpart. Nevertheless, due to the intrinsic difficulty to isolate the ac contribution from other extrinsic similar rf sources in FMR experiments, the majority of publications related to spin pumping phenomena have mainly focused on the dc component alone [110]. As such, the spin pumping-related measurements presented in this Thesis are focused on the detection of the dc component of the pumped spin current in FM/NM bilayers.

It should be noted that the pumped spin current depends on the real and imaginary parts of the spin-mixing conductance, just as in the case of STT (see Eq. 3.24). This feature arises from the fact the spin pumping and STT are actually different manifestations of the same physical reality [53, 107], i.e., the interplay of interfacial

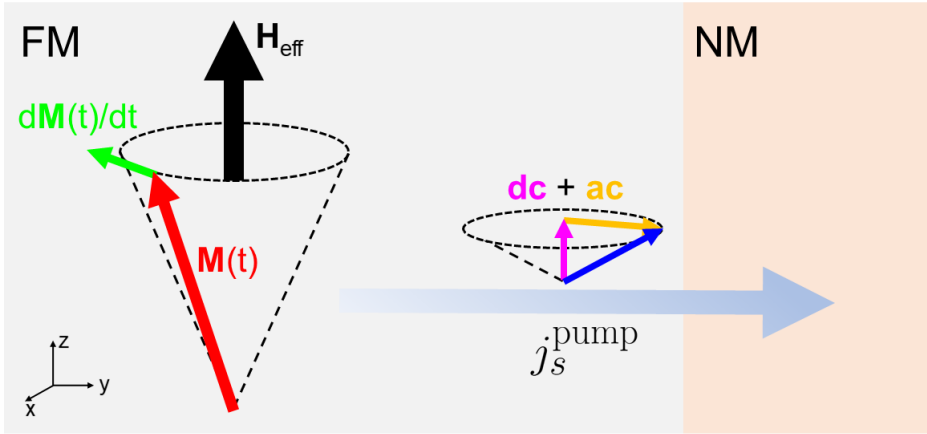


Figure 3.6: Schematic diagram of the spin pumping effect in a ferromagnetic (FM)/non-magnetic (NM) bilayer. The pumped spin current propagates towards the FM/NM interface and is spin polarized perpendicularly to the magnetization vector. The spin polarization is indicated as a blue arrow, and due to the dynamic nature of the system, it has both dc (magenta) and ac (yellow) components. The ac component rotates almost entirely in the  $x - y$  plane.

transverse spin currents with the magnetization of the ferromagnet. The effect of spin pumping on magnetization dynamics can be understood from the fact that the actual emission of spin produces a torque on the magnetization vector proportional to that current, just as in STT. This torque can be conveniently added to the LLG equation, resulting in an equation of the same form but with renormalized gyromagnetic ratio  $\gamma$  and Gilbert damping  $\alpha$  [15, 53, 107, 111]. It was shown by Tserkovnyak et al. [107] that the renormalized quantities read

$$\frac{\gamma}{\gamma'} = 1 - \frac{\gamma \hbar}{4\pi M_s t_{\text{FM}}} G_i, \quad (3.26)$$

$$\alpha' \frac{\gamma}{\gamma'} = \alpha + \frac{\gamma \hbar}{4\pi M_s t_{\text{FM}}} G_r, \quad (3.27)$$

where  $\alpha'$  and  $\gamma'$  are the new Gilbert damping and gyromagnetic ratio upon emission of spins through spin pumping, respectively. In this way, it is easy to see that in Eq. 3.25, the term proportional to  $G_r$  enhances the Gilbert damping parameter, while the term proportional to  $G_i$  changes the precession frequency. In FMR experiments, the effect of  $G_r$  is observed as an increase of the resonance linewidth, whereas that of  $G_i$  is

a displacement of the resonance field. However, in typical  $3d$  transition metals such as Fe, Ni or Co,  $G_i$  is generally much smaller than  $G_r$  [15, 53], and the effect of this term on magnetization dynamics is usually not observed in experiments. As such, one would simply observe an increase of the resonance linewidth after the deposition of the NM layer onto the FM film,

$$\alpha' = \alpha + \frac{\gamma\hbar}{4\pi M_s t_{\text{FM}}} G_r, \quad (3.28)$$

where  $\alpha$  is the Gilbert damping parameter of the FM film alone, and  $\alpha'$  the damping parameter of the FM/NM bilayer. The increase in  $\alpha$  can be intuitively understood if one considers that the spin current emitted by the dynamic magnetization is completely absorbed by the NM adjacent film. In this situation, the role of the NM layer is that of an additional channel of angular momentum dissipation.

So far, this model has assumed that the NM film is an ideal *spin sink* [107], i.e., a film that completely absorbs the pumped spin current. The injected spin current thus produces a spin accumulation in the NM film that decays as a consequence of spin relaxation and diffusion mechanisms. The spin accumulation in the NM follows the spin continuity equation [112, 113] presented in Chapter 2 (see Eq. 2.21). Now, considering that at the FM/NM interface ( $y = 0$ ),  $\partial_y \boldsymbol{\mu}_s = (e/\sigma) j_{s,y}^{\text{pump}} \hat{\boldsymbol{\sigma}}$ , and that at the end of the NM film ( $y = t_{\text{NM}}$ ) the spin current vanishes,  $\partial_y \boldsymbol{\mu}_s = 0$ , one can see that the spin current is [112, 113, 114]

$$j_{s,y}^{\text{pump}} \hat{\boldsymbol{\sigma}}(y) = j_{s,y}^{\text{pump}} \hat{\boldsymbol{\sigma}}(0) \frac{\sinh[(y - t_{\text{NM}})/\lambda_{\text{sd}}]}{\sinh(t_{\text{NM}}/\lambda_{\text{sd}})}, \quad (3.29)$$

being  $j_{s,y}^{\text{pump}} \hat{\boldsymbol{\sigma}}(0)$  the spin current defined by Eq. 3.25, and  $t_{\text{NM}}$  and  $\lambda_{\text{sd}}$  the thickness and spin diffusion length of the NM film. As such, the injected spin current diffuses away from the FM/NM interface inside the NM layer and decays on a length scale of the order of  $\lambda_{\text{sd}}$ . Therefore, it follows that only normal metals with high spin-flip scattering rates can be used as good spin sink materials. This feature is shared by heavy metals with high-SOC such as Pt, W, Ta, or Ir, just to mention a few. Lighter elements such as Al or Cr are less suited as spin sink elements due to their relatively low SOC [111]. In the event that the pumped spin current is not completely absorbed by the NM film, the injected spin accumulation will induce a restoring diffusive spin current towards the FM film. This so-called *backflow* spin current is described by Eq. 3.23 and effectively reduces the injected spin current. In the extreme situation of a backflow spin current being equal to the injected spin current, the net effect of spin pumping on magnetization dynamics is negligible. In this situation, the Gilbert damping parameter would remain constant. In general, in order to account

for backflow spin currents, it is convenient to express the pumped spin current (Eq. 3.25) and the increase of  $\alpha$  (Eq. 3.28) in terms of an effective spin-mixing conductance  $G_{\text{eff}}^{\uparrow\downarrow}$  instead of  $G_r$ .

### 3.4.1 Detection of Spin Pumping

As has been mentioned, the effect of spin pumping on FMR absorption measurements is the enhancement of the Gilbert damping parameter, which is observed as an increase of the resonance linewidth. However, if extrinsic damping mechanisms are non-negligible or dominate magnetic relaxation, this difference may not be clearly observed. Moreover, interfacial SOC may absorb, rotate and flip the spin of the electrons passing through the FM/NM in spin pumping experiments [115]. Magnetic impurities or disorder at the interface may as well contribute to the dissipation of spin currents, preventing them to enter into the NM layer. One way to clarify the injection of spin currents by spin pumping is by measuring the spin pumping-induced inverse spin Hall effect (SP-ISHE) voltage difference. As is mentioned in Chapter 2, high-SOC materials are very suitable for converting spin currents into transverse charge currents. In this way, the injected spin current into the NM layer may be effectively converted to a charge current by means of ISHE and electrically detected. In Fig. 3.7, a schematic diagram of the combined action of spin pumping and ISHE for detecting spin currents in FM/NM bilayers is shown. This experimental methodology is followed in Chapters 4 and 5 for studying the spin injection capabilities of Py,  $\text{La}_{0.92}\text{MnO}_3$ , and  $\text{La}_{2/3}\text{Sr}_{1/3}\text{MnO}_3$ , and the spin-to-charge conversion efficiency of Pt and  $\text{SrIrO}_3$ .

The injected spin current is transformed to a charge current according to Eq. 2.37:  $\mathbf{j}_c = \Theta_{\text{SH}} \mathbf{j}_s \times \hat{\boldsymbol{\sigma}}$ . In this case, taking into account the coordinate system of Fig. 3.6, the transverse charge current is expressed as  $\mathbf{j}_c = \Theta_{\text{SH}} j_s^{\text{pump}} \hat{\mathbf{j}} \times \hat{\mathbf{k}}$ . As a consequence, the voltage difference accompanying this current will be the ISHE voltage signal measured in the experiments, which is directly proportional to the amount of spin current injected into the NM film. The lineshape of this voltage signal can be obtained from the expression of the dc component of the pumped spin current. This component is calculated by performing the time average of Eq. 3.25, i.e., [110]

$$\langle j_{s,y}^{\text{pump}} \hat{\sigma}_z \rangle^{\text{DC}} = \frac{e\omega}{4\pi} G_{\text{eff}}^{\uparrow\downarrow} \Im(m_x^* m_y). \quad (3.30)$$

Moreover, the pumped spin current in FMR experiments arises from microwave-induced magnetization precession, which obeys the LLG equation, as detailed in Section 3.2. In that Section, it is stated that the dynamic susceptibility tensor  $\tilde{\chi}$

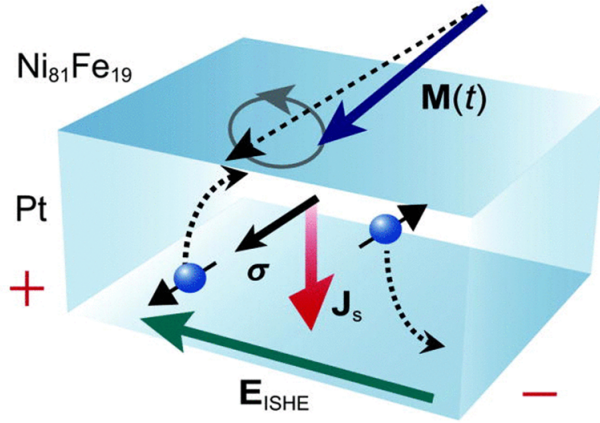


Figure 3.7: Schematic diagram of the measurement setup of spin pumping-induced ISHE currents. This image has been adapted from Ref. [116]

mediates the relation between the dynamic magnetization components ( $m_x(t)$  and  $m_y(t)$ ) and the rf magnetic field  $\mathbf{h}(t)$ :  $\mathbf{m}(t) = \tilde{\chi}\mathbf{h}(t)$ . Therefore, considering that  $h_x(t) = h_y(t) = h_{\text{rf}}$  and substituting Eqs. 3.7 and 3.15 into Eq. 3.30, is easy to see that

$$\langle j_{s,y}^{\text{pump}} \hat{\sigma}_z \rangle^{\text{DC}} = \frac{e\omega}{4\pi} \mathcal{A} h_{\text{rf}}^2 G_{\text{eff}}^{\uparrow\downarrow} \mathcal{L}, \quad (3.31)$$

being  $\mathcal{A} \equiv A_{xy}(A_{xx} - A_{yy})$ , where  $A_{xx}$ ,  $A_{yy}$ , and  $A_{xy}$  are material-dependent quantities defined in the Section 3.2, and  $\mathcal{L}$  is a symmetric lorentzian curve. This result shows that the amplitude of the DC pumped spin current injected into the NM film follows the lineshape of a symmetric lorentzian curve. Consequently, the expected ISHE voltage signal is also a symmetric lorentzian curve. In order to illustrate this property of spin pumping, let's take a look at Eq. 3.25: It states that the spin polarization direction of the pumped spin current  $\hat{\sigma}(t)$  is always perpendicular to  $\mathbf{M}(t)$ . Therefore, for small cone angles of precession, the spin polarization lies almost entirely in plane, resulting in a large ac component and a very small dc component (see Fig. 3.8a). However, at resonance, the cone angle of precession is maximized, and if one exaggerates the effect of this feature (see Fig. 3.8b)  $\hat{\sigma}(t)$  will point mostly out of plane, resulting in a small ac component and a large dc component. Obviously, this model is far from reality. For instance, the typical precession angles found in experiments are below  $10^\circ$  [117, 118]. In addition, it also assumes that the magnetization precession is circular, when it is usually elliptical due to the effect of demagnetizing

fields in thin films. In this way, an ellipticity factor should be included in Eq. 3.31. Nevertheless, it serves to illustrate the increase of amplitude in the spin current DC component upon resonance. A calculated spin current density according to this model as a function of the applied magnetic field is shown in Fig. 3.8c.

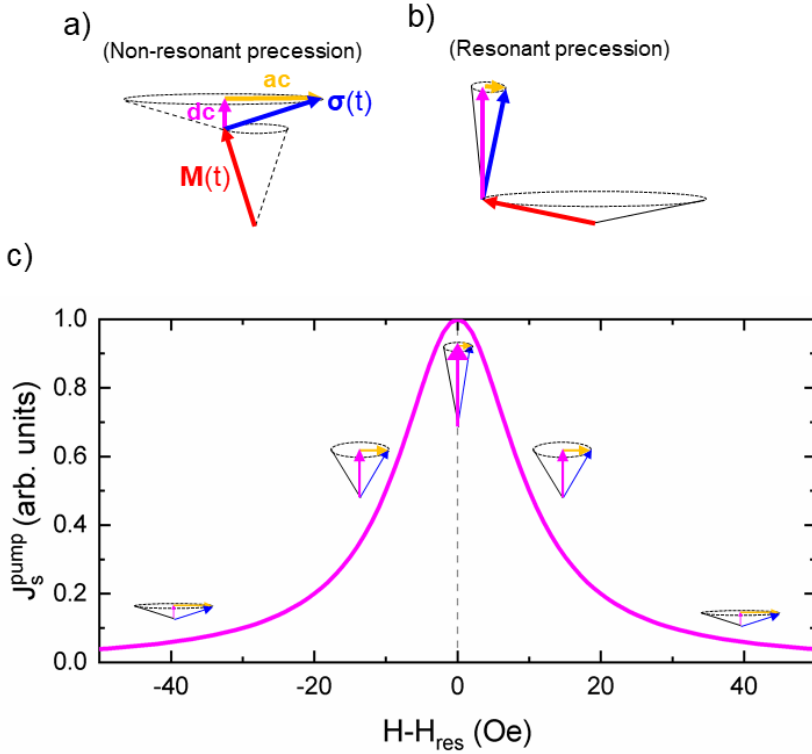


Figure 3.8: (a) Schematic diagram of showing the precession of the magnetization vector  $M(t)$  and the corresponding spin current spin polarization direction  $\hat{\sigma}(t)$ , which should be perpendicular to  $M(t)$ . The ac and dc components of the spin current are denoted by a yellow and magenta arrows. In this case, the precession angle is small and represents a situation far from the resonance conditions. (b) Large precession angle due to FMR, the dc component clearly increases in this scenario. (c) Representative curve denoting the pumped spin current amplitude across the resonance field and the corresponding precession of its spin polarization vector.

## Spin Pumping and Inverse Spin Hall Effect in Permalloy/Pt Bilayers

In this Chapter, the spin pumping (SP) and inverse spin Hall effects (ISHE) of Permalloy ( $\text{Ni}_{80}\text{Fe}_{20}$ , Py)/Pt bilayers are studied by means of ferromagnetic resonance. Due to the length and nature of each study, this Chapter is divided into two main parts: the first one is entirely devoted to the ferromagnetic resonance characterization of this system and the measurement of the SP effect in Py/Pt bilayers, including its evolution with temperature. The second one deals with the voltage measurements carried out in order to detect the ISHE and the difficulties to effectively separate it from other parasitic voltage signals.

Regarding the first part, the structural characterization and growth conditions of the samples as well as their static magnetic properties are introduced in Section 4.1.1. Section 4.1.2 deals with the experimental methods employed in these measurements and covers the entire ferromagnetic resonance characterization of each sample at 300K, as well as the detection of SP. Finally, Section 4.1.3 covers the evolution of the magnetodynamical parameters in Py and Py/Pt with temperature.

Part two starts with a description of the experiment and the experimental setup (Section 4.2.1), in which a brief introduction to the voltage measurements in combination with FMR and its main difficulties is presented. In Section 4.2.2, the new samples prepared for these kind of measurements are described and their complete 300K FMR characterization is addressed. Then, in Section 4.2.3, the first voltage measurements of the samples are shown and discussed. The

result of these measurements is that the dominant contribution to the voltage effectively comes from so-called spin rectifications effect (SRE) instead of from ISHE. In order to circumvent this problem, we hypothesise that a reduction in the sample width  $L$  along the coplanar waveguide (CPW) direction will reduce in accordance the SRE. In order to test this hypothesis, in Section 4.2.4, the complete FMR characterization and voltage measurements of the samples with reduced sample width  $L$  are shown and discussed. Finally, in order to straighten the interpretation of our results, a numerical calculation of the Maxwell's equations of the Si//Py/Pt system with the Landau-Lifshitz-Gilbert (LLG) equation as the constitutive equation of the system is shown (Section 4.2.5).

## 4.1 FMR Characterization and Spin Pumping in Py and Py/Pt Systems

### 4.1.1 Samples Characterization and Growth Conditions

A set of Py ( $\text{Ni}_{80}\text{Fe}_{20}$ )/Pt samples with different Pt capping layer thickness was grown by means of dc magnetron sputtering, at room temperature, on top of  $5 \times 5 \text{ mm}^2$  silicon (Si) substrates (with a natural passivation layer of  $\text{SiO}_2$ ). In order to get an optimal interface between the Py and the Pt layers, the Pt capping layers were deposited *in situ* in the sputtering chamber. The Py layer was grown at 3 mTorr in Ar- $\text{H}_2$  atmosphere, while the Pt was grown at 5 mTorr in the same atmosphere. The overall deposition process was carried out at room temperature. The thickness of the Py samples was approximately 20 nm for all samples, while the Pt layer thickness was different in each sample, i.e., 0 nm, 1.25 nm, 2.5 nm, and 5 nm. An outline of the four samples is presented in Fig. 4.1.

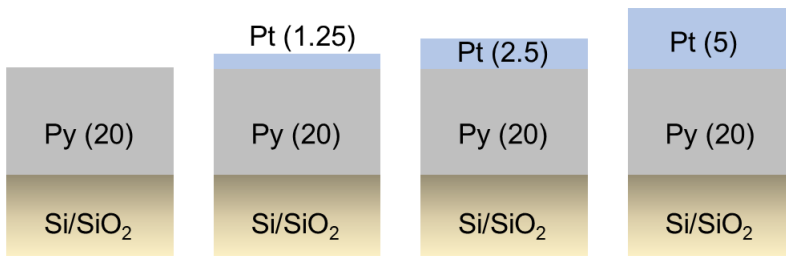


Figure 4.1: Schematic outline of the four samples employed in this section. The number in parenthesis represents the thickness in nanometers of each film.



The growth rate of each material was calibrated by standard X-ray reflectometry (XRR) measurements (using a Siemens D5000 diffractometer), as can be seen in Fig. 4.2. It is important to note that in the case of Pt (Fig. 4.2b) the calibrated growth rate is roughly 4 nm/min, which is quite fast considering that the desired Pt thicknesses oscillates between 1 and 5 nm. In order to overcome this issue, the actual sputtering power employed in the deposition of the Pt capping layers was half of that used in the calibration film (in this case, from 10W in the calibration film to 5W in the layers). Since the growth rate is linearly dependent with the sputtering power, the 4 nm/min calibrated rate should reduce to 2 nm/min, which is more reasonable in this case. The XRR fitting process to determine the thickness of the layers is exposed in the Appendix A.3.2.

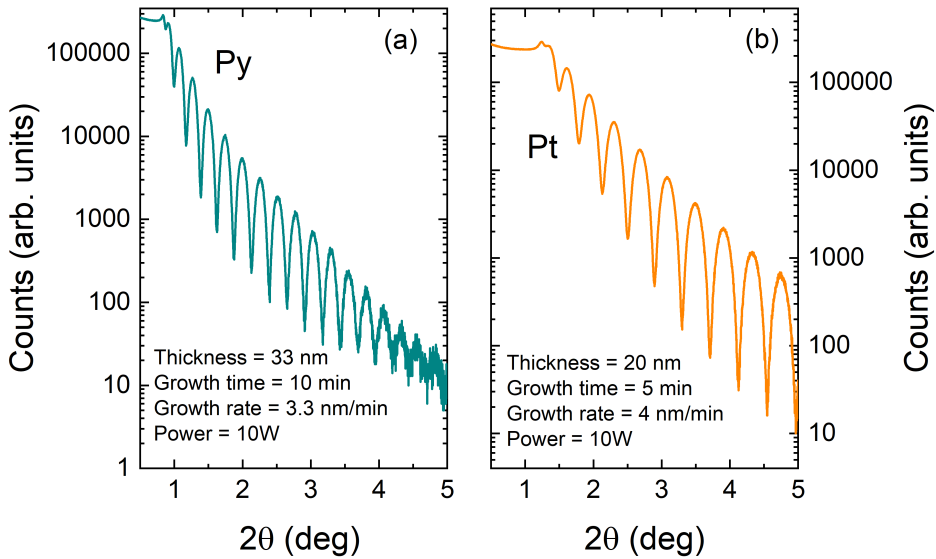


Figure 4.2: Experimental X-ray reflectometry measurements for the calibration of the sputtering growth rate using Py (a) and Pt (b) calibration samples.

Moreover, the static magnetic properties of the Py ferromagnetic layers were studied using SQUID magnetometry measurements (MPMS-XL by Quantum Design). The different measured hysteresis loops as a function of temperature for a Py film (20 nm) are shown in Fig. 4.3. A mild 10% increase in the saturation magnetization from 300K to 10K is observed, as expected from the fact that Py has the Curie point above 500K [119]. Moreover, the characteristic 300K low coercive field of Py (around 3 Oe) is also observed. Additionally, although this coercive field increases at low temperatures, it remains relatively small in comparison with the saturation magnetization value or the FMR magnetic field magnitudes employed, as will be shown, for instance.

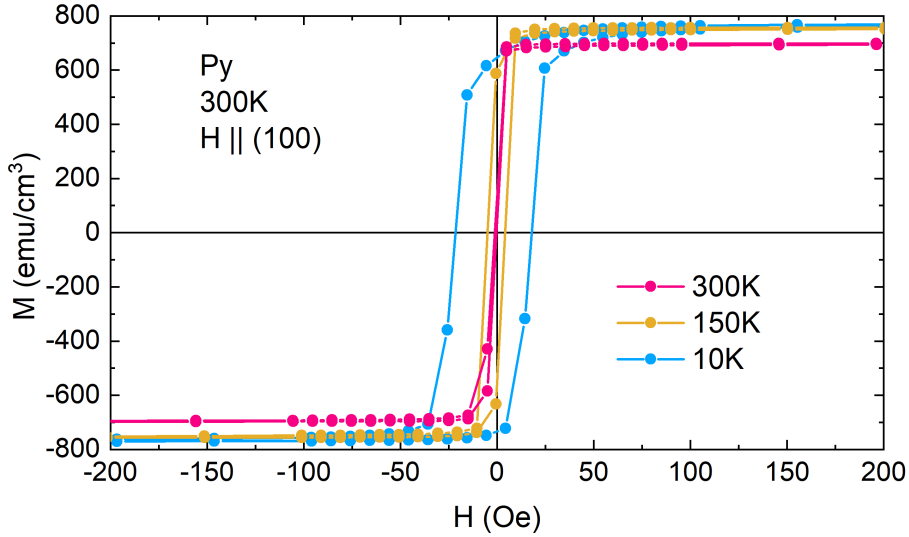


Figure 4.3: Hysteresis loops as a function of temperature measured in a Py film of 20 nm.

#### 4.1.2 Room Temperature FMR and Spin Pumping Characterization of Py and Py/Pt Bilayers

The magnetodynamical properties of the Py and Py/Pt thin films were studied by means of ferromagnetic resonance spectroscopy (FMR) using a broadband coplanar waveguide (CPW) (NanOsc). Both CPW and sample were further inserted in a Physical Properties Measurement System (PPMS by Quantum Design) in order to allow temperature dependent measurements if wanted (see Appendix A.2.2). Each measurement was performed at stabilized, constant temperature using a sweeping external magnetic field at different fixed frequencies (from 2 GHz to 16 GHz).

In a typical FMR experiment, the magnetization direction is fixed by the application of an external magnetic field  $\mathbf{H}_{\text{dc}}$  sufficiently large to saturate the magnetization of the ferromagnetic layer (in the 300K case, for instance, it has to be larger than 3 Oe, i.e., the coercive field of Py). At the same time, a transverse, oscillating magnetic field  $\mathbf{h}_{\text{rf}}$  drives the magnetization to a dynamical, out-of-equilibrium, precessional state around the applied magnetic field. The equation of motion of this system is described by the phenomenological Landau-Lifshitz-Gilbert (LLG) equation (see Chapter 3),

$$\frac{\partial \mathbf{M}(t)}{\partial t} = -\gamma \mathbf{M}(t) \times \mathbf{H}_{\text{eff}} + \frac{\alpha}{M_s} \mathbf{M}(t) \times \frac{\partial \mathbf{M}(t)}{\partial t}, \quad (4.1)$$

where  $\mathbf{H}_{\text{eff}} = \mathbf{H}_{\text{dc}} + \mathbf{h}_{\text{rf}} + \mathbf{H}_d$  is the effective magnetic field, being  $\mathbf{H}_d$  is the demagnetizing field contribution,  $\gamma = g\mu_B/\hbar$  is the gyromagnetic ratio,  $M_s$  is the saturation magnetization of the Py film, and  $\alpha$  is the dimensionless, phenomenological Gilbert damping parameter. The first term on the right hand side of Eq. 4.1 is a conservative term (it does not drive a change in  $\mathbf{M} \cdot \mathbf{H}_{\text{eff}}$ ), while the second one is a dissipative term. The combined action of the oscillating magnetic field  $\mathbf{h}_{\text{rf}}$  and the applied magnetic field  $\mathbf{H}_{\text{dc}}$  on the magnetization induces it to precess around the applied field at a frequency  $\omega_L = \gamma H_{\text{dc}}$ , being  $H_{\text{dc}}$  the magnitude of the applied field and  $\omega_L$  the so-called Larmor frequency. The resonance condition is fulfilled when  $\omega_L$  matches the frequency of the oscillating magnetic field  $\mathbf{h}_{\text{rf}}$ . At this point, the dissipative term becomes large, the sample absorbs energy from the CPW and a Lorentzian-shaped absorption peak  $S$  is observed. In fact, due to the differential lock-in detection method used, a derivative of the absorption peak  $dS/dH$  is observed instead. A representative example of this kind of absorption spectra as a function of frequency is shown in Fig. 4.4.

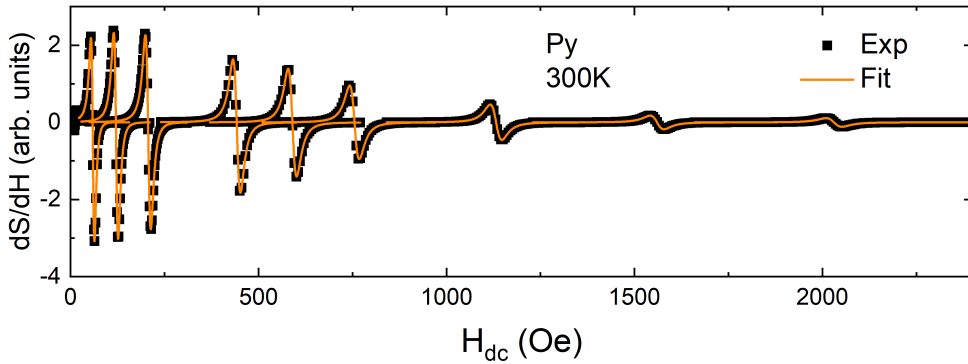


Figure 4.4: Example of ferromagnetic resonance spectra for a Py film (black bold symbols) sample and the fitting of each curve according to Eq. 4.2 (orange lines) at 300K.

Each curve of the absorption spectra shown in Fig. 4.4 can be accurately described as a combination of both symmetric and antisymmetric Lorentzian contributions, i.e.,

$$\frac{dS}{dH} = \frac{d}{dH} \left[ k_s \frac{\Delta H^2}{\Delta H^2 + (H - H_{\text{res}})^2} + k_{as} \frac{\Delta H(H - H_{\text{res}})}{\Delta H^2 + (H - H_{\text{res}})^2} \right], \quad (4.2)$$

where  $k_s$  and  $k_{as}$  are the (dimensionless) symmetric and antisymmetric amplitudes, respectively, and  $\Delta H$  and  $H_{\text{res}}$  are the linewidth and resonance field, respectively (for the sake of clarity, the magnitude of the applied magnetic field  $H_{\text{dc}}$  is denoted as  $H$  in Eq. 4.2 and hereafter). From the frequency dependence of these two fitting parameters ( $\Delta H$  and  $H_{\text{res}}$ ) the dynamical parameters of the sample such as the gyromagnetic ratio  $\gamma$ , the effective magnetization  $M_{\text{eff}}$  and the Gilbert damping parameter  $\alpha$  can

be obtained. The resonance frequency  $f_{\text{res}}$  and the resonance field  $H_{\text{res}}$  are related through the in-plane ( $H||[100]$ ) Kittel equation [120],

$$f_{\text{res}} = \frac{\gamma}{2\pi} \left( H_{\text{res}} + \frac{2K_4}{M_s} \right)^{1/2} \times \left( H_{\text{res}} + 4\pi M_{\text{eff}} + \frac{2K_4}{M_s} \right)^{1/2}, \quad (4.3)$$

where  $K_4$  is the fourth-order term of the magnetic anisotropy, and  $M_{\text{eff}}$  is the effective magnetization. This effective magnetization can be expressed as [79]  $4\pi M_{\text{eff}} = 4\pi M_s - 2K_2/M_s$ , being  $K_2$  the second-order or surface/interface anisotropy constant, which opposes the demagnetizing field. However, in the isotropic Py thin films, the anisotropic contributions (beyond shape anisotropy) are negligible, hence the effective magnetization in this case can be reduced to  $M_{\text{eff}} \approx M_s$  and  $K_4 \approx 0$ . On the other hand, the broadening of the resonance line, characterized by the linewidth  $\Delta H$ , is a direct measure of the magnetic damping of the system. Thus, the linewidth of the FMR spectra is described by a linear dependence on the resonance frequency,

$$\Delta H = \Delta H(0) + \frac{2\pi}{\gamma} \alpha f_{\text{res}}, \quad (4.4)$$

being  $\Delta H(0)$  the so-called inhomogeneous line broadening or damping, which is nearly zero for magnetically and structurally homogeneous systems, and  $\alpha$  the Gilbert damping parameter. The experimental dependence of  $H_{\text{res}}$  and  $\Delta H$  with the resonance frequency  $f_{\text{res}}$  at 300K is shown in Fig. 4.5. From Fig. 4.5a it is obvious that the inhomogeneous damping  $\Delta H(0)$  is close to zero in all samples (see the  $y$ -axis intercept of each line of points), denoting the magnetic homogeneity of the samples. Furthermore, a difference in the slope between the Py alone sample and the Py/Pt ones is significant. This difference, as is pointed out later, is attributed to the spin pumping effect. On the other hand, the overlap of curves in Fig. 4.5b indicates that the static magnetic properties ( $\gamma$ ,  $M_{\text{eff}}$  and  $K_4$ ) of all samples are very similar.

Using equations 4.3 and 4.4 to fit the curves from Fig. 4.5 (orange lines), the main magnetodynamical parameters for the Py alone layer and Py/Pt bilayers were obtained. Values are summarized in Table 4.1. It is important to notice that the saturation magnetization obtained from the FMR fitting matches that measured by SQUID magnetometry (see Fig. 4.3), as expected. The fitted anisotropy fields  $H_4 \equiv 2K_4/M_s$  are found to be negligibly small, as stated above. Additionally, the gyromagnetic ratio  $\gamma$  is nearly constant for all samples and results in a mean  $g$ -factor of about 2.1, in accordance with the reported values in the literature [121, 122, 123, 124].

Moreover, the obtained Gilbert damping parameter  $\alpha$  for the Py alone sample (around  $7 \times 10^{-3}$  at 300K, see Table 4.1) is close to reported values in the literature

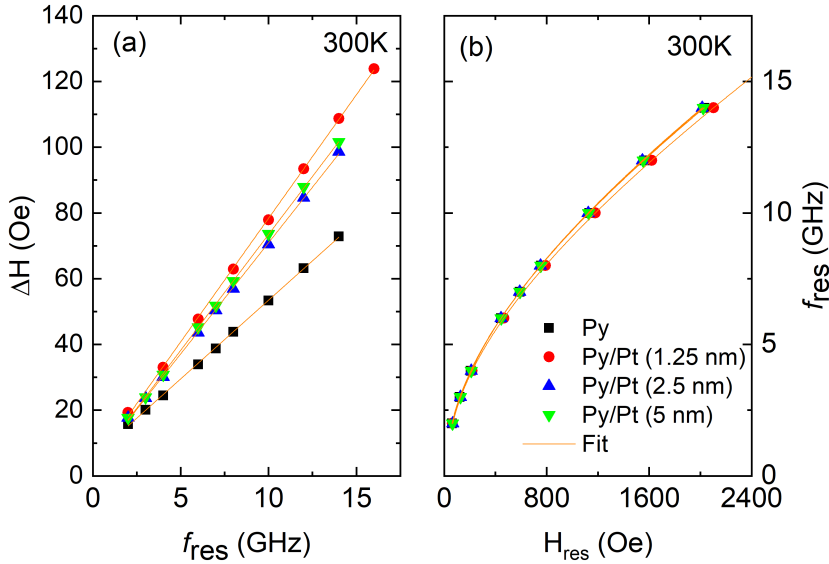


Figure 4.5: Dependence of the resonance linewidth on the resonance frequency. A linear dependence according to Eq. 4.4 is observed (a). Experimental dependence of the resonance frequency on the resonance field fitted by using the Kittel equation (Eq. 4.3) for each sample (b).

Table 4.1: Main magnetodynamical parameters obtained from the fitting of FMR spectra at 300K. Each value is accompanied by its own standard deviation. The observed difference in the Gilbert damping parameter  $\alpha$  between the Py and Py/Pt thin films is a signature of the spin pumping process.

Sample	$M_s$ (emu/cm <sup>3</sup> )	$H_4$ (Oe)	$\gamma/2\pi$ (GHz/T)	$\alpha$ ( $\times 10^{-3}$ )	$\Delta H(0)$ (Oe)
Py	$732.11 \pm 0.05$	$2.36 \pm 0.03$	$29.45 \pm 0.02$	$7.05 \pm 0.04$	$5.6 \pm 0.2$
Py/Pt (1.25 nm)	$676.41 \pm 0.15$	$1.68 \pm 0.11$	$29.72 \pm 0.04$	$11.17 \pm 0.07$	$3.2 \pm 0.5$
Py/Pt (2.5 nm)	$740.07 \pm 1.11$	$-0.4 \pm 0.04$	$29.48 \pm 0.02$	$9.96 \pm 0.07$	$3.3 \pm 0.3$
Py/Pt (5 nm)	$724.15 \pm 2.97$	$-0.68 \pm 0.10$	$29.65 \pm 0.05$	$10.45 \pm 0.05$	$2.9 \pm 0.3$

[125, 126, 127] and confirms the good quality of the sample. Furthermore, an increased  $\alpha$  in the Py/Pt bilayers is also observed. This increase, as stated before, is indicative of the spin pumping process present in FM/NM bilayers, being NM a non-magnetic material with high spin-orbit coupling [15]. Spin pumping implies the opening of an alternative channel for magnetic relaxation, thus enhancing the measured Gilbert damping parameter. Experimentally, this increase is observed in the frequency dependence of FMR linewidth, as shown in Fig. 4.5a. At resonance, the spin current pumped from the Py into the Pt is maximum. This spin current can be

expressed as [111, 116]

$$j_s^{\text{pump}} \hat{\boldsymbol{\sigma}} = \frac{e}{4\pi} G_{\text{eff}}^{\uparrow\downarrow} \left[ \mathbf{m}(\mathbf{r}, t) \times \frac{\partial \mathbf{m}(\mathbf{r}, t)}{\partial t} \right], \quad (4.5)$$

where  $G_{\text{eff}}^{\uparrow\downarrow}$  is the effective spin-mixing conductance, which is a purely interfacial parameter related to the elements of the scattering matrix at the Py/Pt interface (see Chapter 3) and  $\mathbf{m}(\mathbf{r}, t) = \mathbf{M}(\mathbf{r}, t)/M_s$ . It is noticeable the resemblance of this expression with the second term on the right hand side of the LLG equation (Eq. 4.1). In fact, due to the conservation of angular momentum in the dynamic system, the spin torque experienced by the Py resulting from the the spin injected into the Pt, leads to an additional term to the LLG equation [15], which results in a renormalization of the Gilbert damping parameter of the form [107, 114]

$$\alpha' = \alpha_0 + \frac{\gamma \hbar}{4\pi M_s t_{\text{Py}}} G_{\text{eff}}^{\uparrow\downarrow}, \quad (4.6)$$

where  $t_{\text{Py}}$  is the thickness of the Py film,  $\alpha_0$  is the *intrinsic* Gilbert damping parameter of Py, and  $\alpha'$  the Gilbert damping parameter of the Py/Pt bilayer, which includes an *extrinsic* term due to spin pumping (second term on the right hand side of Eq. 4.6). Using Eq. 4.6 and the values in Table 4.1 it is easy to see that the spin-mixing conductance of the Py/Pt system is  $3.24 \pm 0.6 \times 10^{19} \text{ m}^{-2}$  which is in accordance with the reported values in these systems [116, 114, 128].

### 4.1.3 Temperature Dependence of FMR and Spin Pumping

The FMR and spin pumping characteristics of each sample as a function of temperature were studied employing the same methodology from the previous section, i.e., through the fitting of the absorption spectral curves of FMR as a function of frequency in order to extract the resonance field  $H_{\text{res}}$  and linewidth  $\Delta H$  of each curve, which is ultimately used in the determination of the magnetodynamical parameters of each sample from their frequency dependence (see equations 4.3 and 4.4). The  $H_{\text{res}}$  and  $\Delta H$  frequency dependence for each sample as a function of temperature is depicted in Fig. 4.6. At first sight, from the  $\Delta H$  versus  $f_{\text{res}}$  curves (Fig. 4.6a), it is obvious that the inhomogeneous line broadening  $\Delta H(0)$  (the  $y$ -axis intercept of each line) increases at low temperatures. It is also noticeable that at these same lower temperatures the linear behaviour of  $\Delta H$  with  $f_{\text{res}}$  weakens. Moreover, from the  $f_{\text{res}}$  versus  $H_{\text{res}}$  curves (Fig. 4.6b), a shift to the left in the resonance field is easily appreciated. In order to gain insight into these general features and to obtain a proper

explanation for this behaviour, it is important to understand what these curves mean and which information can be obtained from them.

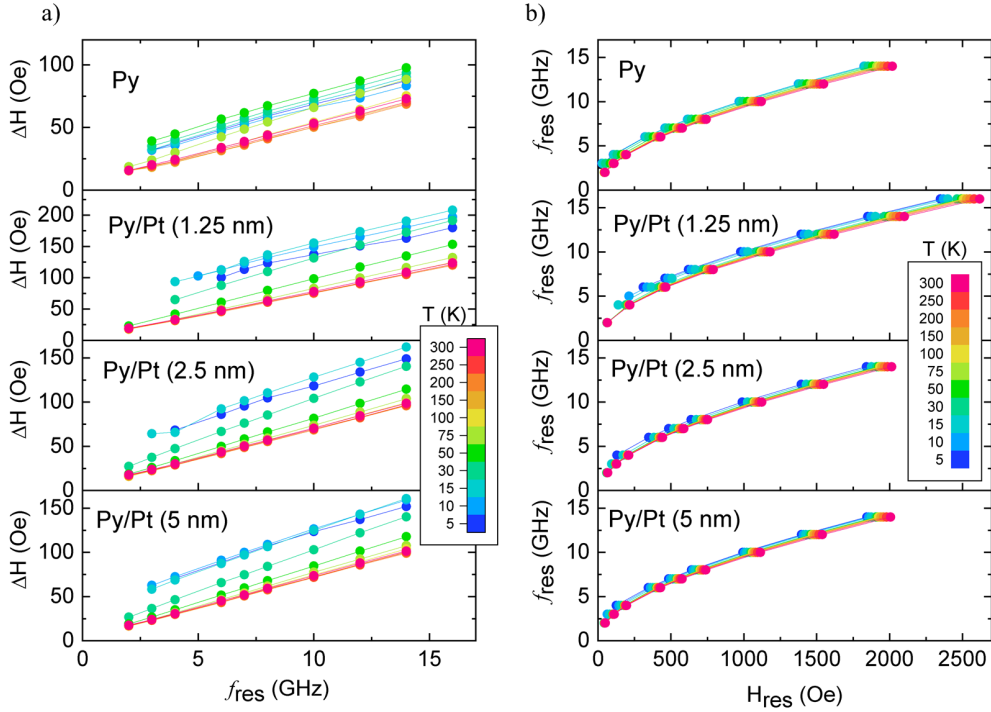


Figure 4.6: Linear dependence between the resonance linewidth and the resonance frequency (a), and the experimental dependence of the resonance frequency with the resonance field (b) for each sample as a function of temperature.

The curves in Fig. 4.6b, corresponding to the resonance frequency  $f_{\text{res}}$  versus resonance field  $H_{\text{res}}$  dependence, are fitted using Kittel's equation (Eq. 4.3). An analysis of the structure of this equation shows that a shift-to-the-left in the resonance field  $H_{\text{res}}$  can be originated from (i) an increase in the saturation magnetization  $M_s$ , and/or (ii) an increase in the anisotropy field  $H_4 \equiv 2K_4/M_s$ <sup>1</sup>. From Fig. 4.3, it is experimentally observed that the low temperature values of saturation magnetization do not exceed more than a 10% its value at 300K. This mild increase is also confirmed from the saturation magnetization values determined by the fitting of the curves in Fig. 4.6b (see Table 4.2). On the other hand, the anisotropy field follows a strong

<sup>1</sup>The gyromagnetic ratio  $\gamma$  value fitted at 300K is used as a fixed parameter in the lower temperature fits. This is justified by the fact that letting  $\gamma$  as a free parameter did not change the quality of the fit and did not differ from its 300K value by much. Thus, in order to not introduce more uncertainty to the determination of  $M_s$  and  $H_4$  at each temperature, the 300K  $\gamma$  value is used.

upturn below about 100K for all samples, suggesting that it might play a major role in the resonance field shift below this temperature. The obtained anisotropy field for all samples as a function of temperature is depicted in Fig. 4.7a. In order to best illustrate this effect, the measured FMR spectral curves and their corresponding fitted resonance field values (at 6 GHz as a representative frequency) as a function of temperature for each sample are shown in Fig. 4.7b and Fig. 4.7c, respectively. As can be observed, from 300K to about 100K, the resonance field small shift is due mainly to the intrinsic, small increase in the saturation magnetization of each sample. From approximately 100K to 5K, the increase in the anisotropy field  $H_4$  is the dominant contribution to the shift. A straightforward comparison between Figs. 4.7a and 4.7c straightens this interpretation. The resulting fitted magnetodynamical parameters at each temperature and for each sample are compiled in Table 4.2.

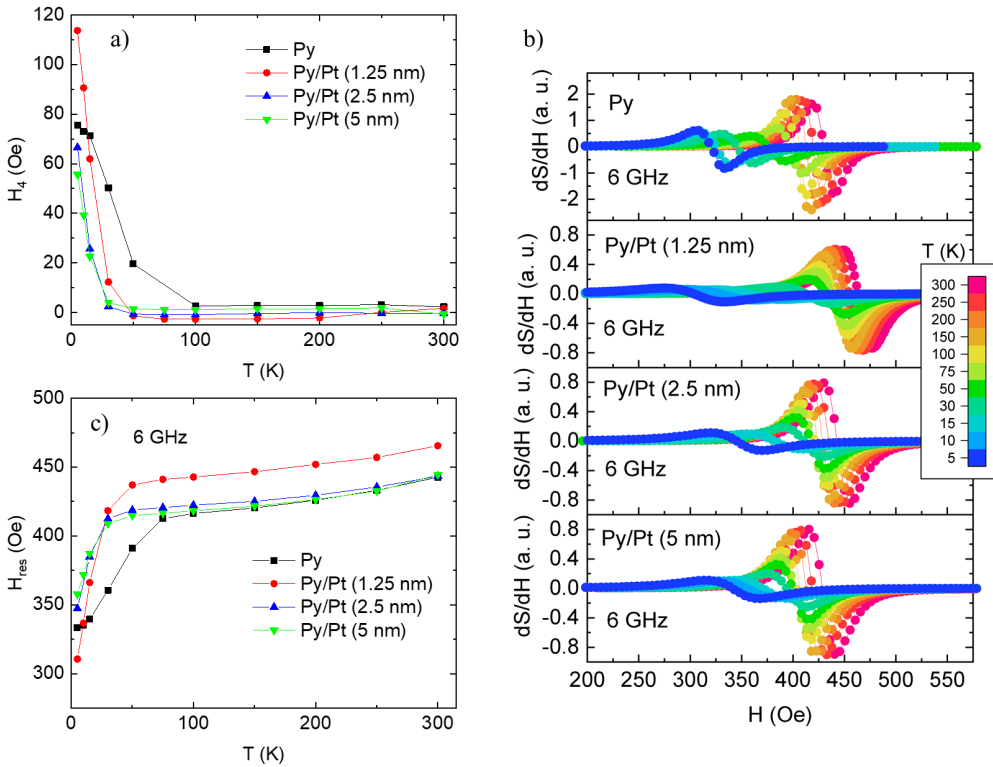


Figure 4.7: (a) shows the temperature dependence of the anisotropy field  $H_4$  for each sample, (b) the FMR spectral curves at 6 GHz as a function of temperature for each sample, and (c) the shift in the resonance field as a function of temperature is clearly appreciated.



Table 4.2: Main magnetodynamical parameters obtained from the fitting of FMR spectra as a function of temperature. Each value is accompanied by its own standard deviation.

Sample	T (K)	$M_s$ (emu/cm <sup>3</sup> )	$H_4$ (Oe)	$\gamma/2\pi$ (GHz/T)	$\alpha$ ( $\times 10^{-3}$ )	$\Delta H(0)$ (Oe)
Py	300	732.11 $\pm$ 0.05	2.36 $\pm$ 0.03	29.45 $\pm$ 0.01	7.05 $\pm$ 0.04	5.6 $\pm$ 0.2
	250	748.03 $\pm$ 0.13	3.13 $\pm$ 0.06	29.45 (fixed)	6.74 $\pm$ 0.04	5.6 $\pm$ 0.4
	200	755.99 $\pm$ 0.16	2.82 $\pm$ 0.08	29.45 (fixed)	6.57 $\pm$ 0.07	5.4 $\pm$ 0.4
	150	771.90 $\pm$ 0.15	2.81 $\pm$ 0.07	29.45 (fixed)	6.72 $\pm$ 0.11	4.7 $\pm$ 0.6
	100	779.86 $\pm$ 0.29	2.72 $\pm$ 0.12	29.45 (fixed)	7.4 $\pm$ 0.09	4.1 $\pm$ 0.5
	75	787.82 $\pm$ 0.18	3.48 $\pm$ 0.08	29.45 (fixed)	7.9 $\pm$ 0.07	24.1 $\pm$ 0.4
	50	795.77 $\pm$ 0.73	19.6 $\pm$ 0.43	29.45 (fixed)	7.9 $\pm$ 0.01	24.1 $\pm$ 0.6
	30	795.77 $\pm$ 0.53	50.3 $\pm$ 0.31	29.45 (fixed)	7.8 $\pm$ 0.09	19.8 $\pm$ 0.5
	15	795.77 $\pm$ 0.32	71.3 $\pm$ 0.19	29.45 (fixed)	7.69 $\pm$ 0.12	17.6 $\pm$ 0.7
	10	795.77 $\pm$ 1.05	73.0 $\pm$ 0.61	29.45 (fixed)	6.88 $\pm$ 0.16	18.4 $\pm$ 0.9
5	795.77 $\pm$ 0.91	75.6 $\pm$ 0.53	29.45 (fixed)	7.4 $\pm$ 0.14	17.8 $\pm$ 0.8	
Py/Pt (1.25 nm)	300	676.41 $\pm$ 0.15	1.68 $\pm$ 0.11	29.70 $\pm$ 0.04	11.16 $\pm$ 0.07	3.2 $\pm$ 0.5
	250	692.32 $\pm$ 0.00	0.05 $\pm$ 0.14	29.70 (fixed)	10.94 $\pm$ 0.07	2.9 $\pm$ 0.5
	200	708.24 $\pm$ 0.19	-2.22 $\pm$ 0.13	29.70 (fixed)	10.85 $\pm$ 0.07	2.5 $\pm$ 0.5
	150	716.20 $\pm$ 0.17	-2.58 $\pm$ 0.11	29.70 (fixed)	10.92 $\pm$ 0.55	2.1 $\pm$ 0.4
	100	724.15 $\pm$ 0.17	-2.74 $\pm$ 0.11	29.70 (fixed)	11.4 $\pm$ 0.06	1.5 $\pm$ 0.4
	75	732.11 $\pm$ 0.17	-2.71 $\pm$ 0.11	29.70 (fixed)	12.13 $\pm$ 0.05	1.3 $\pm$ 0.4
	50	732.11 $\pm$ 0.20	-1.36 $\pm$ 0.12	29.70 (fixed)	13.81 $\pm$ 0.05	4.8 $\pm$ 0.4
	30	740.70 $\pm$ 0.67	12.3 $\pm$ 0.64	29.70 (fixed)	15.70 $\pm$ 0.21	24.2 $\pm$ 1.5
	15	748.03 $\pm$ 0.81	62.00 $\pm$ 0.75	29.70 (fixed)	14.19 $\pm$ 0.33	57.3 $\pm$ 2.3
	10	748.03 $\pm$ 0.95	90.6 $\pm$ 0.94	29.70 (fixed)	12.60 $\pm$ 0.21	62.4 $\pm$ 1.5
5	748.03 $\pm$ 2.72	113.7 $\pm$ 3.05	29.70 (fixed)	11.18 $\pm$ 0.48	59.7 $\pm$ 3.5	
Py/Pt (2.5 nm)	300	740.07 $\pm$ 1.11	-0.40 $\pm$ 0.04	29.48 $\pm$ 0.02	9.96 $\pm$ 0.07	3.3 $\pm$ 0.4
	250	755.99 $\pm$ 0.12	-0.30 $\pm$ 0.06	29.48 (fixed)	9.81 $\pm$ 0.07	3.1 $\pm$ 0.4
	200	763.94 $\pm$ 0.16	-0.10 $\pm$ 0.08	29.48 (fixed)	9.76 $\pm$ 0.06	2.6 $\pm$ 0.3
	150	771.90 $\pm$ 0.13	-0.40 $\pm$ 0.06	29.48 (fixed)	9.87 $\pm$ 0.06	2.1 $\pm$ 0.3
	100	779.86 $\pm$ 0.11	-0.90 $\pm$ 0.05	29.48(fixed)	10.26 $\pm$ 0.05	1.5 $\pm$ 0.3
	75	787.82 $\pm$ 0.18	-0.90 $\pm$ 0.08	29.48(fixed)	10.73 $\pm$ 0.05	1.4 $\pm$ 0.3
	50	787.82 $\pm$ 0.27	-0.70 $\pm$ 0.12	29.48 (fixed)	11.83 $\pm$ 0.04	2.0 $\pm$ 0.2
	30	795.77 $\pm$ 0.40	2.40 $\pm$ 0.17	29.48 (fixed)	13.91 $\pm$ 0.09	9.5 $\pm$ 0.5
	15	803.73 $\pm$ 0.99	25.61 $\pm$ 0.57	29.48 (fixed)	12.9 $\pm$ 0.08	40.2 $\pm$ 0.5
	5	795.77 $\pm$ 0.75	66.6 $\pm$ 0.7	29.48 (fixed)	11.77 $\pm$ 0.03	38.4 $\pm$ 0.2
Py/Pt (5 nm)	300	724.15 $\pm$ 2.12	-0.68 $\pm$ 0.10	29.65 $\pm$ 0.05	10.45 $\pm$ 0.05	3.0 $\pm$ 0.3
	250	740.07 $\pm$ 0.16	1.83 $\pm$ 0.01	29.65 (fixed)	10.3 $\pm$ 0.04	2.7 $\pm$ 0.0
	200	748.03 $\pm$ 0.18	1.52 $\pm$ 0.08	29.65 (fixed)	10.26 $\pm$ 0.05	2.3 $\pm$ 0.0
	150	755.99 $\pm$ 0.26	1.47 $\pm$ 0.12	29.65 (fixed)	10.44 $\pm$ 0.04	1.8 $\pm$ 0.0
	100	763.94 $\pm$ 0.25	1.09 $\pm$ 0.11	29.65 (fixed)	10.80 $\pm$ 0.03	1.8 $\pm$ 0.0
	75	771.90 $\pm$ 0.29	1.10 $\pm$ 0.13	29.65 (fixed)	11.61 $\pm$ 0.05	1.5 $\pm$ 0.0
	50	771.90 $\pm$ 0.29	1.49 $\pm$ 0.13	29.65 (fixed)	12.24 $\pm$ 0.03	2.1 $\pm$ 0.0
	30	779.86 $\pm$ 0.52	4.01 $\pm$ 0.23	29.65 (fixed)	12.92 $\pm$ 0.05	8.4 $\pm$ 0.0
	15	787.82 $\pm$ 0.59	22.60 $\pm$ 0.35	29.65 (fixed)	13.79 $\pm$ 0.09	31.4 $\pm$ 0.1
	10	787.82 $\pm$ 0.45	39.30 $\pm$ 0.30	29.65 (fixed)	13.01 $\pm$ 0.01	37.8 $\pm$ 0.1
5	779.86 $\pm$ 2.12	55.70 $\pm$ 1.6	29.65 (fixed)	12.01 $\pm$ 0.03	40.4 $\pm$ 0.2	

The linewidth  $\Delta H$  versus resonance frequency  $f_{\text{res}}$  lines (Fig. 4.6a) were fitted

using Eq. 4.4. What really stands out in this figure, as is stated at the beginning of this section, is the increase of the inhomogeneous line broadening  $\Delta H(0)$  at low temperature. In addition, the Gilbert damping parameter  $\alpha$  follows a strong upturn below about 100K and a cusp around 30K for the Py/Pt bilayers. The inhomogeneous line broadening and Gilbert damping as a function of temperature for each sample are shown in Fig. 4.8. Their values are also compiled in Table 4.2.

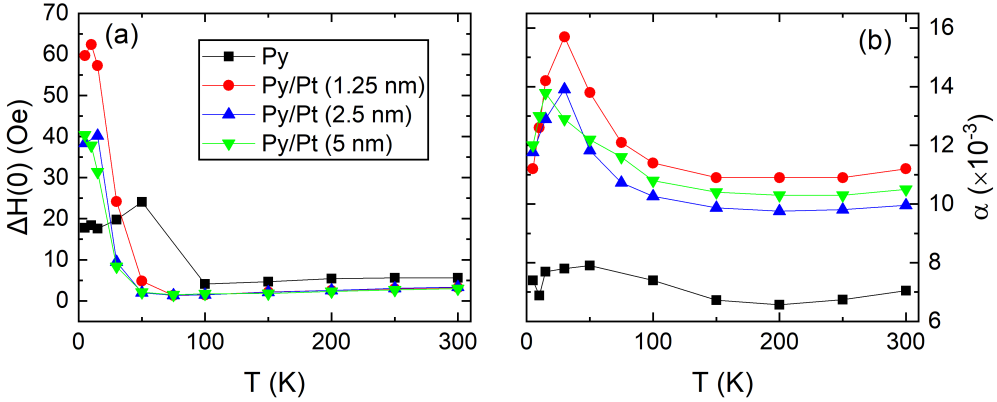


Figure 4.8: Both inhomogeneous line broadening  $\Delta H(0)$  (a) and Gilbert damping  $\alpha$  (b) as a function of temperature for each sample.

The inhomogeneous line broadening or damping, as stated above, is negligible for magnetically and structurally homogeneous systems. It is a form of extrinsic contribution to the magnetic damping which originates from local variations of the magnetization and/or anisotropy constants, including microstructural features of the samples (e.g., impurities, non-uniformity of the sample surface, sample thickness, or strain due to lattice mismatching) [79]. As it is shown in Fig. 4.8a, the inhomogeneous damping for the Py alone sample is constant and close to zero from 300K to approximately 70K, when a sudden, strong increase is detected. The same tendency is observed in the Py/Pt bilayers. In this case, however, the increase occurs at slightly lower temperatures (around 50K) and it is significantly higher than in the Py alone sample. Generally, this low temperature variations can be correlated with variations in the different anisotropy terms (bulk, interfacial, microstructure) present in the sample [129]. By looking at the temperature dependence of the anisotropy field  $H_4 \equiv 2K_4/M_s$  (see Fig. 4.7a), (i) it is evident that  $H_4$  cannot be neglected at low temperatures, and (ii) it correlates perfectly with the increase in the inhomogeneous broadening. In the present Thesis, the origin of the sudden increase at low temperatures has not been clarified, and thus, further work must be addressed with this purpose.

The interpretation of the non-monotonic temperature dependence of  $\alpha$  (see Fig. 4.8b) is a little bit trickier, and previous reports on this topic are diverse. In some

cases [130], a correlation between the ordinary electron scattering time of the ferromagnetic material and the magnon lifetime was established, resulting in a linear dependence between  $\alpha$  and the resistivity of the material. Conversely, other studies [131] observed an independent or slightly decreasing damping with temperature, with no direct correlation with the resistivity of the material whatsoever. Moreover, the temperature dependence of  $\alpha$  as a function of the Py thickness has been addressed by Zhao et al. [125]. In this experiment, a monotonic decrease of damping with temperature was reported for bulk ( $t_{\text{Py}} > 15$  nm) films, whereas a cusp at around 50K for  $t_{\text{Py}} \leq 10$  nm was found. This observation is indicative of the importance of surfaces when the film thickness decreases. At the same time, the Gilbert damping was found to increase with decreasing  $t_{\text{Py}}$ . As a result, the damping was described as the sum of both bulk and surface terms, i.e.,  $\alpha = \alpha_{\text{B}} + \alpha_{\text{S}}/t_{\text{Py}}$  [125]. In the case of Py thin films, the cusp in  $\alpha(T)$  curves has been correlated with thermally induced spin reorientation of the surface magnetization, i.e., the effect of surface anisotropy [132]. However, in our experiment, the observed cusp in  $\alpha(T)$  is even more pronounced in Py/Pt bilayers, while the Py alone sample follows the monotonic decrease with a small cusp at 50K, similar to the previous observation of Zhao et al. [125, 132]. In addition to the spin pumping effect in Py/Pt bilayers, a direct modification of the damping at the interface can be originated from the localization of the interaction between magnons and conduction electrons [133], however, this mechanism does not fully explain the strong increase of  $\alpha$  at low temperature. The systematic study of the temperature dependence of damping dates back to the 1979 pioneering works of Heinrich and Cochran [134, 135]. It was found that the measured damping rates versus temperature had two primarily contributions, i.e., a part that increased with temperature and another part that decreased with temperature [136]. This non-monotonic temperature dependence was already qualitatively described by Kamberský's 1976 torque-correlation model [136, 137]. According to this model, the damping rate in a ferromagnetic metal has two competing contributions: *intra-band* electron-hole transitions and *inter-band* electron-hole transitions. Following the argument of Gilmore, Idzerda, and Stiles [136], these contributions naturally arise from magnetization dynamics if one considers the effective field for the magnetization dynamics  $\mathbf{H}_{\text{eff}} = -\partial\mathcal{E}/\partial\mathbf{M}$  with the magnetic energy defined as  $\mathcal{E} = \sum_{nk} \rho_{nk} \varepsilon_{nk}$ , where  $n$  is the band index,  $\mathbf{k}$  the electron wavevector,  $\rho_{nk}$  the state occupancies, and  $\varepsilon_{nk}$  the single-electron energy. Combining these definitions, the effective field can be expressed as

$$\mathbf{H}_{\text{eff}} = -\frac{1}{M} \sum_{nk} \left[ \rho_{nk} \frac{\partial \varepsilon_{nk}}{\partial \hat{\mathbf{M}}} + \frac{\partial \rho_{nk}}{\partial \hat{\mathbf{M}}} \varepsilon_{nk} \right], \quad (4.7)$$

being  $M$  and  $\hat{\mathbf{M}}$  the magnitude and direction of the magnetization vector, respectively. The first term on the right hand side of Eq. 4.7 describes the variation of the (spin-orbit) energy of the system with respect to the precessing magnetization,

leaving unchanged the occupancy levels. This term is usually referred to as the breathing Fermi surface (BFS) model [138], since it makes the Fermi level to expand and contract as the magnetization precesses. The second term on the right hand side, however, accounts for transitions between states while the band energy remains constant. It fundamentally creates electron-hole pairs by exciting electrons from lower to higher bands. It is known [136, 137] that the first term in Eq. 4.7 (i.e., BFS) gives rise to the intraband contribution, while the second term gives rise to the interband contribution. Additionally, each contribution is related with the electron's relaxation time (not to be confused with the magnon relaxation time) in some manner: the damping arising from the intraband contribution is proportional to the relaxation time, while the one arising from the interband contribution is inversely proportional to the relaxation time. Consequently, since the number of phonons decreases with decreasing temperature and, therefore, the relaxation time increases, intraband transitions dominate, while the interband transitions govern the high-temperature regime. In a particular ferromagnet, the competing effect of each contribution gives rise to the observed non-monotonic dependence of Gilbert damping. Nevertheless, it is worth mentioning that the increase at low temperature of Gilbert damping in our samples is closely correlated with the increase in the inhomogeneous line broadening  $\Delta H(0)$ , as has been stated above. This suggests that the assumption of a nearly zero and frequency independent  $\Delta H(0)$  may not be true and, as a consequence, the separation of the resonance linewidth  $\Delta H$  in frequency-independent extrinsic damping terms and frequency-dependent intrinsic terms, i.e.,  $\Delta H = \Delta H(0) + 2\pi\alpha f_{\text{res}}/\gamma$ , may be no longer valid [139]. In fact, from Fig. 4.6a a loose linear behaviour at low temperatures can be appreciated. Hence, the upturn in damping at low temperature may as well be influenced by extrinsic damping contributions, which could not be fully explained by Kamberský's torque-correlation model since it solely aims to describe intrinsic damping mechanisms.

With respect to the relative magnitude of  $\alpha$  in the whole range of temperatures, it is clear that the presence of a Pt capping layer promotes a strong increase of  $\alpha$  in the whole range of temperatures in comparison with the Py alone sample. As stated in Section 4.1.2, the Pt capping layer acts as an additional angular momentum dissipation channel which experimentally results in the observation of an increased Gilbert damping (see Eq. 4.6). In this case, the damping increases from  $7 \times 10^{-3}$  in the Py alone sample to  $10.5 \pm 0.6 \times 10^{-3}$  (averaged over the three Py/Pt samples) at 300K. It is important, however, to notice that there is not a clear Pt thickness dependence of the damping difference. Theoretically, the spin current injected from the Py diffuses into the Pt up to the so-called spin diffusion length  $\lambda_{\text{sd}}$ , whereby the spin current loses its coherence and is completely absorbed by the Pt film. If the Pt film thickness is less than  $\lambda_{\text{sd}}$ , then a backflow spin current builds up [107, 111] and is reabsorbed by the Py film. Therefore, if the spin current pumped to the Pt layer equals this backflow spin current, there would be no difference in the observed Gilbert

damping parameter. Thus, according to this model, it is expected that the damping difference increases with increasing the Pt thickness up to a saturation thickness value of the order of  $\lambda_{sd}$ , from which the Pt layer would act as a so-called *spin sink*.

The absence of this dependence of damping difference with Pt thickness (see Fig. 4.8b) can be explained by interfacial loss of spin coherence, which may result in the reduction or even the full suppression of the effective spin current being injected into the Pt layer. This problem has been addressed by many groups [59, 115, 140, 141, 142] and introduces many problems such as the precise determination of  $\lambda_{sd}$  or the spin Hall angle  $\Theta_{SH}$  [143]. One method for disentangling this problem is by measuring directly the transverse voltage generated by inverse spin Hall effect (ISHE), i.e., the conversion of a pure spin current into a transverse charge current in non-magnetic materials with high spin-orbit coupling (such as Pt). However, it is well known [93] that the voltage signal detected in FMR experiments in metallic FM/NM systems may have contributions coming from the so-called spin rectification effects (SRE), such as anisotropic magnetoresistance and/or anomalous Hall effect. These parasitic effects appear due to the synchronous coupling between an oscillating eddy current, induced by the magnetic field of the microwave line, and an oscillating resistance in magnetic structures, resulting in a dc voltage/current signal.

At this point, it is appropriate to comment that a study of the transverse voltage measured in the Py/Pt samples of this chapter has already been published, together with the FMR results presented in this chapter, by our group in 2020 [144]. Some time later, we realised that we lacked the necessary technical tools to effectively measure ISHE and to correctly separate it from SRE. As a consequence, a commercial nanovoltmeter (Model 2128A, from Keithley Instruments) was purchased and used for this issue. For this reason, we do not include the ISHE results published in Ref. [144]. The second part of this Chapter deals with the measurements of ISHE in Py and Py/Pt systems, including the difficulties to disentangle it from SRE and the experimental strategy employed to overcome this problem.

## 4.2 Inverse Spin Hall Effect in Py and Py/Pt Systems

### 4.2.1 Description of the Experiment and Experimental Setup

The inverse spin Hall effect (ISHE) is an easy-to-implement process to assess the injection of spin currents through a FM/NM bilayer in spin pumping experiments. The conversion of the injected spin current  $\mathbf{j}_s$  into a transverse charge current  $\mathbf{j}_c$  in the high spin-orbit coupling (SOC) NM material allows it to be measured by the voltage difference across the sample, simplifying, thus, the overall detection process.

The form of this charge current is described in Chapter 2 and reproduced here for simplicity,

$$\mathbf{j}_c = \Theta_{\text{SH}} \mathbf{j}_s \times \hat{\boldsymbol{\sigma}}, \quad (4.8)$$

where  $\hat{\boldsymbol{\sigma}}$  is the spin polarization vector and  $\Theta_{\text{SH}}$  is the spin Hall angle, which quantifies the conversion efficiency between charge and spin currents. Since the voltage signal detected is originated by the same magnetization dynamics which governs FMR, the lineshape of the detected voltage curves is described in the same way as that of the FMR curves (see Eq. 4.2), i.e.,

$$V = V_s \frac{\Delta H^2}{\Delta H^2 + (H - H_{\text{res}})^2} + V_{as} \frac{\Delta H (H - H_{\text{res}})}{\Delta H^2 + (H - H_{\text{res}})^2}, \quad (4.9)$$

where  $V_s$  is the symmetric voltage amplitude and  $V_{as}$  the antisymmetric voltage amplitude, in analogy with FMR. Furthermore, both the linewidth  $\Delta H$  and resonance field  $H_{\text{res}}$  are the same as in FMR absorption, but the relative magnitude between the symmetric and antisymmetric contributions usually differ from the FMR absorption case.

Despite this relative simplicity, it is well known that the spin pumping induced voltage measured in *metallic* FM/NM systems may have contributions coming from the aforementioned SRE. SRE result from the synchronous coupling between an oscillating eddy current, induced in the FM by the rf magnetic field of the microwave, and an oscillating resistance, caused by magnetoresistance in the magnetic structure, giving place to the appearance of a dc voltage/current [93, 145]. In a typical FM/NM system such as the Py/Pt one studied in this case, the dominant SRE are anisotropic magnetoresistance (AMR) and the anomalous Hall effect (AHE). The behaviour of the SRE can be derived from the generalized Ohm's law [93, 145],

$$\mathbf{E} = \rho_{\perp} \mathbf{j} + \frac{\Delta \rho}{M_s^2} (\mathbf{j} \cdot \mathbf{M}) \mathbf{M} - \frac{\rho_{\text{AHE}}}{M_s} (\mathbf{j} \times \mathbf{M}), \quad (4.10)$$

where  $\mathbf{j}$  is the (rf) current density vector,  $\rho_{\perp}$  is the transverse resistivity of Py in this case,  $\Delta \rho$  and  $\rho_{\text{AHE}}$  are the resistivity change due to AMR and AHE, respectively,  $\mathbf{M}$  is the instant magnetization vector (and  $M_s$  its magnitude, which corresponds to the saturation magnetization), and  $\mathbf{E}$  is the electric field vector. The second and third terms on the right hand side of Eq. 4.10 correspond to the corrections coming from AMR and AHE, respectively. From this expression it is evident that the SRE can only arise in a FM medium, i.e., in the Py film. Additionally, thermoelectric contributions

to the voltage signal such as Seebeck or Peltier effects due to the heating of the sample in the absorption process [112] may arise. However, in the Py/Pt system, these effects are negligibly small (a few hundreds of mK according to [146]). In overall, the separation of the voltage generated by ISHE from other parasitic contributions due to SRE in metallic FM systems is a complicated work which has been tackled by several authors in the past few years but is still a pending matter.

In this context, a number of strategies to disentangle the ISHE from SRE have been employed. Among them, some pioneering methods were based on a combination of lineshape analysis of the voltage signal (see Eq. 4.9) and its angular dependence with the applied magnetic field. In this case, some experiments naively assumed that the symmetric voltage contribution arose entirely from ISHE, while the antisymmetric one was regarded as parasitic [17, 116, 147, 148]. This assumption does not hold the experimental evidence [93, 145, 149, 150] and, therefore, it is accepted that while the existence of an antisymmetric contribution to the total voltage signal presumes the existence of parasitic SRE effects, the opposite is not true: SRE do also contribute significantly to the symmetric part of the voltage [93]. Conversely, a more elaborate analysis in this line was carried out by Mosendz et al. [114, 113]. The applicability of this study, however, is severely hampered due to the specific requirements of the experimental setup and experimental conditions. In addition to the lineshape analysis, Bai et al. [151] employed a separation method based on the different angular and field symmetries of ISHE and SRE and, although it successfully determined the spin pumping induced current in Py/Pt bilayers, a very precise control of the field orientation and a high-power microwave source are required, thus limiting the practical application. Moreover, some authors [152] focused on the different dependence of ISHE and SRE with respect to the FM layer thickness. Nevertheless, these methods require a large amount of samples and measurements, as well as a proper account of the thickness dependence of different parameters (e.g., the resistivity of the FM or the spin-mixing conductance at the FM/NM interface). Furthermore, in a totally different fashion, the separation of both contributions under the inversion of the direction of the spin current injected has also been reported [153, 154]. This is justified by the fact that the SRE do not depend on the spin injection direction (see Eq. 4.10), while the ISHE is an odd function of it (Eq. 4.8). By this methodology, in order to obtain the ISHE (SRE) voltage signal, it is enough to make the half subtraction (addition) to the voltage signals measured by inverting the spin injection direction. The main difficulty in this procedure is related to the fact that inverting the stacking order of the bilayer may affect the quality of the FM/NM interface resulting, thus, in a different spin current injection in each case. As a consequence, different injections would result in different voltage signals and the adding and subtracting method would be affected by this experimental error. On the other hand, a different way to invert the spin injection direction consists of growing the bilayer on top of a very thin substrate and allowing it to flip on top of the CPW. However, in order to maintain



the symmetry of the system, it would be necessary to deposit on top of the bilayer a film employing the same material used for the substrate. This step is needed because the induced electric current that gives place to the SRE would be different otherwise. Nevertheless, the main difficulty in this procedure is the requirement to work with sufficiently thin substrates in order to guarantee a good signal-to-noise ratio. A comprehensive overview of these different methods can be found in the 2017 seminal paper by Iguchi and Saitoh [112].

We propose a different method for disentangling the ISHE and SRE signals based on the geometry of the sample. Since the current circulating through the Py layer giving place to SRE is an eddy current and, therefore, is similar to that generated in a conductor by a time-dependent magnetic field, it may be reduced by using the same strategy as well, i.e., laminating the Py layer. According to this, our hypothesis is that at sufficiently short sample widths along the CPW signal line, the circulating eddy current should be almost zero and, consequently, the SRE should vanish. On the other hand, the ISHE should not depend on the amount of current circulating in the Py film nor on the width of the film along the CPW and, therefore, it should not be affected by the absence of current.

Accordingly, we measured the transverse voltage signal generated at FMR as a function of sample width. This transverse voltage signal was measured by an external 2128A Keithley nanovoltmeter which was synchronized with the FMR spectrometer by NanOsc. In this way, both the FMR spectra and the corresponding voltage signal at each frequency were measured simultaneously. For this purpose, the “CPW PPMS IP ISHE” sample holder model produced by NanOsc Instruments [155] was used. The distinctive feature of this sample holder from other standard ones is that it possesses two parallel gold stripes with bumps on both sides of the CPW for enabling the electrical contact with the sample (see Fig. 4.9). More details on the experimental setup are gathered in Appendix A.2.2.

## 4.2.2 Samples Preparation and Characterization

For these measurements, several new samples of Py and Py/Pt bilayers were grown on top of  $5 \times 5 \text{ mm}^2$  Si substrates using the same methodology and deposition conditions as in section 4.1.1. In this study, however, both the thickness of Py films and Pt capping layers were kept constant, i.e., 16-17 nm and 5 nm, respectively. In order to certify the hypothesis mentioned before (i.e., that the shortening of the sample width  $L$  (see Fig. 4.9) effectively reduces the effect of SRE-induced voltages in conductive FM layers), samples with different values of width  $L$ , ranging from the as-grown 5 mm to 20  $\mu\text{m}$ , were prepared by means of optical lithography. Likewise, Py/Pt bilayers with inverted stacking order were grown. The total number of samples



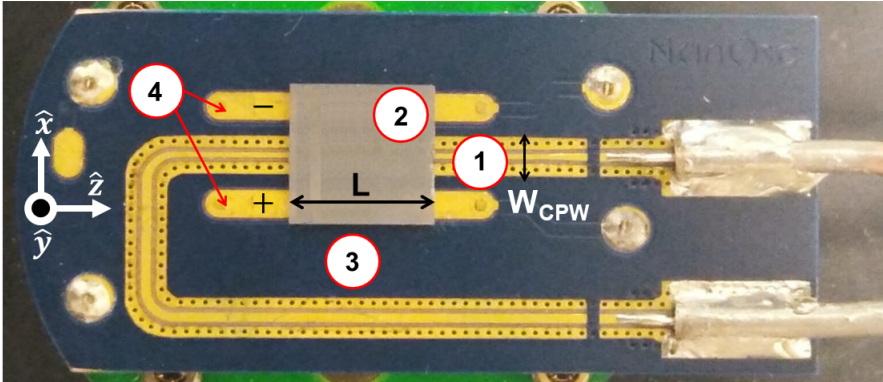


Figure 4.9: Top view photograph of the actual measurement system. The numbers correspond to the following parts: (1) CPW with a total width  $W_{\text{CPW}} = 1.4$  mm (including the RF signal active line in the middle and the two ground lines on both sides). (2) The sample placed upside down on top of the CPW with a total width  $L = 5$  mm. (3) Insulating layer. (4) Contact pads with bumps raised  $20 \mu\text{m}$  above the insulating layer for making electrical contact with the sample by means of Au contacts. The HI and LO ends, represented by + and - signs, respectively, define the polarity of the nanovoltmeter. Finally, Kapton tape is used to fix and tighten the sample onto the CPW (not shown). This sample holder is the “CPW PPMS IP ISHE” model produced by NanOsc Instruments [155].

prepared was: 5 samples of Si// Py; 7 samples of Si// Py/Pt; and 4 samples of Si// Pt/Py. A schematic visualization of these systems is depicted in Fig. 4.10.

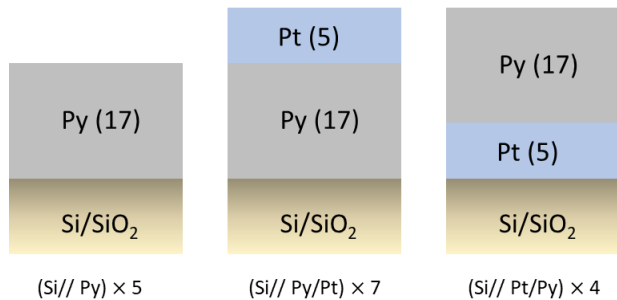


Figure 4.10: Schematic outline of the different kind of samples and systems employed in this section. From left to right: Si// Py, Si// Py/Pt, and Si// Pt/Py. The number in parenthesis represents the thickness in nanometers of each film.

Following the same procedure as in the previous section, the static and dynamic magnetic properties of each sample were characterized by means of FMR spectroscopy. For the sake of clarity, a single, representative sample of each kind of system (i.e., Si//

Py, Si// Py/Pt, and Si// Pt/Py) serves to illustrate the results of all samples within each system. Nevertheless, the extracted fitting parameters for *all* prepared samples are compiled in Table 4.3. In Fig. 4.11, the measured FMR spectral curves at 300K are shown. The overlapping of the absorption derivative lines is indicative of the similar magnetodynamical properties between the different systems. Moreover, each curve was fitted using Eq. 4.2 to obtain both the resonance field  $H_{\text{res}}$  and linewidth  $\Delta H$ . From the fitting of the frequency dependence curves of these two parameters (see Eqs. 4.3 and 4.4), the magnetodynamical parameters for each sample were obtained. These frequency-dependent curves are depicted in Fig. 4.12 and the resulting fitted parameters are summarized in Table 4.3.

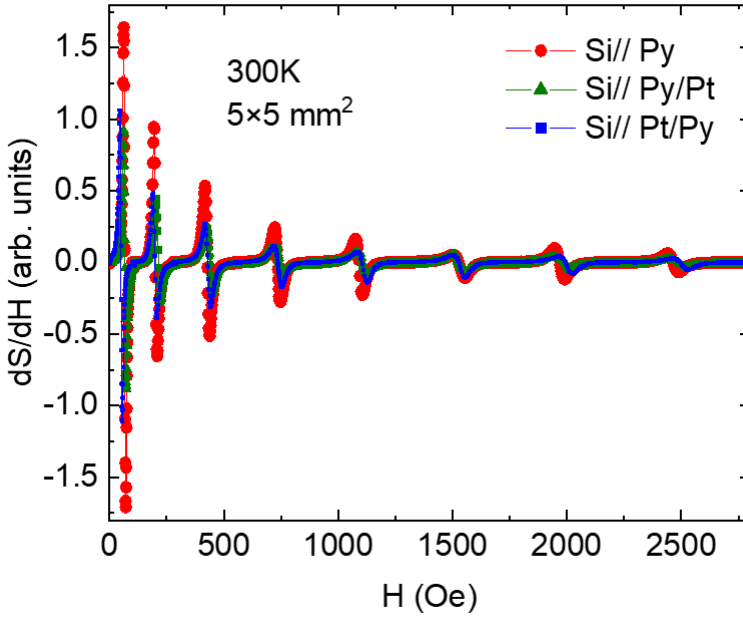


Figure 4.11: Ferromagnetic resonance spectral curves at 300K for three representative samples of each kind. Namely, Si// Py(a), Si// Py/Pt(a), and Si// Pt/Py(b) according to the nomenclature in Table 4.3.

It is already obvious from Fig. 4.12 that the three sets of systems share the same magnetodynamical properties. The overlapping of the Kittel curves in Fig. 4.12a indicates that the three samples share the same static magnetic properties (i.e.,  $M_s$ ,  $\gamma$ , and  $H_4$ <sup>2</sup>). Additionally, the difference in the slope of the lines in Fig. 4.12b denotes a difference in the Gilbert damping parameter between the Py and Py/Pt systems,

<sup>2</sup>It is important to mention that the values of the anisotropy fields  $H_4$  (see Table 4.3), although very small still with respect to the saturation magnetization or resonant fields, differ by some Oe

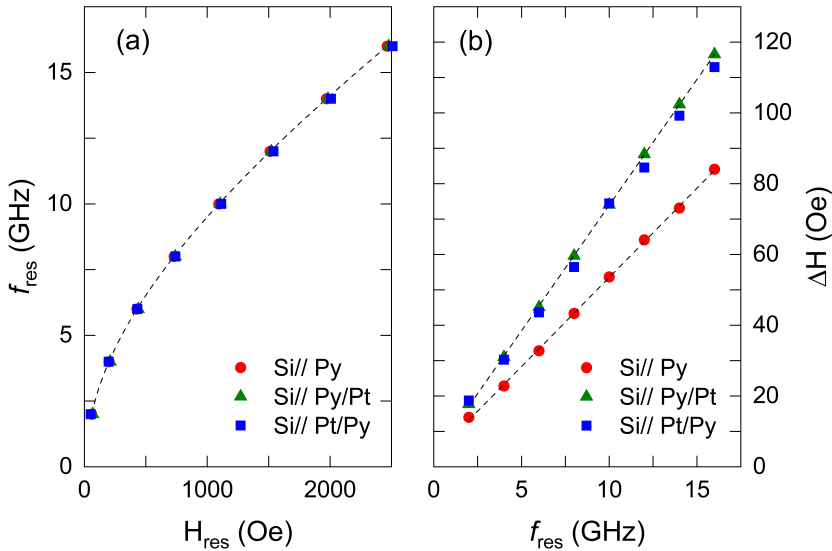


Figure 4.12: Representative curves showing the dependence of the resonant frequency on the magnetic field for the three sets of films at room temperature (a). Frequency dependence of the absorption linewidth at room temperature for a Si//Py layer compared with that of Si//Py/Pt and Si//Pt/Py bilayers. The increase of the damping in the bilayers is clearly shown (b). Sample dimensions:  $5 \times 5 \text{ mm}^2$ . The dotted line is a guide to the eye.

regardless of the Py/Pt stacking order, as expected. This difference in the damping parameter, as in the previous section, is indicative of the existence of the spin pumping effect. The Gilbert damping difference is directly proportional to the effective spin-mixing conductance  $G_{\text{eff}}^{\uparrow\downarrow}$  of the Py/Pt interface. Thus, using Eq. 4.6, the spin-mixing conductance equals  $G_{\text{eff}}^{\uparrow\downarrow} = (2.31 \pm 0.27) \times 10^{19} \text{ m}^{-2}$ , which is in accordance with the value obtained in Section 4.1.2 and references therein.

### 4.2.3 Voltage Measurements for the $L = 5 \text{ mm}$ Samples

The measured transverse voltage curves for each kind of system as a function of the applied magnetic field are shown in Fig. 4.13a. Moreover, both symmetric and

with respect to the  $H_4$  from the previous section (see Table 4.1). This can be explained by the fact that an experimental offset magnetic field might be present at the time of measurement in the former case, thus reporting higher values for the anisotropy field in the fitting process. One way to correct this offset is by performing the same measurement at negative fields at a given frequency and, since the FMR measurement has field inversion symmetry, the difference between the positive and negative resonance fields would correspond to the offset field. In any case, both corrected and uncorrected values do not play a major role at 300K and in this kind of experiment. Consequently, the anisotropy field values will be ignored hereafter.

Table 4.3: Main magnetodynamical parameters obtained from the fitting of FMR spectra at 300K. Each value is accompanied by its own  $\pm$  standard deviation. The observed difference in the Gilbert damping parameter  $\alpha$  between the Py and Py/Pt thin films is a signature of the spin pumping process. The samples in which there is no data correspond to samples which have not been measured but are expected to have the same properties as the others in the same set.

Sample	$M_s$ (emu/cm <sup>3</sup> )	$H_4$ (Oe)	$\gamma/2\pi$ (GHz/T)	$\alpha$ ( $\times 10^{-3}$ )	$\Delta H(0)$ (Oe)
Si// Py (a)	740.1 $\pm$ 3.2	-10.1 $\pm$ 0.1	29.74 $\pm$ 0.06	7.28 $\pm$ 0.06	3.2 $\pm$ 0.4
Si// Py (b)	-	-	-	-	-
Si// Py (c)	748.0 $\pm$ 5.6	-19.0 $\pm$ 0.2	29.68 $\pm$ 0.09	7.48 $\pm$ 0.06	3.1 $\pm$ 0.4
Si// Py (d)	-	-	-	-	-
Si// Py (e)	748.0 $\pm$ 4.0	-12.4 $\pm$ 0.2	29.65 $\pm$ 0.07	7.45 $\pm$ 0.06	3.3 $\pm$ 0.4
Si// Py (f)	-	-	-	-	-
Si// Py (g)	748.0 $\pm$ 4.0	-12.4 $\pm$ 0.2	29.65 $\pm$ 0.07	7.49 $\pm$ 0.05	2.3 $\pm$ 0.6
Si// Py/Pt (a)	748.0 $\pm$ 4.8	-19.8 $\pm$ 0.3	29.67 $\pm$ 0.08	10.79 $\pm$ 0.007	2.8 $\pm$ 0.5
Si// Py/Pt (b)	748.0 $\pm$ 4.8	-12.4 $\pm$ 0.2	29.68 $\pm$ 0.07	10.87 $\pm$ 0.06	2.8 $\pm$ 0.4
Si// Py/Pt (c)	748.0 $\pm$ 3.2	-20.2 $\pm$ 0.1	29.65 $\pm$ 0.06	10.78 $\pm$ 0.05	2.8 $\pm$ 0.3
Si// Py/Pt (d)	732.1 $\pm$ 4.8	-2.7 $\pm$ 0.2	29.74 $\pm$ 0.8	10.56 $\pm$ 0.04	2.9 $\pm$ 0.3
Si// Py/Pt (e)	-	-	-	-	-
Si// Pt/Py (a)	724.2 $\pm$ 3.2	-1.11 $\pm$ 0.2	29.67 $\pm$ 0.05	10.08 $\pm$ 0.05	2.7 $\pm$ 0.4
Si// Pt/Py (b)	-	-	-	-	-
Si// Pt/Py (c)	732.1 $\pm$ 7.4	-0.7 $\pm$ 0.6	29.53 $\pm$ 0.10	10.11 $\pm$ 0.05	2.1 $\pm$ 0.4
Si// Pt/Py (d)	-	-	-	-	-

antisymmetric voltage amplitudes (obtained from the fitting of the voltage curves in Fig. 4.13a by using Eq. 4.9) as a function of frequency are shown in Fig. 4.13b. Again, a representative sample of each set is used to illustrate the overall behaviour of all samples. It is important to say that thick ( $\approx 30$  nm) gold stripes were deposited on both sides of each sample to improve the electrical contact with the sample holder. From Fig. 4.13a it is evident that all samples show the same lineshape as a function of the applied magnetic field. The relative voltage signal intensity, however, is different. This difference can be attributed to numerous causes: small differences in the rf field  $h_{rf}$  absorption for each set of samples due primarily to the Pt layer in between the CPW and the Py film; a different distance between the Py and the CPW; and, last but not least, the contribution coming from the ISHE, which reverses sign when inverting the stacking order, i.e., Si// Py/Pt or Si// Pt/Py. It is also worth noticing that the measured voltage signal is negative, while considering the electrical contacts in our experimental setup, the ISHE-induced voltage signal is expected to be positive in the case of the Si// Py/Pt system. This is easy to visualize if one considers the

coordinate system depicted in Fig. 4.9: The magnetic field is applied parallel to the  $z$ -axis, therefore the spin polarization vector  $\hat{\sigma}$ , which is parallel to the quantization axis of the system, points in the  $z$  direction as well. Additionally, the spin current  $\mathbf{j}_s$  flows from the Py into the Pt, thus pointing in the  $-y$  direction in the Si// Py/Pt system. In overall, by using Eq. 4.8, one finds that the transverse charge current  $\mathbf{j}_c$  generated due to ISHE flows along the  $-x$  direction. This induced current generates a charge accumulation on both sides of the sample which consequently induces an opposing electric field running in the  $+x$  direction resulting, finally, in an ISHE-induced transverse voltage drop. The voltage drop in this experimental setup is by definition  $V \equiv V^+ - V^-$ , where the  $+$  and  $-$  symbols (shown in Fig. 4.9) define the polarity of the electrical contacts. Thus, considering that the voltage drop is defined by the line integral

$$V^{\text{ISHE}} = - \int_a^b \langle \mathbf{E}^{\text{ISHE}} \rangle d\mathbf{x}, \quad (4.11)$$

and recalling that  $V \equiv V^+ - V^-$ , then the integration limits are set to be  $a = +W_{\text{CPW}}/2$  and  $b = -W_{\text{CPW}}/2$ . As a consequence, the result of the integral will be negative but because there is a negative sign in front of it, the overall voltage drop due to ISHE should be positive. Hence, as we obtain the opposite sign, we presume that the dominant voltage contribution in the  $L = 5$  mm samples is due to SRE. In the following section, the voltage drops measured for the  $L < 5$  mm case are presented.

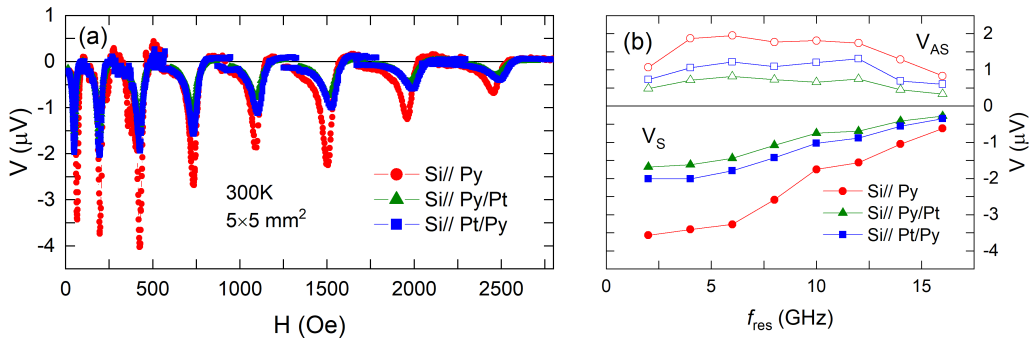


Figure 4.13: a) Representative transverse voltage signals for the three set of samples as a function of the applied magnetic field at 300K, and b) the amplitude of the symmetric (full symbols) and antisymmetric (open symbols) components of the transverse voltage signal of each curve as a function of frequency. Sample dimensions:  $5 \times 5$  mm<sup>2</sup>.

#### 4.2.4 Voltage Measurements as a Function of $L$

The *new* samples are the same as the previous  $L = 5$  mm samples but have been modified by using standard optical lithography methods (using a Micro-writer ML3 from Durham Magneto Optics Ltd, see Appendix A.1.2). For that purpose, samples with different values of width  $L$  were prepared in the form of single stripes in the middle of each sample with dimensions  $5 \times L$  mm<sup>2</sup>. This width  $L$  ranges from 2 mm to 20  $\mu$ m in each set of samples and within each system. However, it is important to mention that the  $L = 20$   $\mu$ m samples are the only ones that do have a different lithographic pattern, i.e., instead of a single stripe with dimensions  $5 \times L$  mm<sup>2</sup>, it is composed of several parallel stripes of dimensions  $2 \times L$  mm<sup>2</sup>. This pattern will be referred to as *fringed* in order to differentiate it from the single-stripe one. An sketch of both patterns is shown in Fig. 4.14. This difference is justified by the fact that as the width along the CPW is reduced, the FMR absorption spectra becomes more and more noisy (since it depends linearly on the amount of material that is being excited, i.e., material present on top of the CPW). The voltage signal, on the other hand, is an intensive quantity and, as such, it does not depend on the amount of sample present on top of the CPW. As a consequence, the voltage signal of a single-striped pattern sample and the one from a fringed pattern sample are exactly the same. This is shown in the Appendix B using two Si// Py/Pt samples with  $L = 50$   $\mu$ m but differing in the type of pattern used.

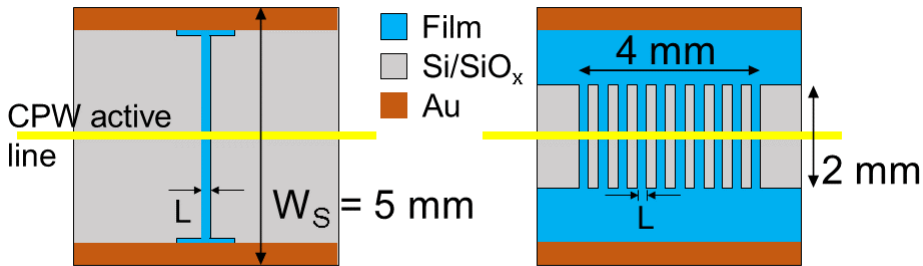


Figure 4.14: Sketch of the two kind of patterns employed in this experiment. The single-stripe pattern (left) consists of a  $L \times 5$  mm<sup>2</sup> stripe in the region within the lateral gold contacts. On the other hand, the fringed pattern (right) consists of multiple parallel stripes (alternating between the substrate and the film) and is only used for the  $L = 20$   $\mu$ m case. In this case, the sample length  $W_s$  is 2 mm, while in the single-stripe pattern is 5 mm.

The dependence of the transverse voltage signal on  $L$  was measured in the three sets of samples, but before showing the results, it is utterly important to make sure that the the  $L < 5$  mm samples share the same magnetodynamical properties as the original  $L = 5$  mm samples. This is the first step towards the verification of the hypothesis by which the SRE could be removed by reducing the sample width

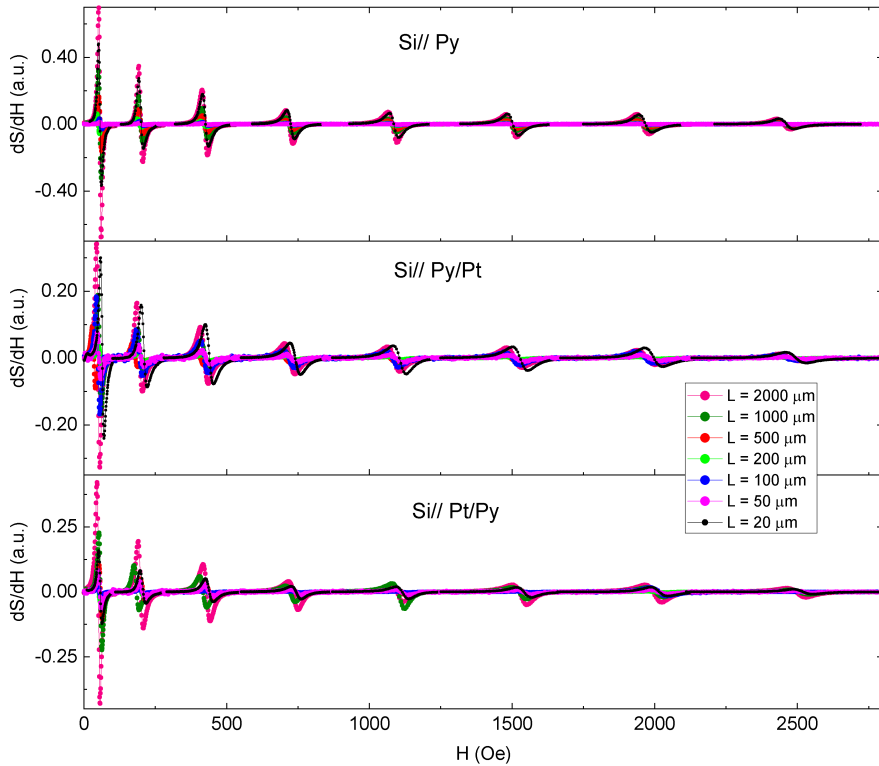


Figure 4.15: FMR absorption spectra for each kind of system and as a function of  $L$ .

along the CPW direction. In Fig. 4.15, the FMR spectra of each system and sample width are shown. As can be observed, there is a clear overlapping of the absorption curves at each frequency within each system, suggesting that the magnetodynamical properties remain the same regardless of the sample width.

Following the methodology of the first part of this chapter, the FMR absorption curves of Fig. 4.15 were fitted using Eq. 4.2 to obtain the resonance field  $H_{\text{res}}$  and linewidth  $\Delta H$  at each frequency for each sample and sample width. Again, the dependence of these two parameters with the resonance frequency is fitted to obtain the basic magnetodynamical parameters of the system (see Eqs. 4.3 and 4.4). In Fig. 4.16 the frequency-dependent curves are shown for each sample and sample width  $L$ , and the resulting fitted parameters are compiled in Table 4.4.

As can be observed in Figs. 4.16a, 4.16b, and 4.16c, the absolute overlapping of the curves show that the resonance field remains the same regardless of the sample width, resulting in the same static magnetic parameters:  $M_s$  and  $\gamma$  (see Table 4.4). Moreover, a similar overlapping is observed in Figs. 4.16d, 4.16e, and 4.16f, showing

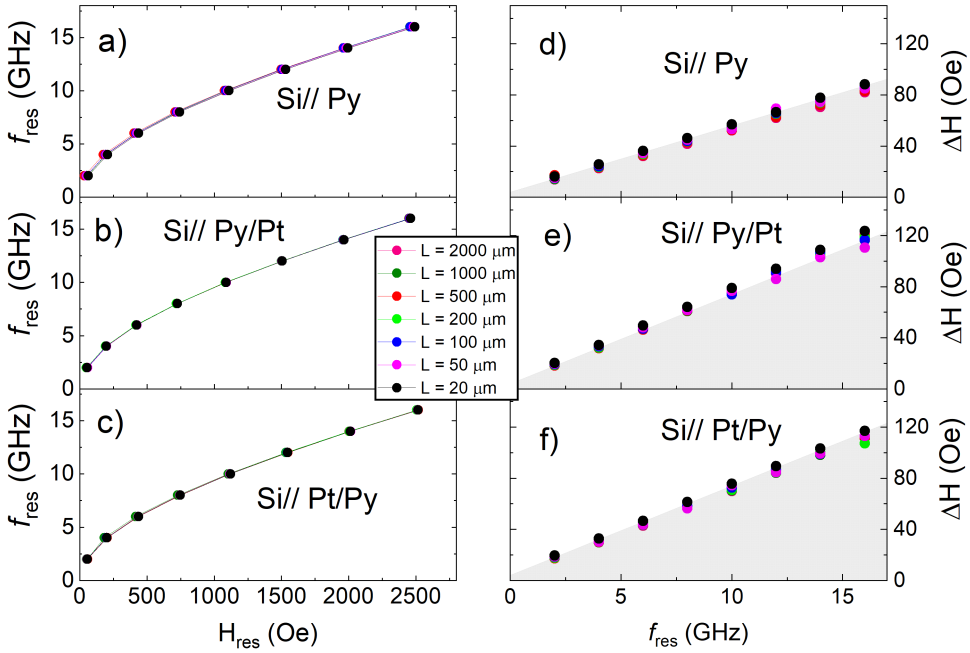


Figure 4.16: Resonance frequency dependence on the resonance field for the three different systems studied and each sample width  $L$  (a, b, c), and the linewidth dependence on the resonance frequency for each system and sample width (d, e, f). The grey area under the curves on the right is to help to visualize the change in the slope between the Py alone sample curves and the bilayers, denoting a change in the Gilbert damping parameter, as expected for these systems.

that the linewidth of the resonance line does not change when varying the sample width. The  $y$ -axis intercept of the resonance linewidth  $\Delta H$  versus frequency lines, which quantifies the so-called inhomogeneous line broadening or damping,  $\Delta H(0)$ , remains the same irrespective of sample width  $L$ . From this observation, one can deduce that the optical lithography procedure does not introduce any sort of magnetic inhomogeneity in the ferromagnetic layer. It is also worth noticing that the slope of the lines in the bilayers increases with respect to that of the Py alone sample, as observed in the  $L = 5$  mm samples and the samples of the first part of this Chapter. As mentioned before, this increase denotes an increase in the Gilbert damping parameter in the bilayers, which is indicative of the injection of spin currents from the Py film to the Pt capping layer. The reason to draw the light grey area under each set of data points (see Figs. 4.16d, 4.16e, and 4.16f) is to visualize more easily this increase of damping between systems. Therefore, it is observed that the Gilbert damping parameter is not affected by the variation of the sample width, indicating that, from the magnetic point of view, the Py films are not affected by the patterning



process. Finally, from the overall results and from the extracted fitted values compiled in Table 4.4, it is worth mentioning the remarkable similarity between the Si//Py/Pt and Si//Pt/Py systems. This similarity demonstrates that, in this particular case, inverting the stacking order of the bilayers does not give place to very different magnetodynamical properties between both systems. This feature leads one to believe that the interface properties of both systems are very similar as well.

In summary, it is shown that the  $L < 5$  mm samples share the same magnetodynamical properties as the original  $L = 5$  mm films (compare Tables and 4.3 and 4.4). Therefore, at this point, we are in conditions to present the transverse voltage measurements as a function of the sample width  $L$  for the three sets of systems.

Table 4.4: Main magnetodynamical parameters obtained from the fitting of FMR spectra at 300K and varying sample width  $L$ . Each value is accompanied by its own  $\pm$  standard deviation. The observed difference in the Gilbert damping parameter  $\alpha$  between the Py and Py/Pt thin films is a signature of the spin pumping process.

Sample	Width $L$ ( $\mu\text{m}$ )	$\mu_0 M_s$ (emu/cm <sup>3</sup> )	$\gamma/2\pi$ (GHz/T)	$\alpha$ ( $\times 10^{-3}$ )	$\Delta H(0)$ (Oe)
Si// Py	2000	740.07 $\pm$ 0.01	29.74 $\pm$ 0.07	7.28 $\pm$ 0.05	3.2 $\pm$ 0.5
Si// Py	1000	748.03 $\pm$ 0.01	29.74 $\pm$ 0.07	7.47 $\pm$ 0.07	3.6 $\pm$ 0.5
Si// Py	500	748.03 $\pm$ 0.01	29.77 $\pm$ 0.07	7.34 $\pm$ 0.05	3.5 $\pm$ 0.4
Si// Py	200	748.03 $\pm$ 0.01	29.72 $\pm$ 0.06	7.54 $\pm$ 0.08	3.6 $\pm$ 0.5
Si// Py	100	748.03 $\pm$ 0.01	29.74 $\pm$ 0.05	7.63 $\pm$ 0.05	3.6 $\pm$ 0.6
Si// Py	50	763.94 $\pm$ 0.01	29.45 $\pm$ 0.11	7.43 $\pm$ 0.21	4.8 $\pm$ 1.5
Si// Py	20 (fringed)	748.03 $\pm$ 0.01	29.45 $\pm$ 0.10	7.66 $\pm$ 0.05	5.3 $\pm$ 0.4
Si// Py/Pt	2000	748.03 $\pm$ 0.01	29.59 $\pm$ 0.08	10.94 $\pm$ 0.10	2.7 $\pm$ 0.7
Si// Py/Pt	1000	748.03 $\pm$ 0.01	29.65 $\pm$ 0.05	10.63 $\pm$ 0.10	3.9 $\pm$ 1.0
Si// Py/Pt	500	763.94 $\pm$ 0.01	29.22 $\pm$ 0.08	10.63 $\pm$ 0.05	3.0 $\pm$ 0.7
Si// Py/Pt	200	748.03 $\pm$ 0.01	29.70 $\pm$ 0.08	10.79 $\pm$ 0.10	3.9 $\pm$ 0.8
Si// Py/Pt	100	740.07 $\pm$ 0.01	29.75 $\pm$ 0.10	10.56 $\pm$ 0.20	4.9 $\pm$ 1.3
Si// Py/Pt	50	732.11 $\pm$ 0.01	29.80 $\pm$ 0.20	9.83 $\pm$ 0.25	8.1 $\pm$ 1.7
Si// Py/Pt	20 (fringed)	740.07 $\pm$ 0.01	29.68 $\pm$ 0.10	10.98 $\pm$ 0.02	5.0 $\pm$ 0.2
Si// Pt/Py	2000	724.15 $\pm$ 0.01	29.67 $\pm$ 0.05	10.08 $\pm$ 0.07	2.7 $\pm$ 0.4
Si// Pt/Py	1000	732.11 $\pm$ 0.01	29.58 $\pm$ 0.05	10.02 $\pm$ 0.05	2.9 $\pm$ 0.4
Si// Pt/Py	500	724.15 $\pm$ 0.01	29.60 $\pm$ 0.06	10.10 $\pm$ 0.07	2.9 $\pm$ 0.5
Si// Pt/Py	200	716.20 $\pm$ 0.01	29.86 $\pm$ 0.07	9.92 $\pm$ 0.24	4.5 $\pm$ 1.6
Si// Pt/Py	100	724.15 $\pm$ 0.01	29.70 $\pm$ 0.09	10.32 $\pm$ 0.17	3.2 $\pm$ 1.1
Si// Pt/Py	50	724.15 $\pm$ 0.01	29.63 $\pm$ 0.10	10.10 $\pm$ 1.7	3.7 $\pm$ 1.2
Si// Pt/Py	20 (fringed)	724.15 $\pm$ 0.01	29.70 $\pm$ 0.06	10.41 $\pm$ 0.05	5.1 $\pm$ 0.3

In Fig. 4.17 the transverse voltage measurements for all the samples with  $L < 5$

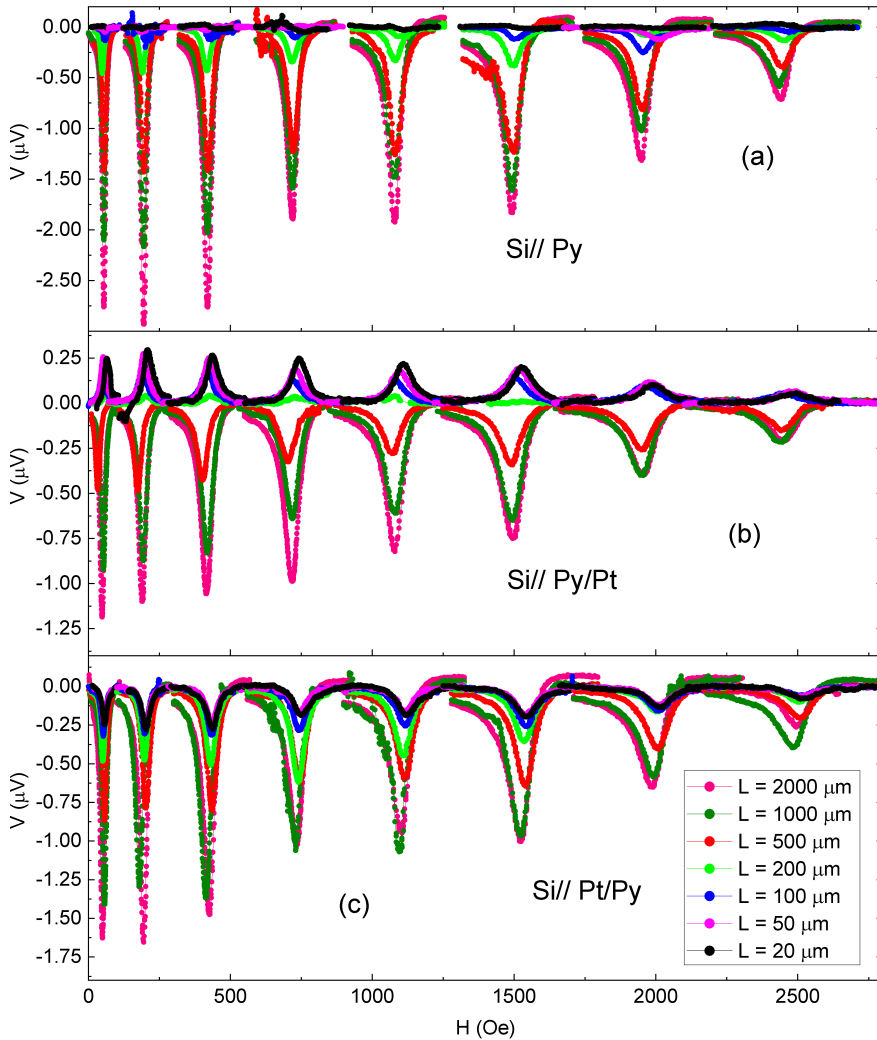


Figure 4.17: Transverse voltage measurements as a function of the sample width  $L$  for the three sets of systems: Si// Py (a), Si// Py/Pt (b), and Si// Pt/Py (c).

mm and for each system are shown. In addition, both symmetric and antisymmetric voltage amplitudes as a function of sample width for four representative resonant frequencies (i.e., 2 GHz, 6 GHz, 10 GHz, and 14 GHz) are depicted in Fig. 4.18. These voltage amplitudes, again, are obtained from the fitting of the curves of Fig. 4.17 using Eq. 4.9. We start by discussing the results of each system individually, starting with the results from the Py alone samples and ending with the ones from the Si// Pt/Py system.

### 1. Si// Py samples:

The transverse voltage measurements of the Si// Py samples as a function of the sample width are shown in Fig. 4.17a, and the corresponding symmetric and antisymmetric voltage amplitudes are gathered in Fig. 4.18a. As evidenced in Fig. 4.17a, the transverse voltage signal measured is always negative in sign irrespective of  $L$  and decreases with decreasing  $L$ . Additionally, from Fig. 4.18a, it is also observed that the amplitude of the symmetric component decreases when increasing the resonant frequency, while the antisymmetric one remains almost constant for all frequencies. The relative magnitude between both symmetric and antisymmetric amplitudes, however, converges at the smaller sample widths. It is also worth mentioning that this convergence tends to zero at sufficiently small samples widths (i.e.,  $L < 100 \mu\text{m}$ ), as can be appreciated in more detail in Fig. 4.18d.

### 2. Si// Py/Pt samples:

The transverse voltage measurements of the Si// Py/Pt samples as a function of sample width are shown in Fig. 4.17b, and the corresponding symmetric and antisymmetric voltage amplitudes are gathered in Fig. 4.18b. When compared with the results obtained in the Py alone samples, the first remarkable feature is that the voltage signal reverses sign and becomes positive for  $L < 200 \mu\text{m}$ . It is also worth noticing, from Fig. 4.18b, that the symmetric voltage amplitude decreases with decreasing  $L$  for above  $L = 200 \mu\text{m}$ . Below this point, however, the voltage amplitude signal almost saturates at some constant, positive value. Regarding the antisymmetric voltage amplitude, it decreases with decreasing  $L$  and becomes vanishing small for  $L < 200 \mu\text{m}$  (see Fig. 4.18e for a detailed closeup of the  $L < 200 \mu\text{m}$  region). As a consequence, the measured transverse voltage signal below  $200 \mu\text{m}$  is fully symmetric and positive, irrespective to the frequency of the measurement.

### 3. Si// Pt/Py samples:

The transverse voltage measurements of the Si// Pt/Py samples as a function of sample width are shown in Fig. 4.17c, and the corresponding symmetric and antisymmetric voltage amplitudes are gathered in Fig. 4.18c. The idea behind the set of samples with inverted stacking order is to take advantage of the different behaviour of ISHE and SRE under the inversion of the spin current injection direction. In fact, as can be observed in Fig. 4.17c, the transverse voltage signal, as in the Py alone samples, is always negative regardless of sample width. Nevertheless, contrary to the Py alone samples case, a closer look at their symmetric and antisymmetric voltage components reveals that the amplitude of the antisymmetric contribution becomes vanishing small with decreasing  $L$ , while the amplitude of the symmetric component decreases with decreasing  $L$  but remains at an almost constant, negative value below  $L = 200 \mu\text{m}$  (see Fig. 4.18f). As a consequence, the

measured transverse voltage signal below  $200 \mu\text{m}$  is fully symmetric and negative, irrespective of the frequency of the measurement.

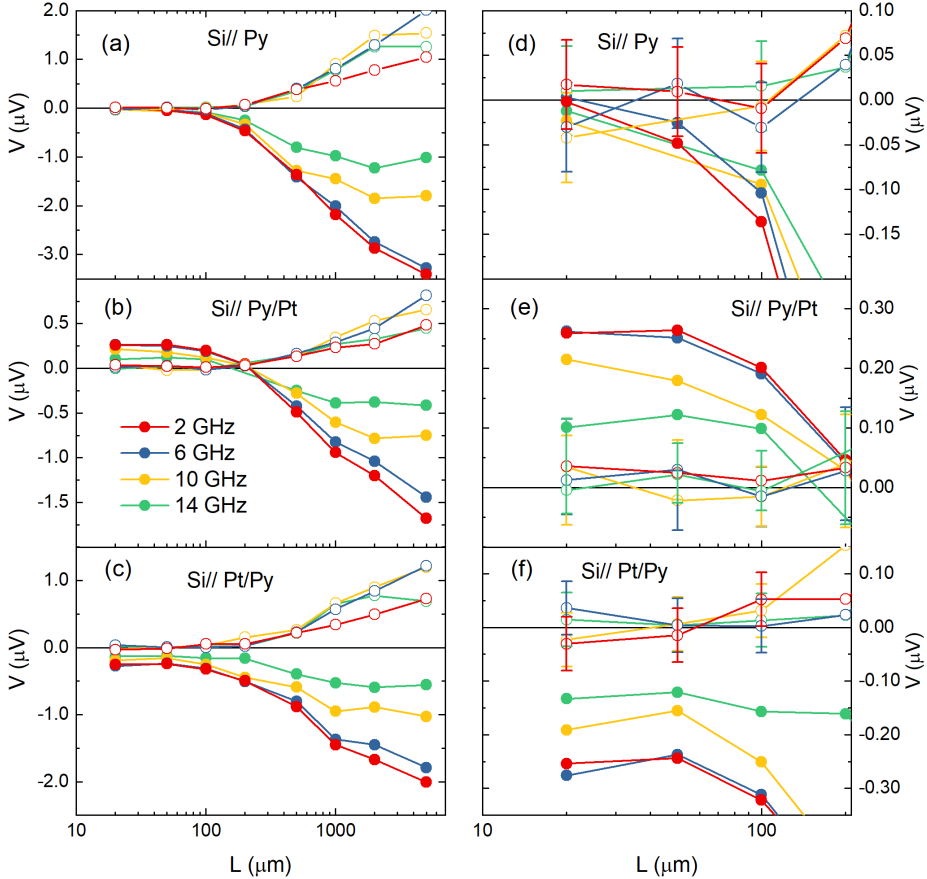


Figure 4.18: Voltage symmetric and antisymmetric amplitude constants dependence on the sample width  $L$  for the three sets of systems (left, a, b, c) and an expanded image of the  $L < 200 \mu\text{m}$  region for each system (right, d, e, f), respectively. The bold symbols correspond to the symmetric voltage amplitude, while the empty symbols represent the antisymmetric contribution.

As can be observed, the transverse voltage measurements are very sensitive to the variation of sample width  $L$ . Moreover, these results demonstrate that the behaviour in each system is both quantitative and qualitative different from each other, although the physical mechanisms and effects that lie beneath should be the same. In order to give physical meaning and understand the Si//Py voltage measurements (see Figs. 4.17a and 4.18a) it is important to account for all the possible sources of voltage in a system where the NM is absent. In this scenario, there are primarily three

possible voltage sources: (i) the SRE thoroughly mentioned in this chapter; (ii) the self-induced ISHE, which has been recently reported for some FM materials [156, 157, 158]; and (iii) the so-called magnonic charge pumping (MCP) effect, or inverse spin-orbit torque (ISOT), which arises in systems with lack of spatial inversion symmetry and high spin-orbit coupling [159, 160].

The first of these sources are the SRE, which are generated by a microwave eddy current circulating through the Py layer induced by the incident microwave radiation carried by the CPW, in close similarity with an eddy current generated in a conductor by a changing magnetic field, as mentioned before. In this sense, it is likely that at sufficiently short sample widths  $L$ , this induced electric current gets vanishing small. As a consequence, without the presence of any sort of driving electric current circulating in the Py film, the SRE should vanish as well (this is the  $\mathbf{j} = 0$  case in Eq. 4.10). This hypothesis would be in accordance with the experimental evidence, and would suggest that at some sample threshold width ( $L < 200 \mu\text{m}$  in Fig. 4.18a) the induced electric current circulating in the Py layer disappears and the overall measured transverse voltage signal, which would be originated entirely from SRE, is suppressed.

The other two possible sources of voltage, namely the self-induced ISHE and the MCP effect, rely on spin-orbit interactions but are conceptually different. On one hand, MCP is the direct conversion of spin waves into charge currents *via* spin-orbit coupling (SOC), but only arises in systems or materials which exhibit broken inversion symmetry. The fundamental difference between MCP and the conventional ISHE is that the former does not depend on a spin sink NM material with high SOC attached to the FM layer to make the spin-charge conversion. Therefore, only two ingredients are necessary to achieve MCP in a single FM layer: inversion symmetry breaking and high SOC. In particular, this inversion symmetry breaking exists in all surfaces and interfaces (such as in heterostructures comprising thin FM layers), but there can also exist bulk inversion symmetry breaking (e.g., in zinc-blende crystal structures such as (Ga,Mn)As) [160]. In addition, some authors [147] have suggested that Py exhibits high SOC, while others even have estimated a 1% spin-charge conversion efficiency for single Py layers [156]. In our experiment, although the Si//Py system exhibits inversion symmetry breaking (due to interfaces) and assuming that it has high SOC, it does not explain satisfactorily the voltage dependence on  $L$ , since both inversion symmetry and SOC should not depend on the width of the sample, at least at the scale of  $\mu\text{m}$ . Therefore, we conclude that MCP, although might play a (minor) role on the overall measured voltage in Si//Py films, is not the dominant contribution to it. On the other hand, the self-induced ISHE arises from the different spin-dependent scattering at different interfaces with the FM film [157]. In our case, these different interfaces would be (i) the interface between the Py and the Si substrate, and (ii) the Py/vacuum interface (actually, the Py surface is partially oxidized, therefore it

would be the Py/oxidation layer interface instead). The different spin accumulation at both interfaces would drive a diffusive spin current flow across the FM film, which is ultimately converted to a transverse charge current due to the intrinsic SOC of the FM. Experimentally, the current evidence for self-induced ISHE in Py layers is diverse and misleading. An experiment conducted by Tsukahara, et al. [156] reported the measurement of self-induced ISHE in Py thin films at room temperature. Some time later, Gladii, et al. [157], through a series of temperature-dependent voltage measurements at resonance, found that the self-induced ISHE in Py films follows a non-monotonic temperature dependence, starting with no voltage at room temperature and a cusp around 95K. This result is in direct contradiction with the previous one from Tsukahara, et al. and with our own experimental findings (see Figs. 4.13 and 4.17), where voltage is reported at 300K. Additionally, in this same experiment, the authors repeated the measurements for two Py/Pt bilayers with inverted stacking order (i.e., //Py/Pt and //Pt/Py). They concluded by stating that the Py alone film “behaves similarly to a buffer Pt layer [i.e., //Pt/Py], as the spin current is towards the substrate. In this scenario, spin and subsequent charge currents in the Pt and NiFe [Py] layers adds up for the Pt buffer layer and subtract for the Pt capping case” [157, p. 5]. This result is also in contradiction with our experimental evidence: In our case, the magnitude of the Si// Py system voltage signal for  $L > 200 \mu\text{m}$  is consistently larger than its Py/Pt bilayers counterparts. As a consequence, we rule out the possibility that the self-induced ISHE is behind the observed voltage signal in the Si// Py system.

From this discussion, it seems that the most satisfactory explanation is that the voltage signal measured in the Si// Py system is due predominantly to SRE. This conclusion can be extended to the behaviour of the Py film in both the Si// Py/Pt and Si// Pt/Py systems, assuming that the differences observed in the  $L < 200 \mu\text{m}$  region are originated entirely from the ISHE in the Pt capping and buffer layers, respectively. In fact, as stated before, the magnetodynamical properties of both bilayers are very similar. This feature led us to believe that their corresponding interface quality and spin transparency should be alike as well. In this line, a direct comparison of the  $L < 200 \mu\text{m}$  regions in Si// Py/Pt and Si// Pt/Py systems (see Figs. 4.18e and 4.18f, respectively) shows that, for the smaller values of  $L$ , the voltage signal measurements from the Si// Pt/Py are in fact just a mirror image of the ones from the Si// Py/Pt system. In particular, in order to better visualize this property, the voltage signal lines of both bilayers for the cases of  $L = 50 \mu\text{m}$  and  $L = 20 \mu\text{m}$  and their corresponding voltage amplitudes as a function of resonance frequency are shown in Fig. 4.19. The similarity between systems is astonishing and the observed differences are attributed to the experimental error and the fact that both bilayers were grown separately. This inversion symmetry is important because it is in accordance with a purely ISHE-induced voltage signal considering the inversion of the spin current injection direction (see Eq. 4.8). Conversely, the SRE

are independent of the spin current direction and, thus, cannot by themselves explain the observed behaviour at the smaller widths.

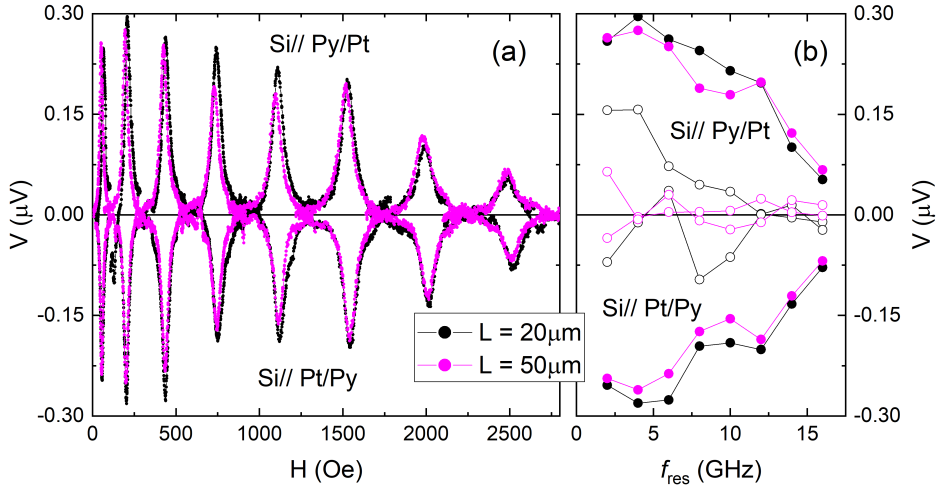


Figure 4.19: (a) Direct comparison of the voltage signals measured in the Si// Py/Pt and Si// Pt/Py systems for  $L = 50 \mu\text{m}$  (magenta circles) and  $L = 20 \mu\text{m}$  (black circles). It shows that both signals are a mirror image of each other. This symmetry is in accordance with the inverted spin current injection direction presumed between systems. (b) The corresponding voltage symmetric (full symbols) and antisymmetric (empty symbols) amplitudes as a function of resonance frequency.

Moreover, as we state in Section 4.2.3 when studying the voltage measurements at  $L = 5 \text{ mm}$ , a positive voltage sign ( $V > 0$ ) is expected for a purely ISHE-induced voltage signal in the Si// Py/Pt system. Therefore, by symmetry, a negative one ( $V < 0$ ) is expected for the Si// Pt/Py system, as observed. Finally, in order to straighten this interpretation, the analysis of the lineshape of the voltage spectral lines (see Fig. 4.19b) shows that the voltage signals are fully symmetric in both bilayers for  $L < 200 \mu\text{m}$ . This result by itself would not fully explain that the measured signal corresponds entirely to ISHE, since it has been mentioned before that the SRE exhibit both symmetric and antisymmetric contributions. Nevertheless, it is important to consider the fact that, in the Py alone samples, for the smaller  $L$  the voltage signal vanishes, and that the dominant contribution to the voltage in this case are SRE. This observation indicates that the symmetric voltage amplitude in the bilayers (regardless of  $L$ ) must arise only from two sources: (i) SRE, which depend on  $L$ , and (ii) ISHE, which is independent of  $L$ . Formally, one could write

$$V_s^k = V_{\text{SRE}}^k(L) \pm V_{\text{ISHE}}^k, \quad (4.12)$$



where  $k = \{\text{Si// Py/Pt} ; \text{Si// Pt/Py}\}$ , the + sign corresponds to the Si// Py/Pt system and the - sign to Si// Pt/Py, and the dependence of  $V_{\text{SRE}}$  with  $L$  is such that  $V_{\text{SRE}} \rightarrow 0$  when  $L \rightarrow 0$ . As a result, we are confident that the measured voltage below a sample width of 200  $\mu\text{m}$  is due predominantly to ISHE.

In order to better visualize all these results, the symmetric voltage amplitudes as a function of sample width for the three kinds of systems studied at a given frequency are compiled in Fig. 4.20a. Additionally, the half-sum ( $V_s^+$ ) and half-difference ( $V_s^-$ ) of the bilayer symmetric voltage amplitudes with respect to  $L$  are shown in Fig. 4.20b. These quantities are defined as

$$V_s^+ = \frac{1}{2} \left( V_s^{\text{Si// Py/Pt}} + V_s^{\text{Si// Pt/Py}} \right), \quad (4.13)$$

$$V_s^- = \frac{1}{2} \left( V_s^{\text{Si// Py/Pt}} - V_s^{\text{Si// Pt/Py}} \right), \quad (4.14)$$

where  $V_s^{\text{Si// Py/Pt}}$  and  $V_s^{\text{Si// Pt/Py}}$  correspond to the voltage  $V_s^k$  defined in Eq. 4.12. Consequently, if Eq. 4.12 holds, then

$$V_s^+ = \langle V_{\text{SRE}}(L) \rangle, \quad (4.15)$$

and

$$V_s^- \approx V_{\text{ISHE}}^{\text{Si// Py/Pt}}. \quad (4.16)$$

These assumptions match the experimental evidence: in our case, the half-sum  $V_s^+$ , corresponding to the average SRE, is a function that depends on  $L$  in some manner and, at sufficiently small sample widths, vanishes. This feature has been observed in the Py alone samples, where the SRE were the dominant contribution to the voltage line. Furthermore, the half-difference  $V_s^-$ , corresponding to the ISHE voltage signal, does not depend on the sample width and exhibits a constant value irrespective of  $L$ , as expected. From this result, one could think that the half-sum and half-difference procedure by itself would be enough to disentangle the contributions coming from ISHE and SRE, as has already been claimed in some papers [153, 154] and that, as a consequence, the shortening of the sample width presented in this work is unnecessary for that matter. Nevertheless, as is mentioned at the beginning of Section 4.2.1 when presenting the different strategies that have been employed for the separation of ISHE and SRE, the inversion of the bilayer stacking order does not guarantee the same interface properties or that both systems share the same magnetodynamical properties, for instance. Thus, if this symmetry is not guaranteed, the half-sum and half-difference method is not viable. In our particular case, since both bilayer systems presented the same magnetodynamical properties, the half-sum and half-difference method was expected to work and, for this reason, it was ultimately used



just to validate the hypothesis which states that the reduction of the sample width is a valid method for suppressing the SRE.

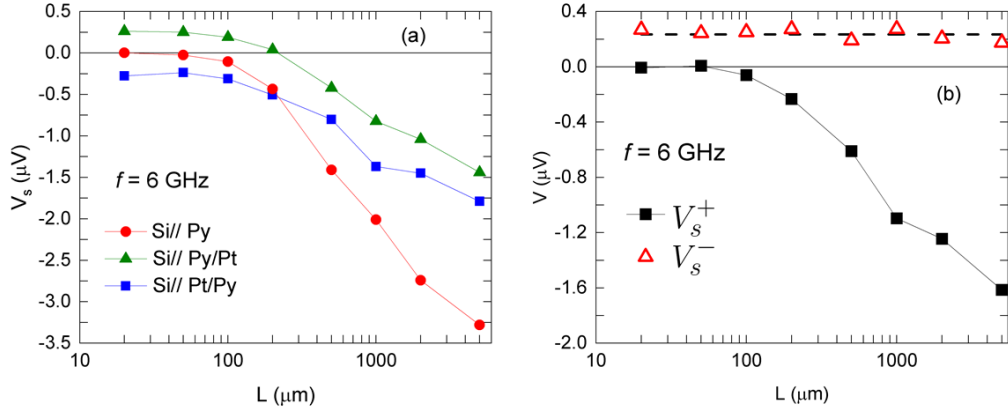


Figure 4.20: (a) Dependence of the amplitude of the symmetric component of the transverse voltage signal of each sample set at room temperature as a function of sample width at 6 GHz. (b) Half-sum ( $V_s^+$ ) and half-difference ( $V_s^-$ ) of the symmetric voltage amplitudes of the Si//Py/Pt and Si//Pt/Py samples at 6 GHz and room temperature. Error bars are about the size of the symbols used.

## Spin Hall Angle

The spin Hall angle  $\Theta_{\text{SH}}$  quantifies the spin-to-charge conversion efficiency of a given material. This feature makes it one of the most important figures of merit in spintronics. We estimate the  $\Theta_{\text{SH}}$  of Pt based on the Si//Py/Pt  $L = 20 \mu\text{m}$  transverse voltage measurements presented in this Chapter.  $\Theta_{\text{SH}}$  is related to the ISHE voltage through the relation [161]

$$V_{\text{ISHE}} = wR\Theta_{\text{SH}}\lambda_{\text{sd}} \tanh\left(\frac{t_{\text{Pt}}}{2\lambda_{\text{sd}}}\right) j_s, \quad (4.17)$$

being  $j_s$  given by [161]

$$j_s \approx \left(\frac{\hbar G_{\text{eff}}^{\uparrow\downarrow}}{8\pi}\right) \left(\frac{\mu_0 h_{\text{rf}} \gamma}{\alpha'}\right)^2 \left[ \frac{\mu_0 M_s \gamma + \sqrt{(\mu_0 M_s \gamma)^2 + (4\pi f_{\text{res}})^2}}{(\mu_0 M_s \gamma)^2 + (4\pi f_{\text{res}})^2} \right] \left(\frac{2e}{\hbar}\right). \quad (4.18)$$

In this case,  $V_{\text{ISHE}}$  corresponds to the symmetric voltage amplitude  $V_s$ , the resistance of the Py/Pt film is denoted as  $R$ ,  $w$  is the width of the CPW signal line (200  $\mu\text{m}$ ),  $h_{\text{rf}}$  is the magnitude of the rf magnetic field,  $G_{\text{eff}}^{\uparrow\downarrow}$  is the spin-mixing conductance, and  $\alpha'$  is the Gilbert damping parameter of the Py/Pt bilayer. For the calculation, the spin diffusion length  $\lambda_{\text{sd}}$  has been fixed to 5 nm, according to the resistivity value of the Pt capping layer [162, 163]. However, a better estimation of this value in our system could be obtained by measuring a series of Py/Pt bilayers with varying Pt thickness, as proposed by some authors [114, 164]. Concerning  $h_{\text{rf}}$ , we must say that the CPW manufacturer (NanOsc) does not disclose too much details about the CPW. So, we cannot know exactly the value of  $h_{\text{rf}}$  (an estimate value of  $h_{\text{rf}} \approx 50 \mu\text{T}$  is provided by the manufacturer) nor its possible dependence on frequency and/or temperature<sup>3</sup>. In accordance with this, the  $h_{\text{rf}}$  value used here is fixed to 50  $\mu\text{T}$ , as stated by some authors using the same experimental setup [161, 165, 166]. Altogether, the value of  $\Theta_{\text{SH}}$  presented here must be understood as an estimation of the actual value due to the uncertainty in some of the parameters employed in the calculation. The resulting  $\Theta_{\text{SH}}$  as a function of the resonance frequency  $f_{\text{res}}$  is shown in Fig. 4.21. As can be observed, the mean value of  $\Theta_{\text{SH}}$  is equal to  $1.55 \pm 0.48 \%$ , which is in accordance with reported values from the literature in similar systems [162, 114, 167].

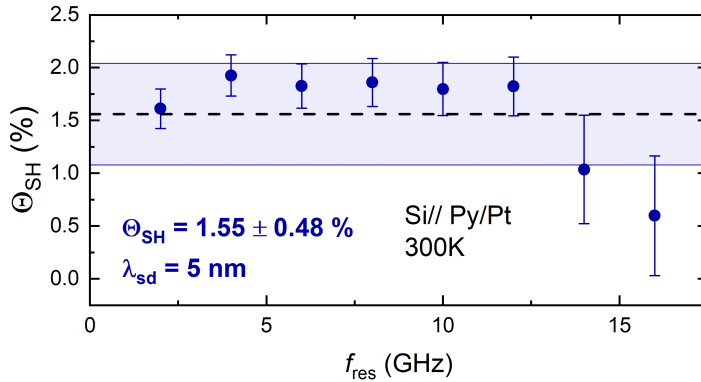


Figure 4.21: Spin Hall angle  $\Theta_{\text{SH}}$  of Pt as a function of the resonance frequency. The dashed line corresponds to the mean value, while the blue region comprises its standard deviation. The error bars at each point, denoted by  $\delta\Theta_{\text{SH}}$ , for instance, have been calculated according to  $\delta\Theta_{\text{SH}} = (\delta\Theta_{\text{SH}}/\delta V)\delta V$ , where  $\delta V = 0.01 \mu\text{V}$  (i.e., the nanovoltmeter detection limit), and  $\delta\Theta_{\text{SH}}/\delta V = 1/[Rw\lambda_{\text{sd}} \tanh(t_{\text{Pt}}/2\lambda_{\text{sd}})j_s]$ .

In summary, in this Section a method for disentangling the transverse voltage contributions coming from SRE and ISHE in metallic FM systems during FMR based entirely on the geometry of the sample is presented. Additionally, this method avoids

<sup>3</sup>One must expect that the impedance of the CPW will depend on both parameters and that this could alter the intensity circulating by and consequently the value of  $h_{\text{rf}}$ .

the tedious angular and field dependent measurements commonly used in this kind of experiments. Moreover, it allows to easily estimate the spin Hall angle directly from the transverse voltage measurements. In general, this method can be extended to any metallic FM system where the SRE are present. In the following section, a numerical study for the quantitative understanding of the behaviour of the SRE based on the Si// Py/Pt is presented.

#### 4.2.5 Numerical Study of the SRE in the Si// Py/Pt System

To gain a deeper insight into the behaviour of the induced current circulating through the Py layer, a numerical study of the SRE in the metallic Si// Py/Pt bilayers was performed to clarify their contribution to the measured transverse voltage signal<sup>4</sup>.

Let's start by defining the coordinate system used as well as the main quantities involved in the calculation. This can be visualized in Fig. 4.22. As can be observed from the figure, the quantities involved in the system have both ac and dc components. These quantities include: (i) an externally applied static magnetic field pointing in the  $z$  direction  $\mathbf{H} = H\hat{\mathbf{k}}$ ; (ii) an oscillating magnetic field carried by the CPW whose components are perpendicular to the static field,  $\mathbf{h}(t) = h_x(t)\hat{\mathbf{i}} + h_y(t)\hat{\mathbf{j}}$ ; (iii) a magnetization vector which includes both dynamic and static components,  $\mathbf{M}(t) = \mathbf{m}(t) + M_s\hat{\mathbf{k}}$ , being  $\mathbf{m}(t) = m_x(t)\hat{\mathbf{i}} + m_y(t)\hat{\mathbf{j}}$ ; and (iv) the induced, oscillatory eddy current inside the sample  $\mathbf{j}$ , which points in the  $z$  direction (perpendicular to the oscillating magnetic field). It is important to note that the magnitude of the magnetization vector can be approximated to  $M_s$  as a first approximation due to the small nature of the oscillating parts.

Now, let's consider the generalized Ohm's law (see Eq. 4.10), where both AMR and AHE terms induce components of the electric field that are perpendicular to the current density  $\mathbf{j}$ . In the particular case of this system, both the induced current  $\mathbf{j}$  and  $\mathbf{m}(t)$  have the same oscillating frequency  $\omega$  plus a given phase:  $\phi_j$ ,  $\phi_{m_x}$ , and  $\phi_{m_y}$  respectively. Hence, both quantities can be expressed as

$$\mathbf{j} = j_z(t)\hat{\mathbf{k}} = j_z e^{(i\omega t + \phi_j)}\hat{\mathbf{k}}, \quad (4.19)$$

$$\mathbf{m}(t) = m_x(t)\hat{\mathbf{i}} + m_y(t)\hat{\mathbf{j}} = m_x e^{(i\omega t + \phi_{m_x})}\hat{\mathbf{i}} + m_y e^{(i\omega t + \phi_{m_y})}\hat{\mathbf{j}}. \quad (4.20)$$

From this, by substituting Eqs. 4.19 and 4.20 into Eq. 4.10, it is easy to calculate the expressions for the AMR and AHE contributions to the electric field,

<sup>4</sup>It is important to say that this calculation has been developed mainly by Dr. Carlos Frontera with the fruitful conversations with Dr. M. Kostylev.

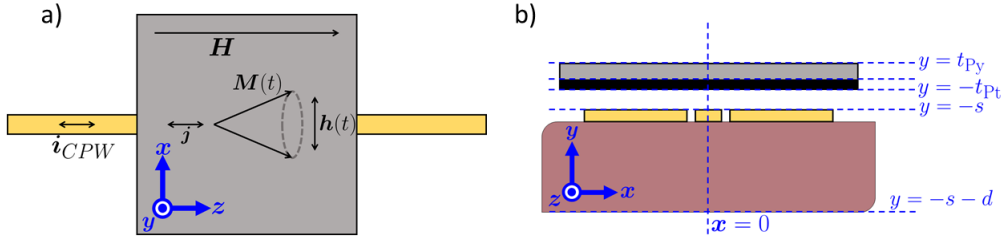


Figure 4.22: a) Top view of the coordinate system chosen for describing the SRE due to the synchronous variation of magnetization and intensity in the sample. The CPW corresponds to the yellow thin stripe and the sample is the grey square. It is important to note that the sample is oriented upside down, i.e., with the Pt film on the top of CPW. b) Transverse section of the system showing the sample on top of the CPW and the distances between elements. The thickness of the Py (Pt) film is denoted by  $t_{\text{Py}}$  ( $t_{\text{Pt}}$ ),  $s$  is the spacing between the CPW line and the Pt film surface, and  $d$  is the thickness of the CPW substrate. It is important to note that the CPW is composed of three elements: the signal line in the middle, and two ground lines on both sides.

$$\mathbf{E}^{\text{AMR}} = \frac{\Delta\rho}{M_s} \left( j_z(t)m_x(t)\hat{\mathbf{i}} + j_z(t)m_y(t)\hat{\mathbf{j}} + j_z(t)M_s\hat{\mathbf{k}} \right), \quad (4.21)$$

$$\mathbf{E}^{\text{AHE}} = -\frac{\rho^{\text{AHE}}}{M_s} (-j_z(t)m_y(t)\hat{\mathbf{i}} + j_z(t)m_x(t)\hat{\mathbf{j}}). \quad (4.22)$$

However, since the transverse voltage is ultimately measured along the  $\mathbf{x}$  direction according to Fig. 4.22, the only components that matter are the ones parallel to it, i.e.,

$$E_x^{\text{AMR}} = \frac{\Delta\rho}{M_s} j_z(t)m_x(t), \quad (4.23)$$

and

$$E_x^{\text{AHE}} = \frac{\rho^{\text{AHE}}}{M_s} j_z(t)m_y(t). \quad (4.24)$$

The dc components of the field are obtained by averaging over time the real ( $\Re$ ) part these contributions. Formally, one can write,

$$\begin{aligned}
 \Re \langle j_z(t) m_i(t) \rangle &= j_z m_i \langle \cos(\omega t + \phi_j) \cos(\omega t + \phi_{m_i}) \rangle \\
 &= \frac{1}{2} j_z m_i (\cos \phi_j \cos \phi_{m_i} + \sin \phi_j \sin \phi_{m_i}) \\
 &= \frac{1}{2} \Re (j_z(t) m_i^*(t)),
 \end{aligned} \tag{4.25}$$

being the subscript  $i$  equal to  $x$  for AMR and to  $y$  for AHE. Therefore, substituting Eq. 4.25 into Eqs. 4.23 and 4.24, one finally gets the appropriate expressions for the SRE,

$$\langle E_x^{\text{AMR}} \rangle = \frac{\Delta \rho}{2M_s} \Re (j_z(t) m_x^*(t)), \tag{4.26}$$

$$\langle E_x^{\text{AHE}} \rangle = \frac{\rho^{\text{AHE}}}{2M_s} \Re (j_z(t) m_y^*(t)). \tag{4.27}$$

The goal of this numerical study is to find the dynamic magnetization  $\mathbf{m}(t)$  and the induced current  $\mathbf{j}$  in order to understand the behaviour of AMR and AHE in our system. In Chapter 3, an expression for the magnetization response to an oscillating rf magnetic field was obtained by solving the Landau-Lifshitz-Gilbert equation (Eq. 4.1). It was found that the dynamic magnetization vector is related to the time-varying magnetic field  $\mathbf{h}(t)$  through the susceptibility tensor  $\tilde{\chi}$  in the following way,

$$\begin{pmatrix} m_x \\ m_y \\ 0 \end{pmatrix} = \begin{pmatrix} \chi_{xx} & i\chi_{xy} & 0 \\ -i\chi_{xy} & \chi_{yy} & 0 \\ 0 & 0 & 0 \end{pmatrix} \begin{pmatrix} h_x \\ h_y \\ 0 \end{pmatrix}, \tag{4.28}$$

being  $\chi_{xx}$ ,  $\chi_{xy}$ , and  $\chi_{yy}$  the components of such tensor. These quantities generally depend on the magnetodynamical properties of the ferromagnetic film and the particularities of the overall system. A detailed, quite general expression of  $\tilde{\chi}$  for the macroscopic case can be found in Chapter 3. On the other hand, the mathematical treatment of the current induced by an oscillating magnetic field in ferromagnetic media is a more complicated subject. Following the available literature regarding this topic, one finds the 1996 work by E. van de Riet and F. Roozeboom [168], in which they develop an analytical model to describe the effect of eddy currents and FMR on the magnetic permeability of FeTaN thin films. However, some of the approximations used in this study are quite crude. For instance, the time-varying magnetic field which induces the eddy currents in the sample is assumed to oscillate in the  $x$  direction alone according to the coordinates of 4.22. Furthermore, the study focuses on a resonant cavity setup while our experimental one is based on a coplanar waveguide. Moreover, a second group that has a long series of papers on this topic is that

of M. Kostylev and co-workers [169, 170, 171, 172, 173]. This series of articles ends with a comprehensive paper on the subject [174]. In this work, all the details of the complete recipe to numerically solve Maxwell's equations for single and multilayered FM films are presented for the case in which the magnetic field is created by a CPW or a microstrip line (MSL). The remaining part of this section is devoted to the application of the methodology developed in Ref. [174] (and references therein) to our problem in order to obtain analytical expressions for  $h_x$ ,  $h_y$ ,  $m_x$ , and  $m_y$  inside the Si//Py/Pt system. Once these parameters are known, the calculation of the induced current  $j_z$  is straightforward and, as a result, the determination of both the AMR and AHE is achieved <sup>5</sup>.

Before dealing with the problem itself, it is important to clarify that the electric and magnetic field components of the electromagnetic wave carried by a CPW (or a stripline) transducer may be affected when a metallic sample is placed on top of it. In this case, it is said that there is a *shielding* of the electric or magnetic field due to capacitive or inductive coupling with the sample, respectively. The shielding of the electric field, due to the capacitive coupling between the sample and the signal and ground lines of the CPW, leads to a microwave current flowing from the signal to the ground lines through the sample along the  $x$  direction according to Fig. 4.22 [174]. A detailed study on this effect as a function of sample conductivity and CPW geometry can be found in Ref. [175]. Furthermore, magnetic shielding due to magnetic induction between the sample and the signal line gives place to a microwave current in the opposite direction of the current in the signal line, i.e., opposite to  $i_{\text{CPW}}$  (see Fig. 4.22a) [174]. It is precisely this microwave current which drives the SRE in the system.

Without loss of generality, the work of M. Kostylev et al. contains some previous assumptions for simplifying the numerical calculation process. In that regard, one assumption is to consider that the system (i.e., sample and CPW) has translational invariance in the  $z$  direction. This assumption allows the decomposition of the problem into a two-dimensional one. In addition, the signal line of the CPW is assumed to be infinitely thin and behaving as a perfect conductor. With these assumptions, it is granted that magnetization, magnetic field, and electric field only depend on  $x$  and  $y$ . This results in an electric field with only non-vanishing components along the  $z$  direction and magnetic field and magnetization oscillatory parts in the  $x$ - $y$  plane. The solution for the dynamic magnetic field  $\mathbf{h}(t)$  inside the films is attained from solving the Maxwell's equations in the electric-bias free approximation [174]:

---

<sup>5</sup>We must clarify that we do not know some of the parameters used in the calculation (NanOsc did not disclose some technical details of the CPW). Consequently, the calculation is not intended to provide an exact description for our situation but to show a representative result to help us interpret our experimental findings

$$\nabla \times \mathbf{h}(t) = \sigma \mathbf{E}, \quad (4.29)$$

$$\nabla \cdot \mathbf{h}(t) = -\nabla \cdot \mathbf{m}(t), \quad (4.30)$$

$$\nabla \times \mathbf{E} = -i\omega\mu_0 [\mathbf{h}(t) + \mathbf{m}(t)]. \quad (4.31)$$

However, even in two dimensions, solving Eqs. 4.29–4.31 in real space presents several difficulties because of the scale incompatibility between various quantities (for instance, between the CPW substrate thickness  $d$  and the bilayer thickness  $t_{\text{Py}} + t_{\text{Pt}}$ , or between the width of the CPW and that of the sample). One way to circumvent this problem is by taking advantage of the translational symmetry of the film in the  $x$  direction. Using this property, it is possible to Fourier transform Eqs. 4.29–4.31 and the LLG from which Eq. 4.28 was obtained to simplify the problem and obtain physical solutions. At the end of the calculation, an inverse Fourier transformation can be applied in order to return to real space quantities. Thus, the electric field  $\mathbf{E}$ , dynamic magnetization  $\mathbf{m}(t)$ , and dynamic magnetic field  $\mathbf{h}(t)$  are written in Fourier space as

$$\mathbf{E}_k, \mathbf{m}_k, \mathbf{h}_k = \frac{1}{2\pi} \int_{-\infty}^{+\infty} \mathbf{E}, \mathbf{m}, \mathbf{h} e^{ikx} dx, \quad (4.32)$$

being the subscript  $k$  indicative of Fourier space and the  $k$  appearing in the exponential the wavenumber. Additionally, an exponential dependence on  $y$  of these Fourier components is essayed, i.e.,  $\mathbf{E}_k, \mathbf{m}_k(t), \mathbf{h}_k(t) \propto e^{qy}$ . As a consequence, in Fourier space, and using Eq. 4.28 to express  $\mathbf{m}(t)$  as  $\mathbf{m}(t) = \tilde{\chi}\mathbf{h}(t)$ , Eqs. 4.29–4.31 are expressed as

$$qE_{zk} = -i\omega\mu_0 [h_{xk}(1 + \chi_{xx}) + ih_{yk}\chi_{xy}] \quad (4.33)$$

$$ikE_{zk} = -i\omega\mu_0 [h_{yk}(1 + \chi_{yy}) - ih_{xk}\chi_{xy}] \quad (4.34)$$

$$\sigma E_{zk} = -ikh_{yk} - qh_{xk} \quad (4.35)$$

$$0 = -ik [h_{xk}(1 + \chi_{xx}) + ih_{yk}\chi_{xy}] + q [h_{yk}(1 + \chi_{yy}) - ih_{xk}\chi_{xy}]. \quad (4.36)$$

It is important to note that by combining this system of equations with Eq. 4.28, it is possible to express in terms of  $h_{xk}$ , for instance, all the other Fourier coefficients ( $h_{yk}$ ,  $E_{zk}$ ,  $m_{xk}$ , and  $m_{yk}$ ). A glimpse on the structure of each equation in the system shows that Eq. 4.36 can be expressed as a combination of Eqs. 4.33 and 4.34. Thus, by disregarding it and working on the remaining equations, one ends up with a system of two linear homogeneous equations with two uncertainties:  $h_{xk}$  and  $h_{yk}$ . This system of equations has the form:

$$h_{xk} [-i\chi_{xy} - qk\delta^2] + h_{yk} [(1 + \chi_{yy}) - i(k\delta)^2] = 0 \quad (4.37)$$

$$h_{xk} [i(1 + \chi_{xx}) - (q\delta)^2] + h_{yk} [-\chi_{yy} - iqk\delta^2] = 0 \quad (4.38)$$

being  $\delta \equiv (\sigma\mu_0\omega)^{-1/2}$  the classical skin depth. In order to have solutions different from the trivial ones (i.e.,  $h_{xk} = h_{yk} = 0$ ), the determinant of the system must be equal to zero. This renders a dispersion relation between  $q$  and  $k$ ,

$$(q^2 - k^2)(1 + \chi_{xx}) - i\delta^{-2} [(1 + \chi_{xx})^2 - \chi_{xy}^2] = 0. \quad (4.39)$$

The susceptibility tensor components  $\chi_{xx}$ ,  $\chi_{xy}$ , and  $\chi_{yx}$  are obtained by using the same methodology as in Chapter 3, i.e., by solving the LLG equation and imposing a relation between  $\mathbf{m}(t)$  and  $\mathbf{h}(t)$  through the susceptibility tensor  $\hat{\chi}$  (see Eq. 4.28). In this case, however, the resulting expressions are different. This difference is due to (i) the fact that the calculation is done in Fourier space and not in real space and, thus, the quantities  $\mathbf{m}_k(t)$  and  $\mathbf{h}_k(t)$  are used instead, and (ii) the substitution of the demagnetizing field  $\mathbf{H}_d$  in  $\mathbf{H}_{\text{eff}}$  (see Eq. 4.1) by an exchange field term which reads  $\mathbf{h}_{\text{ex}} = \alpha_{\text{ex}} \nabla^2 \mathbf{m}(t)$ , being  $\alpha_{\text{ex}}$  the exchange constant of Py (not to be confused with the exchange stiffness constant  $A$ ). This substitution is justified by the fact that the magnetization has to be treated locally (point-to-point) and, after all, the demagnetizing field will ultimately appear when imposing the boundary conditions on the system. Therefore, the components of the susceptibility tensor, obtained from solving the LLG equation in Fourier space, and considering the exchange field and the exponential dependence on  $y$ , are

$$\chi_{xx} = \frac{i\gamma' M_s [i\gamma' H - i\gamma' M_s \alpha_{\text{ex}} (q^2 - k^2) - \alpha]}{1 + [-i\gamma' H + i\gamma' M_s \alpha_{\text{ex}} (q^2 - k^2) + \alpha]^2}, \quad (4.40)$$

$$\chi_{yy} = \chi_{xx}, \quad (4.41)$$

$$\chi_{xy} = \frac{\gamma' M_s}{1 + [-i\gamma' H + i\gamma' M_s \alpha_{\text{ex}} (q^2 - k^2) + \alpha]^2}, \quad (4.42)$$

where  $\gamma' \equiv \gamma/\omega$ . The substitution of Eqs. 4.40–4.42 into Eq. 4.39 renders a polynomial of order 3 in  $q^2$ . Therefore, in the magnetic part of the system (i.e., in the Py), for every  $k$  there are six possible values of  $q$ . In the non-magnetic part of the system (i.e., in the Pt), however, since the susceptibility tensor components are exactly zero, the dispersion relation (Eq. 4.39) renders two possible values of  $q$  for every  $k$ . As a



consequence, the general solution for  $h_{xk}$  is a linear combination of eight exponential terms (two inside the Pt film and six in the Py film), i.e.,

$$h_{xk} = \sum_{j=1}^8 h_{jk} e^{q_j y}. \quad (4.43)$$

This expression for  $h_{xk}$ , as has been mentioned before, can be used in combination with Eqs. 4.33 – 4.35 to derive the expressions for the remaining Fourier coefficients:  $h_{yk}$ ,  $m_{xk}$ ,  $m_{yk}$ , and  $E_{zk}$ . In overall, for every value of  $k$ , the problem has eight coefficients ( $h_{jk}$ ) that are determined by imposing the appropriate boundary conditions<sup>6</sup>. Hence, after applying these boundary conditions, the system results in eight linear equations on these coefficients with one of the free terms different from zero. Once the system is solved and the Fourier components  $h_{xk}$  found, all the other quantities are straightforwardly computed. Quantities in real space are then obtained by performing the inverse Fourier transform, as has been mentioned.

In Fig. 4.23 the dependence on the sample depth ( $y$ -axis) of some quantities at the center of the CPW ( $x = 0$ ) are shown. As can be observed, the oscillating magnetic field  $h_x$  is partially absorbed by the Pt film before entering the Py layer due to the finite skin depth of the former (see Fig. 4.23a). Moreover, the current density  $j_z$  abruptly decreases when crossing the Py/Pt interface due to the difference in the resistivity of each material (Fig. 4.23b). Regarding the magnitude of the dynamic magnetic components (Figs. 4.23c and 4.23d), it is observed that the maximum is

<sup>6</sup>According to Ref. [174], the boundary conditions to be fulfilled are:

1. At Pt surface ( $y = 0$ ), due to the presence of the microwave current flowing through the CPW, there is the electrodynamic boundary condition:

$$h_{yk} \coth [ |k|(d + s) ] - i \frac{|k|}{k} h_{xk} = i \frac{\sinh (|k|d)}{\sinh [ |k|(d + s) ]} \frac{|k|}{k} j_k,$$

where  $d$  is the thickness of the CPW substrate and  $s$  the separation between the Pt surface and the CPW (see Fig. 4.22). The Fourier coefficients of the intensity carried by the CPW are denoted by  $j_k$ . The details on the specific form of  $j_k$  are found in Ref. [174].

2. At the Py/Pt interface, the continuity of  $h_x$  and  $b_y = h_y + m_y$  must be satisfied. Therefore, the continuity of the corresponding Fourier coefficients must be fulfilled as well.
3. At the Py/Pt interface and at the end of the Py film, surface anisotropy is neglected, implying that  $\partial \mathbf{m}(t) / \partial y = 0$  at both surfaces. This is the exchange boundary condition.
4. At the top end of the Py film ( $y = t$ ), the electromagnetic boundary condition reads:

$$h_{yk} + m_{yk} + i h_{xk} \frac{|k|}{k} = 0.$$

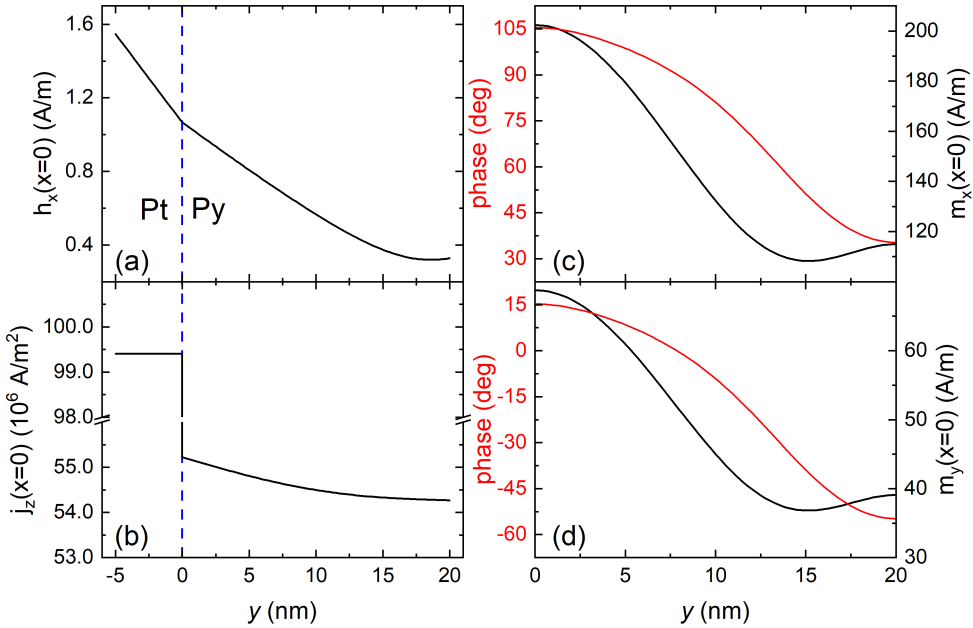


Figure 4.23: Calculated variation of some quantities across the sample thickness (in the middle region,  $x = 0$ ), being: (a) the modulus of the  $x$  component of the oscillating magnetic field; (b) the current density; and (c) and (d) the  $x$  and  $y$  magnetization components modulus (black, right axis), respectively, and their corresponding phase (red, left axis). The parameters used for the calculation are:  $s = 20 \mu\text{m}$ ;  $W = 400 \mu\text{m}$  (width of the signal line in the CPW);  $\Delta = 400 \mu\text{m}$  (spacing between the signal and ground lines in the CPW);  $d = 500 \mu\text{m}$ ;  $f = 10$  GHz;  $\gamma/2\pi = 28.9$  GHz/T;  $\mu_0 M_s = 0.9$  T ( $M_s = 7.16 \cdot 10^5$  A/m);  $\alpha = 0.01$ ;  $\delta_{Pt} = 1.1239 \mu\text{m}$ ;  $\delta_{Py} = 1.5078 \mu\text{m}$ ;  $t_{Pt} = 5$  nm;  $t_{Py} = 20$  nm;  $\alpha_{ex} = 6.3 \cdot 10^{-8} \mu\text{m}^{-2}$ ; intensity by the CPW = 1 mA. The  $y < 0$  region corresponds to Pt, while the  $y > 0$  one corresponds to Py. The applied field is close to the calculated resonance at 10 GHz, in this case.

found close the Py/Pt interface, as expected since it is the closest point to the CPW in the film. Moreover, in Fig. 4.24, the dynamic magnetic components  $m_x$  and  $m_y$  as well as their phase shifts are represented as a function of the applied dc magnetic field. The resonance field can be appreciated as a the maximum in the magnitudes of  $m_x$  and  $m_y$ , which correspond to a maximum oscillation of the magnetization. Additionally, a phase shift of  $180^\circ$  across resonance is obtained, as expected from FMR theory (see Section 3.2 from Chapter 3).

At this point, the obtained results can be inserted into Eqs. 4.26 and 4.27 in order to numerically compute the SRE voltage contributions. This voltage  $V^{\text{SRE}}$  is given by the expression

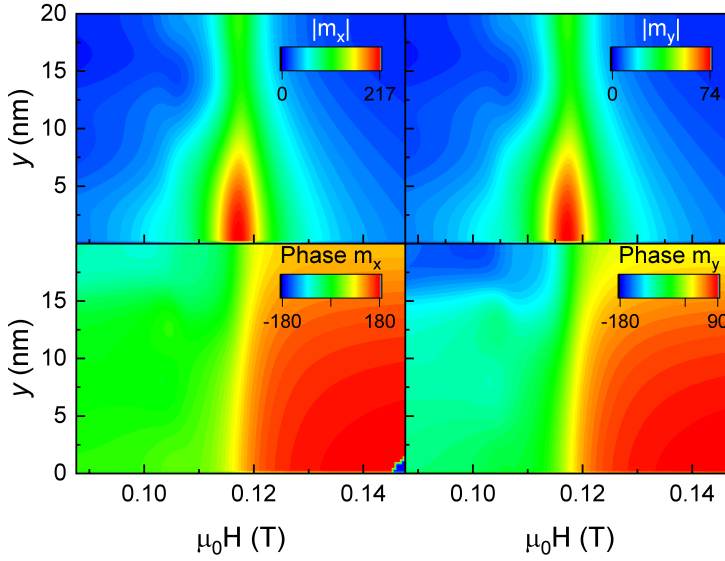


Figure 4.24: Magnitude (in A/m) and phase (in degrees) of  $m_x$  (left) and  $m_y$  (right) across the film (at  $x = 0$ ) as a function of the static dc magnetic field variation across the resonance. All parameters (except for  $H$ ) are the same as in Fig. 4.23.

$$V^{\text{SRE}} = - \int_{-\infty}^{+\infty} \langle E_x \rangle dx, \quad (4.44)$$

being  $\langle E_x \rangle \equiv \langle E_x^{\text{AMR}} \rangle + \langle E_x^{\text{AHE}} \rangle$ . Thus,

$$V^{\text{SRE}} = - \frac{\Delta\rho}{2M_s} \int_{-\infty}^{+\infty} \Re(j_z m_x^*) dx - \frac{\rho_{\text{AHE}}}{2M_s} \int_{-\infty}^{+\infty} \Re(j_z m_y^*) dx. \quad (4.45)$$

These last integrals can be computed in Fourier space using Parseval's identity<sup>7</sup>, resulting in

$$V^{\text{SRE}} = -\pi \frac{\Delta\rho}{M_s} \Re \left( \int_{-\infty}^{+\infty} j_{zk} m_{xk}^* dk \right) - \pi \frac{\rho_{\text{AHE}}}{M_s} \Re \left( \int_{-\infty}^{+\infty} j_{zk} m_{yk}^* dk \right), \quad (4.46)$$

<sup>7</sup>Parseval's identity is defined as [176]

$$\int_{-\infty}^{+\infty} f(x) \cdot g(x)^* dx = \frac{1}{2\pi} \int_{-\infty}^{+\infty} \hat{f}(\xi) \cdot \hat{g}(\xi)^* d\xi,$$

where the first and second terms give the AMR and AHE contributions to the overall SRE, respectively. In Fig. 4.25, the factors accompanying the parameters  $\Delta\rho$  and  $\rho_{\text{AHE}}$  are plotted. Since  $j_{zk}$ ,  $m_{xk}$ , and  $m_{yk}$  depend on  $y$ , so it does the voltage created by SRE, as illustrated in Figs. 4.25a and 4.25b.

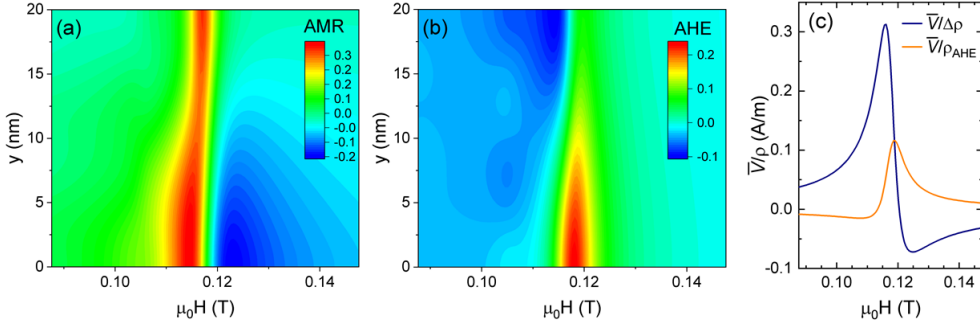


Figure 4.25: Spin rectification voltage calculated using Eq. 4.45, where (a) shows the expected contribution to the voltage coming from AMR (divided by  $\Delta\rho$  in A/m), and (b) that of AHE (divided by  $\rho_{\text{AHE}}$  in A/m). The average of these quantities over  $y$ , denoted by  $\overline{V}/\rho$ , being  $\rho$  equal to  $\Delta\rho$  ( $\rho_{\text{AHE}}$ ) in the case of AMR (AHE), is depicted in (c). All parameters used for the calculations, except for  $H$ , are the same as in Fig. 4.23. It is worth noting that the sign convention in this figure is the opposite to that in Figs. 4.13 and 4.17.

The average along  $y$  is plotted in Fig. 4.25c. This figure shows that the factor accompanying the AMR and AHE terms (labeled as  $V/\Delta\rho$  and  $V/\rho_{\text{AHE}}$ , respectively) are of the same order of magnitude. Therefore, in order to determine which term dominates the SRE voltage contribution, the pre-factors  $\Delta\rho$  and  $\rho_{\text{AHE}}$  must be known. In this line, a Si//Py thin film of 20 nm was prepared using the same methodology as the other samples in this chapter. Furthermore, the sample was patterned in the form of the typical Hall-bar geometry by means of optical lithography (the dimensions  $l \times w$  of the bar being  $600 \times 60 \mu\text{m}^2$ ). Standard transport measurements were employed for measuring both AMR and AHE. For the case of AMR, the longitudinal resistance ( $R_{xx}$ ) at different in-plane field orientations with respect to the electric current has been measured. On the other hand, for the case of AHE, transverse resistance ( $R_{xy}$ ) measurements at different field magnitudes but pointing out-of-plane were performed. The obtained experimental results are shown in Fig. 4.26. From Fig. 4.26a, one finds that the amplitude of the curve, corresponding to the AMR pre-factor, is  $\Delta R \approx 0.6 \Omega$ , while from Fig. 4.26b, the half-difference at  $\mu_0 H = 0$ , corresponding to the pre-factor of the AHE, is  $R_{\text{AHE}} \approx 0.0196 \Omega$ . Therefore, the AMR contribution is found to be roughly 30 times larger than the AHE contribution. Additionally, this experimental result is in accordance with existing data in the literature [177, 178, 179]. As a consequence, the dominant contribution to the SRE in the system is

due to AMR and the AHE contribution can be neglected. Finally, by looking at the lineshape of the calculated AMR curve (dark blue line in Fig. 4.25c), one finds that the symmetric contribution slightly dominates over the antisymmetric one. This result is in accordance with our experimental findings, where the voltage signal at the regime where SRE dominates is more symmetric than antisymmetric (see Figs. 4.13 and 4.17).

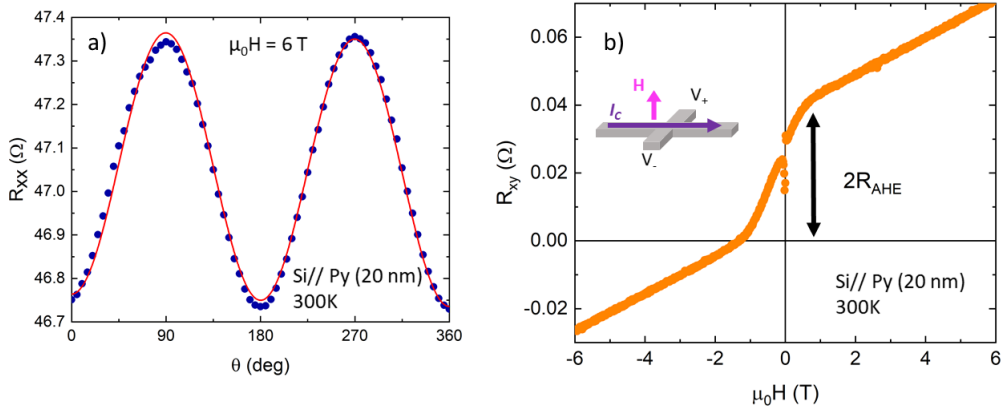


Figure 4.26: (a) Angle-dependent measurements of the longitudinal resistivity and fixed magnetic field magnitude. The curve has been fitted using the expression:  $R(\theta) = R_0 + \Delta R \cos^2 \theta$  (red line). (b) Field-dependent measurements of the transverse resistivity and out-of-plane magnetic field. The gap at  $\mu_0 H = 0$  determines the AHE contribution  $R_{\text{AHE}}$ .

At this point it is of major relevance to highlight that, although the coordinate system used for the calculation and the experimental measurements are equal, the integration limits are opposite in each case, i.e., in Eq. 4.46 the integration runs from negative to positive  $x$ , while in Eq. 4.11 runs from positive to negative  $x$ . It is just a matter of convention. This difference explains, however, why the calculated and experimental SRE have opposite signs. The situation for the ISHE voltage sign case is the same: by inverting the integration order the calculated sign inverts as well. Nevertheless, the main result of the calculation is that the SRE and ISHE do have opposite signs with respect to each other, in accordance with the experimental evidence.

### Introduction to finite size along $z$

So far, the  $z$  coordinate was assumed to be infinite as one of the axioms of the calculations presented in section 4.2.5. However, the main hypothesis of our experiment

was that by reducing the width of the sample along the direction of the CPW, the SRE would vanish. Since the sample width along the CPW is parallel to the  $z$  axis (see Fig. 4.9) it would be necessary to estimate how the induced current calculated in section 4.2.5 depends on  $z$ . In order to do so, one has to evaluate the effect of the finite size of the sample along the direction of the CPW. The main feature of this finite size is the effect of the walls at the end of the sample, which induces a charge accumulation on them due to the current created inside the sample. This charge accumulation will be treated as a perturbation of the exact,  $z$ -independent solution presented above. Thus, one can write

$$\mathbf{E} = \mathbf{E}^\infty - \Delta\mathbf{E}(z), \quad (4.47)$$

being  $\mathbf{E}^\infty$  the electric field found for an infinitely long sample, and  $\Delta\mathbf{E}(z)$  the electric field created by the charge accumulation which, for simplicity, is assumed to be along the  $z$  direction only. The charge accumulated at the ends of the sample can be described as a linear charge density  $\lambda$ , as the length of the sample along the CPW is always much larger than its thickness. In general, the  $z$  component of the electric field created at a point  $(x, 0, z)$  by an arbitrary linear charge density  $\lambda(x)$  placed along  $x$  is given by the expression

$$E_z = \frac{z}{4\pi\epsilon_0} \int_{-\infty}^{\infty} d\xi \frac{\lambda(\xi)}{[(x - \xi)^2 + z^2]^{3/2}}. \quad (4.48)$$

Making use of the convolution theorem<sup>8</sup> this equation can be expressed in Fourier space in terms of the modified Bessel function of the second kind  $K_1(|kz|)$ <sup>9</sup>, i.e.,

---

<sup>8</sup>The convolution theorem [180] states that the Fourier transform of two convoluted functions is equal to the product of the Fourier transform of each individual function, i.e., being  $r(x) = \int_{-\infty}^{\infty} g(\tau)h(x-\tau) d\tau$  a function denoting the convolution between  $g(x)$  and  $h(x)$ , its Fourier transform will be

$$\mathcal{F}[r(x)] = \mathcal{F}[g(x)] \cdot \mathcal{F}[h(x)].$$

<sup>9</sup>The modified Bessel function of the second kind can be expressed in the form of an integral such [181]

$$K_\nu(z) = \frac{\Gamma(\nu + \frac{1}{2})(2z)^\nu}{\sqrt{\pi}} \int_0^\infty \frac{\cos t}{(t^2 + z^2)^{3/2}} dt,$$

being  $\nu$  an integer and  $\Gamma(n) = (n-1)!$  the Gamma function.

$$E_{zk} = -\lambda_k \frac{|k|}{2\pi\epsilon_0} K_1(|kz|), \quad (4.49)$$

where  $\lambda_k = \frac{1}{2\pi} \int_{-\infty}^{\infty} dx \lambda(x) e^{ikx}$  are the Fourier components of the linear charge density. Now, if the size of the system along  $z$  is  $L$ , we can consider that there are two opposite linear charge distributions at  $z = L/2$  and  $z = -L/2$  with opposite charges. Therefore, the Fourier components of  $\Delta E_{zk}$  are given by

$$\Delta E_{zk} = -\lambda_k \frac{|k|}{2\pi\epsilon_0} \left[ K_1 \left( \left| k \left( \frac{L}{2} - z \right) \right| \right) - K_1 \left( \left| k \left( z - \frac{L}{2} \right) \right| \right) \right] \equiv -\frac{\lambda_k}{2\pi\epsilon_0} \Delta_L(k). \quad (4.50)$$

By using Eq. 4.47, the Fourier components of the charge current density can be expressed accordingly as  $j_{zk} = j_{zk}^{\infty} + \sigma \Delta E_{zk}$ , where  $j_{zk}^{\infty}$  is the current density previously calculated and  $\sigma$  is the conductivity of the system. Moreover, due to the fact that the linear charge density  $\lambda_k$  is generated by the current arriving to the end of the sample, it will be given by

$$\lambda_k = \int_0^t d\tau \int_{-t_{Pt}}^{t_{Py}} dy j_{zk}. \quad (4.51)$$

It is important to divide the integral along  $y$  into the two materials, i.e.,  $\int_{-t_{Pt}}^{t_{Py}} dy j_{zk} = \int_{-t_{Pt}}^0 dy j_{zk} + \int_0^{t_{Py}} dy j_{zk}$ , where

$$\int_{-t_{Pt}}^0 dy j_{zk} = \int_{-t_{Pt}}^0 dy j_{zk}^{\infty} + \sigma_{Pt} t_{Pt} \Delta E_{zk}, \quad (4.52)$$

and

$$\int_0^{t_{Py}} dy j_{zk} = \int_0^{t_{Py}} dy j_{zk}^{\infty} + \sigma_{Py} t_{Py} \Delta E_{zk}. \quad (4.53)$$

For the sake of clarity, the notation is simplified to:

$$\int_{-t_{Pt}}^0 dy j_{zk} \equiv J_{Pt}, \quad \int_0^{t_{Py}} dy j_{zk} \equiv J_{Py}, \quad \int_{-t_{Pt}}^0 dy j_{zk}^{\infty} \equiv J_{Pt}^{\infty}, \quad \int_0^{t_{Py}} dy j_{zk}^{\infty} \equiv J_{Py}^{\infty}.$$

As a consequence, combining Eqs. 4.50, 4.51, 4.52, and 4.53 and using the simplified notation, one arrives at the following expression:

$$\dot{\lambda}_k = J_{\text{Pt}}^\infty + J_{\text{Py}}^\infty - \frac{1}{2\pi\epsilon_0} (\sigma_{\text{Pt}}t_{\text{Pt}} + \sigma_{\text{Py}}t_{\text{Py}}) \lambda_k \Delta_L(k). \quad (4.54)$$

Thus, assuming an  $\exp(-i\omega t)$  dependence on  $\lambda_k$  for solving Eq. 4.54, and combining it with Eqs. 4.52 and 4.53, it can be shown that the Fourier components of the integrated current density at the Py film as a function of the sample width  $L$  are

$$J_{\text{Py}} = \frac{J_{\text{Py}}^\infty [1 + i\gamma_{\text{Pt}}\Delta_L(k)] - i\gamma_{\text{Py}}\Delta_L(k)J_{\text{Pt}}^\infty}{1 + i(\gamma_{\text{Pt}} + \gamma_{\text{Py}})\Delta_L(k)}, \quad (4.55)$$

where  $\gamma_n \equiv \sigma_n t_n / (2\pi\epsilon_0\omega)$  ( $n = \text{Pt}$  or  $\text{Py}$ ). This result allows to compute the average rectification effect as a function of the sample width  $L$ , as can be observed in Fig. 4.27. In this figure, AMR is represented instead of AHE or both of them because it is the dominant contribution to the SRE, as has been mentioned. It is important to notice that this AMR has been multiplied by  $-1$  in order to obtain the same voltage sign as in the experimental measurements.

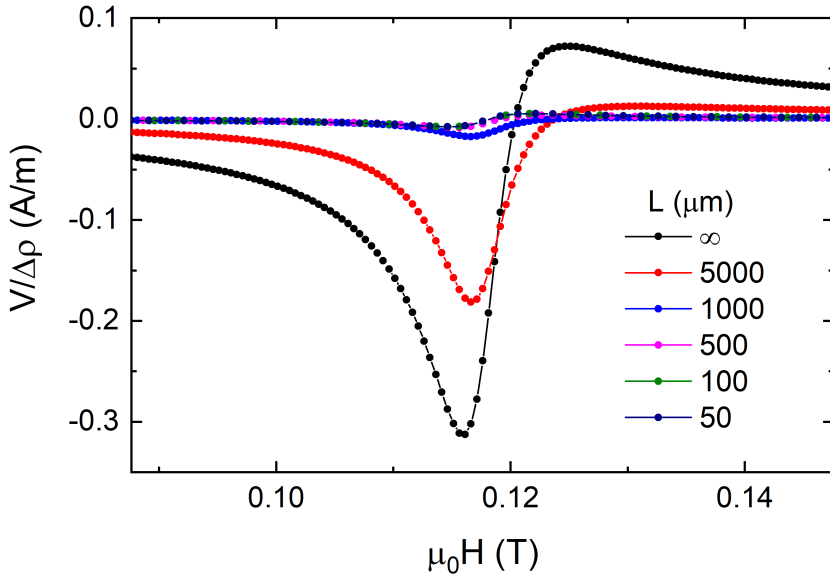


Figure 4.27: Calculated dependence of AMR on the sample width  $L$ . All parameters used for the calculations, except for  $H$ , are the same as in Fig. 4.23.



As can be observed in Fig. 4.27, the reduction in the sample width  $L$  is accompanied by a progressive reduction of the SRE. The fact that this progressive reduction happens at a faster pace than in the observed, experimental evidence, suggests that this result is only an approximation of the real situation. In fact, for instance, the electric field generated by the accumulation of charge was assumed to be along the  $z$  direction only, but a non-negligible  $y$  component might play a certain role.

In any case, the conclusions of the calculations, which are in accordance with the experimental evidence presented throughout this chapter, are obvious:

1. The sign of the ISHE and SRE (i.e., AMR and AHE) voltage signals are opposite to each other,
2. the SRE are a combination of symmetric and antisymmetric Lorentzian curves, and
3. the reduction in the sample width  $L$  is accompanied by a progressive reduction of the SRE.



## Spin Pumping and Inverse Spin Hall Effect in Complex Oxide Heterostructures

In the previous Chapter, the injection of spin currents by spin pumping and their subsequent detection by means of inverse spin Hall effect were effectively measured for the case of Py and Py/Pt bilayers. One of the goals of this Thesis, however, is to inject, manipulate and detect spin currents using complex oxide heterostructures. For this purpose, two different complex oxide materials are used as candidates for effective spin injectors in the system:  $\text{La}_{0.92}\text{MnO}_3$  (LMO) and  $\text{La}_{2/3}\text{Sr}_{1/3}\text{MnO}_3$  (LSMO). In Section 5.1, the experimental evidence of spin pumping and inverse spin Hall effect in LMO/Pt as a function of temperature is shown. In Section 5.2, however, the complex oxide perovskite  $\text{SrIrO}_3$  (SIO) is used instead of Pt in the LSMO/SIO bilayer system.

### 5.1 Inverse Spin Hall Effect Measurements in $\text{La}_{0.92}\text{MnO}_3/\text{Pt}$ Bilayers

#### 5.1.1 Samples Characterization and Growth Conditions

Unlike any other sample grown in this Thesis, the  $\text{La}_{0.92}\text{MnO}_3$  complex oxide films were grown by chemical deposition methods, specifically by polymer assisted deposition (PAD), on top of (100)- $\text{SrTiO}_3$  (STO) single-crystal substrates. Although

high-vacuum physical deposition methods such as dc magnetron sputtering or molecular beam epitaxy offer unquestionable advantages (i.e., crystal quality, precise control of composition, atomic-scale thickness precision, etc [182]), affordable chemical deposition methods are desirable because they are easier to scale up and offer the possibility to grow films over large areas at low cost while allowing an easy tuning of the stoichiometry [183]. In particular, PAD has appeared as a competitive route for environment friendly approaches as it is based on the deposition of cationic aqueous solutions [182, 184]. Nevertheless, in the last few decades, there have been some concerns regarding the suitability of films prepared by chemical methods for challenging applications which require microstructural quality and sharp interfaces, as in spintronics, although some achievements have been already made in the past few years [182, 185, 186]. Moreover, since the energy balance involved during the deposition process is quite delicate, chemical methods may lead to a defect landscape different to that present in high-vacuum, physical deposition methods, resulting in the modification of the physical properties of the film. In this regard, it has been observed [183] that relevant parameters for the development of spintronic devices, such as magnetic damping, magnetic anisotropy or spin mixing conductance, may be substantially different from that observed in the same films prepared by physical deposition methods. Conversely, the particular growth conditions of PAD, which works closely to thermodynamic equilibrium conditions, have revealed to be very appropriate for the epitaxial deposition of complex oxide thin films of a broad variety of materials, including  $\text{LaMnO}_3$  [186, 187, 188].

Bulk stoichiometric  $\text{LaMnO}_3$  is an A-type antiferromagnetic insulator [189], however, due to structural strain in thin films [190] or by introducing cationic vacancies (in both La or Mn sites) [189], it may become a ferromagnet. Moreover, La vacancies promote the appearance of a  $\text{Mn}^{+3}$ – $\text{Mn}^{+4}$  mixed valence state in order to maintain charge neutrality, resulting in a double-exchange mediated FM and metallic state [189], contrary to the insulating FM state in stoichiometric films, as has been mentioned. Taking this into account, in a previous work by our group [191],  $\text{LaMnO}_3$  thin films with an 8% of La vacancies were deposited on top of STO substrates by PAD methods. The  $\text{La}_{0.92}\text{MnO}_3$  (LMO, from now on) thin films obtained exhibited robust ferromagnetic ordering with a Curie temperature  $T_c = 290\text{K}$  and saturation magnetization  $M_s(5\text{K}) \approx 330 \text{ emu/cm}^3$ , which is significantly lower than the expected theoretical value for the LMO composition ( $\approx 568 \text{ emu/cm}^3$ ). In order to explain this reduction of the saturation magnetization, three possible mechanisms were invoked in Ref. [191]: i) the existence of a non-magnetic dead layer in the STO//LMO interface due to relaxation of biaxial stress during growth [192]; ii) a deficit in oxygen content in the films, thus promoting oxygen vacancies which result in a reduction of the concentration of  $\text{Mn}^{+4}$  cations; and iii) an over-oxidation of the films, which would result in the formation of  $\text{Mn}^{+4}$  clusters. These clusters would enhance antiferromagnetic correlations between  $\text{Mn}^{+4}$  cations which would hamper the full FM state [189]. The

dead layer mechanism was dismissed because the thickness of the dead layer tends to be of the order of two unit cells and, therefore, it cannot by itself explain the strong deviation from the expected, theoretical value. As a result, the reduction of the saturation magnetization must be related to the oxygen content in the films. However, according to the available data, it was not possible to discern between the second and third mechanisms to explain the results observed in Ref. [191]. Additionally, it was shown that the LMO thin films were flat (rms  $\approx$  0.25 nm), presented high crystallinity and an excellent out-of-plane orientation, being in a fully strained state on top of the substrate [191].

For this Chapter, however, new LMO films were grown by PAD with slightly different growth conditions in order to improve the magnetic properties with respect to the previous work. For this purpose, the annealing temperature and time after the polymeric layer deposition were raised to 990 °C and 90 min (instead of the 950 °C and 30 min from Ref. [191]), and the spinning velocity was lowered to 4000 rpm (instead of 5000 rpm) for the same 90 seconds. At this point, it is important to mention that all the PAD samples were grown by one of our colleagues (Dr. Hailin Wang) employing the methodology described in Refs. [191] and [193]. Moreover, he did also study the optimal deposition conditions for tuning the appropriate LMO thin films magnetic and microstructural properties.

In this way, LMO samples were prepared on top of (100)-STO single-crystal substrates. Systematic  $\theta - 2\theta$  scans in X-ray measurements showed that only the (001) STO reflections of the film and substrate are present, indicating the excellent purity of the phase and the optimum  $c$ -axis alignment of the grown films (Fig. 5.1a). Additionally, reciprocal space maps (RSM) around the  $(\bar{1}03)_{\text{STO}}$  reflections were used for studying the strain state of the LMO film (Fig 5.1b). The fact that the LMO and STO peaks lie on the same  $Q_{\text{ip}}$  coordinate line suggests that the LMO is fully strained. As a consequence, the in-plane lattice parameter  $a_{\parallel}$  of the LMO film must match that of the STO substrate, i.e., 3.905 Å, resulting in a pseudocubic volume of 59.3 Å<sup>3</sup>. Moreover, the surface topography of the as-grown film was obtained by means of atomic force microscopy (AFM) (Asylum Research MFP-3D), and showed a relatively flat surface with a rms roughness of about 1 nm (see Fig. 5.2).

After the deposition process, a 6 nm thick Pt capping layer was grown *ex situ* on top of the LMO film by means of dc magnetron sputtering. Prior to this deposition, the surface of the LMO film was cleaned using a combination of acetone and ethanol. Then, it was heated up from room temperature to 500 °C, where it stayed for one minute, and cooled down to room temperature again in an overall 400 mTorr O<sub>2</sub> atmosphere. Finally, the Pt was deposited in a 5 mTorr Ar-H<sub>2</sub> atmosphere for one minute and room temperature. The magnetization *vs* temperature curves M(T) of the LMO film before and after the Pt deposition are depicted in Fig. 5.3. As can be

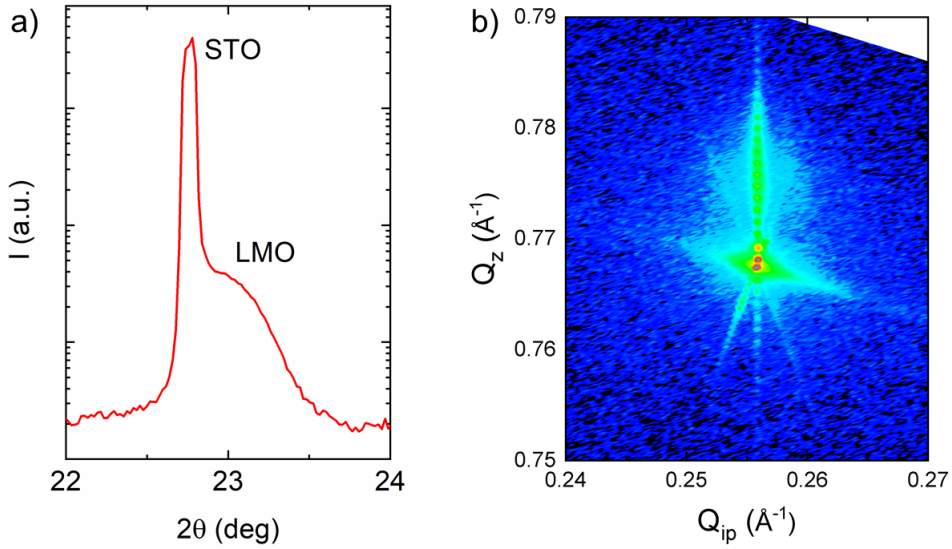


Figure 5.1: a)  $\theta - 2\theta$  scan around the (001) STO reflection, and b) reciprocal space map (RSM) of the  $(\bar{1}03)_{\text{STO}}$  peak revealing in-plane compressive strain in the film.

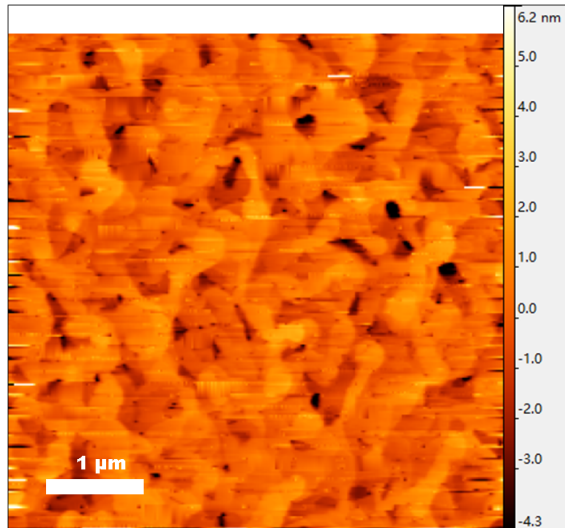


Figure 5.2: Topography of the LMO thin film obtained *via* atomic force microscopy (AFM) in tapping mode. The rms roughness is about 1 nm

observed, the Curie temperature in both cases is around 320K, which is a higher value than the previous one obtained in Ref. [191], denoting an improvement in deposition

conditions of LMO films. The absolute value of the saturation magnetization after the Pt deposition, however, is slightly lower than the one from the LMO alone film. This reduction may be attributed to minute changes of the oxygen content during the Pt deposition, in which a slightly reducing atmosphere to prevent oxidation was used.

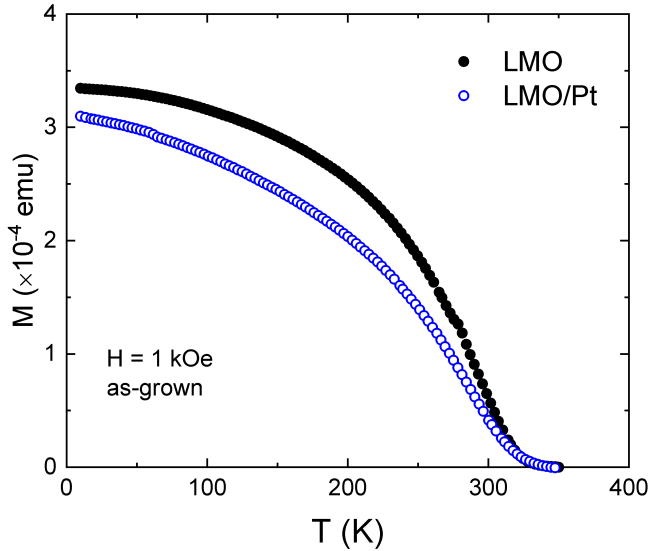


Figure 5.3: Comparison of the magnetization *vs* temperature curves of the LMO film before and after Pt deposition.

Besides the microstructural and magnetic properties of the LMO films before and after the Pt deposition process, the LMO/Pt interface quality is of the utmost importance due to the key role played by interfaces in spin transport phenomena [194]. On this behalf, the LMO/Pt interface was analysed by means of scanning transmission electron microscopy (STEM) (see Fig. 5.4). The STEM characterization was carried out by Drs. R. Manzorro and C. Magén from the University of Zaragoza (Spain), and the technical details regarding this measurement are specified in the caption of Fig. 5.4. As can be observed from Fig. 5.4a, the LMO thin film is epitaxial, offering an excellent crystalline quality with no defects. The Pt capping layer, in turn, presents a nice polycrystalline ordering and no structural modifications are observed at the interface. Additionally, chemical analysis close to the LMO/Pt interface (in the regions marked in Fig. 5.4b) was performed by Electron Energy Loss Spectroscopy (EELS) and shown in Fig. 5.4c. As can be observed, the Mn-L<sub>2,3</sub> edge shows a uniform fine structure when monitored deep into the LMO film. On the other hand, the L<sub>3</sub> line experiences a gradual shift of  $\approx 0.8$  eV to lower energy at the interface, in the last two to three unit cells of the LMO film below Pt. This *redshift* indicates qualitatively a higher abundance of Mn<sup>+3</sup>, thus indicating a Mn reduction at an interface with lower

oxygen content than the inner part of the LMO film. This result would be consistent with the observed reduction of the saturation magnetization from Fig. 5.10, which was previously related to changes in the oxygen content at the LMO/Pt interface, being the reducing atmospheric conditions during the Pt growth responsible for it.

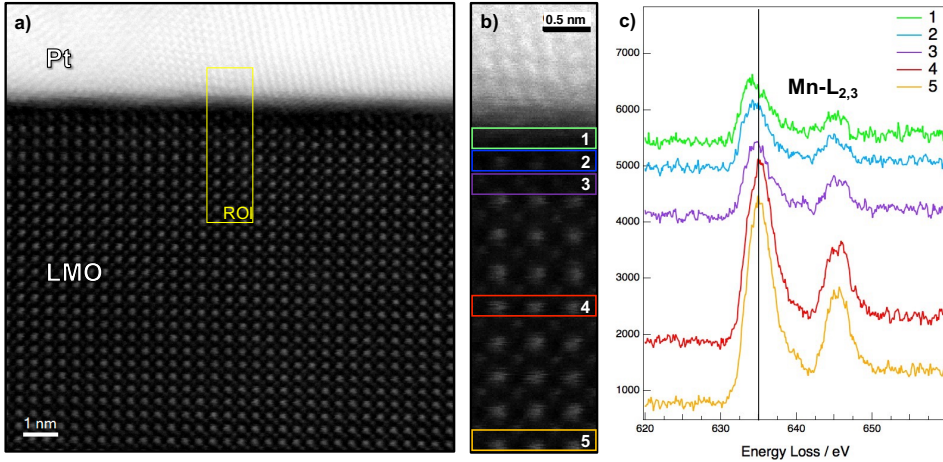


Figure 5.4: a) Atomic resolution HAADF image of the Pt/LMO interface. b) Annular dark field (ADF) image corresponding to the interface, where EELS experiment has been performed. c) Mn-L<sub>2,3</sub> EELS spectra after noise reduction, extracted from the marked regions in (b). Aberration corrected STEM characterization has been carried out in a probe-corrected FEI Titan 60-300 operated at 300 kV, and equipped with a high-brightness field emission gun (X-FEG), a CETCOR aberration corrector for the probe (from CEOS), and a Tridiem GIF spectrometer 866 ERS from Gatan. Atomically resolved images with Z contrast were acquired by high-angle annular dark field (HAADF); the convergence semiangle of the probe was 24 mrad to yield a probe size less than 1 Å. STEM spectrum imaging was performed by combining HAADF imaging with Electron Energy Loss Spectroscopy (EELS) with a beam current of 180 pA, and energy dispersion of 0.1 eV, and a collection semiangle of about 45 mrad. EELS spectra were collected with an exposure time of 0.5 s [195], and afterwards noise-filtered by Principal Component Analysis (PCA) [196].

Moreover, in Fig. 5.5, a complete high-angle annular dark field (HAADF) image of the overall STO//LMO/Pt system is shown. At first glance, from Fig. 5.5a, one could infer that the thickness of the LMO film is about 25 nm. However, the EELS chemical analysis across three different regions of the system (i.e., at the substrate; near the STO//LMO interface; and far from the interface) shows an overlapping of Mn and Ti atoms near the STO//LMO interface (see Fig. 5.5b), indicative of cationic diffusion at the interface. This interfacial diffusion is probably related to the high temperature used in the LMO deposition process (990°C), but it could also explain the excellent crystalline quality and defect-free structure observed far from the substrate. In other words, the relaxation of the LMO thin film on top of the STO substrate is a direct consequence of interfacial cationic diffusion. Additionally, the



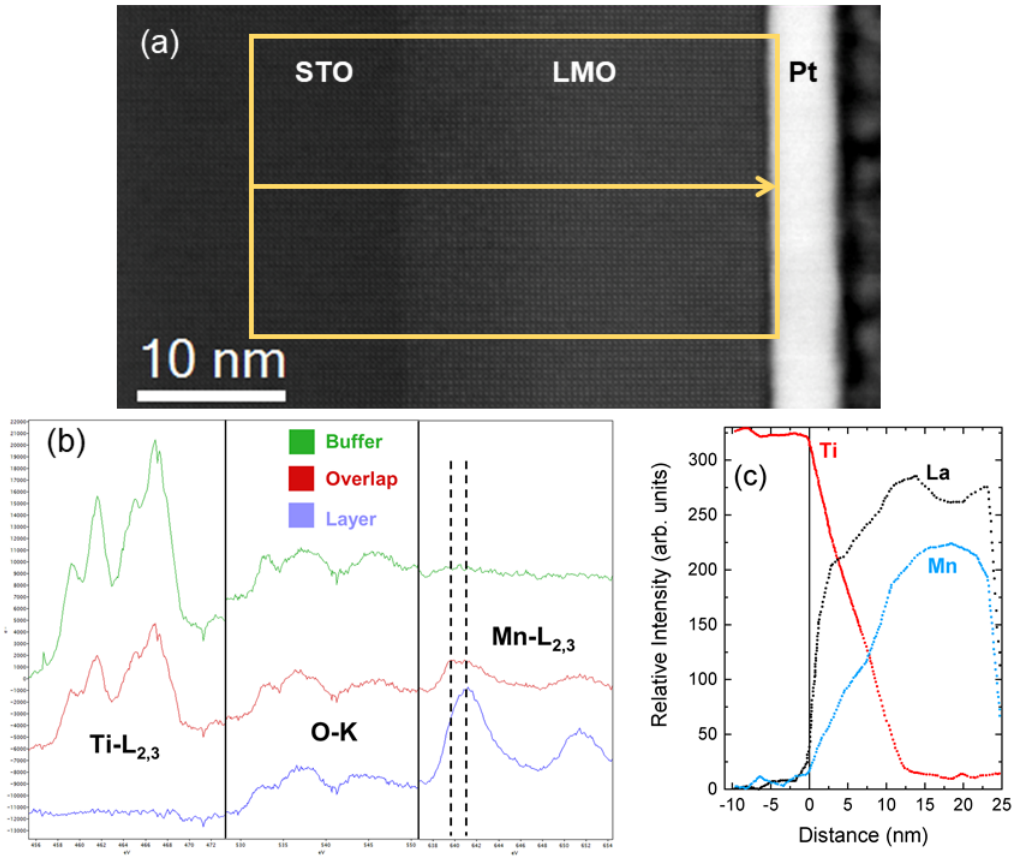


Figure 5.5: (a) HAADF image of the overall STO//LMO/Pt system. (b) EELS chemical analysis performed in three specific regions of the system, namely in the STO substrate (*buffer*), near the STO//LMO interface from the LMO side (*Overlap*), and finally far from the STO//LMO interface (*layer*). (c) Elements line profile analysis evaluated along the yellow line in (a) showing the diffusion of Ti from the substrate to the LMO film.

elements line profile of the system (along the yellow arrow in Fig. 5.5a) is depicted in Fig. 5.5c and confirms that La abruptly increases at the interface, while the Mn increases gradually, in a similar way to the decay of Ti in the overlapping region, which comprises almost half of the total LMO film thickness. Nevertheless, it is important to note that above 7 – 8 nm the Mn and La species dominate. Moreover, a direct comparison between Fig. 5.5a and Fig. 5.4 suggests that the LMO thin film structural properties and stoichiometry are maintained up to the diffusive region with Ti. As such, we are confident that above this diffusive region the LMO thin film has the desired structural and magnetic properties and stoichiometry. Therefore, in this regard, in the absence of additional information regarding our STO//LMO interface, we approximate the thickness of our LMO film to  $\approx 17$  nm, which corresponds to the

thickness at which the La and Mn dominate and thus is expected to contribute the most to the magnetism of the overall sample.

Now, heading back to the  $M(T)$  curves shown above, it is important to note that in Fig. 5.3 the magnetization is expressed in emu instead of the usual  $\text{emu}/\text{cm}^3$ . This is because the excess of material at the edges and corners of the substrate is an intrinsic byproduct of the PAD process, resulting in an unknown sample volume. In order to overcome this problem, optical lithography was used to imprint a circular pattern of diameter  $d = 4.4$  mm on the as-grown film. After this, an acid treatment analogous to that described in Refs. [191] or [193] was used to eliminate the excess material at corners and edges. In this way, the volume of the film can be expressed easily as  $V = \pi r^2 t_{\text{sample}}$ , being  $r = 2.2$  mm the radius of the circular pattern and  $t_{\text{sample}}$  the thickness of the sample (LMO + Pt). A schematic drawing of the resulting pattern is shown in Fig. 5.6.

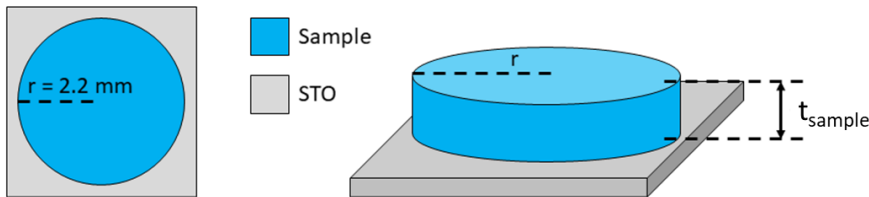


Figure 5.6: Top view (left) and overall schematic representation (right) of the LMO/Pt system after the lithographic and acid treatment.

At this point, it is important to estimate the amount of material that has been removed after the patterning process (i.e., lithography plus acid treatment). A correct estimation will allow us to express the saturation magnetization of the LMO film in units of  $\text{emu}/\text{cm}^3$ . Therefore, in order to do so, the  $M(T)$  curves of the as-grown LMO/Pt bilayer (i.e., thin film plus excess) and the same after the patterning process (i.e., circular pattern of diameter  $d = 4.4$  mm with no excess) are depicted in Fig. 5.7. As one would expect, the absolute magnetization magnitude is lower in the patterned case, while the Curie temperature remains the same (320K). Obviously, this difference is explained by the different amount of material present at the time of measurement. Nevertheless, in order to check the reliability this statement, an additional magnetic characterization process must be addressed.

For this purpose, ferromagnetic resonance (FMR) measurements of the sample before and after the patterning process were carried out: In the event that both FMR measurements are equal with respect to each other, the difference in magnetization

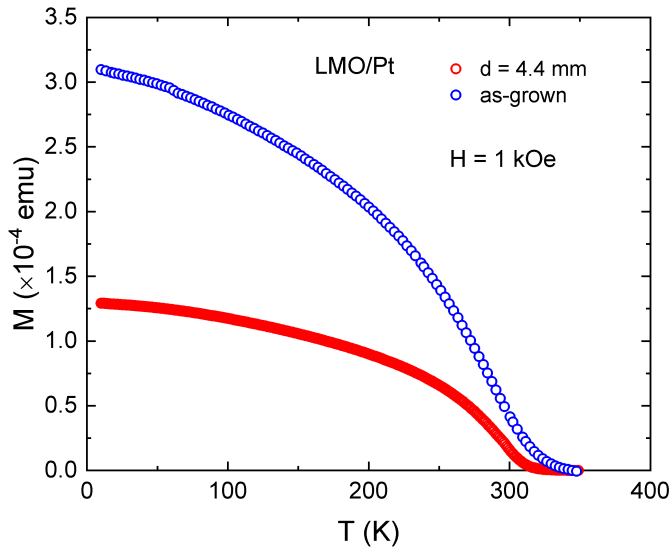


Figure 5.7: Comparison of the magnetization *vs* temperature curves of the LMO/Pt bilayer before (as-grown) and after ( $d = 4.4$  mm) the lithographic plus acid treatment process. The observed reduction in the overall signal is due to the material removal process.

observed in Fig. 5.7 should be attributed entirely to the material removal process and not to discernible differences between the sample before and after the patterning process. It is worth mentioning that the FMR methodology presented here is completely analogous to that described in Chapter 4. In this regard, the FMR curves at 200K for the as-grown and patterned LMO/Pt bilayer are shown in Fig. 5.8, and as can be observed, both resonance spectra overlap with each other. Their relative intensities, however, differ. This difference in intensity can be attributed to the different amount of material present on top of the CPW at the time of measurement. However, the fact that both spectra overlap with each other means that the magnetic properties ( $M_s$ ,  $\gamma$ ,  $H_4$ ) before and after the patterning process remain unchanged. In order to clearly illustrate this conclusion, the frequency dependence curve of the resonance field ( $H_{\text{res}}$ ), obtained from the fitting of the resonance lines in Fig. 5.8 by using Eq. 4.2, is depicted in Fig. 5.9.

As can be observed, a small shift-to-the-left in the resonance field is observed at high frequencies. Nevertheless, this mild difference can be attributed to experimental error and, thus, one can conclude that the overlapping of both curves is excellent. As a result, one can further conclude that the saturation magnetization of the LMO/Pt bilayer before and after the patterning process is the same and, therefore, that the difference between the  $M(T)$  curves in Fig. 5.7 can be attributed entirely to the different sample volume at the time of measurement. Thus, in Fig. 5.10, the  $M(T)$

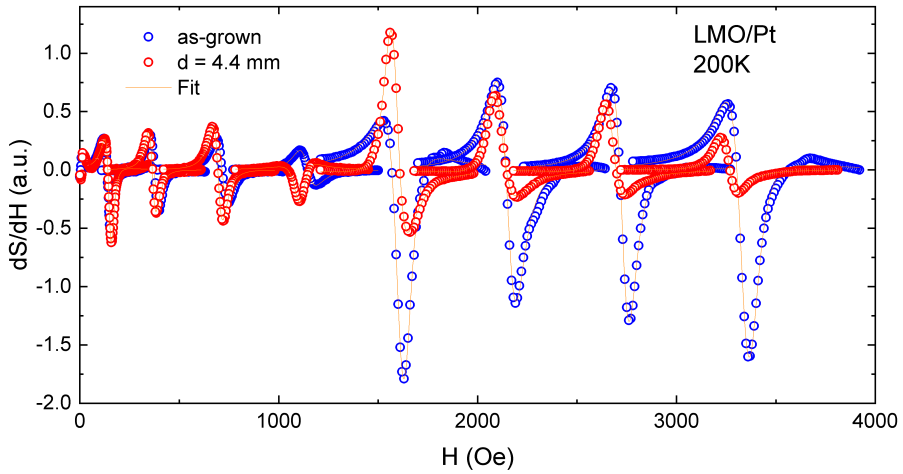


Figure 5.8: FMR spectra comparison of the LMO/Pt system before (blue) and after (red) the patterning process. The fitting of each curve (orange line) has been done according to Eq. 4.2.

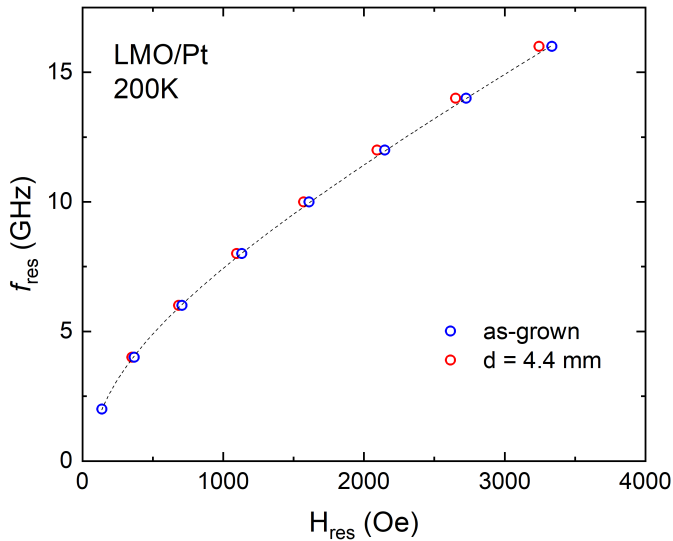


Figure 5.9: Resonance frequency  $f_{\text{res}}$  dependence on resonance field  $H_{\text{res}}$  comparison of the LMO/Pt thin film before (blue) and after (red) the patterning process. The dashed curve is a guide to the eye.

curves of the LMO and LMO/Pt film in units of  $\text{emu}/\text{cm}^3$  are shown. The LMO curve corresponds to the same one in Fig. 5.3 (black full circles), but in this case, it was scaled by applying a proportionality factor of 0.42 to account for the material removal

process. This proportionality factor corresponds to the ratio between the curves in Fig. 5.7. In overall, this means that 42% of the as-grown film was removed from the edges and corners after the patterning process. In conclusion, from Fig. 5.10, the observed 10K saturation magnetization value of the LMO film is around  $550 \text{ emu/cm}^3$ , which is in excellent agreement with the theoretical value of  $568 \text{ emu/cm}^3$  for  $\text{La}_{0.92}\text{MnO}_3$  films.

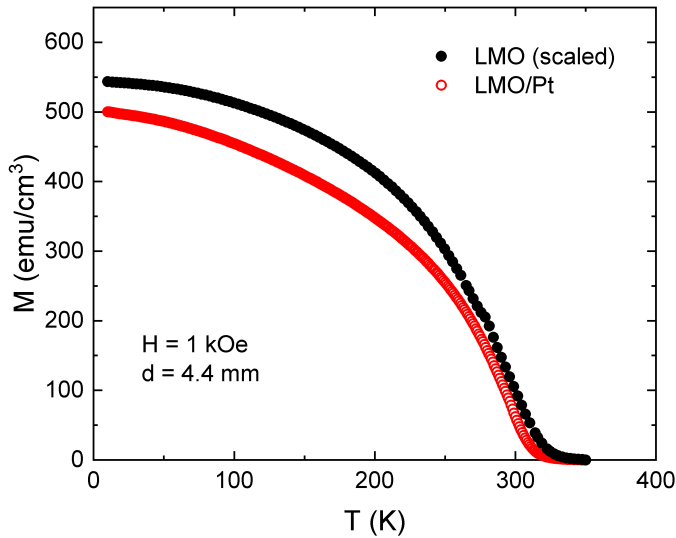


Figure 5.10: Comparison of the magnetization *vs* temperature curves of the LMO/Pt sample after the patterning process (red empty symbols) and of the LMO prior to Pt deposition but scaled in order to account for the amount of material removed (black full symbols). The  $M(T)$  curve of the LMO is the same as that from Fig. 5.3 (black full symbols) but multiplied by a scale factor of 0.42.

At this point, now that the volume of the sample is known, the hysteresis loops at different temperatures were measured and the resulting  $M(H)$  curves are shown in Fig. 5.11. The coercive field  $H_C$  as a function of temperature is also included in the figure. As can be observed, the symmetric, square-shaped  $M(H)$  curves denote the robust ferromagnetic behaviour of the LMO thin films. Additionally, these features are indicative of the lack of any secondary magnetic phases or inhomogeneities in our samples. Moreover, the coercive field  $H_C$  increases with decreasing temperature, as expected, up to a 10K value of  $H_C(10\text{K}) \approx 86 \text{ Oe}$ . In summary, the overall magnetic characterization measurements confirm that the PAD LMO thin films exhibit low disorder and strong ferromagnetic behaviour driven by a double-exchange mechanism.

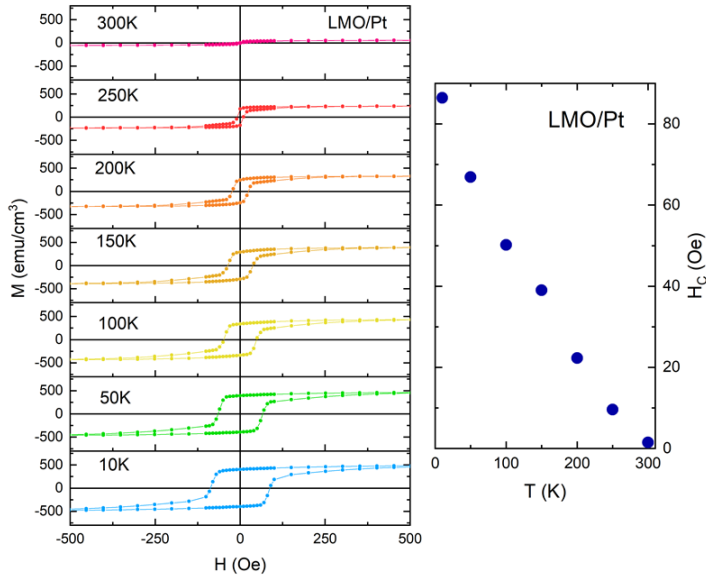


Figure 5.11: Magnetization *vs* applied field curves for the patterned LMO/Pt sample at different temperatures (left). The coercive field  $H_C$  (right) decreases linearly when increasing the temperature.

### 5.1.2 Spin to Charge Conversion in $\text{La}_{0.92}\text{MnO}_3/\text{Pt}$ Bilayers

In the previous section, the microstructural characterization of the chemically deposited LMO magnetic films before and after the Pt deposition process is addressed. Moreover, the static magnetic properties such as the Curie point, saturation magnetization, and coercive field are also determined by SQUID magnetometry. In summary, the LMO/Pt system presents a strong ferromagnetic behavior with high Curie point (320K) and a saturation magnetization close to the theoretically predicted one. Regarding the structural analysis, a fully strained LMO film lying on top of the STO substrate is observed. In addition, the LMO/Pt interface is found to be sharp, structurally homogeneous, and defect free. Thus, given its excellent structural and magnetic properties, the goal of this section is to study the spin transport phenomena of the LMO/Pt bilayer.

For doing so, in an analogous manner as in Chapter 4, FMR spectroscopy is used to generate and inject a spin current from the precessing, dynamic magnetization of the LMO film to the Pt capping layer, i.e., the spin current is generated by means of the spin pumping effect. Then, this spin current is electrically detected by using the inverse spin Hall effect (ISHE) occurring in the Pt capping layer. The exper-

imental equipment used in this section is also the same as that as in Chapter 4, that is: a broadband FMR spectrometer (by NanOsc) with the sample placed in the custom-made coplanar waveguide (CPW) (“CPW PPMS IP ISHE” model [155]). In overall, the whole system (sample plus CPW) is inserted in a Physical Properties Measurement System (PPMS from Quantum Design) in order to allow temperature-dependent measurements. Finally, the electrical measurements are performed by an external, commercial Keithley 2128A nanovoltmeter synchronized with the FMR spectrometer. As is shown in Chapter 4, the application of FMR spectroscopy is twofold: on one hand, it is used to generate and inject spin currents in FM/NM bilayers. On the other hand, it characterizes the dynamic magnetic properties of the magnetic system. Therefore, we start this section by addressing the complete FMR characterization of the LMO film before and after the Pt deposition process at 200K, well below the Curie temperature.

The FMR spectral curves of the LMO and LMO/Pt systems at 200K are shown in Fig. 5.12. As can be observed, with respect to the LMO alone film, the resonance lines of the LMO/Pt bilayer are shifted to the right, i.e., present larger resonance fields than the LMO alone thin film. This displacement is in accordance with the decrease of the LMO saturation magnetization after the Pt deposition observed in the  $M(T)$  curves measured by SQUID magnetometry (see Figs. 5.3 and 5.10). Moreover, each FMR curve is fitted as the sum of symmetric and antisymmetric Lorentzian derivative lines (using Eq. 4.2 from Chapter 4). Thus, from the fitting of each curve, both the resonance field  $H_{\text{res}}$  and linewidth  $\Delta H$  are obtained. The crucial magnetodynamical parameters that govern spin dynamics in each system can be found from the curves which relate the resonance frequency  $f_{\text{res}}$  with  $H_{\text{res}}$  and  $\Delta H$ .

These frequency-dependent curves for the LMO and LMO/Pt systems are shown in Fig. 5.13. From Fig. 5.13a, the shift in the resonance field  $H_{\text{res}}$  upon Pt deposition is clearly illustrated. Additionally, both  $H_{\text{res}}$  vs  $f_{\text{res}}$  curves follow the typical square-rooted shape described by Kittel equation, which is presented and used in Chapter 4 and included here for clarity:

$$f_{\text{res}} = \frac{\gamma}{2\pi} \left( H_{\text{res}} + \frac{2K_4}{M_s} \right)^{1/2} \times \left( H_{\text{res}} + M_{\text{eff}} + \frac{2K_4}{M_s} \right)^{1/2}, \quad (5.1)$$

where  $\gamma$  is the gyromagnetic ratio,  $K_4$  is the four-fold in-plane anisotropy constant, and  $4\pi M_{\text{eff}} \equiv 4\pi M_s - 2K_2/M_s$  is the effective magnetization, being  $K_2$  the second-order surface/interface anisotropy constant, which opposes the demagnetizing field, and  $M_s$  is the saturation magnetization. By imposing the saturation magnetization value  $M_s$  measured by SQUID magnetometry (see Fig. 5.10), one finds that a surface/interface anisotropy term  $K_2$  must be included in order to obtain a proper fit in

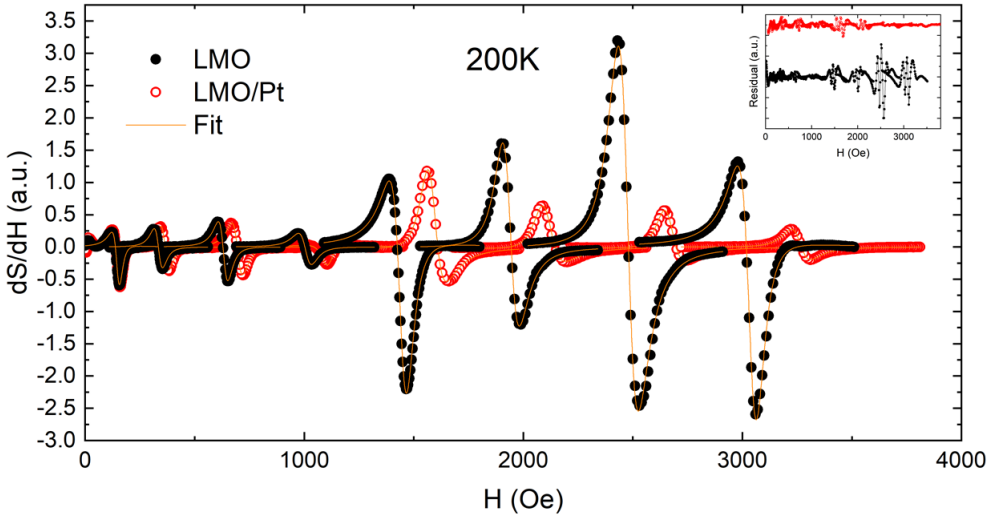


Figure 5.12: FMR spectra of the LMO thin film (black full circles) and the LMO/Pt bilayer (red empty circles). The fitting of each curve corresponds to the orange line. The inset shows the difference between the experimental points and the fitting curve. The whole scale of the inset corresponds to 0.3 units relative to the main panel scale.

Fig. 5.13a. Nevertheless, it should be bore in mind that the saturation magnetization obtained from SQUID magnetometry has a component of uncertainty associated to the fact that the sample thickness was estimated. As such, an underestimation of  $M_s$  entails an overestimation of  $K_2$  and vice versa. Despite this clarification, the actual presence of a large surface/interface anisotropy field in the system is evident. The resulting magnetodynamical parameters are compiled in Table 5.1. It is worth mentioning that, in this case, a negative second-order surface/interface anisotropy constant  $K_2$  favors the in-plane alignment of the magnetization [197, 198].

Table 5.1: Main magnetodynamical parameters obtained from the fitting of FMR spectra at 200K. Each value is accompanied by its own standard deviation. It is important to notice that  $H_2 \equiv 2K_2/M_s$  and  $H_4 \equiv 2K_4/M_s$  are the anisotropy fields.

Sample	$M_s$ (emu/cm <sup>3</sup> )	$\mu_0 H_2$ (mT)	$\mu_0 H_4$ (mT)	$\gamma/2\pi$ (GHz/T)	$\alpha$ ( $\times 10^{-3}$ )	$\Delta H(0)$ (Oe)
LMO	411.7 (fixed)	$-210 \pm 19$	$-8.5 \pm 0.2$	$29.2 \pm 0.3$	$10.7 \pm 1.3$	$40.5 \pm 9.2$
LMO/Pt	348.6 (fixed)	$-180 \pm 10$	$-6.4 \pm 0.2$	$29.4 \pm 0.2$	$11.8 \pm 1.6$	$39.9 \pm 11.3$

In Fig. 5.13b, the linewidth  $\Delta H$  dependence on the resonance frequency  $f_{\text{res}}$  for the LMO and LMO/Pt systems at 200K is shown. As one can see, the expected linear behaviour is loosely followed. In order to illustrate that we can rule out the



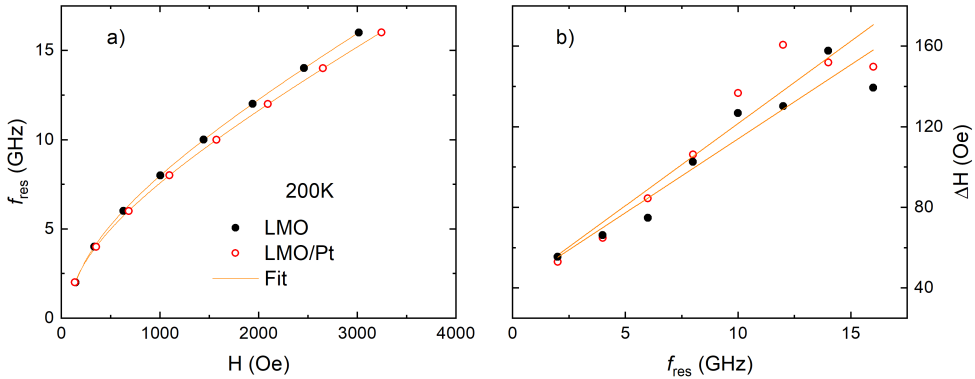


Figure 5.13: Plots of the frequency dependence on the resonance field  $H_{\text{res}}$  (a) and linewidth  $\Delta H$  dependence on the frequency (b) for the LMO alone film (black full circles) and LMO/Pt bilayer (red empty circles). The fitting of each curve, by using equations 5.1 and 4.4 in (a) and (b), respectively, is represented by an orange line.

possibility that this result is a direct consequence of bad fitting, the difference between the experimental points and the fitting curve (i.e., the residual line) is shown as an inset in Fig. 5.12. The residual of the LMO/Pt system is flat with little dispersion of points, while the one from the LMO system shows a substantial dispersion of points at large fields. Nevertheless, the non-linearity of the resonance linewidth is observed in both systems. Therefore, one can conclude that the fitting process is not responsible for the lack of linearity and, as a consequence, it must be of physical origin.

The linear dependence of the resonance linewidth  $\Delta H$  with the microwave frequency  $f_{\text{res}}$  is a direct consequence of the resolution of the Landau-Lifshitz-Gilbert (LLG) equation assuming a magnetically homogeneous system with no defects nor impurities and a Gilbert-type, intrinsic magnetic relaxation mechanism. Thus, the lack of linearity is directly connected to magnetic inhomogeneities in the sample, structural defects, and extrinsic damping mechanisms [199, 200]. As a consequence, the overall resonance linewidth can be expressed as the sum of a frequency-independent line broadening  $\Delta H(0)$  term, an intrinsic, Gilbert term  $\alpha$  linear with the frequency, and extrinsic, frequency-dependent linewidth contributions [201]. Eddy currents present in the sample [202], a small spread of crystal plane orientations (mosaicity) [201, 203], and two-magnon scattering [199, 200, 204, 205] may give rise to additional resonance line broadening and non-linear frequency contributions. In fact, a knee-like shape frequency dependence similar to that observed in Fig. 5.13b has been reported for manganese-based Heusler alloys [205, 206] and attributed to defect-mediated two-magnon scattering. Specifically, the large diffusion layer found at the STO//LMO interface (see Fig. 5.5) may certainly play a role on the enhancement of  $\Delta H$ . In fact, the large surface/interface anisotropy field found in the sample before and after

the Pt deposition (see Table 5.1) suggests that it arises from the STO//LMO interface and not from the LMO/Pt one, which is clearly more homogeneous and sharp. Physically, the effect of a large anisotropy at this interface is the pinning of the local magnetization, which results in an alteration of the spin precession near the interface. As a result, non-vanishing secondary spin wave modes may arise and couple to the external magnetic field, giving rise to an enhancement of  $\Delta H$  [83] or the appearance of secondary peaks besides the fundamental one [207]. On the other hand, due to the presence of Mn in this diffusive interface, the existence of a gradient of magnetization across it could also contribute to this enhancement as well.

The goal of the present work, however, is the study of the spin transport properties across the LMO/Pt interface to prove the suitability of the chemically deposited LMO films as effective spin current injectors. The systematic study of the different extrinsic magnetic relaxation mechanisms occurring in our films, thus, is beyond the scope of this work. Consequently, the fitting of the curves in Fig. 5.13b was carried out in the same way as in Chapter 4, i.e., assuming only the linear dependence of  $\Delta H$  with  $f_{\text{res}}$  (see Eq. 4.4). In this case, however, the correct quantification of the extracted fitting parameters is problematic and, therefore, the observation of an increased Gilbert damping after the Pt deposition (see Table 5.1) is untrustworthy. As a result, this uncertainty precludes the evaluation of the spin current injected based on the difference in Gilbert damping before and after the Pt deposition process (i.e., spin pumping). One way to circumvent this problem and to prove the injection of spin current from the LMO magnetic film into the Pt capping layer is by directly measuring the inverse spin Hall effect (ISHE) induced transverse voltage signal: If some spin current is being injected into the Pt thin film, it will be transformed to a transverse, electrically measurable charge current. These transverse voltage measurements, as mentioned before, are performed in the same way as in Chapter 4 and using the same experimental setup.

The voltage curves of the LMO/Pt bilayers measured at 200K are shown in Fig. 5.14. As can be observed, all voltage lines are positive and strongly symmetric. In general, as is thoroughly discussed in Chapter 4, an experimentally measured voltage curve may have contributions coming from ISHE but also from spin rectification effects (SRE) (which arise from the synchronous coupling between the induced rf current in the ferromagnetic film and its precessing magnetization), however, it is important to recall that in our own experimental setup (which is presented in section 4.2 from Chapter 4), the ISHE voltage signal in Pt should be positive, while that of SRE negative. In addition to that, the ISHE voltage signal is also expected to present a purely symmetric line shape while SRE a mixture of symmetric and antisymmetric components [93]. Moreover, it is important to mention that, in our samples, the spin rectification effects (SRE) are expected to be negligible due to the highly resistive nature of the LMO films. Specifically, the LMO film resistivity is roughly 1000 times

more resistive than Py, according to Ref. [191]. In fact, we tried to measure the ISHE voltage signal of the LMO film before the Pt deposition in order to check if there was any contribution from SRE. The fact that it was impossible to make proper electrical contact between the sample and the CPW sample holder is indicative of this highly resistive nature. In overall, these facts straighten the interpretation that SRE should not play a major role in this system. As a consequence, the overall observed features in the voltage resonance lines (i.e., highly symmetric, positive in sign, and no voltage in the LMO alone samples) indicate that ISHE is the dominant contribution to the overall measured voltage signal.

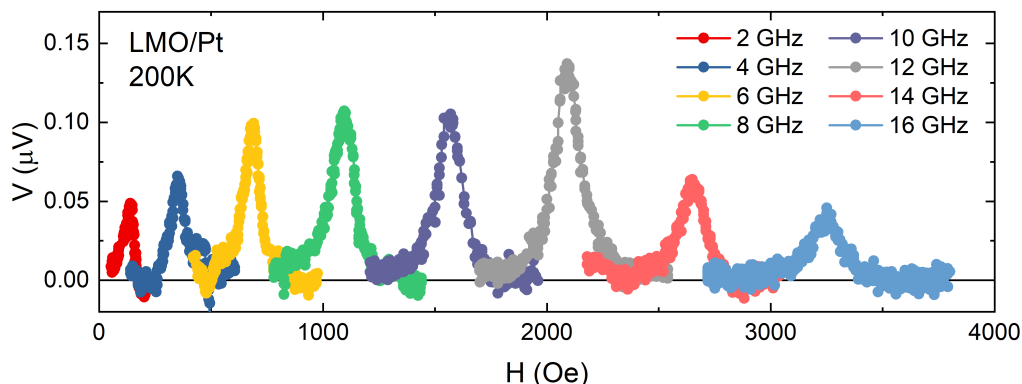


Figure 5.14: Transverse voltage curves of the LMO/Pt bilayer at 200K for different resonance frequencies as a function of the applied magnetic field.

However, besides ISHE and SRE, a temperature increase in the system during measurement could induce a perpendicular thermal gradient which could result in non-negligible thermoelectric effects [112, 208] through which a net voltage signal could arise. It is important to consider that this thermal gradient does not depend on the magnetic field direction, while the ISHE-induced voltage is an odd function of it. Therefore, one way to check the weight of thermoelectric effects in spin pumping induced voltage experiments is to perform voltage measurements by reversing the direction of the magnetic field [208, 209]. In Fig. 5.15, the 6 GHz voltage curves for positive and negative fields (i.e., reversed 180°) are shown. As can be observed, the voltage lines are completely symmetrical upon magnetic field inversion. As a consequence, one can conclude that the thermoelectric effects are also negligible in our system. This result further supports the fact that ISHE is the main effect behind the measured voltage signals in Fig. 5.14. In the following section, the ISHE measurements as a function of temperature are addressed, and their dependence on temperature and resonance frequency is discussed.

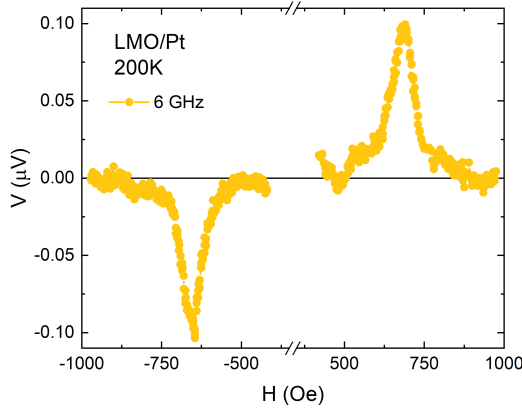


Figure 5.15: Positive ( $H > 0$ ) and negative ( $H < 0$ ) transverse voltage curves of the LMO/Pt bilayer at 200K and 6 GHz as a function of the applied magnetic field.

### 5.1.3 Temperature Dependence of Inverse Spin Hall Effect in $\text{La}_{0.92}\text{MnO}_3/\text{Pt}$ Bilayers

In this section, the ISHE voltage signal as a function of temperature is studied. The methodology followed at each temperature is analogous to that used in the previous one: FMR spectroscopy is used to obtain the main magnetodynamical parameters which characterize the magnetization dynamics of the LMO/Pt system, while the ISHE voltage signal is obtained by using an external nanovoltmeter synchronized with the FMR spectrometer. The range of temperatures studied is from 280K to 100K, i.e., near and far away from the Curie temperature, respectively. We start by addressing the complete FMR characterization of the LMO/Pt bilayer at different temperatures in order to understand the evolution of the LMO/Pt magnetization dynamics with temperature.

In Fig. 5.16, the FMR spectra at each temperature is shown. As can be observed, as the temperature decreases, the FMR spectral curves gradually shift to the left. This shift, which is more pronounced close to  $T_c$ , is directly related to the intrinsic variation of the saturation magnetization with temperature (see Fig. 5.10). Additionally, it can be observed that the intensity of the resonance lines is smaller in the high temperature region, i.e., near  $T_c$ , as expected [92, 120].

Each FMR spectral curve was fitted according to Eq. 4.2 in order to obtain both the resonance field  $H_{\text{res}}$  and linewidth  $\Delta H$ . The curves relating these two parameters with the resonance frequency  $f_{\text{res}}$  at each temperature are shown in Fig. 5.17. It is important to notice that the above mentioned resonance field shift-to-the-left when decreasing temperature is clearly appreciated in Fig. 5.17a. Moreover, the linewidth

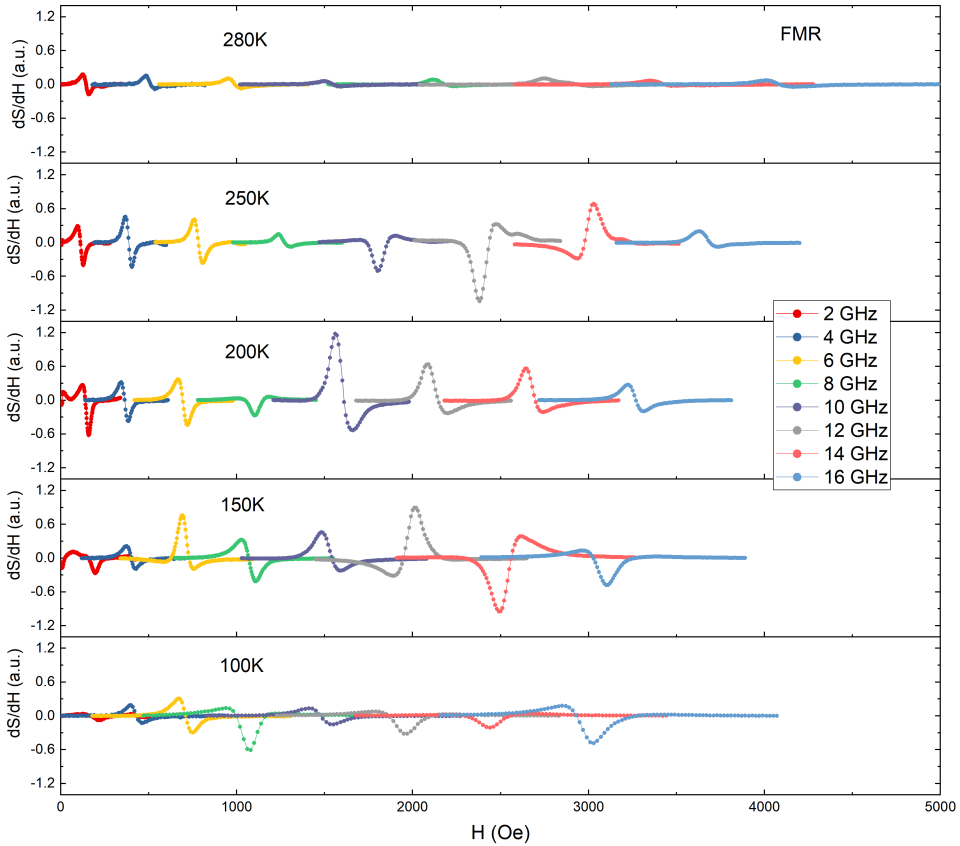


Figure 5.16: FMR spectra of the LMO/Pt bilayer obtained for several temperatures, i.e., from 280K to 100K.

$\Delta H$  dependence on the resonance frequency is shown in Fig. 5.17b and, as can be observed, the lack of linearity is manifested regardless of the temperature considered. The main parameters that govern the magnetodynamical properties of the system are obtained by fitting each of these curves. Each curve from Fig. 5.17a was fitted by using Kittel's equation (Eq. 5.1), while only the Gilbert, linear term with frequency was considered for the fitting of the points in Fig. 5.17b. In summary, the resulting fitted parameters are compiled in Table 5.2.

Just as in the fitting process from the previous section (using Eq. 5.1), a second-order surface/interface magnetic anisotropy  $K_2$  term is needed to obtain a proper fit in Fig. 5.17a when imposing the saturation magnetization value measured by SQUID magnetometry. This anisotropy is expressed as  $H_2 \equiv 2K_2/M_s$  in Table 5.2 and as can be observed, it is consistently large for all temperatures. In order to better visualize these results, in Fig. 5.18 the effective magnetization  $M_{\text{eff}}$  and fourfold in-

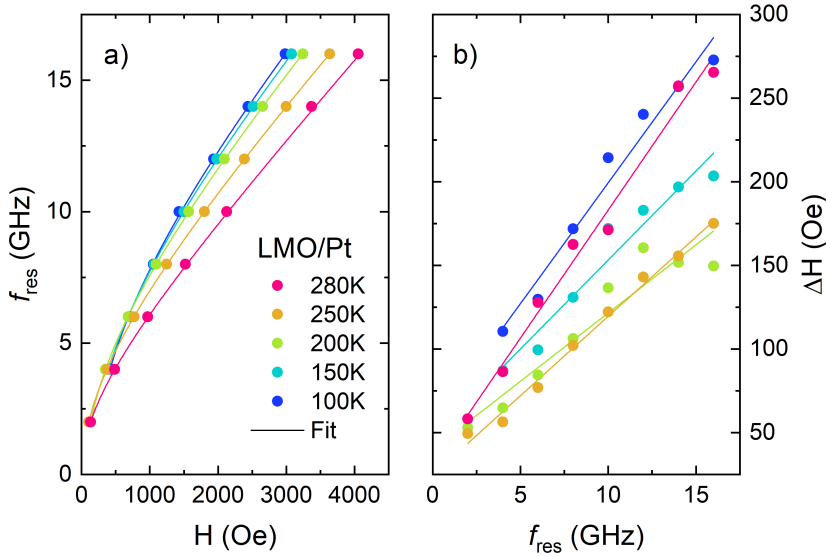


Figure 5.17: a) Resonance magnetic field  $H_{\text{res}}$  dependence on the resonance frequency  $f_{\text{res}}$  at each temperature. b) Dependence of the resonance linewidth  $\Delta H$  with the  $f_{\text{res}}$  at each temperature. Each curve on (a) has been fitted using Eq. 5.1, while in (b), Eq. 4.4 has been used.

Table 5.2: Main magnetodynamical parameters obtained from the fitting of FMR spectra at several temperatures. Each value is accompanied by its own standard deviation. It is important to notice that  $H_2 \equiv 2K_2/M_s$  and  $H_4 \equiv 2K_4/M_s$  are the anisotropy fields. The saturation magnetization value  $M_s$  is taken as a fixed imposed value for the fitting process.

T (K)	$M_s$ (emu/cm <sup>3</sup> )	$\mu_0 H_2$ (mT)	$\mu_0 H_4$ (mT)	$\gamma/2\pi$ (GHz/T)	$\alpha_{\text{eff}}$ ( $\times 10^{-3}$ )	$\Delta H(0)$ (Oe)
280	156.8 (fixed)	$-140 \pm 20$	$0.0 \pm 0.8$	$29.2 \pm 0.3$	$22.2 \pm 1.2$	$30.1 \pm 8.3$
250	255.4 (fixed)	$-200 \pm 10$	$-1.2 \pm 0.2$	$28.4 \pm 0.2$	$13.8 \pm 0.5$	$24.7 \pm 3.6$
200	348.6 (fixed)	$-180 \pm 10$	$-6.4 \pm 0.2$	$29.4 \pm 0.2$	$11.8 \pm 1.6$	$39.9 \pm 11.3$
150	409.0 (fixed)	$-170 \pm 30$	$-13.0 \pm 0.6$	$29.9 \pm 0.5$	$15.4 \pm 1.7$	$46.8 \pm 12.4$
100	454.4 (fixed)	$-210 \pm 120$	$-18.7 \pm 1.6$	$29.3 \pm 1.7$	$20.9 \pm 1.6$	$54.9 \pm 11.9$

plane anisotropy field  $H_4$  are shown. The effective magnetization, as was mentioned, is defined as  $M_{\text{eff}} = M_s - H_2$ , while the anisotropy field is  $H_4 \equiv 2K_4/M_s$ . These effective magnetization and anisotropy values are in accordance with the ones obtained from our previous work [191] and are similar to reported values for manganese-based thin films [210, 211, 212]. Additionally, in the inset of Fig. 5.18b the dependence between the normalized anisotropy constant  $K_4$  and the normalized magnetization is shown. In this case, the normalized anisotropy and magnetization are defined as  $K_4(T)/K_4(T_0)$

and  $M_s(T)/M_s(T_0)$ , respectively, being  $T_0$  a low temperature value. In our particular case,  $T_0 = 100$  K, which corresponds to the smaller temperature available. It is expected that both quantities are related through a power law with the exponent of which is related to the anisotropy order [120]:  $K_4(T)/K_4(T_0) = [M_s(T)/M_s(T_0)]^\xi$ . The fitting of the experimental points from the inset in Fig. 5.18b (orange solid line) shows that these quantities are related by a power law with exponent  $\xi = 4 \pm 0.2$ .

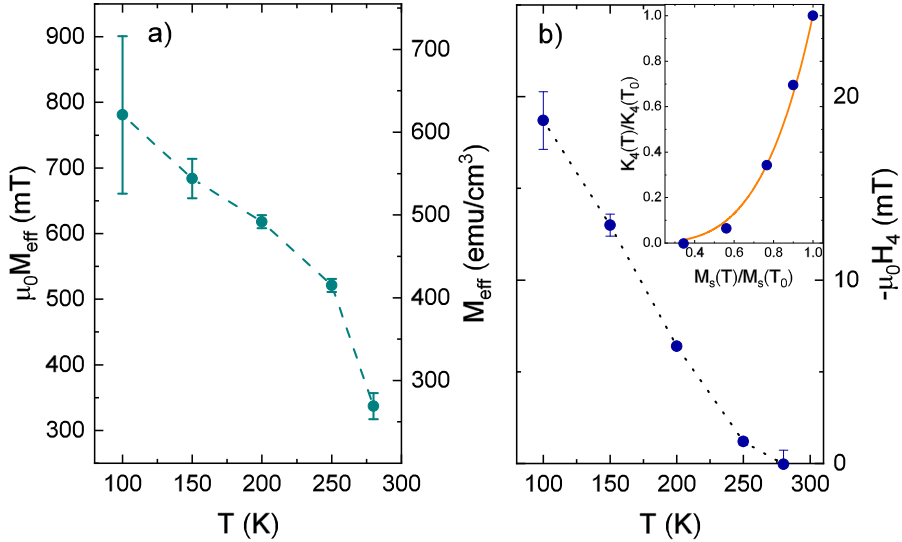


Figure 5.18: a) Effective magnetization as a function of temperature. It is defined as  $M_{\text{eff}} = M_s - H_2$ , and expressed in mT (left axis) and in  $\text{emu}/\text{cm}^3$  (right axis). b) Temperature dependence of the fourfold in-plane anisotropy field  $H_4$ . Dotted lines are a guide to the eyes. The inset shows the power law dependence of the normalized in-plane anisotropy  $K_4(T)/K_4(T_0)$  with the normalized magnetization  $M_s(T)/M_s(T_0)$ .

Now, let's put the focus on Fig. 5.17b. In the previous section, it was shown that the dependence of  $\Delta H$  with  $f_{\text{res}}$  at 200K for the LMO and LMO/Pt systems was loosely linear irrespective of the system studied. This feature precluded the observation of a Gilbert damping difference between the LMO and LMO/Pt systems, which would be indicative of spin current injection from the LMO into the Pt. However, the voltage measurements resulted in a clear voltage signal compatible with ISHE. A possible explanation for these apparently contradicting results is that non-linear, extrinsic terms (such as those coming from the anisotropy at the STO//LMO, for instance) besides the usual Gilbert damping term are playing an important role on the overall damping measured, masking the expected damping difference between systems. As a consequence, in this section, the fitted damping is denoted as  $\alpha_{\text{eff}}$ , i.e., *effective* damping, in order to highlight the presence of these extrinsic terms. Taking this into account, the temperature evolution of this effective damping  $\alpha_{\text{eff}}$  and the

inhomogeneous line broadening  $\Delta H(0)$  is depicted in Fig. 5.19. As expected, the effective damping has a maximum at high temperature, close to the Curie point (see Fig. 5.19a). This can be understood considering that near  $T_c$  the scattering of the uniform FMR mode with spin waves and magnetic fluctuations is an important source of damping [120]. For lower temperatures, however, it presents a non-monotonic relation with temperature: It decreases down to 200K and increases again below it, resulting an overall U-shaped, temperature dependent curve with a cusp at about 200K. The non-monotonic evolution of damping with temperature was already observed and discussed in detail in Chapter 4 for the case of Py and Py/Pt films. In that case, Kamberský's phenomenological torque-correlation model [136, 137] was invoked to qualitatively describe the observed behaviour. Nevertheless, this model only considers the damping arising from intrinsic magnetic relaxation mechanisms and, as is pointed out in this Section, the damping measured from LMO and LMO/Pt films is expected to have major contributions coming from extrinsic terms. Therefore, this change of the extrinsic contributions with temperature surely has an effect on how the measured effective damping changes with temperature. On the other hand, the inhomogeneous line broadening shows a constant, mild increase with decreasing temperature (Fig. 5.19b).

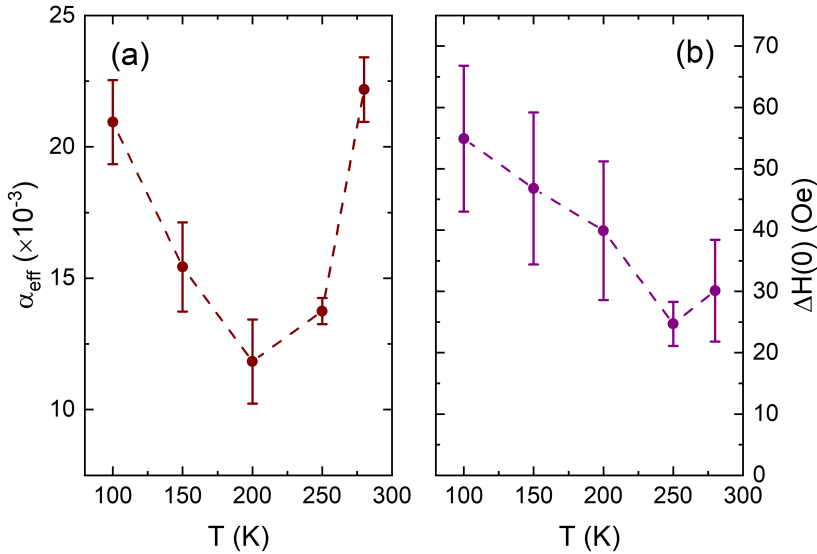


Figure 5.19: Effective damping  $\alpha_{\text{eff}}$  (a) and inhomogeneous line broadening  $\Delta H(0)$  (b) dependence on temperature.

Finally, before showing the ISHE voltage curves measured at each temperature, it is worth showing the temperature dependence of  $H_{\text{res}}$  and  $\Delta H$ , extracted from the fitting of the curves in Fig. 5.16. These curves are depicted in Fig. 5.20 and, as can be observed, the temperature dependence in each case is the same regardless



of the frequency considered, as expected. Specifically, the resonance field follows a decrease (Fig. 5.20a) which is compatible with the opposite increase of  $M_{\text{eff}}$  (see Fig. 5.18), as expected from the symmetry of Eq. 5.1. Additionally, the linewidth dependence on temperature (Fig. 5.20b) is similar to that found in the effective damping discussed before: a non-monotonic temperature dependence with a minimum at about 200K, suggesting a major role of extrinsic magnetic relaxation mechanisms at high and low temperatures, respectively. In fact, a strong increase of damping on reducing temperature has been reported recently [213] for  $\text{La}_{2/3}\text{Sr}_{1/3}\text{MnO}_3$  thin films (which are magnetically very similar to our LMO films). In that work, the increase of damping was attributed to the appearance of an insulating and magnetically active layer at the interface with the substrate, caused by the lowering of double exchange mechanisms at surface and interfaces. These authors stated that this extrinsic dead layer acted as a spin sink, thus enhancing the Gilbert damping term.

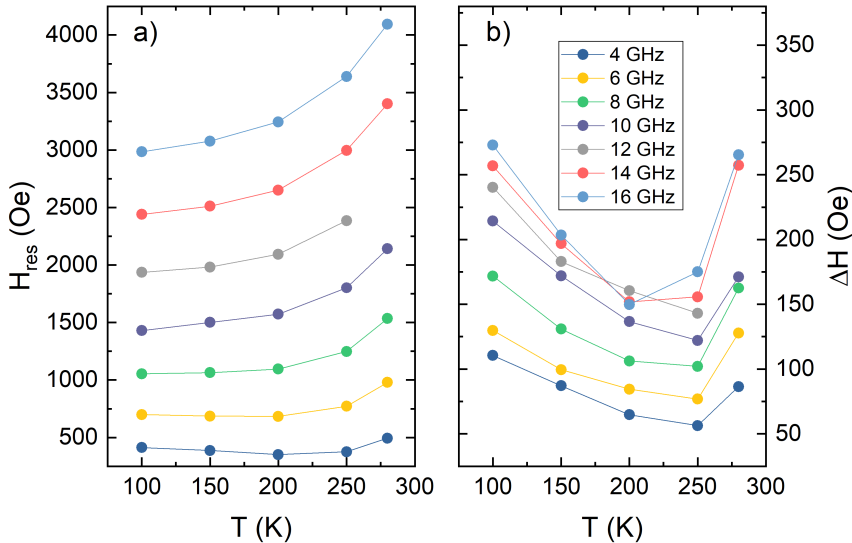


Figure 5.20: Resonance magnetic field  $H_{\text{res}}$  (a) and linewidth  $\Delta H$  (b) dependence on temperature.

Hereafter, the experimental ISHE voltage curves as a function of temperature for the LMO/Pt bilayer, shown in Fig. 5.21, are discussed. As expected, the overall ISHE voltage signal decreases when approaching  $T_c$  since, as can be observed in Fig. 5.16, for instance, the FMR absorption close to  $T_c$  is minimal. As a consequence, one can infer that the net spin current generated in this temperature regime is minimal as well. Additionally, it is observed that at 100K the overall intensity of the voltage lines decreases a little with respect to the other temperature regime, being in general substantially noisier. In fact, it is observed that below 100K the voltage signal completely vanishes and the corresponding FMR spectra presents anomalous secondary

spin-wave resonance peaks overlapped with the uniform FMR peak. The FMR and voltage lines measured at 50K are shown in Fig. 5.22 for completeness.

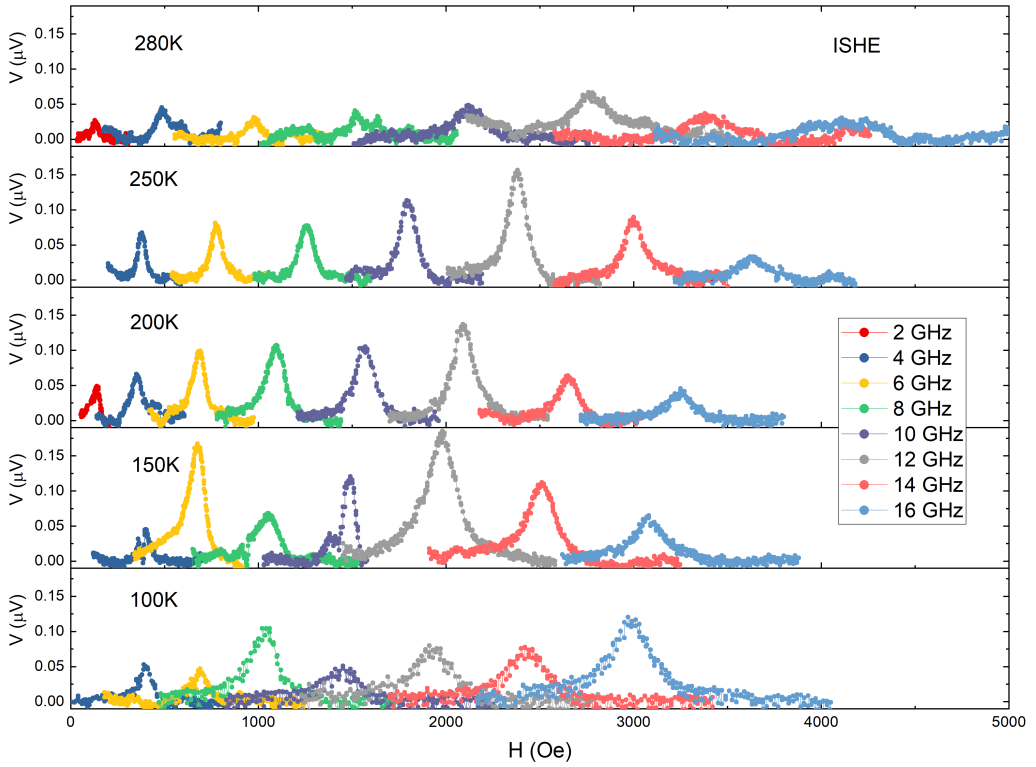


Figure 5.21: ISHE voltage curves as a function of temperature.

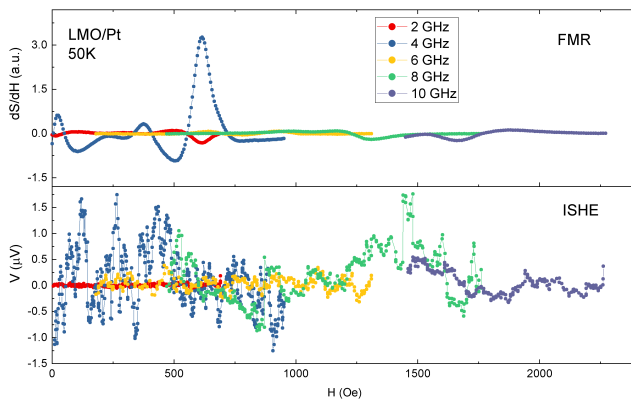


Figure 5.22: FMR spectra and voltage signals measured at 50K.

In overall, this temperature dependence might be related with the observed increase

of the resonance linewidth  $\Delta H$  or the effective damping  $\alpha_{\text{eff}}$  (see Figs. 5.20 and 5.19, respectively) at 100K, which is not due to an enhancement of the spin pumping efficiency but due to the action of additional extrinsic relaxation mechanisms occurring in the LMO film, as was mentioned. Currently, systematic studies focusing on the temperature dependence of ISHE voltage are scarce and sometimes contradictory. For instance, the temperature dependence of the ISHE voltage has been reported in  $\text{La}_{0.7}\text{Sr}_{0.3}\text{MnO}_3/\text{SrRuO}_3$  (LSMO/SRO) bilayers [164]. In this study, it is observed how the ISHE voltage signal decreases when approaching room temperature, near the  $T_c$  of the LSMO ferromagnetic film. However, due to the fact that the ferromagnetic phase transition of the SRO capping layer occurs at about 155K, it precludes the access to the low temperature behaviour of ISHE. Moreover, Atsarkin et al. [214, 215] have conducted a series of experiments regarding the temperature dependence of ISHE voltage in LSMO/Pt bilayers. Their results show that the ISHE voltage follows a temperature dependence similar to that followed by the saturation magnetization, i.e., decreasing when approaching  $T_c$  and an approximately constant value below about 200K. Unfortunately, the experiment is truncated at 100K, so the behaviour of ISHE at lower temperatures cannot be inferred. On the other hand, a temperature-dependent study on the spin pumping efficiency in YIG/Pt bilayers conducted by Shigematsu et al. [216] shows a significant reduction of the ISHE voltage with decreasing temperature and the further disappearance of it at 80K, similar to our own experimental observation. In that case, the vanishing of the ISHE voltage signal is explained by an increase of magnetic damping at low temperatures, which is correlated with an increase of impurity-mediated magnetic relaxation mechanisms present in YIG films [217, 218].

According to the analysis of Azevedo et al. [150] and after some algebra, an expression for the ISHE voltage signal is obtained [161, 214]:

$$V = AR\lambda_{\text{sd}}\Theta_{\text{SH}} \tanh\left(\frac{t_{\text{Pt}}}{2\lambda_{\text{sd}}}\right) p \frac{G_{\text{eff}}^{\uparrow\downarrow}}{\Delta H^2}, \quad (5.2)$$

where  $A = ef_{\text{res}}h_{\text{rf}}^2w/2$  (being  $h_{\text{rf}}$  the magnitude of the rf magnetic field supplied by the CPW and  $w$  the width of the CPW signal line) is a temperature-independent factor,  $R$  is the resistance of the overall LMO/Pt bilayer, and  $\lambda_{\text{sd}}$ ,  $\Theta_{\text{SH}}$  and  $t_{\text{Pt}}$  are the spin diffusion length, spin Hall angle, and thickness of the Pt capping film. The resonance linewidth is denoted by  $\Delta H$ ,  $G_{\text{eff}}^{\uparrow\downarrow}$  is the effective spin-mixing conductance, and  $p$  is a dimensionless factor that accounts for demagnetizing fields and the ellipticity of the spin precession in the LMO film. This ellipticity  $p$ -factor may be expressed in terms of  $H_{\text{res}}$  and  $M_{\text{eff}}$  as [215]

$$p = \frac{2\pi f_{\text{res}} (H_{\text{res}} + 4\pi M_{\text{eff}})}{\gamma (2H_{\text{res}} + 4\pi M_{\text{eff}})^2}. \quad (5.3)$$

It should be noted that Eq. 5.2 is completely equivalent to Eq. 4.17 from Chapter 4. The specific temperature dependence of the different parameters in Eq. 5.2 should clarify the temperature evolution of the ISHE voltage. In this way, as has been pointed out in Refs. [214, 215], the ellipticity  $p$ -factor should be almost constant down to the low temperature regime. In Fig. 5.23, the  $p$ -factor calculated according to Eq. 5.3 as a function of temperature and resonance frequency is shown. Additionally, the resistance dependence on temperature of the LMO/Pt system is also included in the figure. As can be observed, the ellipticity factor abruptly decreases just below  $T_c$  and stabilizes at a constant value for lower temperatures, as expected (see Fig. 5.23b). Moreover, the resistivity of the LMO/Pt system does not present any abnormal behaviour and follows the linear decreasing relation with temperature expected for metallic systems (see Fig. 5.23a).

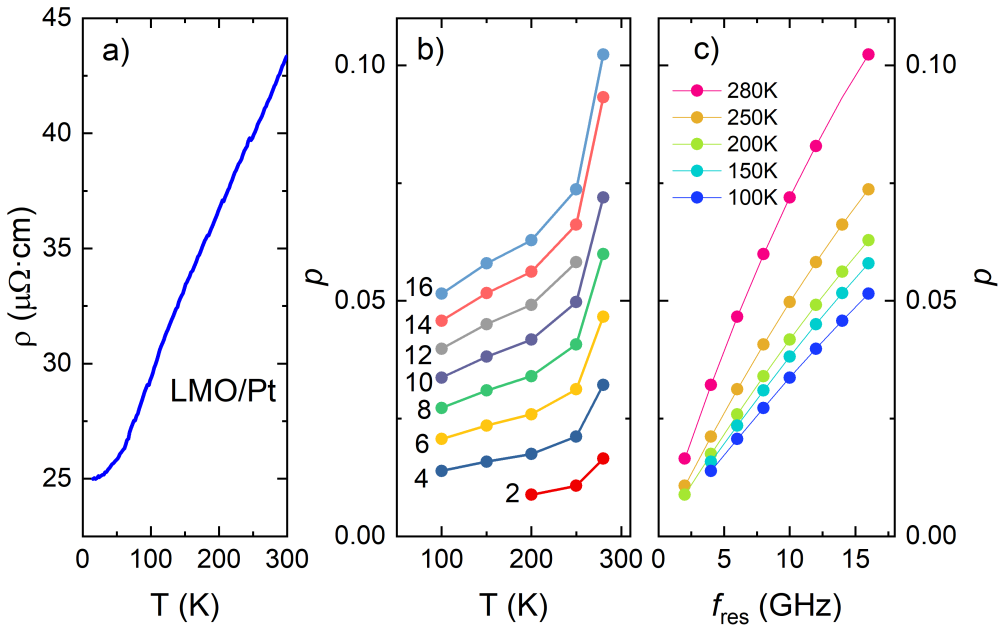


Figure 5.23: Resistivity of the LMO/Pt system measured as a function of temperature (a), and ellipticity  $p$ -factor as a function of temperature for each frequency (b) and as a function of the resonance frequency for each temperature (c). The numbers in (b) correspond to the resonance frequency in GHz. The  $p$ -factor has been calculated according to Eq. 5.3.

The temperature dependence of  $\lambda_{\text{sd}}$ ,  $\Theta_{\text{SH}}$ , and  $G_{\text{eff}}^{\uparrow\downarrow}$  is somewhat more controversial. According to Atsarkin et al. [214, 215], the effective spin-mixing conductance  $G_{\text{eff}}^{\uparrow\downarrow}$

dependence on temperature should resemble that of the square of the magnetization. Therefore, once the saturation magnetization value is reached,  $G_{\text{eff}}^{\uparrow\downarrow}$  should be temperature independent. Regarding to this, a different set of studies based on YIG/Pt bilayers performed well below the Curie point of YIG showed that it is effectively temperature-independent [219, 220]. On the other hand, the reported temperature dependence of  $\lambda_{\text{sd}}$  and  $\Theta_{\text{SH}}$  presents more variability. For instance, in an experiment conducted by Meyer et al. [221], it was found that the  $\lambda_{\text{sd}}$  of Pt and the  $G_{\text{eff}}^{\uparrow\downarrow}$  of the YIG/Pt interface were independent of temperature, while the Pt spin Hall angle  $\Theta_{\text{SH}}$  decreased from 1.1 % at room temperature to 0.75 % at 10K, i.e., a 30% reduction in overall. Nevertheless, this result is in contradiction with subsequent reports [222] in which the Pt spin Hall angle was found to be almost constant with temperature, while the spin diffusion length was also constant down to 100K, from which it increased linearly with decreasing temperature. More recent studies, however, have suggested that when intrinsic mechanisms dominate,  $\Theta_{\text{SH}}$  should scale with the Pt resistivity, whereas  $\lambda_{\text{sd}}$  should scale with the Pt conductivity [223, 224]. This result is in accordance with previous studies [219, 225] that argued that  $\lambda_{\text{sd}}$  must have a clear temperature dependence since it depends on the sample's magnetic relaxation mechanisms. In overall, these authors often invoke the Elliot-Yafet theory [163, 226] whereby the spin relaxation is mediated by the scattering between the spin of conducting electrons and atom impurities in the lattice.

In summary, the expected qualitative temperature dependence of the ISHE voltage can be calculated by considering the temperature dependence of the different quantities included in Eq. 5.2. The curves shown in Fig. 5.24 are the result of this calculation. In this case, the temperature dependence of  $R$ ,  $p$  and  $\Delta H$  from Eq. 5.2 is extracted from the experimental data<sup>1</sup> (see Figs. 5.23 and Fig. 5.20, respectively), while the effective mixing conductance  $G_{\text{eff}}^{\uparrow\downarrow}$  is estimated to follow the same temperature dependence as  $M(T)^2$ , as explained in Refs. [214, 215]. Additionally, for the temperature dependence of  $\lambda_{\text{sd}}$  and  $\Theta_{\text{SH}}$ , four scenarios are considered: i) that both quantities depend on T (black curve in Fig. 5.24); ii) that only  $\lambda_{\text{sd}}$  depends on T (red curve); iii) that only  $\Theta_{\text{SH}}$  depends on T (green curve); and iv) that both quantities are independent of T (blue curve). Regarding their temperature dependence, the spin diffusion length is set to be inversely proportional to the Pt resistivity,  $\lambda_{\text{sd}} \propto 1/\rho(T)$ , while the spin Hall angle is set to follow the same temperature dependence as the  $\rho(T)$ , as pointed out by Sagasta et al. [223]. In all four situations, the calculated ISHE voltage follows a non-monotonic dependence on temperature, increasing up to a maximum at around 200K and then decreasing back for lower temperatures (see Fig. 5.24). In fact, this behavior is a mirror image of the one observed in Figs. 5.19a and 5.20b, in which the effective Gilbert damping and resonance linewidth, respectively,

<sup>1</sup>It is considered that the temperature dependence of  $p$  and  $\Delta H$  does not depend on the resonant frequency, so the qualitative behaviour of each quantity should be the same regardless of the frequency.

are plotted against temperature. The correlation between an increase of these quantities with a decrease of the ISHE voltage is explicit in Eq. 5.2, but it has also been experimentally tested, as discussed in the work by Shigematsu et al. [216] mentioned earlier. Consequently, we may infer that the strong reduction of the ISHE voltage signal below about 100K is mostly attributed to the increase of Gilbert damping (and resonance linewidth), triggered by extrinsic relaxation mechanisms occurring in the film.

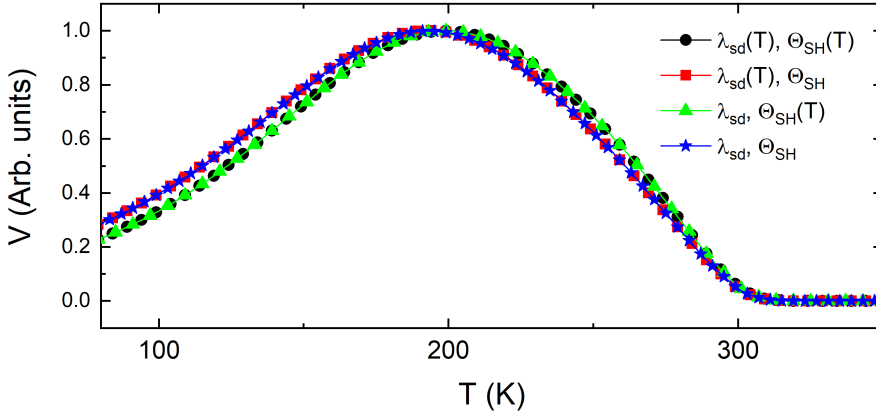


Figure 5.24: Calculated temperature dependence of the ISHE voltage in the LMO/Pt films by taking into account the different temperature dependence of the parameters in Eq. 5.2 and considering four possible scenarios regarding the temperature dependence of  $\lambda_{sd}$  and  $\Theta_{SH}$ : The black curve considers that both quantities change with temperature; the red one considers a constant  $\Theta_{SH}$  and a temperature dependent  $\lambda_{sd}(T)$ ; the green one considers a constant  $\lambda_{sd}$  and a temperature dependent  $\Theta_{SH}(T)$ ; and, finally, the blue curve considers that both quantities do not depend on temperature.

It is important to notice that the qualitative voltage temperature dependence outlined in Fig. 5.24, although it is useful for characterizing the *general* ISHE voltage dependence with temperature in our system (see Fig. 5.21), does not satisfactorily explain the temperature evolution of *some* of the voltage curves (see Fig. 5.21). For example, the  $f_{res} = 16$  GHz voltage curve increases almost linearly with decreasing temperature. On top of that, at each temperature, it is observed that the intensity of the voltage curves from Fig. 5.21 presents a non-monotonous dependence with the resonance frequency which should be carefully taken into consideration. In theory, the spin current generated by spin pumping is expected to be proportional to the precession frequency  $f_{res}$  [15]. Therefore, the corresponding ISHE voltage signal should be proportional to it as well (see Eq. 5.2, for instance). However, some authors [60, 227] have observed that actually the spin current slightly decreases with increasing frequency. This behaviour is explained [227] by some sort of compensation effect between the magnetization precession frequency and the spin current generated by

a cycle of precession, which is proportional to the elliptical area of the magnetization precession trajectory. Nevertheless, this behaviour cannot explain the observed non-linear frequency dependence from Fig. 5.21. In an experiment conducted by Castel et al. [209], a non-linear ISHE voltage dependence on frequency is found at low frequencies. This behaviour is explained by the action of *secondary* spin-wave modes contributing to the overall spin pumping effect in some way. The effect of these secondary modes, however, vanishes for frequencies larger than 4 GHz. On the other hand, an important remark found in this work by Castel et al., is that at some frequencies, the microstrip (transmission) line induces an artificial increase in their ISHE voltage signal [209]. In a similar way, Singh and Bedanta [228] correlate their observed non-linear voltage dependence with the corresponding observed non-linear FMR signal absorption.

Therefore, in order to check the effect of the FMR absorption signal on the ISHE voltage, we compared the total FMR absorption, which corresponds to the total area of the FMR signal, with the corresponding voltage signal maximum  $V_s$  (see Eq. 4.9). The area of the FMR absorption curves was obtained by numerically integrating each FMR curve in Fig. 5.16 to obtain the area under the curve. In a sense, this area is an estimate of the total FMR absorption of the system, since it takes into account the height (peak) of the FMR signal as well as its linewidth and shape. On the other hand, we only considered the voltage maximum  $V_s$  because its value depends on additional parameters besides FMR absorption, as deduced from Eq. 5.2. In Fig. 5.25, the total FMR absorption is plotted on top of the corresponding ISHE voltage peak maximum. Fig. 5.25a shows the temperature dependence at each frequency, while in Fig. 5.25b the frequency dependence at each temperature is shown. The total FMR absorption is denoted as “FMR” in the figure.

As can be clearly observed from Fig. 5.25b, the variation of the ISHE voltage curves with frequency mimics the variation of the FMR absorption. Therefore, similarly to the result found in Ref. [228], it can be concluded that the different amplitudes of the FMR signal are the primary reason for the frequency dependence of the ISHE voltage curves in our system. With regard to the temperature dependence depicted in Fig. 5.25a, it can be observed that the correlation between the FMR amplitude and the ISHE voltage exists. Specifically, the odd increase of the  $f_{\text{res}} = 16$  GHz ISHE voltage signal with decreasing temperature mentioned before can be explained by the corresponding increase of the FMR absorption amplitude with decreasing temperature. Still, the temperature dependence of the ISHE voltage curves is best described by a combination of intrinsic system properties (such as the interplay of parameters from Eq. 5.2 discussed before) and extrinsic experimental features such as this frequency dependent FMR absorption. In the end, FMR absorption does also depend on the specific features of the sample.

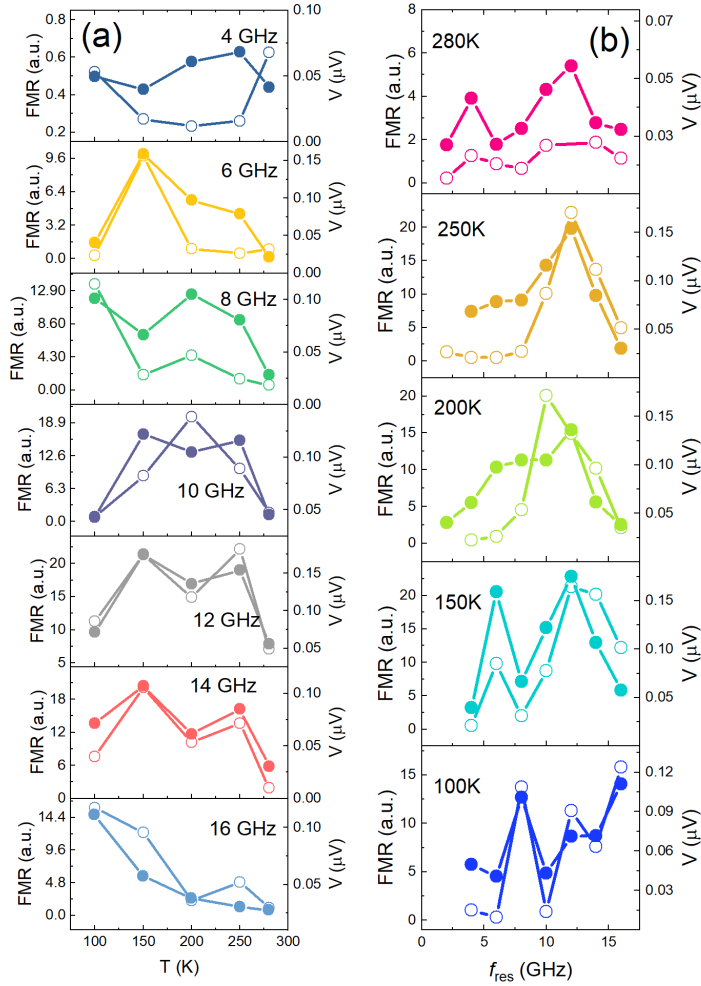


Figure 5.25: FMR absorption amplitude (area of the integrated curve) (empty circles) on top of the corresponding ISHE voltage amplitudes (bold circles) at each frequency as a function of temperature (a), and at each temperature as a function of resonance frequency (b).

## Spin Hall Angle

The spin Hall angle  $\Theta_{\text{SH}}$  of Pt in this system is calculated using Eq. 4.17, just as in the Py/Pt bilayer from the previous Chapter. Nevertheless, in this case, a few issues must be considered in advance. On one hand, as is observed in Fig. 5.13b, the difference of damping before and after the Pt deposition is hard to establish. As such, it is indeed very difficult to obtain a precise value of  $G_{\text{eff}}^{\uparrow\downarrow}$ , which is explicitly included in Eq. 4.17 and is crucial for calculating  $\Theta_{\text{SH}}$ . In this regard, we used the values of



damping obtained from the fits at 200K and compiled in Table 5.1, which result in a difference of damping  $\Delta\alpha = 0.11 \times 10^{-3}$  and  $G_{\text{eff}}^{\uparrow\downarrow} = 4.23 \times 10^{18} \text{ m}^{-2}$ . However, due to the large error associated with these quantities, the estimated  $\Theta_{\text{SH}}$  presented here should be taken with caution since it is affected by a large error bar. On the other hand, according to the resistivity of Pt in this system ( $\approx 40 \mu\Omega\text{-cm}$ ), the spin diffusion length  $\lambda_{\text{sd}}$  should be around 3 nm, as reported in the literature [223, 162]. The remaining parameters needed for the calculation are identical to those employed in Chapter 4. In Fig. 5.26, the spin Hall angle as a function of the resonance frequency at 200K is shown.

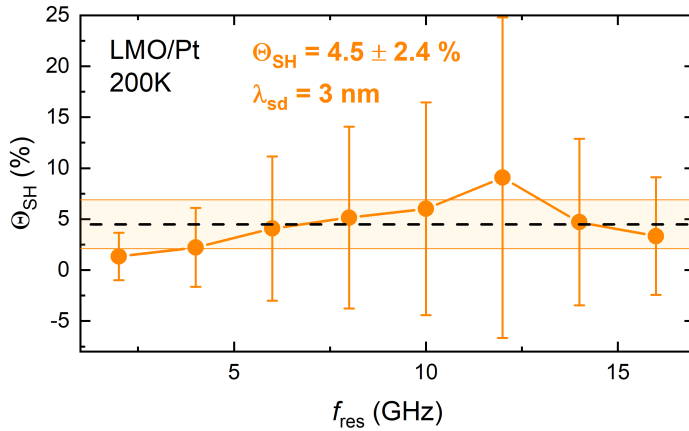


Figure 5.26: Spin Hall angle  $\Theta_{\text{SH}}$  value and standard deviation at 200K as a function of frequency calculated according to Eq. 4.17 and by fixing the spin diffusion length  $\lambda_{\text{sd}}$  to 3 nm. The dashed horizontal line corresponds to the average value, whereas the colored regions its standard deviation. The parameters used for the calculations are:  $w = 200 \mu\text{m}$ ;  $\mu_0 h_{\text{rf}} = 50 \mu\text{T}$ ;  $G_{\text{eff}}^{\uparrow\downarrow}(200\text{K}) = 4.23 \times 10^{18} \text{ m}^{-2}$ .

As can be observed, the obtained value is  $\Theta_{\text{SH}} = 4.5 \pm 2.4 \%$ , which is threefold larger than the one obtained for Py/Pt. This difference may be attributed to the larger Pt resistivity present in LMO/Pt compared to that from Py/Pt. In Pt, larger resistivities are commonly associated to lower spin diffusion lengths and slightly larger spin Hall angles, as reported in the literature [162, 223]. Another possible explanation is related to the fact that it was calculated at a lower temperature (i.e., 200K in front of 300K). However, following the discussion regarding the different temperature dependencies from Section 5.1.3, all evidence suggests that  $\Theta_{\text{SH}}$  decreases lightly. Lastly, this difference might be strongly affected by the uncertainty associated with the value of  $G_{\text{eff}}^{\uparrow\downarrow}$ , which directly stems from the observed minute difference of damping (see Fig. 5.13b).

In conclusion, this Section shows that the LMO/Pt bilayer is an effective system for the generation, injection and detection of spin current signals in a broad range of

temperatures. Moreover, it demonstrates the suitability of polymer-assisted deposited LMO epitaxial thin films for spintronic-related applications. In addition to that, it shows that PAD allows obtaining LMO films with excellent crystalline and interface quality. The electrical measurements performed in this system suggest that the main source of voltage comes from ISHE and, as a consequence, that the contributions of SRE or thermoelectric effects are negligible. In overall, these results indicate that chemical solution grown LMO is a promising perovskite building block for all-oxide multifunctional high-frequency spintronic devices.

## 5.2 Inverse Spin Hall Effect Measurements in $\text{La}_{2/3}\text{Sr}_{1/3}\text{MnO}_3/\text{SrIrO}_3$ Bilayers

### 5.2.1 Samples Preparation and Description of the Experiment

In the last few years, the ability to tune and fabricate complex oxide heterostructures has resulted in the discovery of emergent phenomena and new functionalities [229, 230]. Moreover, due to the ever-increasing demand for more efficient, less energy-consuming, and fast electronic devices, complex oxide electronics has attracted a great deal of attention due to the rich diversity of oxide compounds and functional properties available [231]. In the context of this Thesis, it is thus desirable to find effective functional complex oxide heterostructures with the object to dynamically inject and detect spin currents.

In this Section, we study the spin injection and spin-to-charge conversion processes in all-oxide heterostructures. The capabilities of the archetypal lanthanum manganite complex oxide LSMO for the generation of pure spin currents under FMR conditions is investigated. The high spin-orbit coupling (SOC) non-magnetic element of the system is  $\text{SrIrO}_3$  (SIO). SIO is specially suitable for this subject not only due to its inherent high SOC (which arises from the  $5d$  heavy element iridium), but also due to its semimetallic nature and easy tuning of physical properties *via* electron correlation effects [232]. Single-crystal (100)- $\text{SrTiO}_3$  (STO) is used as the substrate and, contrary to the LMO sample from the previous part, all films are deposited by means of RF magnetron sputtering. The spin injection capability of LSMO has been demonstrated over the years in systems as diverse as LSMO/Pt [233, 234, 235], LSMO/ $\text{SrRuO}_3$  [164, 236], LSMO/ $\text{LaNiO}_3/\text{SrRuO}_3$  [237], and LSMO/ $\text{C}_{60}/\text{Co}$  [238]. On the other hand, SIO has just recently begun to attract interest regarding its role as spin-to-charge converter. Regarding to this, it has been investigated in systems such as Py/SIO [239, 240] and even LSMO/SIO [241, 242]. However, as far as we know, a clean and systematic measurement of spin pumping induced ISHE voltage

in LSMO/SIO bilayers has not been realized before. It is the object of this part to achieve this goal.

Prior to the deposition of the SIO capping layers, however, it is of the utmost importance to certify the suitability of our LSMO films as effective spin injectors. In this way, we first use Pt as the capping film instead of SIO since its feasibility as spin-to-charge converter was widely demonstrated in Py/Pt (see Chapter 4) and LMO/Pt (see Section 5.1), as well as in reported experiments from several groups [233, 234, 235], as has been mentioned. Additionally, this first result will allow us to compare the spin injection properties of the LSMO film with those from Py and LMO.

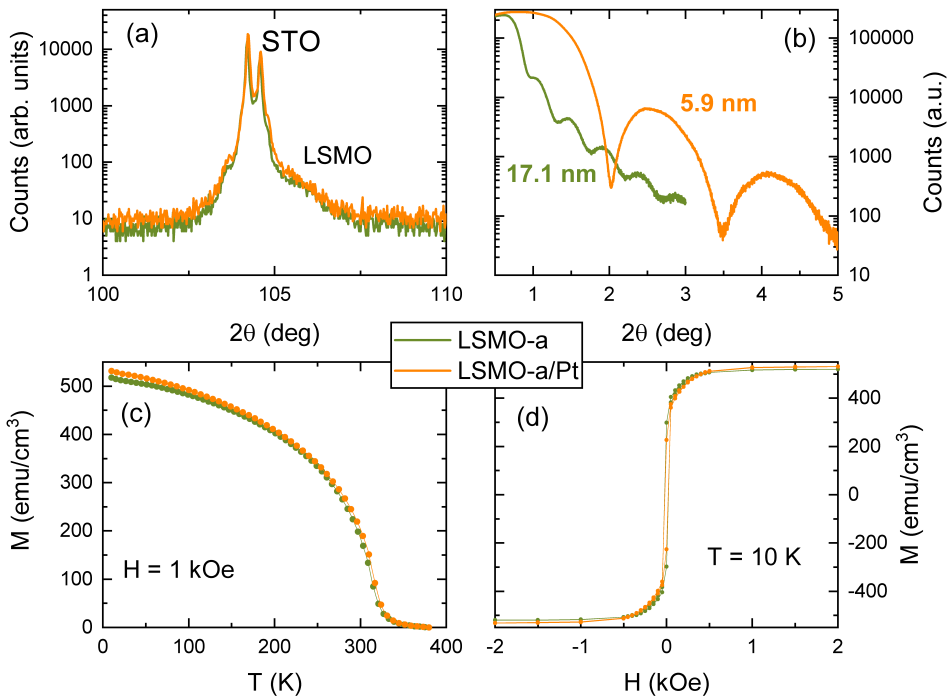


Figure 5.27: a)  $\theta - 2\theta$  scan of the STO-(004) reflection. b) X-ray reflectivity curves showing the calculated thickness of each film (17.1 nm for LSMO and 5.9 nm for Pt). c) Magnetization *vs* temperature curves with the magnetic field applied in-plane. d) Magnetization hysteresis loops at 10K. Figures show the results for the system before the Pt deposition (green lines) and after the Pt deposition (orange lines).

A LSMO film (labelled as LSMO-a) was deposited on top of a STO substrate by means of RF magnetron sputtering. The film was grown at 900°C and 140 mTorr of pressure in an Ar-O<sub>2</sub> atmosphere for 25 min. Then, an one-hour thermal treatment at 900°C in high-pressure oxygen atmosphere was applied. Moreover, the Pt capping

layer was deposited *Ex situ* at room temperature and 5 mTorr in Ar-H<sub>2</sub> atmosphere for 1 minute. The X-ray diffraction (XRD) characterization (Siemens D5000 diffractometer) and the magnetic properties (by SQUID, MPMS-XL by Quantum Design) of the LSMO-a film before and after the Pt deposition are shown in Fig. 5.27. As can be observed from the X-ray reflectivity (XRR) curves in Fig. 5.27b, the thickness of the LSMO-a film is 17.1 nm, while that of the Pt is 5.9 nm. It is worth noting that the XRR orange curve in Fig. 5.27b corresponds to the XRR measurement of the overall LSMO-a/Pt bilayer, but since the Pt contribution completely dominates it, it is easy to discern its thickness. Additionally, its magnetic properties before and after the Pt deposition are depicted in Figs. 5.27c and 5.27d. It is observed from these figures that the film presents a high  $T_c$  ( $\approx 310\text{K}$ ) and a saturation magnetization at 10K of  $\approx 550\text{ emu/cm}^3$ .

In addition, the surface of the sample was mapped by scanning electron microscopy (SEM). Moreover, the reciprocal space maps (RSM) of the (103)<sub>STO</sub> peak reveals that the LSMO-a film is fully strained on top of the substrate. These measurements are shown in Fig. 5.28. The characteristic twins formed at the surface of LSMO films when deposited on top of STO [243, 244] are clearly appreciated in the SEM image of the LSMO-a/Pt surface (see Fig. 5.28a). This observation indicates that the Pt capping layer is continuous and flat and, as such, perfectly follows the LSMO surface structure underneath.

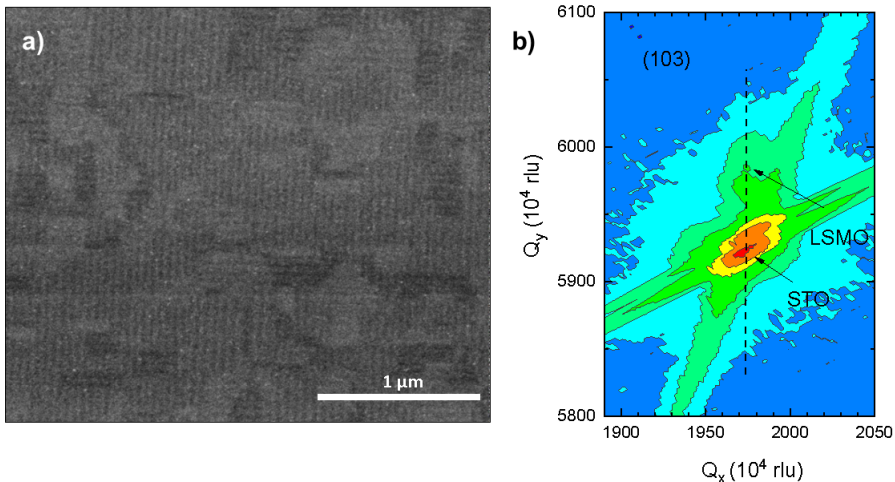


Figure 5.28: a) Scanning electron microscopy (SEM) image of the surface of the LSMO-a/Pt bilayer. The characteristic LSMO twins are clearly appreciated. b) reciprocal space map (RSM) of the (103)<sub>STO</sub> peak revealing in-plane compressive strain in the film.

### 5.2.2 Magnetodynamical Properties of $\text{La}_{2/3}\text{Sr}_{1/3}\text{MnO}_3/\text{Pt}$

Now that the LSMO-a/Pt bilayer structural and magnetic properties are characterized, we can address the main goal of this section, i.e., to probe the injection of spin currents from an LSMO film into Pt. For doing so, we follow the methodology described in section 5.1 for studying the LMO/Pt system. In this way, FMR spectroscopy (NanOsc) is used for i) extracting the main parameters which govern magnetization dynamics; and ii) generating and injecting spin currents in the Pt. The sample holder used in this case is the same as in the previous measurements (“CPW PPMS IP ISHE” model [155] from NanOsc). Likewise, this injected spin current is detected *via* ISHE occurring in the Pt capping layer. The electrical detection of the transverse charge current generated is carried out by an external nanovoltmeter (Keithley 2128A). We start by presenting the magnetodynamical properties of the system.

The FMR spectral curves at each resonance frequency  $f_{\text{res}}$  as a function of the magnetic field are shown in Fig. 5.29. The measurement was performed at 250K. The resonance field  $H_{\text{res}}$  and linewidth  $\Delta H$  of each individual FMR absorption curve were obtained by fitting each curve according to Eq. 4.2 from Chapter 4. In Fig. 5.30 the dependence of these two quantities on  $f_{\text{res}}$  is shown and, as can be observed, the  $H_{\text{res}}$  vs  $f_{\text{res}}$  curve (Fig. 5.30a) exactly follows the relation set by Kittel’s equation (Eq. 5.1). On the other hand, the relation between  $\Delta H$  and  $f_{\text{res}}$  (Fig. 5.30b) is clearly non-linear, specially at high frequencies ( $f_{\text{res}} > 10$  GHz) where  $\Delta H$  saturates at about 70 Oe. As is discussed in the previous section when studying the magnetodynamical properties of the LMO/Pt system, the observed non-linearity in this kind of curves could arise from extrinsic relaxation mechanisms originating in the film or at the film interfaces. In fact, it has been reported that two-magnon scattering mechanisms are quite common in LSMO thin films [235, 236].

In order to gain insight into this phenomenon, the main magnetodynamical parameters of the system were obtained from the fitting of the curves (dashed lines) in Fig. 5.30. It is worth noticing that the  $\Delta H$  vs  $f_{\text{res}}$  curve is only fitted in the linear, low-frequency regime. The resulting magnetodynamical parameters of the system are compiled in Table 5.3. As can be seen, in order to obtain a proper fit in Fig. 5.30a, the second order surface/interface and fourth-fold in-plane anisotropy fields, namely  $H_2$  and  $H_4$ , respectively, must be taken into consideration. A similar situation is also observed in the LMO/Pt system at the same temperature (see Table 5.2). In fact, by comparing those previous values with the ones presented here, one finds that the sign and magnitude of each anisotropy field in both cases is very similar as well. It is important to recall that a negative  $H_2$  anisotropy field means that it favours the in-plane alignment of the magnetization. In the LMO/Pt sample, it was inferred that the large negative surface/interface anisotropy field  $H_2$  found in the sample before

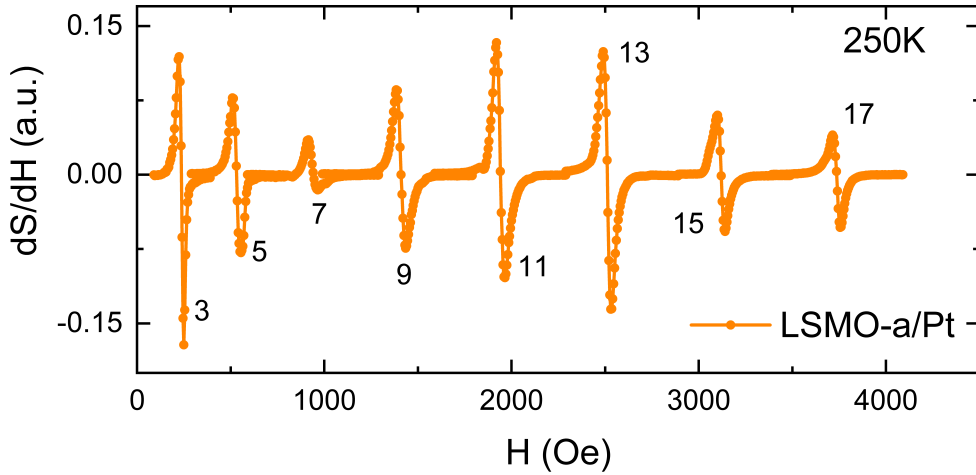


Figure 5.29: FMR spectra as a function of the applied magnetic field at each resonance frequency and at 250K. The number at each resonance line denote the corresponding resonance frequency.

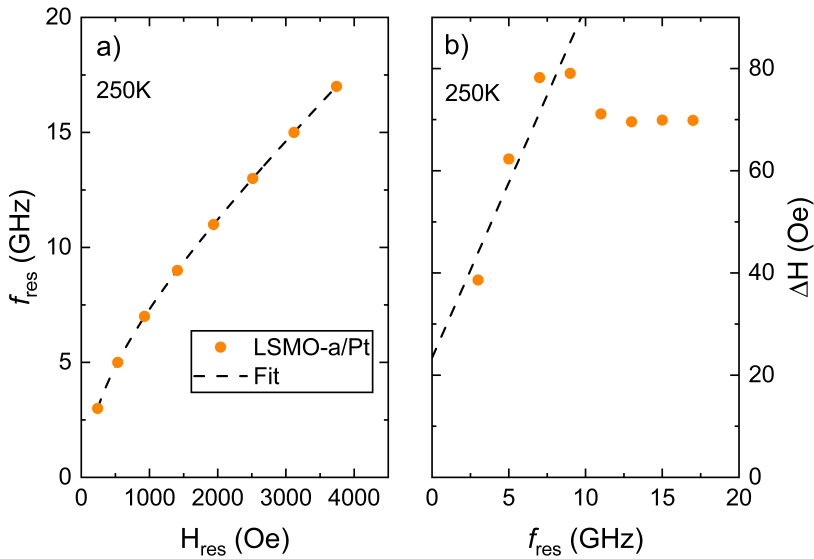


Figure 5.30: a) Resonance frequency  $f_{\text{res}}$  dependence on the resonance field  $H_{\text{res}}$  and fitted according to Eq. 5.1. b) Resonance linewidth  $\Delta H$  dependence on  $f_{\text{res}}$  showing a clearly non-linear dependence for higher frequencies. The fitting has been performed in the linear regime using Eq. 4.4 from Chapter 4.

and after the Pt deposition arose from the large Ti diffusion layer in the STO// LMO interface. It was further stated that the effect of large anisotropy at this interface

is the pinning of the local magnetization, resulting in the hampering of spin precession near the interface. As a consequence of that, non-vanishing secondary spin wave modes may arise and couple to the external magnetic field, giving rise to an enhancement of  $\Delta H$  or to the appearance of secondary peaks besides the fundamental one [83]. In the present case, the current experimental evidence supports this hypothesis, unfortunately, the information about the structure and chemical composition of the STO// LSMO-a/Pt sample interfaces is still lacking. In order to clarify the origin of this large anisotropy field, additional STEM and EELS chemical analysis are needed.

Table 5.3: Main magnetodynamical parameters obtained from the fitting of FMR spectra at 250K. Each value is accompanied by its own standard deviation. It is important to notice that  $H_2 \equiv 2K_2/M_s$  and  $H_4 \equiv 2K_4/M_s$  are the anisotropy fields. The saturation magnetization value  $M_s$  is taken as a fixed, imposed value for the fitting process.

Sample	$M_s$ (emu/cm <sup>3</sup> )	$\mu_0 H_2$ (mT)	$\mu_0 H_4$ (mT)	$\gamma/2\pi$ (GHz/T)	$\alpha_{\text{eff}}$ ( $\times 10^{-3}$ )	$\Delta H(0)$ (Oe)
LSMO-b/Pt	318.30 (fixed)	$-237.9 \pm 7.0$	$-6.34 \pm 1.5$	$27.97 \pm 0.11$	$4.8 \pm 1$	$23.4 \pm 12$

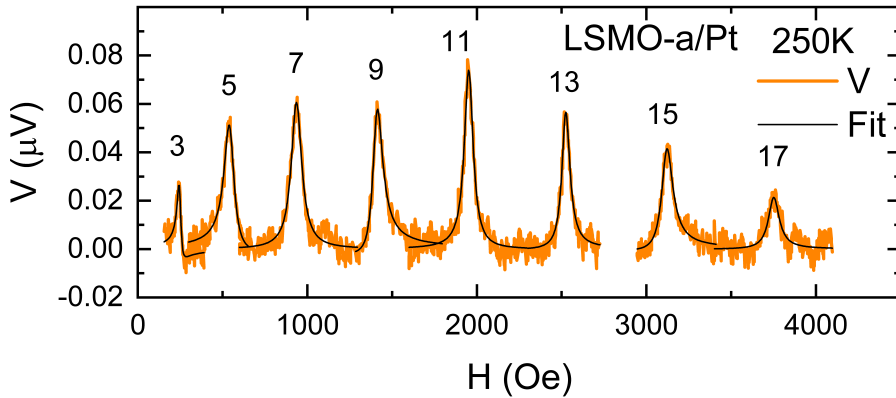


Figure 5.31: Voltage signal lines as a function of the applied magnetic field at each resonance frequency and at 250K. The number at each resonance line denote the corresponding resonance frequency, while the fitting of each signal has been performed according to Eq. 4.9

The voltage signal lines of the LSMO-a/Pt bilayer at 250K are shown in Fig. 5.31. As can be observed in the figure, the obtained voltage signal lines are very similar to those measured in section 5.1 for the LMO/Pt system (see Fig. 5.21), meaning that they are i) symmetric; ii) positive; and iii) almost identical in magnitude. On top of that, it is important to consider that the electric transport properties of LMO and LSMO films are very similar to each other. In this way, we can be confident that, just as in the LMO/Pt bilayer, the voltage contribution of the SRE is mild compared to that from ISHE. In addition to that, in order to evaluate the contributions coming from thermoelectric effects, a 7 GHz voltage measurement with the direction of the magnetic field reversed is performed and the obtained result is shown in Fig. 5.32.

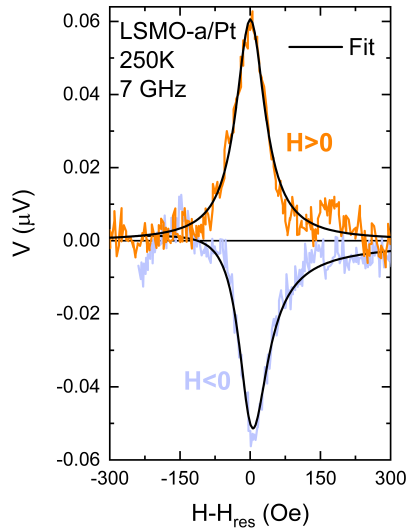


Figure 5.32: Voltage signals at  $f_{\text{res}} = 7\text{ GHz}$  and at  $250\text{K}$  under field inversion.

As can be observed, the voltage signals oppose each other while their magnitudes remain the same, being the small difference attributed to the experimental error. Consequently, we can be confident and conclude that the main contribution to the LSMO-a/Pt voltage signal lines observed in Fig. 5.31b comes from ISHE, being the effects from spin rectification and temperature negligible in this system.

## Spin Hall Angle

Just as in the previous systems, the spin Hall angle  $\Theta_{\text{SH}}$  for the LSMO-a/Pt sample is calculated according to Eq. 4.17. Again, the spin diffusion length is fixed to  $\lambda_{\text{sd}} = 3\text{ nm}$  since this system presents similar values of resistivity as in the LMO/Pt system. However, it should be clarified by experiments in the future for better results. The difference in damping before and after the Pt deposition process was calculated by considering the damping value of the LSMO-d single-film from Section 5.2.3<sup>2</sup> (see Table 5.5). So, the resulting  $250\text{K}$   $\Theta_{\text{SH}}$  as a function of the resonance frequency is shown in Fig. 5.33. It is worth noting the scattering of points and the error in the high-frequency values, which is reflected in the standard deviation (orange region in Fig. 5.33). The resulting mean spin Hall angle at  $250\text{K}$  is  $\Theta_{\text{SH}} = 0.79 \pm 0.34\%$ , which

<sup>2</sup>It is worth mentioning that although the LSMO-d film thickness is different than the one considered here (i.e.,  $12.8\text{ nm}$  in front of the  $17.1\text{ nm}$  of the LSMO-a film) the measured damping does not change. This was confirmed by measuring the damping of an equivalent LSMO single-film of  $17\text{ nm}$ , but it is not shown here for simplicity.



is, within the experimental error, similar to that obtained in Py/Pt from Chapter 4 and to reported values in similar LSMO/Pt systems [245].

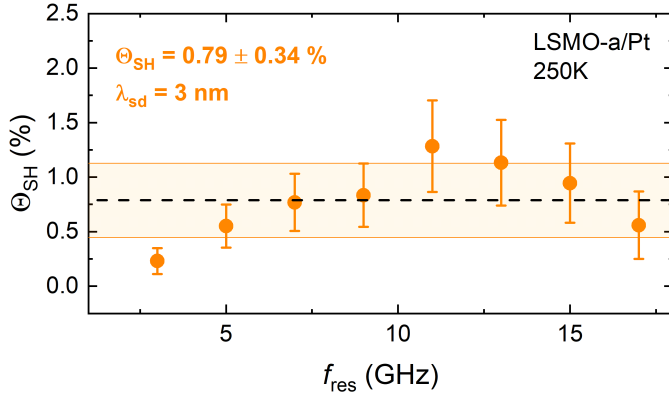


Figure 5.33: Spin Hall angle  $\Theta_{\text{SH}}$  value estimated according to Eq. 4.17. The dashed line and colored region correspond to its mean and standard deviation, respectively. The parameters used for the calculation are:  $w = 200 \mu\text{m}$ ;  $\mu_0 h_{\text{rf}} = 50 \mu\text{T}$ ;  $G_{\text{eff}}^{\uparrow\downarrow} = 1.53 \times 10^{19} \text{ m}^{-2}$ ; and  $\lambda_{\text{sd}} = 3 \text{ nm}$ .

In this first section, we demonstrate the high-quality spin injection capabilities of the LSMO in contact with Pt. It is the topic of the next section to probe the spin-to-charge conversion efficiency of SIO in LSMO/SIO bilayers.

### 5.2.3 Spin to Charge Conversion in $\text{La}_{2/3}\text{Sr}_{1/3}\text{MnO}_3/\text{SrIrO}_3$ Bilayers

As is previously seen, spin injection processes in FM/NM heterostructures depend on the quality of interfaces that modulate the interface mixing conductance. Thus, one way to influence the spin injection processes is by modifying the interface. With this objective in mind, in this section we prepare samples of the LSMO/SIO system with different interfaces. Specifically, two distinct LSMO/SIO samples on top of STO substrates were prepared. The difference between these two samples strives in the fact that one has the SIO deposited *Ex situ*, while in the other one the SIO is deposited *In situ*. Therefore, presumably the LSMO/SIO interface will be clearly different. In both cases, the deposition conditions of the LSMO and SIO films are completely equal. The growth conditions of the LSMO films are exactly the same as those described in the previous section, i.e., growth at  $900^\circ\text{C}$  and 140 mTorr of pressure in Ar- $\text{O}_2$  atmosphere for 25 min, followed by a thermal treatment at  $900^\circ\text{C}$  in high-pressure oxygen atmosphere for one hour. The SIO was also deposited at  $900^\circ\text{C}$ , but at a relatively lower pressure (110 mTorr) in  $\text{O}_2$  atmosphere for 20 min. In addition, no thermal treatment was applied at the end of the deposition. For simplicity, the

sample in which the SIO capping film was deposited *Ex situ* is labelled as LSMO-b/SIO, while the other one is called LSMO/SIO-c. The XRD characterization and magnetic properties of these two samples are shown in Fig. 5.34. The similarities between these samples and the LSMO-a/Pt one are clear. The SIO (004) peak in the  $\theta - 2\theta$  scans is appreciated in both samples (see Fig. 5.34a). The LSMO thickness is 15.4 nm in the LSMO-b/SIO sample, as determined from the XRR curve of the LSMO-b film (i.e., before the SIO deposition), which corresponds to the dark blue curve in Fig. 5.34b. On the other hand, since the XRR curve of the LSMO/SIO-c sample is a superposition of both LSMO and SIO contributions (see the red curve in Fig. 5.34b), it is difficult to disentangle the thickness of each film separately. In order to overcome this issue, the XRR curve of each bilayer was simulated by means of the *xrayutilities* package from Python [246]. The resulting fitted curves correspond to the black dashed lines in Fig. 5.34b. The outcome of this simulation is that the thickness of the LSMO film in the LSMO/SIO-c sample is 14.02 nm, whereas the thickness of the SIO capping layer is 9.6 nm in the LSMO-b/SIO sample and 10.1 nm in the LSMO/SIO-c sample. However, in order to check the validity of this result, an additional SIO film was prepared on top of STO for calibration. The deposition conditions and deposition time of this film are exactly the same as the ones from LSMO-b/SIO and LSMO/SIO-c. Its XRD characterization, including the XRR measurement, are shown in Fig. 5.35. The XRR curve of this calibration film gives a thickness of 9 nm, which is in accordance with the simulated curves.

The SQUID magnetic characterization of the films is included in Figs. 5.34c and 5.34d. As can be observed, the  $T_c$  is about 310K (just as in the LSMO-a/Pt sample), while the saturation magnetization at 10K of the LSMO-b/SIO sample is about 525 emu/cm<sup>3</sup>, whereas that of LSMO/SIO-c is only 460 emu/cm<sup>3</sup>. This difference may have a component of uncertainty arising from a bad estimation of the LSMO thickness in the LSMO/SIO-c sample. Nevertheless, regardless of the absolute value of magnetization, the magnetic behaviour of both samples is almost identical.

The SEM images of the SIO surface in both systems as well as their respective RSM are shown in Fig. 5.36. As can be observed from the SEM images in Figs. 5.36a and 5.36b, the surface morphology in each sample is very different. In Fig. 5.36a, which corresponds to the LSMO-b/SIO sample, the characteristic LSMO twins are clearly appreciated and the surface in general resembles that of the LSMO-b/Pt sample (see Fig. 5.28a). This observation indicates that the SIO film is flat and continuous, and follows the LSMO-b surface structure underneath. Conversely, the surface depicted in Fig. 5.36b, which corresponds to the LSMO/SIO-c sample, presents randomly scattered clusters of square-shaped structures on top of the LSMO surface (the twins of which can be observed underneath). On the other hand, the RSM of the (103)<sub>STO</sub> peak reveals that the LSMO/SIO-c sample is fully strained on top of the STO substrate (Fig. 5.36d), while the SIO peak in the LSMO-b/SIO sample is

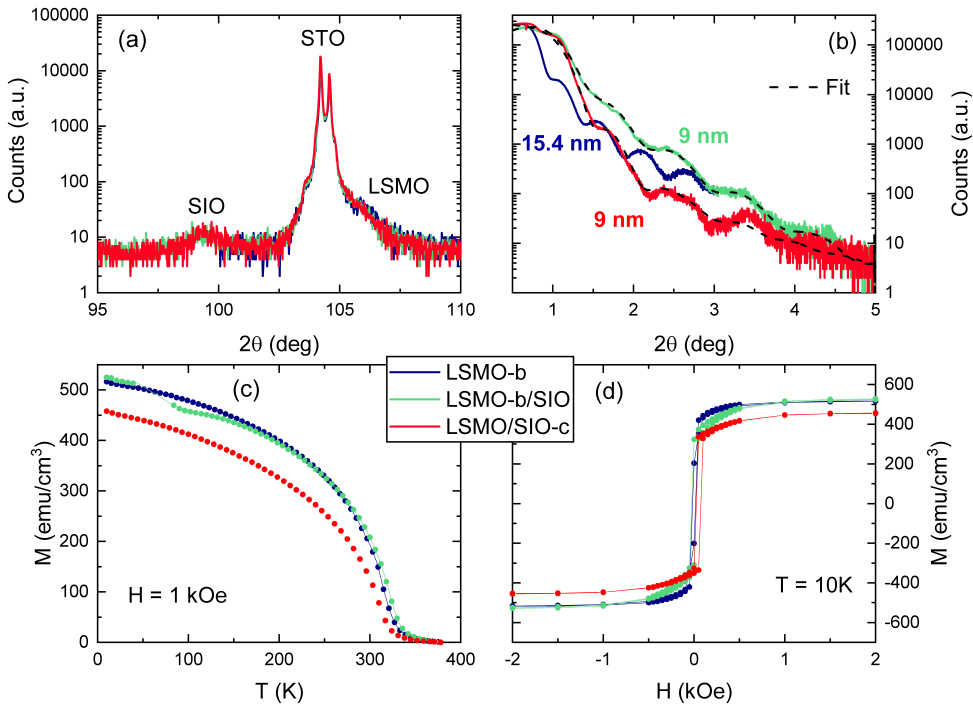


Figure 5.34: a)  $\theta - 2\theta$  scan of the STO-(004) reflection. b) X-ray reflectivity curves showing the calculated thickness of each film. The black dashed lines correspond to the simulation performed by the *xrayutilities* package from Python. In overall, the thickness of the LSMO film is 15.4 nm in the LSMO-b/SIO sample and 14.02 nm in the LSMO/SIO-c sample. While that of SIO is 9.6 nm in the LSMO-b/SIO sample and 10.1 nm in the LSMO/SIO-c sample. c) Magnetization *vs* temperature curves with the magnetic field applied in-plane. d) Magnetization hysteresis loops at 10K.

slightly displaced to the right with respect to the STO and LSMO peaks (Fig. 5.36c)

The FMR spectral curves at each resonance frequency  $f_{\text{res}}$  as a function of the magnetic field are shown in Fig. 5.37. The measurement was performed at 250K. The resonance field  $H_{\text{res}}$  and linewidth  $\Delta H$  of each FMR absorption curve was obtained by fitting each FMR curve according to Eq. 4.2 from Chapter 4. The  $f_{\text{res}}$  dependence on  $H_{\text{res}}$  is shown in Fig. 5.38a, while the  $f_{\text{res}}$  dependence on  $\Delta H$  is depicted in 5.38b. As can be observed from Fig. 5.38a, the LSMO/SIO-c sample resonates at slightly larger magnetic fields than LSMO-b/SIO. This difference may be attributed to a smaller value of magnetization in the former case, which would be in accordance with the magnetic characterization results presented in Figs. 5.34c and 5.34d. Nevertheless, the shift-to-the-right observed in Fig. 5.38a is too small to explain the difference in magnetization from SQUID measurements. This may suggest that there has been

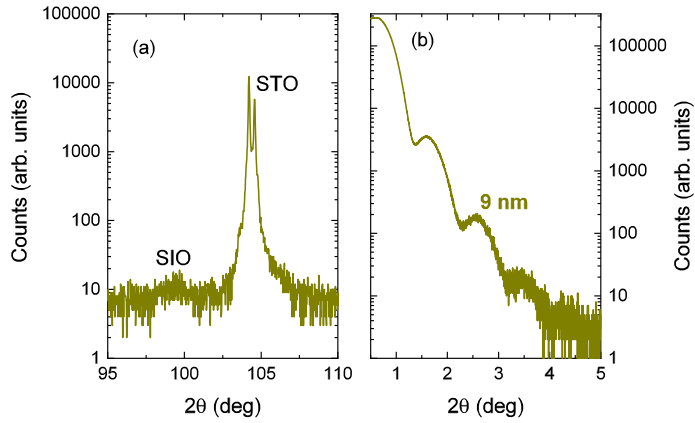


Figure 5.35: a)  $\theta - 2\theta$  scan of the STO-(004) reflection. b) X-ray reflectivity curve showing the calculated thickness of the calibration SIO film (9 nm)

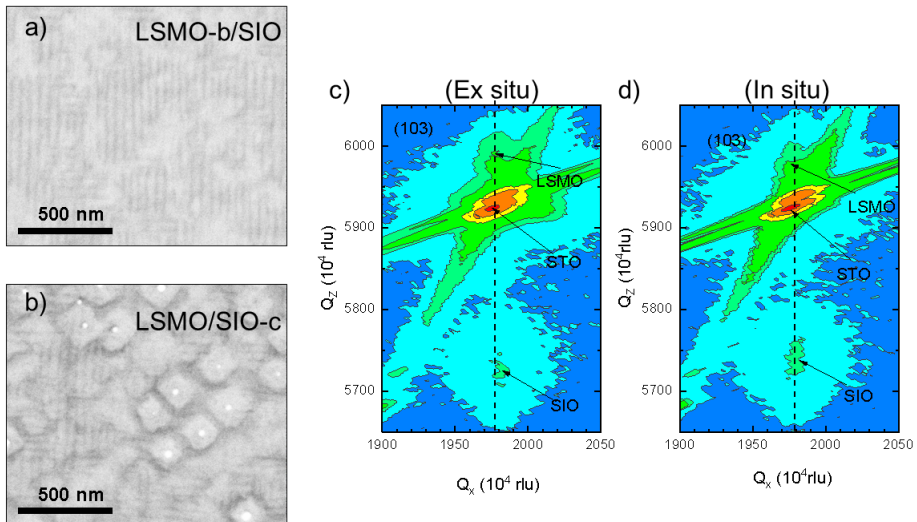


Figure 5.36: a) SEM image of the surface from the LSMO-b/SIO sample. b) SEM image of the surface from the LSMO/SIO-c sample. c) RSM of the (103)<sub>STO</sub> peak of the LSMO-b/SIO sample. d) RSM of the (103)<sub>STO</sub> peak of the LSMO/SIO-c sample.

an overestimation of the LSMO thickness value in the LSMO/SIO-c sample and that the real value may be actually lower than 14 nm. Moreover, the  $\Delta H$  dependence on  $f_{\text{res}}$  (see Fig. 5.38b) is different in each sample. This difference indicates that the overall magnetic relaxation mechanisms and even the spin transport properties of the LSMO/SIO interface are different. On top of that, it can be observed that the

resonance linewidths of the LSMO/SIO-c sample are consistently larger than the ones from the LSMO-b/SIO sample in the whole range of frequencies studied. This feature could be related with the square-shaped structures *only* observed at the LSMO/SIO-c surface (see Fig. 5.36b), which could be viewed as the result of some sort of granular growth. In this picture, the structure-to-structure boundaries (or *grain boundaries*) would act as additional scattering centers for magnetic relaxation, thus enhancing  $\Delta H$  [247]. Furthermore, regarding the linear dependence between  $\Delta H$  and  $f_{\text{res}}$ , it can be observed that in the case of the LSMO/SIO-c sample this dependence is loosely linear. On the other hand, in the LSMO-b/SIO sample, the linear relation is completely lost for  $f_{\text{res}} > 10$  GHz, exactly like in the LSMO-a/Pt sample. Nevertheless, while in the latter, for  $f_{\text{res}} > 10$  GHz,  $\Delta H$  reached and maintained a constant value of 70 Oe, in the LSMO-b/SIO sample the  $\Delta H$  dependence with frequency above 10 GHz is more disperse and vague, oscillating around 150 Oe.

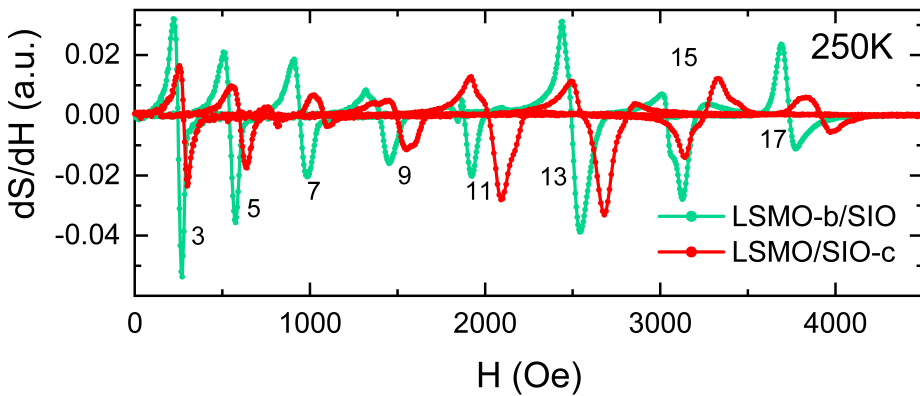


Figure 5.37: FMR curves of both samples at 250K as a function of the magnetic field and at each frequency.

The main magnetodynamical parameters obtained from the fits in Fig. 5.38 (see the dashed lines) are compiled in Table 5.4. It should be noted that, in both samples, the saturation magnetization  $M_s$  has been fixed using the value obtained by SQUID magnetometry (see Fig. 5.34c). As has been mentioned, however, the  $M_s$  from the LSMO/SIO-c sample is underestimated due to the overestimation of the LSMO film thickness. Thus, the fact that the surface/interface anisotropy field  $H_2$  enters in the Kittel equation as  $4\pi M_{\text{eff}} = 4\pi M_s - H_2$  (see Eq. 5.1) means that an underestimation of  $M_s$  entails an overestimation of  $H_2$  and vice versa. As a result, the  $H_2$  value of the LSMO/SIO-c sample that appears in Table 5.4 must be read with caution. Despite this, the fitted values are not very different from the ones obtained in the LSMO-a/Pt sample (see Table 5.3) nor from the LMO/Pt system (Table 5.2), as expected owing to their similarities.

Now we move on to present the transverse voltage measurements from LSMO-

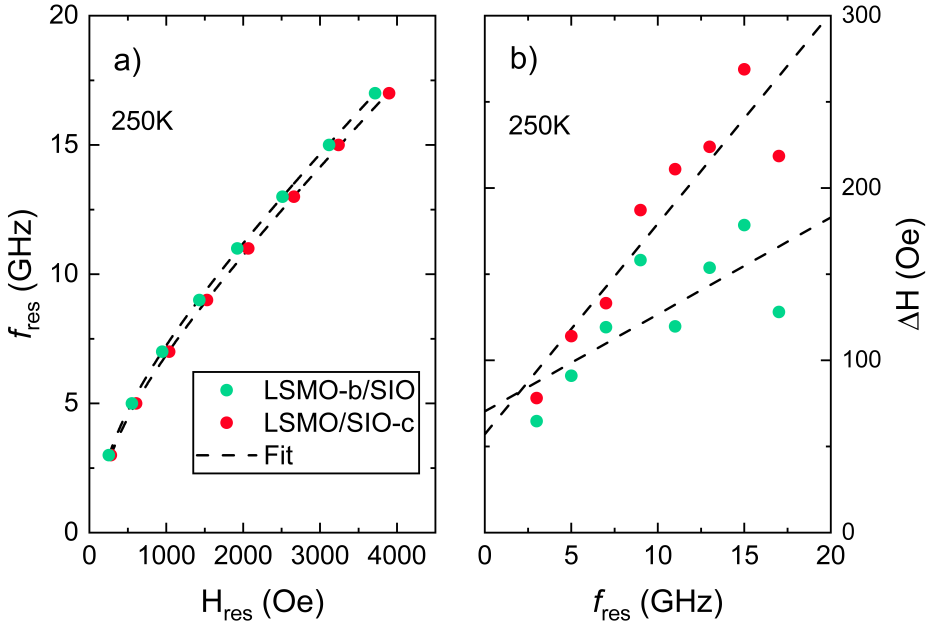


Figure 5.38: a) Resonance frequency  $f_{\text{res}}$  dependence on the resonance field  $H_{\text{res}}$  and fitted according to Eq. 5.1. b) Resonance linewidth  $\Delta H$  dependence on  $f_{\text{res}}$  showing the non-linear dependence followed. The fitting has been performed by using Eq. 4.4 from Chapter 4.

Table 5.4: Main magnetodynamical parameters obtained from the fitting of FMR spectra at 250K. Each value is accompanied by its own standard deviation. It is important to notice that  $H_2 \equiv 2K_2/M_s$  and  $H_4 \equiv 2K_4/M_s$  are the anisotropy fields. The saturation magnetization value  $M_s$  is taken as a fixed, imposed value for the fitting process.

Sample	$M_s$ (emu/cm <sup>3</sup> )	$\mu_0 H_2$ (mT)	$\mu_0 H_4$ (mT)	$\gamma/2\pi$ (GHz/T)	$\alpha_{\text{eff}}$ ( $\times 10^{-3}$ )	$\Delta H(0)$ (Oe)
LSMO-b/SIO	326.27 (fixed)	$-184 \pm 8$	$-7.7 \pm 1.5$	$28.77 \pm 0.5$	$4.1 \pm 1.5$	$70.4 \pm 22.7$
LSMO/SIO-c	255.73 (fixed)	$-192 \pm 3$	$-8.15 \pm 0.8$	$29.21 \pm 0.4$	$8.9 \pm 1.5$	$57.1 \pm 22.3$

b/SIO and LSMO/SIO-c samples. The 250K voltage signal lines at each frequency as a function of the magnetic field are shown in Fig. 5.39. The first striking feature in these measurements is that the voltage lines are only observed at some resonance frequencies (the missing voltage curves are not included for the sake of clarity). A concise explanation of why are there missing frequencies is difficult to make, but it may be related with the fact that the actual magnitude of the voltage signals (i.e., peak maximum) is close to the detection limit of the equipment ( $\approx 0.01 \mu\text{V}$ ). In addition to this, it may as well be noted that the resistivity of SIO is larger than the one from Pt, for instance, and that may hamper the electrical contact quality between the sample itself and the sample holder, resulting in noisier measurements.

On top of that, it is important to recall that, as far as we know, the voltage signal has a non-monotonic dependence on the resonance frequency, so there may possibly be voltage signals the magnitude of which is lower than the detection limit of the equipment. In overall, we believe that a combination of these three situations could explain why some of the voltage lines are missing in the first place.

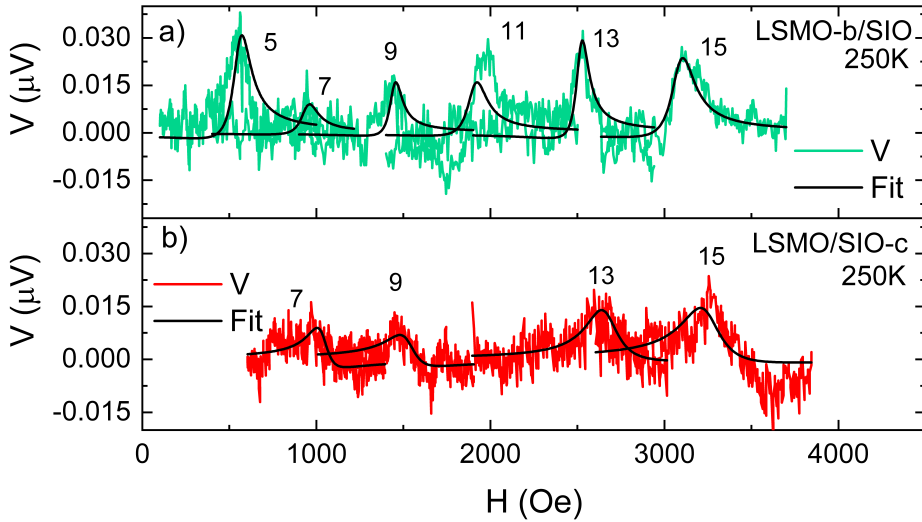


Figure 5.39: Voltage signal lines as a function of the applied magnetic field at each resonance frequency and at 250K. The number at each resonance line denote the corresponding resonance frequency, while the fitting of each signal has been performed according to Eq. 4.9

With respect to the actual measured voltage signal lines in both samples, it is found that they are all positive, just as in the previous samples where ISHE was measured. However, as mentioned earlier, the magnitude of the signals is close to the detection limit of the equipment, thus the noise of the measurement becomes an important source of error, making it impossible to discern the relative weight of symmetric and antisymmetric contributions. This is more evident in the voltage signal lines of the LSMO/SIO-c sample (see Fig. 5.39b). Despite this, just as in the previous samples, the voltage signal was measured by reversing the magnetic field direction in order to evaluate the possible thermoelectric effects contributions. These results are shown in Fig. 5.40. As can be observed from Fig. 5.40a, which corresponds to the results of the LSMO-b/SIO sample, the positive and negative voltage signals are very different from each other. Specifically, the voltage signals at 7 GHz do actually have opposite signs but their magnitude and lineshape are different. A similar situation is also found for the 13 GHz voltage lines, in which we were unable to realise a proper fit on the negative 13 GHz voltage line. Moreover, in Fig. 5.40b, the positive and negative voltage signals of the LSMO/SIO-c sample are very similar but highly embedded in noise.

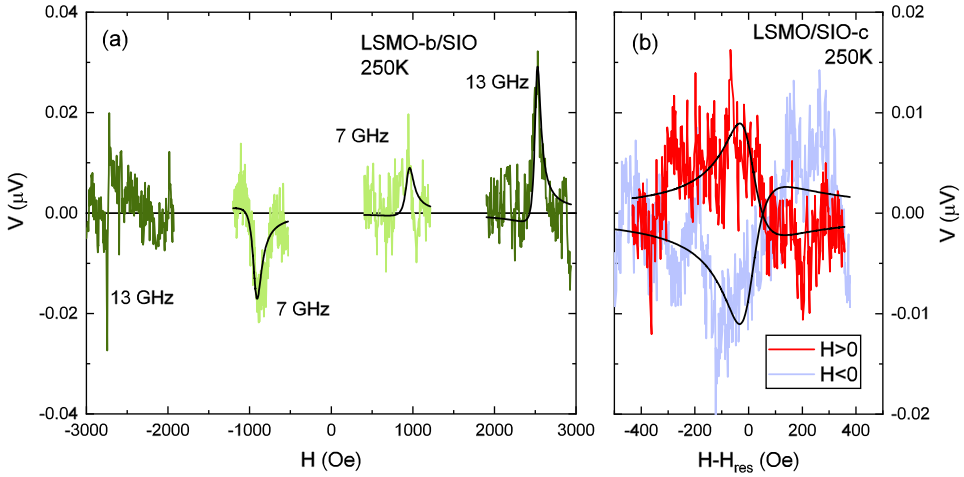


Figure 5.40: a) Voltage signals of the LSMO-b/SIO sample at  $f_{\text{res}} = 7$  GHz and  $f_{\text{res}} = 13$  GHz and at 250K under field inversion. b) Voltage signals of the LSMO/SIO-c sample at  $f_{\text{res}} = 7$  GHz and at 250K under field inversion. The fitting of each signal (black lines) has been performed according to Eq. 4.9

Consequently, by looking at these results (Figs. 5.39 and 5.40), we are unable to unambiguously conclude that ISHE is the main contribution to the voltage measurements observed. We identify the small magnitude of the voltage signals as the main problem, since in this regime the detection limit of the equipment and the actual voltage signals are of the same order of magnitude. As a result, the current experimental goal is to obtain LSMO/SIO bilayers in which the ISHE voltage signal increases. For doing so, we did prepare yet another STO// LSMO/SIO sample with the SIO deposited *Ex situ*. The deposition conditions of both LSMO and SIO films are the same as in the previous samples. However, we changed the deposition time. In the new sample, the LSMO film did grow for 20 min (instead of the 25 min employed in the old samples), whereas the SIO capping layer did grow for 11 min (instead of 20 min). This did obviously result in thinner films. This decision follows directly from Eq. 5.2, in which the dependence of the ISHE voltage signal on different parameters is specified. In this case, a thinner LSMO film should result in an increased difference of damping (see Eq. 4.6), while a thinner SIO will presumably shorten the difference between  $t_{\text{SIO}}$  and  $\lambda_{\text{sd}}$ , being  $t_{\text{SIO}}$  and  $\lambda_{\text{sd}}$  the thickness and spin diffusion length of SIO, respectively. The overall resistance of the bilayer should increase as well. In overall, according to Eq. 5.2, these changes should result in an increased ISHE voltage signal. For simplicity, we label this sample as LSMO-d/SIO. The remaining part of this section is devoted to presenting the characterization and voltage measurements of this new sample.



In Fig. 5.41, the XRD and magnetic characterization of the LSMO-d/SIO sample is shown. As can be observed from Fig. 5.41b, the thickness of the LSMO-d film is about 12.8 nm. On the other hand, the thickness of the SIO capping layer is estimated to be around 5 nm. This thickness was estimated from the growth rate established from the calibration SIO film (see Fig. 5.35b). The magnetic characterization of the sample (Figs. 5.41c and 5.41d) shows that the  $T_c$  of the sample is 290K, while its saturation magnetization at  $T = 10\text{K}$  is about  $420 \text{ emu/cm}^3$ . Compared with the preceding samples, both  $T_c$  and saturation magnetization are lower. This may simply be related with the reduction of the LSMO thickness, as pointed out by some authors [211]. In either case, the sample presents robust ferromagnetic order and very low coercive field. Additionally, the SEM image of the LSMO-d/SIO surface is shown in Fig. 5.42. As can be observed, the characteristic LSMO twins are clearly appreciated, thus indicating that the SIO film is flat and continuous. Unlike in the previous samples, the RSM of this sample was not measured.

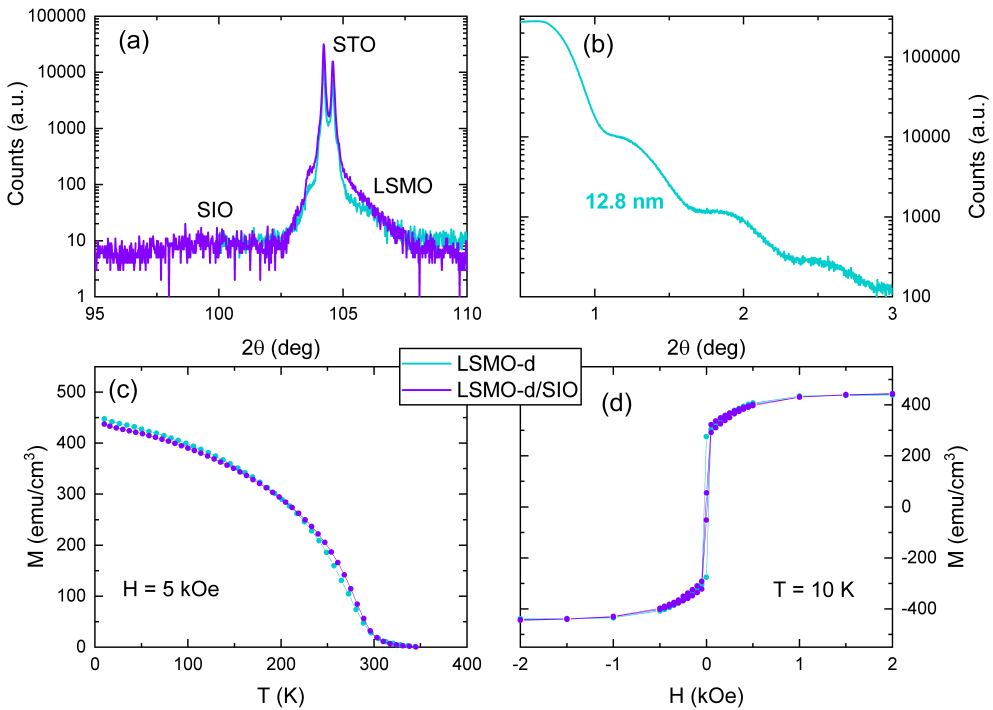


Figure 5.41: a)  $\theta - 2\theta$  scan of the STO-(004) reflection of the sample before and after the SIO deposition. b) X-ray reflectivity curve showing the calculated thickness of the LSMO-d film (12.8 nm). c) Magnetization *vs* temperature curves with the magnetic field applied in-plane. d) Magnetization hysteresis loops at 10K. Figures show the results for the system before the SIO deposition (light blue lines) and after the SIO deposition (purple lines).

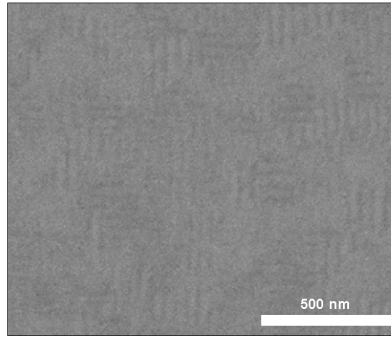


Figure 5.42: Scanning electron microscopy (SEM) image of the LSMO-d/SIO sample surface.

Now we move on to present the FMR characterization of the LSMO-d/SIO sample before and after the SIO deposition. The 250K FMR spectra is shown in Fig. 5.43. Each FMR curve was fitted using Eq. 4.2 in order to extract their respective resonance field  $H_{\text{res}}$  and linewidth  $\Delta H$ . The resonance frequency  $f_{\text{res}}$  dependence curves of these quantities for the sample before and after the SIO deposition are shown in Fig. 5.44. It can be observed that the curves in Fig. 5.44a nearly overlap with each other. The small shift to the right after the SIO deposition may be due to a small decrease in the saturation magnetization, but according to the magnetization *vs* temperature curve in Fig. 5.41c, the magnetization of the sample before and after the SIO deposition is almost identical. Therefore, the observed shift must be related with the change of some other quantity. In fact, by fixing the saturation magnetization value and fitting each curve with the Kittel equation (Eq. 5.1), one can see that the surface/interface anisotropy field  $H_2$  in both samples is a bit different (see Table 5.5).

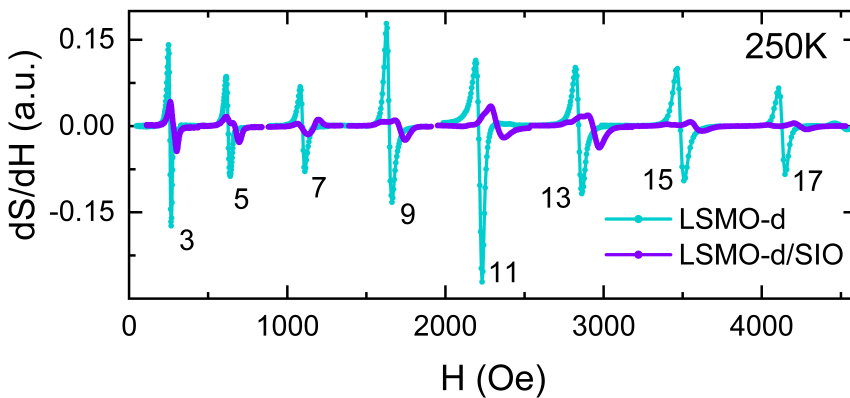


Figure 5.43: FMR spectra as a function of the magnetic field of the LSMO-d/SIO sample before and after SIO deposition. The measurement has been performed at 250K. The numbers beside denote the resonance frequency of each individual absorption line.

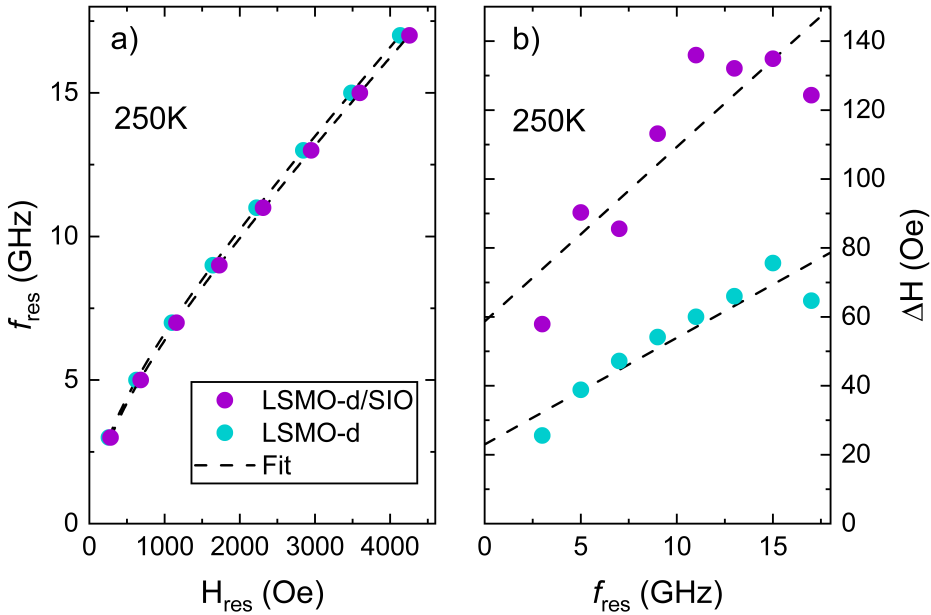


Figure 5.44: a) Resonance frequency dependence on the resonance field for the sample before and after SIO deposition. The fits are made according to Eq. 5.1. b) Resonance linewidth dependence on the resonance frequency for the sample before and after SIO deposition. The fits are made according to Eq. 4.4. Both measurements are performed at 250K.

Moreover, the  $\Delta H$  dependence on  $f_{\text{res}}$  (Fig. 5.44b), shows a general increase of  $\Delta H$  upon SIO deposition in the whole range of frequencies studied, which is translated into an increased Gilbert damping  $\alpha$ : from  $2.2 \times 10^{-3}$  for the LSMO-d film alone to  $3.6 \times 10^{-3}$  for the LSMO-d/SIO bilayer. From the difference in damping the spin mixing conductance of the LSMO-d/SIO bilayer can be estimated (see Eq. 4.6), obtaining a value of  $G_{\text{eff}}^{\uparrow\downarrow} = 4.08 \times 10^{18} \text{ m}^{-2}$ , which is larger than previously reported values in LSMO/SIO systems [241, 242]. The experimental data was fitted according to Eq. 4.4 and the obtained parameters are listed in Table 5.5. In overall, the magnetodynamical properties of the LSMO-d/SIO sample are very similar to those observed in the previous LSMO-a/Pt, LSMO-b/SIO, and LSMO/SIO-c samples. The  $H_2$  anisotropy field has a similar value in all cases, thus suggesting that it arises from the STO//LSMO interface, as discussed before. Nevertheless, a STEM study followed by EELS chemical analysis of these samples (in progress) should clarify the origin of this large anisotropy.

The 250K transverse voltage measurements of this sample are presented in Fig. 5.45. In this case, it can be observed that the average magnitude of the voltage signal lines has increased with respect to the previous LSMO-b/SIO and LSMO/SIO-c

Table 5.5: Main magnetodynamical parameters obtained from the fitting of FMR spectra at 250K. Each value is accompanied by its own standard deviation. It is important to notice that  $H_2 \equiv 2K_2/M_s$  and  $H_4 \equiv 2K_4/M_s$  are the anisotropy fields. The saturation magnetization value  $M_s$  is taken as a fixed, imposed value for the fitting process.

Sample	$M_s$ (emu/cm <sup>3</sup> )	$\mu_0 H_2$ (mT)	$\mu_0 H_4$ (mT)	$\gamma/2\pi$ (GHz/T)	$\alpha$ ( $\times 10^{-3}$ )	$\Delta H(0)$ (Oe)
LSMO-d	183.02 (fixed)	$-230.2 \pm 5.7$	$-2.9 \pm 0.3$	$28.44 \pm 0.1$	$2.2 \pm 0.3$	$23.0 \pm 0.5$
LSMO-d/SIO	183.02 (fixed)	$-194.4 \pm 1.6$	$-3.6 \pm 0.8$	$28.53 \pm 0.2$	$3.6 \pm 0.8$	$58.7 \pm 1.3$

samples. Moreover, contrary to what is observed in these previous measurements, the voltage signals in this case are clearly appreciated in the whole range of frequencies studied. In addition, it should be noted the resemblance between these measurements and the previous results from Py/Pt, LMO/Pt and LSMO-a/Pt. The measured voltage is symmetric and positive, and its magnitude is similar but a bit lower to the one obtained when using Pt as the capping layer. Moreover, just as in the LSMO-a/Pt sample, we presume that the SRE contributions are scarce.

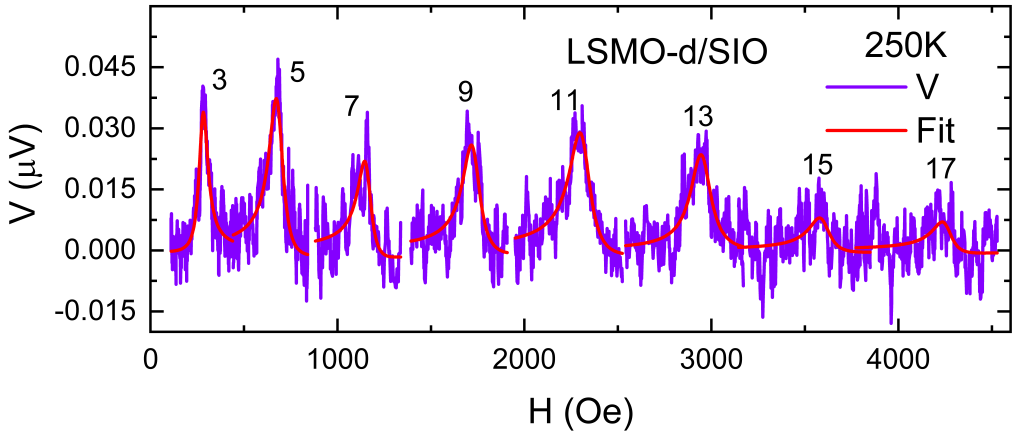


Figure 5.45: Transverse voltage signal lines at 250K of the LSMO-d/SIO sample as a function of the magnetic field. The numbers beside each curve represent the resonance frequency employed.

The voltage signal lines at 5 GHz, 9 GHz, and 13 GHz were measured upon magnetic field inversion in order to evaluate the role of thermoelectric effects in the system. These measurements are shown in Fig. 5.46. Despite the error induced by the experimental noise, it is obvious that the transverse voltage signals completely reverse upon field inversion, and share the same magnitudes (with opposite sign) and lineshapes. Therefore, we can conclude that the transverse voltage signals from Fig. 5.45 are entirely due to ISHE, being the SRE and temperature contributions mild in this case.

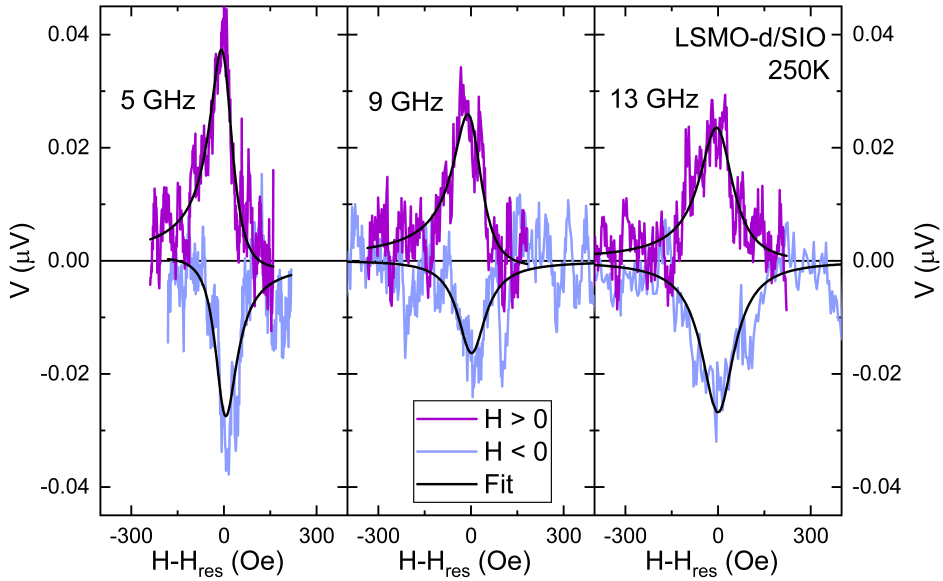


Figure 5.46: Transverse voltage signal lines at 250K of the LSMO-d/SIO sample with the magnetic field direction reversed at 5 GHz, 9 GHz, and 13 GHz. The fitting of each signal (black lines) has been performed according to Eq. 4.9

## Spin Hall Angle

Owing to the quality of these measurements, we can finally estimate the spin Hall angle  $\Theta_{\text{SH}}$  of SIO from the LSMO-d/SIO sample voltage results. For this calculation, a spin diffusion length of about 1 nm (lower than the estimated one for Pt  $\approx 3$  nm) is used, according to previous reports in the literature [240, 241, 242]. The resistance of the sample is taken from Ref. [239], but a careful estimation of actual values in our samples is required for a better quantification of  $\Theta_{\text{SH}}$ . The calculated  $\Theta_{\text{SH}}$  of the LSMO-d/SIO sample at 250K is shown in Fig. 5.47. Again, the points at higher frequencies present large error bars. In average, however, the spin Hall angle of SIO is determined to be  $1.12 \pm 0.45$  %, which is remarkably similar to that obtained for the well-known Py/Pt system, therefore suggesting that SIO could be a good spin-Hall material. This result may be envisioned as a first step towards the development of high-quality spin-to-charge conversion devices based on all-oxide heterostructures.

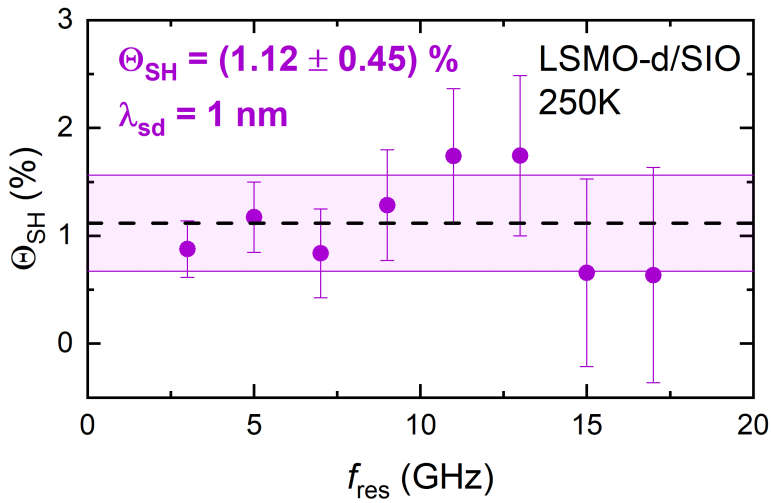


Figure 5.47: Spin Hall angle  $\Theta_{\text{SH}}$  value according to Eq. 4.17. The dashed lines and colored region correspond to its mean and  $\pm$  standard deviation, respectively. The parameters used for the calculations are:  $w = 200 \mu\text{m}$ ;  $\mu_0 h_{\text{rf}} = 50 \mu\text{T}$ ;  $R = 25 \Omega$ ;  $G_{\text{eff}}^{\uparrow\downarrow} = 4.08 \times 10^{18} \text{ m}^{-2}$ ;  $\lambda_{\text{sd}} = 1 \text{ nm}$ .

# Spin Hall Magnetoresistance in $\text{La}_2\text{CoMnO}_6/\text{Pt}$ bilayers

In this Chapter, the novel spin Hall magnetoresistance is measured in the  $\text{La}_2\text{CoMnO}_6/\text{Pt}$  bilayer system. In Section 6.1 the effect itself and the main experimental aspects regarding its measurement are presented. Moreover, in Section 6.2, the deposition conditions and the characterization of the  $\text{La}_2\text{CoMnO}_6/\text{Pt}$  bilayer are included. Section 6.3 shows all the angular-dependent and field-dependent magnetoresistance measurements as a function of temperature. The discussion and interpretation of these results is the object of this section. Finally, in Section 6.4 a theoretical model is used for interpreting the obtained results with the object of disclosing the surface magnetic state at the LCMO/Pt interface.

## 6.1 Description of the Experiment

The novel spin Hall magnetoresistance (SMR) is a magnetoresistive effect that arises from the combined action of both spin Hall (SHE) and inverse spin Hall (ISHE) effects in ferromagnetic insulator/normal metal (FMI/NM) hybrid systems [14, 57]. When a charge current is applied in the NM layer of the system, a transverse spin current is generated *via* SHE and directed towards the sample edge, i.e., the FMI/NM interface, resulting in a net spin accumulation within the NM film. Then, the spin current can be either reflected at the interface when the magnetization vector  $\mathbf{M}$  of the FMI is parallel to the spin polarization  $\hat{\sigma}$  of the spin current, or absorbed by the FMI by means of spin transfer torque when  $\mathbf{M}$  is perpendicular to  $\hat{\sigma}$ , leading to an

increase of resistance in the NM layer in the latter case [93, 248, 249]. An schematic illustration of this effect is shown in Fig. 6.1. More interestingly, due to the surface sensitive nature of SMR [250], it may be envisioned as a convenient tool for studying the surface magnetization of FMI films [251, 252, 253].

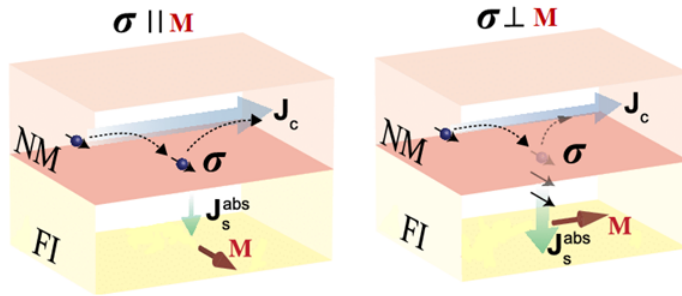


Figure 6.1: Spin Hall magnetoresistance schematic diagram. A charge current  $j_c$  induces a transverse spin current toward the normal metal (NM)/ferromagnetic insulator (FI) interface due to spin Hall effect (SHE). When the spin polarization  $\sigma$  is parallel to the magnetization vector of the FI ( $M$ ), the spin current is only partially absorbed or completely reflected back to the NM layer, in which it is transformed to a charge current again *via* inverse SHE (ISHE). On the other hand, when  $\sigma$  is perpendicular to  $M$ , the spin current induces a torque on  $M$ , being absorbed in the process and not being able to contribute to the preceding charge current by means of ISHE. This difference gives rise to two differentiated resistance states. This image has been adapted from Ref. [254].

Experimentally, SMR can be measured by performing a combination of angular-dependent (ADMR) and field-dependent (FDMR) magnetoresistance transport measurements. Namely, the ADMR measurements consist in mapping the *longitudinal* resistivity  $\rho_L$  of the system, i.e., the resistivity measured along the charge current direction, while rotating the applied magnetic field. The three main angles of rotation are labeled as  $\alpha$ ,  $\beta$ , and  $\gamma$  and the magnitude of the magnetic field is fixed. The FDMR measurements, on the other hand, measure  $\rho_L$  as a function of the magnetic field magnitude in each of the three orthogonal directions ( $x$ ,  $y$ ,  $z$ ). The geometry of the measurement, including the main angles of rotation, is sketched in Fig. 6.2. The orange Hall bar depicted in the figure represents the FMI/NM system, and its specific features are commented in the next section when discussing the sample preparation. Additionally, it is important to mention that these transport measurements were performed in a Physical Properties Measurement System (PPMS by Quantum Design), which controls the magnetic field magnitude and direction. The applied electric current was generated by a Keithley 6221 current source meter and the voltage difference was measured with a Keithley 2182A nanovoltmeter (see Appendix A.2.3 for further details on the experimental setup).



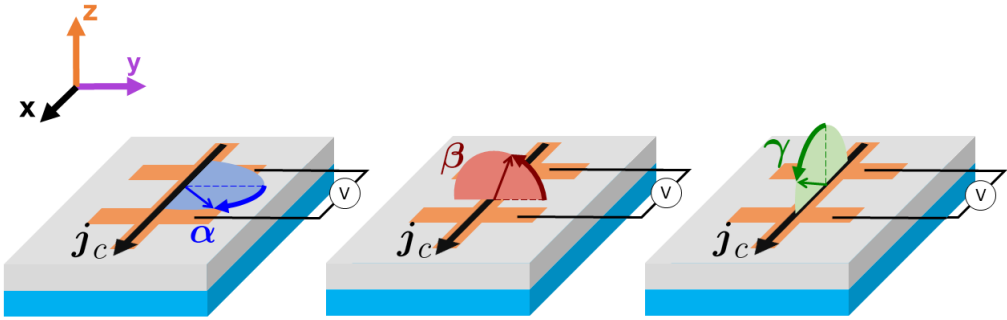


Figure 6.2: Spin Hall magnetoresistance experimental setup. The three main rotation angles are represented by the angles  $\alpha$ ,  $\beta$ , and  $\gamma$  and define the angles of rotation of the magnetic field in the ADMR measurements. It is important to note that  $\alpha = 0$  corresponds to the magnetic field pointing in the  $y$  direction,  $\beta = 0$  to the magnetic field parallel to the  $y$  direction, and  $\gamma = 0$  to the magnetic field pointing again in the  $z$  direction. The axes and colours which define the FDMR measurements, denoted by  $x$ ,  $y$ , and  $z$  are shown at the top-left corner of the image.

According to the coordinate system depicted in Fig. 6.2, the spin current generated by SHE in the NM is directed to the interface ( $-z$  direction) with its spin polarization vector  $\hat{\sigma}$  parallel to the  $y$ -axis. As a consequence, since SMR depends on the relative orientation between the magnetization vector of the FMI and  $\hat{\sigma}$ , one would expect to observe experimentally a modulated response in  $\rho_L$  at the  $\alpha$  and  $\beta$  ADMR measurements (with the same magnitude), while a constant, flat response at  $\gamma$ . This specific angular dependence is different from the one expected to arise from anisotropic magnetoresistance (AMR), for instance. In this case, since AMR depends on the relative orientation between the magnetization and the applied charge current (denoted as  $\mathbf{j}_c$  and parallel to the  $x$ -axis in Fig. 6.2), one would expect to observe a modulated response in  $\rho_L$  with respect to  $\alpha$  and  $\gamma$ , while no modulation at all with respect to  $\beta$  [249]. Therefore, in the event that the FMI/NM system presents AMR (e.g., due to the partial magnetization of the NM film for being in close contact with the FMI layer), ADMR measurements are a convenient way to discern between it and SMR. Moreover, it is expected that the magnetic properties of the ferromagnetic insulator film will be reproduced in some way in the FDMR measurements. For instance, the trace and retrace FDMR measurements should present hysteresis around the coercive field values of the film. In addition to that, a gap at  $H = 0$  should be observed as a consequence of the different resistivity states when measuring  $\rho_L(H_{x,z})$  and  $\rho_L(H_y)$ , being  $\rho_L(H_i)$  the FDMR measurement along the  $i$ -th magnetic field direction ( $i = x, y, z$ ) [14, 249].

Formally, according to SMR theory [14, 250], the longitudinal resistivity of the NM

layer is given by

$$\rho_L = \rho_0 + \Delta\rho_0 + \Delta\rho_1 (1 - m_y^2), \quad (6.1)$$

where  $\mathbf{m} = (m_x, m_y, m_z) = \mathbf{M}/M_s$  are the normalized projections of the magnetization of the FMI film with respect to the three main axes (see Fig. 6.2) and  $M_s$  is the saturation magnetization. The Drude resistivity is denoted by  $\rho_0$ , and  $\Delta\rho_0$  represents a correction due to spin-orbit coupling [14]. The SMR amplitude is represented by  $\Delta\rho_1$ . Additionally,  $\Delta\rho_0$  and  $\Delta\rho_1$  can be expressed in terms of the spin-mixing conductance at the interface  $G^{\uparrow\downarrow} = G_r + iG_i$  as [248]

$$\begin{aligned} \Delta\rho_0 &= 2\Theta_{\text{SH}}^2\rho_0 - 2\Theta_{\text{SH}}^2\rho_0\frac{\lambda_{\text{sd}}}{t_{\text{NM}}}\tanh\left(\frac{t_{\text{NM}}}{2\lambda_{\text{sd}}}\right), \\ \Delta\rho_1 &= 2\Theta_{\text{SH}}^2\rho_0\frac{\lambda_{\text{sd}}}{t_{\text{NM}}}\Re\left[\frac{2\lambda_{\text{sd}}G^{\uparrow\downarrow}\tanh^2\left(\frac{t_{\text{NM}}}{2\lambda_{\text{sd}}}\right)}{\sigma_0 + 2\lambda_{\text{sd}}G^{\uparrow\downarrow}\coth\left(\frac{t_{\text{NM}}}{\lambda_{\text{sd}}}\right)}\right], \end{aligned} \quad (6.2)$$

where  $\Theta_{\text{SH}}$  is the spin Hall angle,  $\lambda_{\text{sd}}$  is the spin diffusion length, and  $t_{\text{NM}}$  and  $\sigma_0 = 1/\rho_0$  are the thickness and conductivity of the NM layer. It is worth noting the dependence of SMR on the square of the Hall angle, due to the fact that it is a second order effect on spin-charge current Hall interconversion.

In this Chapter, we present and discuss the ADMR and FDMR measurements in a sample composed by the ferromagnetic insulator  $\text{La}_2\text{CoMnO}_6$  in contact with Pt, which acts as the non-magnetic, high spin-orbit coupling metallic part of the system. The magnetic properties of the double perovskite manganite  $\text{La}_2\text{CoMnO}_6$  are strongly dependent on the B-site cationic ordering of the double perovskite structure. This follows from the fact that the ferromagnetism in these films is mediated by superexchange interaction between  $\text{Co}^{+2}$  and  $\text{Mn}^{+4}$  cations [255]. In this scenario, cationic disorder promotes the appearance of  $\text{Mn}^{+4}-\text{O}-\text{Mn}^{+4}$  and  $\text{Co}^{+2}-\text{O}-\text{Co}^{+2}$  bonding, generating antiferromagnetic superexchange interactions and lowering both the saturation magnetization and Curie temperature in partially disordered samples [256]. Regarding to this, full B-site cationic order results in a  $\text{La}_2\text{CoMnO}_6$  with a relatively high Curie temperature ( $T_c \approx 230$  K) and a saturation magnetization of 6  $\mu_{\text{B}}/\text{f.u.}$ .

At this point, it is important to mention that the experimental findings and the subsequent discussion presented here are the result of a fruitful, joint collaboration between our research group in ICMAB-CSIC at Barcelona (Spain) and the Nanodevices group from the BRTA CIC nanoGUNE, in Donostia-San Sebastián (Spain).

## 6.2 Samples Preparation

$\text{La}_2\text{CoMnO}_6$  (LCMO hereafter) films were prepared by means of RF magnetron sputtering on top of a (100)- $\text{LaAlO}_3$  (LAO) single-crystal substrate. Films were prepared following the same deposition conditions described in Refs. [256, 257]. These conditions consist in growing the film at  $900^\circ\text{C}$  and 360 mTorr pressure in oxygen atmosphere. In this case, the deposition time was one hour. Once the deposition time was over, a two hour long thermal treatment at  $900^\circ\text{C}$  and high pressure in oxygen atmosphere took place. In Fig. 6.3, the X-ray reflectometry (XRR) (Siemens D5000 diffractometer) curve used to extract the thickness of the film is shown. In this case, the film thickness is about 15.6 nm.

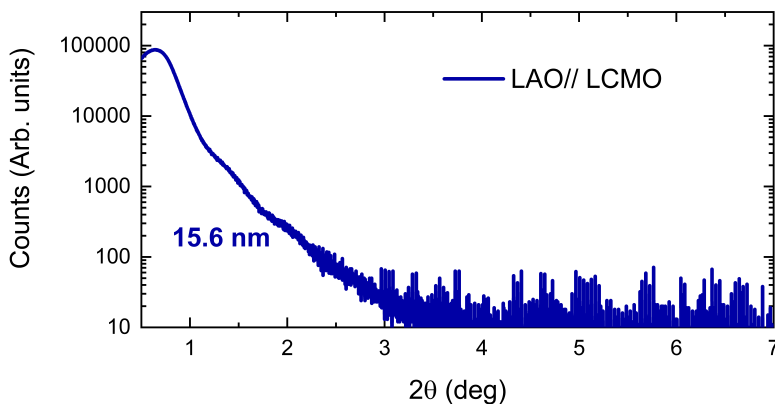


Figure 6.3: X-ray reflectometry measurement of the LCMO thin film grown on top of LAO.

The magnetic characterization of the film was carried out by means of SQUID magnetometry (MPMS-XL by Quantum Design). In Fig. 6.4, the zero-field-cooled/field-cooled (zfc/fc) magnetization curves (see Appendix A.2.1) at  $H = 1$  kOe and magnetization hysteresis loop,  $M(H)$ , at  $T = 10$  K are shown. It is important to mention that the magnetic field was applied parallel to the sample surface. From the zfc/fc curves depicted in Fig. 6.4a, it can be observed that the LAO//LCMO thin film has a Curie temperature of 255K. Moreover, the magnetization hysteresis loop at 10K depicted in Fig. 6.4b shows that the film presents a saturation magnetization of  $\approx 5 \mu_{\text{B}}/\text{f.u.}$  and a coercive field of  $\approx 10$  kOe. It is important to recall that cationic order is crucial for obtaining LCMO films with the optimal magnetic properties. As already mentioned, oxygen vacancies [258] or cationic disorder [259] promote the appearance of antiferromagnetic interactions. As a consequence, as mentioned before, full cationic ordering of  $\text{Co}^{+2}/\text{Mn}^{+4}$  allows achieving the theoretical saturation magnetization value of  $6 \mu_{\text{B}}/\text{f.u.}$  and  $T_c \approx 230$  K [256]. Thus, one may infer that there exist some level of disorder in our films, since the  $T_c$  is relatively high but the sat-

uration magnetization is only  $5 \mu_B/\text{f.u.}$ . In fact, the small bumps at 70K observed in Fig. 6.4a have been correlated with the existence of oxygen vacancies in the film by some authors [258]. As a final remark, it is observed that the easy magnetization axis lies on the film plane. This feature arises from the fact that LCMO film is under compressive strain due to the lattice mismatch with the LAO substrate [48, 260, 261].

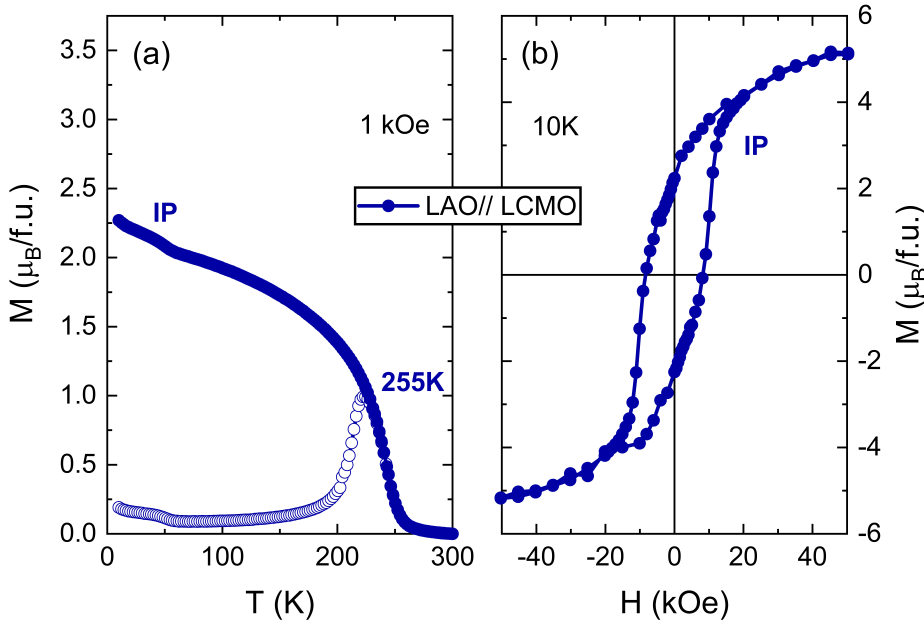


Figure 6.4: (a) Zero-field-cooled (empty symbols) and field cooled (full symbols) curves of the magnetization against temperature at 1 kOe. (b) Magnetization versus magnetic field hysteresis curve at 10K with the magnetic field applied in the plane of the film (IP).

The next step is the Pt deposition process. Prior to this deposition, however, the LCMO surface was cleaned by using a combination of acetone and ethanol followed by an annealing of the whole system at  $200^\circ\text{C}$  for 5 minutes on top of a heating plate. Then, the Pt capping layer was grown by means of DC magnetron sputtering at room temperature, a pressure of 5 mTorr in Ar- $\text{H}_2$  atmosphere and 22W of power for one minute. The thickness of the Pt film is about 5 nm according to the deposition rate in these conditions. This rate was obtained by performing a narrow scratch in a much thicker Pt film deposited in the same conditions and measuring the difference in height in the scratch with atomic force microscopy. Furthermore, it is important to mention that the Pt target was manipulated and placed at the farthest possible distance from the film in our equipment ( $\approx 13 \text{ cm}^1$ ) in order to minimize possible accidental damage of the LCMO film surface <sup>2</sup>.

<sup>1</sup>In the previous chapters, the Pt target-to-substrate distance was 6 cm.

<sup>2</sup>The reason behind this is that initially we believed that the Pt deposition process was effectively

The last step of the sample preparation process is the fabrication of the Hall bar for transport measurements. In this case, the dimensions of the Hall bar are: length  $l = 800 \mu\text{m}$  and width  $w = 100 \mu\text{m}$ . Optical lithography (Micro-writer ML3 by Durham Magneto Optics Ltd.) was employed to imprint the pattern on the sample. Right after that, ion milling (from TSST) was used to subtract the excess of material. The overall process is analogous to that used in Chapter 4 for making the strips in the Py/Pt bilayers, for instance. In Figure 6.5a, an actual image of the resulting Hall bar employed in the measurements is shown. For the measurements, the sample was placed in a rotating sample holder (*rotation pucks*), which are PPMS sample holders specifically designed to rotate the sample with respect to the applied magnetic field. The puck shown in Fig. 6.5b covers the  $\beta$  and  $\gamma$  rotation angles, while the one from Fig. 6.5c is specific for in plane rotations ( $\alpha$  angle). The electrical contacts between the sample and puck were made by means of wire bonding (Ultrasonic Wire Bonder 4526 by Kuliche & Soffa).

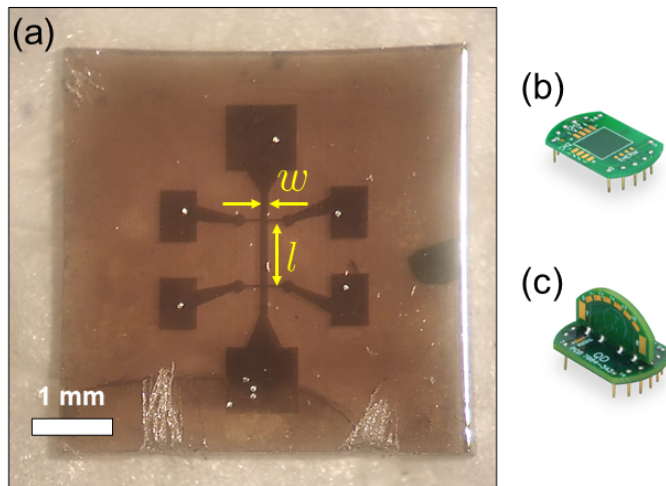


Figure 6.5: (a) Actual image of the Hall bar used for the measurements obtained from the lithographic process. In this case, the length  $l$  is  $800 \mu\text{m}$  and the width  $w$  is  $100 \mu\text{m}$ . The (b) and (c) panels correspond to the rotation pucks (i.e., PPMS sample holders) used for the measurements where the magnetic field is allowed to rotate out-of-plane and in-plane, respectively. The images in (b) and (c) have been retrieved from [262].

Finally, in Fig. 6.6, the measured longitudinal resistivity  $\rho_L$  as a function of temperature of the Pt capping layer is shown. The resistivity is defined as  $\rho_L = wtR_L/l$ , where  $t$  is the Pt thickness, and  $R_L = V_L/I_c$  is the longitudinal resistance, calculated

damaging the LCMO surface and, thus, that much *softer* deposition conditions were needed. For clarity, the ADMR and FDMR measurements obtained in previously fabricated LAO//LCMO/Pt systems using different Pt deposition conditions in each case are compiled in Appendix C.

from the voltage measured along the Hall bar  $V_L$  and the intensity applied ( $I_c = 60 \mu\text{A}$ ). The  $\rho_L(T)$  curve shows that the Pt is metallic in the whole range of temperatures and that its resistivity at 300K is about  $43 \mu\Omega \cdot \text{cm}$ . This value, which is four times larger than that of bulk Pt, is in accordance with other Pt thin films deposited on complex oxides [101, 253]. More interestingly, it has recently been found that *moderately dirty* Pt films (i.e., with high resistivity) present larger spin Hall angles than Pt films with low resistivity when the SHE is dominated by intrinsic mechanisms [223].

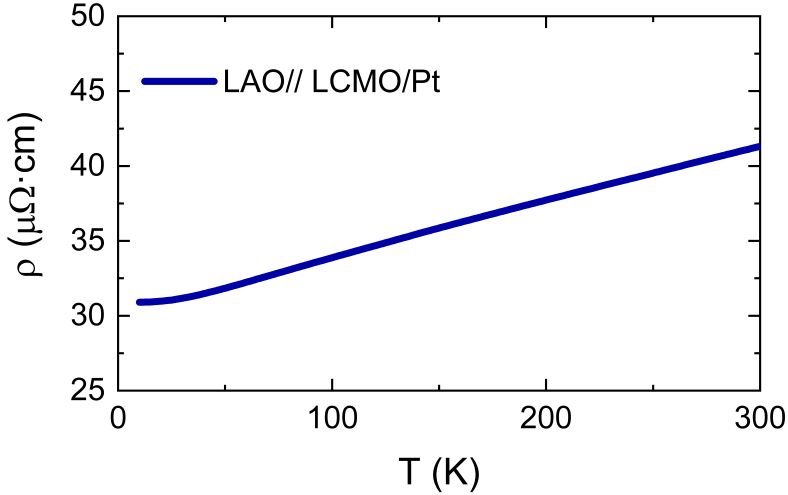


Figure 6.6: Longitudinal resistivity of the Pt capping layer in the LCMO/Pt sample as a function of temperature.

### 6.3 Spin Hall Magnetoresistance Measurements and Results

In Fig. 6.7, the ADMR measurements at different temperatures below and above  $T_c$  are shown. In addition, in Fig. 6.8 the FDMR measurements at the same set of temperatures are presented. As can be observed from Fig. 6.7, the ADMR normalized amplitude signal, denoted by  $\Delta\rho_L/\rho_L$ , presents a  $\sin^2(\alpha, \beta)$  dependence with respect to the rotation angles  $\alpha$  and  $\beta$ . This result follows directly from the  $m_y^2$  projection dependence presented in Eq. 6.1. Moreover, the signal is completely flat with respect to  $\gamma$ . This angular dependence, as is mentioned in Section 6.1, is in accordance with the symmetry expected for SMR (see Eq. 6.1) and thus precludes the existence of AMR in our system. On the other hand, the observed magnetoresistance (MR) clearly increases when increasing the applied magnetic field from 1T to 9T. This behaviour

is unexpected in our system since the magnetization of the LCMO thin film should be saturated at 4T according to the  $M(H)$  curve in Fig. 6.4b. Therefore, one could expect the increase in amplitude observed from 1T to 4T, but not from 4T to 9T. In other words, once the saturation magnetization is achieved, the SMR signal should not depend on the magnetic field magnitude.

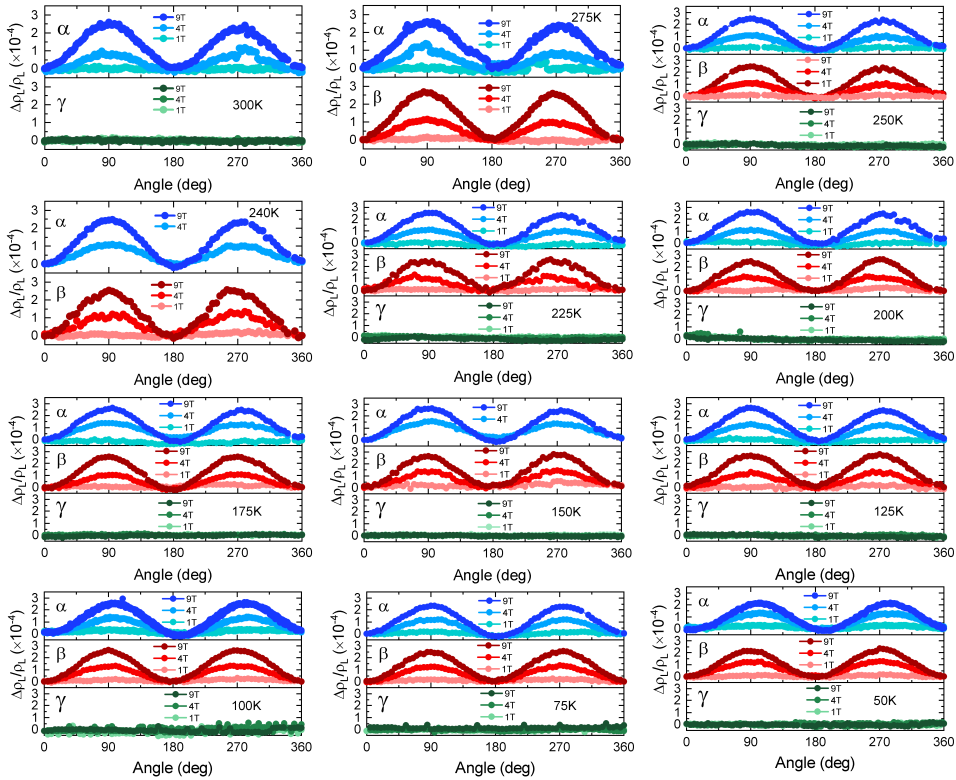


Figure 6.7: ADMR measurements at several temperatures in the main rotation angles defined in Fig. 6.2:  $\alpha$  (blueish points),  $\beta$  (reddish points), and  $\gamma$  (greenish points). Each measurement has been performed at three different magnetic fields magnitudes: 1T, 4T, and 9T.

The dependence of the SMR signal on the magnitude of the magnetic field can be more clearly appreciated in the FDMR measurements from Fig. 6.8. In this case, as can be observed, the normalized amplitude signals measured when the field points in the  $x$  and  $z$  directions (denoted as  $H_x$  and  $H_z$  in Fig. 6.8, respectively) overlap with each other and increase almost linearly in the whole range of temperatures studied. Moreover, when the magnetic field points in the  $y$  direction ( $H_y$ ), the signal is completely flat, as expected (since in this case, the magnetization is parallel to the build-up spin accumulation at the interface) down to 100K. At this temperature and below, however, the MR is non-zero and negative, gradually increasing with respect

to the magnetic field magnitude. Additionally, it is important to mention that the FDMR curves shown in Fig. 6.8 present the measurements with the magnetic field running from 9T to  $-9$ T. Thus, in Fig. 6.9, the 100K and 50K FDMR measurements with the field running from 9T to  $-9$ T and then back from  $-9$ T to 9T (i.e., the trace and retrace configurations, respectively) are shown in order to probe the hysteretic nature of the FDMR measurements. In this case, however, the observed results are in sharp contrast with those observed in other magnetic systems in the literature such as YIG/Pt [249, 250, 263] or  $\text{CoFe}_2\text{O}_4/\text{Pt}$  [253], in which the hysteresis of the magnetic film is reproduced in the FDMR measurements. Moreover, the usual gap due to the different resistivity states at  $H = 0$  for different field directions is also absent in our measurements for the whole range of temperatures.

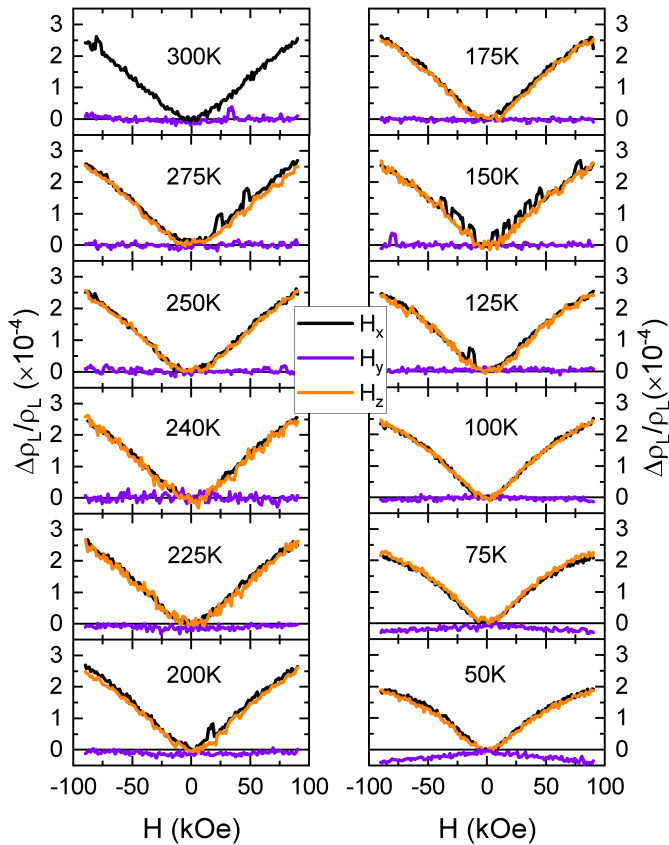


Figure 6.8: FDMR measurements at several temperatures in the main axes defined in Fig. 6.2:  $x$  (black lines),  $y$  (violet lines), and  $z$  (orange lines).

Nevertheless, the most surprising feature in Figs. 6.7 and 6.8 is that the normalized amplitude signal is maintained well above  $T_c$  (255K according to Fig. 6.4a), even at



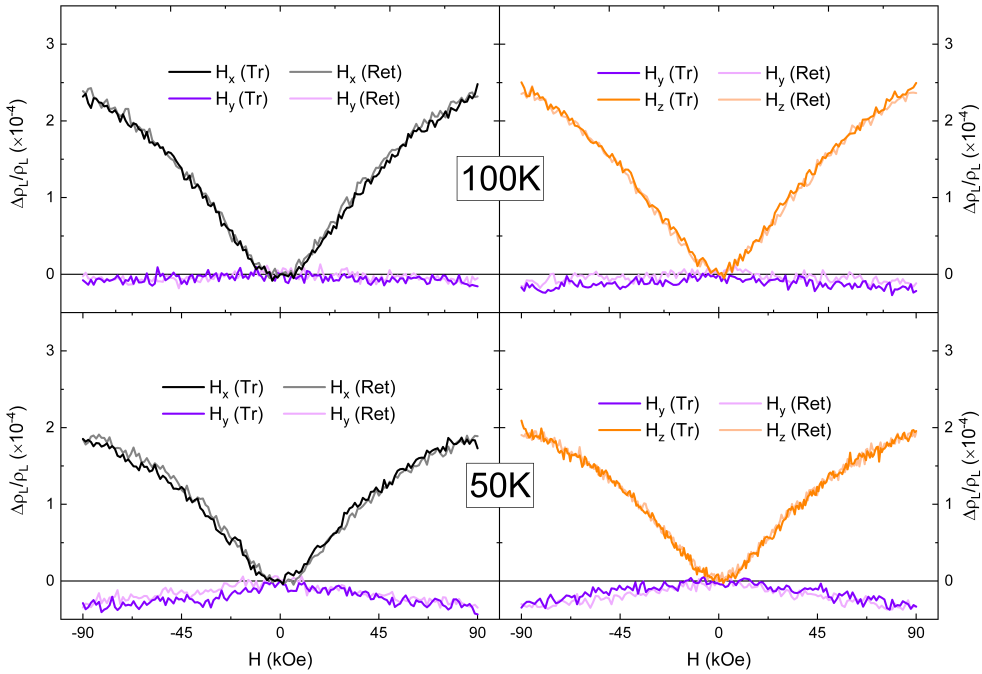


Figure 6.9: FDMR measurements at 100K and 50K in the main axes with the field in each case running from 9T to  $-9$ T (trace, denoted by Tr) and from  $-9$ T to 9T (retrace, denoted by Ret).

room temperature without decreasing its amplitude. In general, one would expect an abrupt decrease of the SMR signal at the ferromagnetic-paramagnetic transition temperature, but this is clearly not the case in our sample. In order to better visualize this result, Fig. 6.10 shows the SMR normalized amplitude  $\Delta\rho_1/\rho_L$  at 1T, 4T, and 9T as a function of temperature, from 320K to 10K. These values were extracted from the fitting of the ADMR curves in Fig. 6.7 by using Eq. 6.1. It is clearly observed that the SMR amplitude is constant in the whole range of temperatures down to 50K, from which a mild decrease is observed. For completeness, the ADMR and FDMR measurements performed at 25K and 10K are added in Fig. 6.11. In this case, as can be observed, an anomalous positive MR in the  $H_y$  direction develops in the 25K and 10K FDMR measurements (see Fig. 6.11a). The origin of this parabolic contribution, which adds up to the SMR-like MR at higher temperatures, is not clear. In addition, these low-temperature effects, which are not observed for any other set of temperatures, might be at the origin of the decrease in the SMR signal below 50K observed in Fig. 6.10. It is beyond the scope of this Thesis to clarify the origin of this low-temperature behaviour.

At this point, it might be convenient summarize the main results and observations

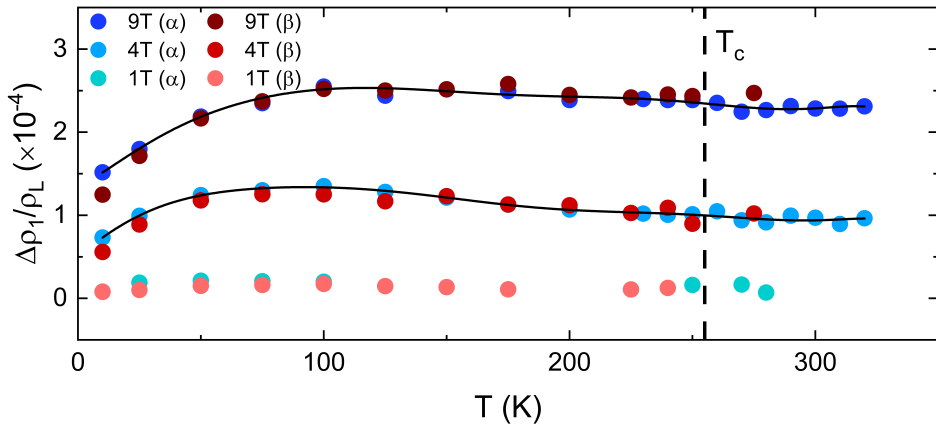


Figure 6.10: SMR normalized amplitude ( $\Delta\rho_1/\rho_L$ ) as a function of temperature at different magnetic field magnitudes extracted from the  $\Delta\rho_L(\alpha)/\rho_L$  and  $\Delta\rho_L(\beta)/\rho_L$  ADMR measurements in Fig. 6.7. The solid black lines are guides to the eyes.

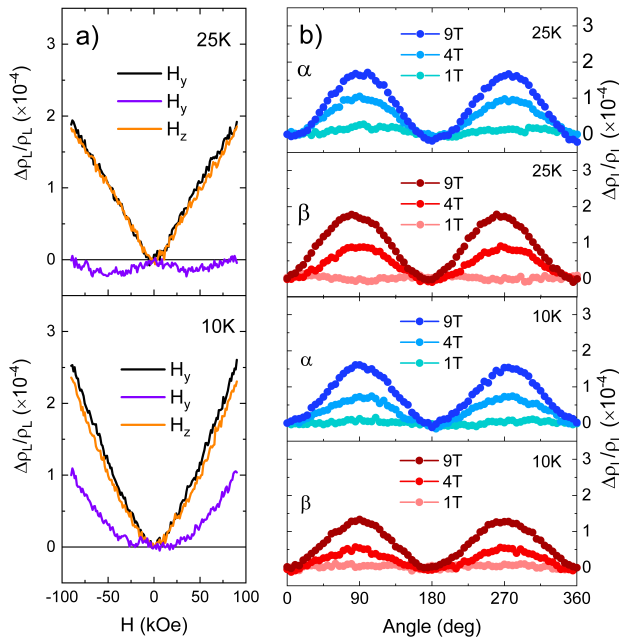


Figure 6.11: FDMR (a) and ADMR (b) measurements at 25K and 10K. It is observed an anomalous parabolic-like positive MR in the  $y$ .

derived from the ADMR and FDMR measurements (Figs. 6.7–6.11):

1. The ADMR normalized amplitude signal has the symmetry of SMR (see Eq. 6.1),

thus the existence of AMR due to magnetic proximity effects can be dismissed (Fig. 6.7).

2. The SMR amplitude increases with increasing the magnitude of the magnetic field in the whole range of temperatures studied (Figs. 6.7, 6.8, and 6.11).
3. The trace and retrace FDMM curves in the three main directions do not reproduce the hysteretic nature of the LCMO film nor present the characteristic  $H = 0$  gap (Fig. 6.9).
4. The FDMM measurements below 100K present an unexpected negative MR in the  $H_y$  direction which increases with decreasing temperatures (Fig. 6.8). At the lowest studied temperatures (10K and 25K), an anomalous parabolic-like positive MR is observed in the same  $H_y$  direction (Fig. 6.11).
5. The SMR amplitude does not vanish nor decrease even above  $T_c$ , maintaining a constant value of  $\approx 2.5 \times 10^{-4}$  (at 9T) almost from 320K to 50K, from which it decreases presumably due to the above mentioned positive MR at low temperatures.

Altogether, one could wonder if these results indicate that the magnetic response of the LCMO surface is decoupled from its bulk. Moreover, another possible scenario could be that of a LCMO/Pt interface in which any kind of interaction between the spin accumulation within the Pt and the magnetization of the LCMO film is forbidden. This last possibility, however, entails yet another question: If the spin accumulation cannot interact with the magnetic system underneath, what does produce the observed ADMR and FDMM curves in Figs. 6.7 and 6.8? The rest of this section is devoted to clarify these questions.

In general, the dependence of the SMR signal with respect to the field magnitude in these kind of experiments has been associated with the so-called Hanle MR (HMR) [248, 264], a magnetoresistive effect theoretically predicted some years ago by Dyakonov [74]. Contrary to the SMR effect, HMR does not arise from the interaction between the spin current and the magnetization at the FMI/NM interface, but from the combined action of spin precession and dephasing due to the magnetic field [248], i.e., the Hanle effect. Nevertheless, both effects share the same angular dependence since they rely on the interaction between this spin current and an external source. In fact, an expression similar to Eq. 6.1 from SMR can be obtained from spin diffusion theory in a system in which the MI is absent [248, 264],

$$\rho_L = \rho_0 + \Delta\rho_0 + \Delta\rho_1 (1 - n_y^2). \quad (6.3)$$

In this case, the angular dependence is defined by  $\mathbf{n} = (n_x, n_y, n_z) = \mathbf{H}/H$ , which are the magnetic field projections with respect the three main axes, with  $\mathbf{H}$  being

the magnetic field vector and  $H$  its magnitude. Furthermore, a direct comparison between Eqs. 6.1 and 6.3 shows that both effects have indeed equal angular symmetry. Moreover, the prefactors  $\Delta\rho_0$ , and  $\Delta\rho_1$  in Eq. 6.3 can be expressed as [248]

$$\begin{aligned}\Delta\rho_0 &= 2\Theta_{\text{SH}}^2\rho_0 - 2\Theta_{\text{SH}}^2\rho_0\frac{\lambda_{\text{sd}}}{t_{\text{NM}}}\tanh\left(\frac{t_{\text{NM}}}{2\lambda_{\text{sd}}}\right), \\ \Delta\rho_1 &= 2\Theta_{\text{SH}}^2\rho_0\left\{\frac{\lambda_{\text{sd}}}{t_{\text{NM}}}\tanh\left(\frac{t_{\text{NM}}}{2\lambda_{\text{sd}}}\right) - \Re\left[\frac{\Lambda}{\lambda_{\text{NM}}}\tanh\left(\frac{t_{\text{NM}}}{2\Lambda}\right)\right]\right\},\end{aligned}\tag{6.4}$$

where  $(1/\Lambda) = \sqrt{1/\lambda_{\text{sd}}^2 + i/\lambda_m^2}$  with  $\lambda_m = \sqrt{D/\mu_0\gamma H}$ , and  $D$ ,  $\gamma$ ,  $\mu_0$ , and  $H$  are, respectively, the diffusion coefficient, gyromagnetic ratio, vacuum permeability, and magnitude of the magnetic field. It is worth noticing that the spin-mixing conductance is absent in Eq. 6.4.

Hence, the HMR mechanism could explain why the measured MR does not vanish above  $T_c$  since it only affects the Pt capping layer, although normally the amplitude of the HMR is one order of magnitude lower than its SMR counterpart [248, 264]. Nevertheless, precisely because HMR has also the same angular symmetry as SMR, it cannot by itself explain the negative MR observed below 100K in Fig. 6.8 when the magnetic field points in the  $y$  direction<sup>3</sup>. Moreover, the fact that this negative MR vanishes at 100K and not near  $T_c$ , for example, suggests that it is not related with the magnetic properties of the LCMO film. Consequently, we infer that the most probable explanation for the results presented in this Chapter is that of the magnetically decoupled surface layer in the LCMO thin film.

In order to assess the validity of this hypothesis, the cross section of the LCMO/Pt interface was analysed by means of scanning transmission electron microscopy (STEM). The STEM characterization was carried out by the Centro Nacional de Microscopía Electrónica (ICTS-CNME), at the Universidad Complutense de Madrid (UCM) (Spain), and the technical details regarding this measurement are specified in the caption of Fig. 6.12. In this figure, the high-resolution high-annular dark-field (HAADF) STEM image of the LAO// LCMO/Pt system as well as the EELS chemical analysis of the LCMO/Pt interface are presented. As can be observed from Fig. 6.12a, the LAO// LCMO interface presents several misfit dislocations, seen as dark spots in the image, suggesting a partially relaxed LCMO layer, which does not show any other crystallographic defect. Actually, the LCMO surface just below the Pt layer is crystalline, defect-free and atomically flat. The EELS chemical analysis of the LCMO/Pt interface (see Fig. 6.12b) reveals that the surface of the LCMO film has a different chemical composition with respect to the bulk: in this region, the

---

<sup>3</sup>Note that  $\Delta\rho_0$  in Eq. 6.4 does not depend on the applied field.

Co map shows that there are two Co atomic planes missing in the topmost region of the LCMO layer when compared with the Mn map (see the green and red element maps in Fig. 6.12b), leaving a single perovskite  $\text{LaMnO}_3$  structure at the interface. Interestingly, bulk stoichiometric  $\text{LaMnO}_3$  is a Mott insulator and a A-type antiferromagnet, however, it may become a ferromagnet in thin film form due to i) structural strain [190] or ii) by introducing cationic vacancies [189]. Therefore, the chemistry, and thus the magnetic properties, of the LCMO film at the interface with the Pt differ from that of the bulk. This result supports the existence of a magnetically decoupled layer at the surface of the LCMO film.

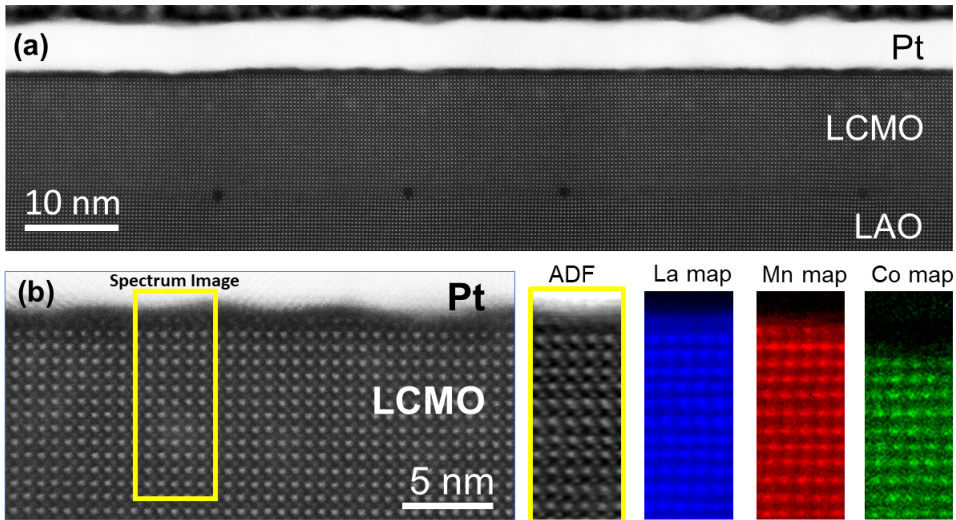


Figure 6.12: (a) Scanning tunneling electron microscopy (STEM) image of the LAO//LCMO/Pt system as a whole. (b) Closeup image of the interface between the LCMO film and the Pt capping layer. The EELS chemical analysis in the region enclosed by the yellow rectangle shows that, at the topmost layer of the film, Co vanishes, leading to a crystalline  $\text{LaMnO}_3$  layer at the LCMO/Pt interface. Aberration-corrected STEM was used for microstructural analysis with atomic resolution. The sample was characterized using a JEOL JEM ARM200cF operated at 200 kV, equipped with a CEOS aberration corrector and GIF Quantum ER spectrometer, at the Universidad Complutense de Madrid (Spain). The STEM images were acquired in high-angle annular dark-field (HAADF) imaging mode. The STEM specimens were prepared using a FEI Helios nanolab 650, at SEM-FIB microscopy service of the Universidad de Málaga (Spain).

Similar results have also been recently reported by Vélez et al. in a  $\text{LaCoO}_3$ /Pt system [252].  $\text{LaCoO}_3$  in thin film form is a ferromagnetic insulator perovskite complex oxide. In that case, the results obtained were very similar to our own (i.e., the SMR amplitude increasing with the magnetic field magnitude; signal above  $T_c$ ; no reproducible hysteresis nor  $H = 0$  gap observed in the FDMR measurements; and

negative MR below  $T_c$ ) and it was actually observed that the  $\text{LaCoO}_3$  surface was structurally amorphous and Co-rich. As a result, it was concluded that the reported peculiar SMR measurements were consistent with a magnetically decoupled, Co-rich surface layer that behaves as a low-dimensional (1D or 2D) Heisenberg ferromagnet. In these systems, long-range magnetic order is strongly suppressed due to the effect of thermal fluctuations [265]. In addition, the Mermin-Wagner theorem [266, 267] for 1D and 2D isotropic and short-range interacting Heisenberg systems precludes the existence of spontaneous ferro- or antiferromagnetic phase transitions at  $T > 0$ . In a way, it resembles to some extent a superparamagnet, which can be described as a collection of independent clusters of local moments with no long-range magnetic order nor phase transition. In this context, it is the topic of the next section to disentangle the magnetic state of the surface layer found in our LCMO/Pt system. Specifically, we focus on two different models: a 2D Heisenberg ferromagnet and a superparamagnet.

## 6.4 Surface Magnetic State of the $\text{La}_2\text{CoMnO}_6$ Film

It is the goal of this section to disclose the surface magnetic state of the LCMO film in order to correctly explain the ADMR and FDMR measurements obtained. For doing so, we use the microscopic theoretical formalism developed in Ref. [57] and employed in the above-mentioned work by Vélez et al. [252]. This formalism describes the spin dependent scattering occurring at a magnetic insulator (MI)/NM interface *via* a microscopic model based on the  $sd$  coupling between the itinerant  $s$ -electrons in the NM and the local ( $d$ ) moments on the MI surface [57]. The main difference between this formalism and the first theories on SMR [14, 248, 249] is that the parameters which govern interface scattering (e.g., spin mixing conductances) are not regarded as phenomenological but instead are expressed in terms of the  $sd$  coupling and the spin expectation values. The latter are determined by the specific magnetic behaviour of the MI layer. As a consequence, different magnetic textures can be accordingly fitted into the formalism. For instance, it has recently been used for studying the above mentioned low-dimensional ferromagnetic surface state in the  $\text{LaCoO}_3/\text{Pt}$  system [250], for measuring SMR in a system composed by the paramagnetic insulator  $\text{Gd}_3\text{Ga}_5\text{O}_{12}$  in contact with Pt [101], to gain insight into the SMR temperature dependence of the ferromagnetic insulator EuS with Pt as the capping layer [268], and more recently, to study the SMR characteristics of Pt in contact with the van der Waals antiferromagnet  $\text{MnPSe}_3$  [269].

The aim of the model is to relate the spin mixing conductances which govern the spin transport at the MI/NM interface with the spin-relaxation times of the conduction electrons. Finally, these relaxation times can be expressed in terms of the

spin expectation values which depend on the magnetic state of the MI. The model starts by introducing an intermixing, fictitious layer of thickness  $b$  near the MI/NM interface and within the NM film. It is assumed that  $b \ll t_{\text{NM}}$  and for the calculation the  $b \rightarrow 0$  limit is taken. In Fig. 6.13, a schematic diagram of the system is shown. The  $sd$  exchange interaction between the itinerant electrons in the NM and the local moments in the MI occurs within this fictitious layer, and can be expressed as

$$\mathcal{H}_{sd} = -J_{sd} \sum_i \mathbf{S}_i \cdot \mathbf{s}(\mathbf{r}_i), \quad (6.5)$$

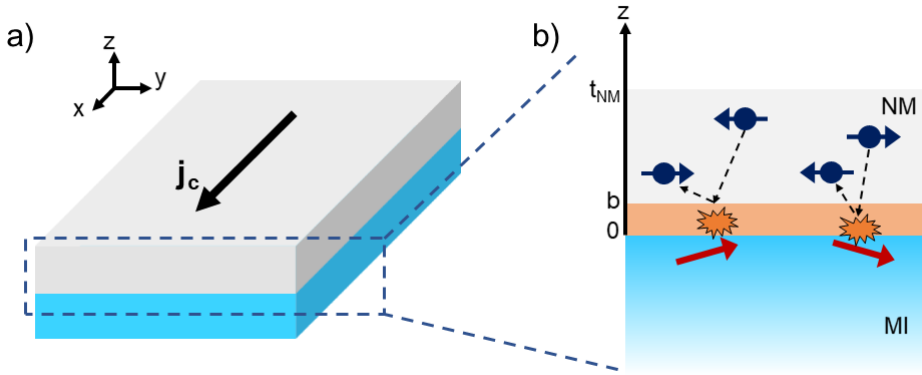


Figure 6.13: (a) Schematic diagram of the LCMO/Pt system with the charge current pointing in the  $x$  direction. (b) Closeup diagram of the interface between the MI (LCMO) film and the NM (Pt) capping layer. The orange region denotes the fictitious  $b$  layer, in which the  $sd$  interaction between the itinerant electrons of the Pt and the local magnetic moments of the LCMO takes place.

where  $J_{sd}$  is the exchange coupling constant,  $\mathbf{S}_i$  is the localized spin operator, and  $\mathbf{s}(\mathbf{r}_i)$  is the spin density of conduction electrons at position  $\mathbf{r}_i$ . It is assumed that the movement of electrons is diffusive and random, thus scattering off at the MI/NM interface once in a while. Having scattered away, the electron returns to the interface after a long time<sup>4</sup> and, thus, it is further assumed that either the spin coherence of the electron is lost or the state of the local moments resets. In this way, each interaction has no memory from the previous one. Moreover, the continuity equation for the non-equilibrium spin accumulation in the NM, including the  $b$ -layer, reads [56, 57, 101, 252]

<sup>4</sup>On the order of the diffusion time  $\tau_D$ , which is defined as  $\tau_D = t_{\text{NM}}^2/D$ , being  $t_{\text{NM}}$  the thickness of the NM film and  $D$  its diffusion coefficient.



$$\partial_t \mu_s^\alpha - \frac{1}{e\nu_F} \partial_i \mathcal{J}_{s,i}^\alpha - \omega_L \epsilon_{\alpha\beta\gamma} n_\beta \mu_s^\gamma = -\Gamma_{\alpha\gamma} \mu_s^\gamma, \quad (6.6)$$

where  $\epsilon_{\alpha\beta\gamma}$  is the Levi-Civita tensor,  $\mu_s^\alpha$  is the spin accumulation polarized in the  $\alpha$  direction,  $\nu_F$  is the density of states at the Fermi level,  $\mathcal{J}_{s,i}^\alpha$  is the spin current tensor spin polarized in the  $\alpha$  direction and flowing in the  $i$  direction. The effective (renormalized) Larmor frequency, which includes the interfacial exchange field due to  $\langle S_{\parallel} \rangle$ , is  $\omega_L = \omega_B - \delta_b(z) n_s J_{sd} \langle S_{\parallel} \rangle$ , being  $\omega_B = \gamma \mu_0 H$  with  $\gamma$  the gyromagnetic ratio,  $\mu_0$  the vacuum permeability, and  $H$  the magnitude of the magnetic field. The function  $\delta_b(z)$  is equal to  $1/b$  inside the intermixing layer ( $0 < z < b$ ) and 0 elsewhere.  $\langle S_{\parallel} \rangle$  is the expectation value of the spin parallel to  $\mathbf{H}$  and  $n_s$  is the number of localized spins per unit area at the surface of the MI. Finally,  $\Gamma_{\alpha\gamma}$  corresponds to the spin-relaxation tensor, which can be defined as

$$\Gamma_{\alpha\gamma} = \frac{\theta(z-b)}{\tau_s} \delta_{\alpha\gamma} + \theta(z)\theta(b-z) \left[ \frac{\delta_{\alpha\gamma}}{\tau_{\perp}} + \left( \frac{1}{\tau_{\parallel}} - \frac{1}{\tau_{\perp}} \right) n_{\alpha} n_{\gamma} \right]. \quad (6.7)$$

In this case,  $\tau_s$  is the isotropic spin-relaxation time, which is induced by the spin-orbit coupling of the NM film. The transverse and longitudinal spin relaxation times in the interaction region are denoted by  $\tau_{\perp}$  and  $\tau_{\parallel}$ , respectively. On one hand,  $\tau_{\parallel}$  is the relaxation time of the longitudinal spin component  $\mu_{\parallel} = \boldsymbol{\mu}_s \cdot \mathbf{n}$ , and is due to spin-flip processes in the itinerant electrons which result in the creation of a spin excitation (i.e., a magnon) in the MI. On the other hand,  $\tau_{\perp}$  is the decoherence time of the transverse spin components  $\boldsymbol{\mu}_{\perp} = \mathbf{n} \times (\mathbf{n} \times \boldsymbol{\mu}_s)$ , and is due to spin dephasing. This dephasing contribution arises from the fact that the electron spin, being in a superposition of spin-up and spin-down states, acquires a precession phase about the  $n$  direction [57]. Finally,  $\delta_{\alpha\gamma}$  is the Kronecker delta and  $\theta(x)$  is the Heaviside step function. According to Vélez et al. [252], these relaxation times are related to the spin expectation values as

$$\begin{aligned} \frac{1}{\tau_{\parallel}} &= \frac{1}{\tau_s} + \frac{\pi\nu_F J_{sd}^2}{\hbar b} n_s \langle \mathbf{S}_{\perp}^2 \rangle, \\ \frac{1}{\tau_{\perp}} &= \frac{1}{\tau_s} + \frac{\pi\nu_F J_{sd}^2}{\hbar b} n_s \left[ \langle S_{\parallel}^2 \rangle + \frac{\langle \mathbf{S}_{\perp}^2 \rangle}{2} \right], \end{aligned} \quad (6.8)$$

being  $S_{\parallel}$  and  $\mathbf{S}_{\perp}$  the components of the spin operator parallel and perpendicular to  $\mathbf{H}$ , respectively. Both components are related through the equivalence

$$S(S+1) = \langle \mathbf{S}_{\perp}^2 \rangle + \langle S_{\parallel}^2 \rangle, \quad (6.9)$$



being  $S(S+1)$  the eigenvalue of  $\langle S^2 \rangle$  and  $S$  the spin angular momentum of the atoms which conform the local moments of the MI film. The dependence of  $\langle S_{\parallel} \rangle$ ,  $\langle S_{\parallel}^2 \rangle$ , and  $\langle S_{\perp}^2 \rangle$  on  $\mathbf{H}$  and  $T$  are determined by the type of magnetic order at the interface [252]. Now, integrating Eq. 6.6 and considering Eq. 6.7, the spin current *inside* the  $b$ -layer can be expressed as

$$-\frac{1}{e\nu_{\text{F}}} [\mathcal{J}_{s,z}^{\alpha}(b) - \mathcal{J}_{s,z}^{\alpha}(0)] = b\omega_{\text{L}}\epsilon_{\alpha\beta\gamma}n_{\beta}\mu_s^{\gamma} - \frac{b}{\tau_{\perp}}\mu_s^{\alpha} - \left(\frac{b}{\tau_{\parallel}} - \frac{b}{\tau_{\perp}}\right)n_{\alpha}(\mathbf{n} \cdot \boldsymbol{\mu}_s). \quad (6.10)$$

By requiring that the spin current vanishes at  $z = 0$ , we can express Eq. 6.10 at  $z = b$  in vector notation as

$$-\frac{1}{e\nu_{\text{F}}}j_{s,z}\hat{\boldsymbol{\sigma}}(b) = -\frac{b}{\tau_{\parallel}}\boldsymbol{\mu}_s + \left(\frac{b}{\tau_{\parallel}} - \frac{b}{\tau_{\perp}}\right)\mathbf{n} \times (\boldsymbol{\mu}_s \times \mathbf{n}) + b\omega_{\text{L}}\mathbf{n} \times \boldsymbol{\mu}_s. \quad (6.11)$$

And finally, taking the limit  $b \rightarrow 0$  and considering the boundary condition by which the spin current and the MI/NM interface is (see Eq. 3.23 from Section 3.3 in Chapter 3)

$$-ej_{s,z}\hat{\boldsymbol{\sigma}}(0) = G_s\boldsymbol{\mu}_s + G_r\mathbf{n} \times (\boldsymbol{\mu}_s \times \mathbf{n}) + G_i\mathbf{n} \times \boldsymbol{\mu}_s, \quad (6.12)$$

we can extract the spin-mixing conductances from direct comparison with Eq. 6.11 and using Eq. 6.8,

$$\begin{aligned} G_r &= \frac{\pi\nu_{\text{F}}^2 J_{sd}^2 e^2 n_s}{\hbar} \left[ \langle S_{\parallel}^2 \rangle - \frac{\langle \mathbf{S}_{\perp}^2 \rangle}{2} \right], \\ G_i &= -\frac{\nu_{\text{F}} J_{sd} e^2 n_s}{\hbar} \langle S_{\parallel} \rangle, \\ G_s &= -\frac{\pi\nu_{\text{F}}^2 J_{sd}^2 e^2 n_s}{\hbar} \langle \mathbf{S}_{\perp}^2 \rangle. \end{aligned} \quad (6.13)$$

Note that for a ferromagnetic system, almost all spins are aligned with the field direction, therefore, well below  $T_c$ ,  $\langle \mathbf{S}_{\perp}^2 \rangle \ll \langle S_{\parallel}^2 \rangle$ . In this way it is obvious that  $G_r \sim \langle S_{\parallel}^2 \rangle$ , which is another way of stating that the real part of the spin-mixing conductance is proportional to the square of the saturation magnetization,  $M_s^2$ . It is worth recalling that this result was already mentioned in the previous chapter when

dealing with the temperature dependence of the ISHE voltage in the LMO/Pt films. In that case it was based on experimental experience (see for instance Atsarkin et al. [214, 215]) but here, however, the dependence arises naturally from first principles.

Now, we move on to present the MR of the system just as in the previous section. The general expression for the longitudinal resistivity is found to be [252]  $\rho_L = \rho_0 + \Delta\rho_0 + \Delta\rho_1(1 - n_y^2)$ , where  $n_y$  is the  $y$  component of  $\mathbf{n} = \mathbf{H}/H$  and  $\rho_0$  the Drude resistivity of the NM. The corrections to the resistance  $\Delta\rho_0$  and  $\Delta\rho_1$  in this case are expressed as [252]

$$\begin{aligned} \Delta\rho_0 &= 2\Theta_{\text{SH}}^2\rho_0 - 2\Theta_{\text{SH}}^2\rho_0 \frac{\lambda_{\text{sd}}}{t_{\text{NM}}} \frac{\tanh\left(\frac{t_{\text{NM}}}{2\lambda_{\text{sd}}}\right) - G_s\lambda_{\text{sd}}\rho_0}{1 - 2G_s\lambda_{\text{sd}}\rho_0 \coth\left(\frac{t_{\text{NM}}}{\lambda_{\text{sd}}}\right)} \\ \Delta\rho_1 &= 2\Theta_{\text{SH}}^2\rho_0 \left\{ \frac{\lambda_{\text{sd}}}{t_{\text{NM}}} \frac{\tanh\left(\frac{t_{\text{NM}}}{2\lambda_{\text{sd}}}\right) - G_s\lambda_{\text{sd}}\rho_0}{1 - 2G_s\lambda_{\text{sd}}\rho_0 \coth\left(\frac{t_{\text{NM}}}{\lambda_{\text{sd}}}\right)} \right. \\ &\quad \left. - \Re \left[ \frac{\Lambda}{t_{\text{NM}}} \frac{\tanh\left(\frac{t_{\text{NM}}}{2\Lambda}\right) - \mathcal{G}\Lambda\rho_0}{1 + 2\mathcal{G}\Lambda\rho_0 \coth\left(\frac{t_{\text{NM}}}{\Lambda}\right)} \right] \right\}, \end{aligned} \quad (6.14)$$

where  $(1/\Lambda) = \sqrt{1/\lambda_{\text{sd}}^2 + i/\lambda_{\text{m}}^2}$  with  $\lambda_{\text{m}} = \sqrt{D/\gamma\mu_0 H}$ , and  $D$  is the NM diffusion coefficient,  $\gamma$  the gyromagnetic ratio, and  $\mathcal{G} = G_r - G_s + iG_i$  is the *total* spin-mixing conductance.

Equations 6.13 and 6.14 constitute the main result of this microscopic model. It should be noticed that the theory developed in Refs. [57, 252] and reproduced here generalizes and completes the original SMR/HMR theory. The first quantitative theories of SMR [14, 249] assumed a system in which the magnetic film was a ferromagnetic insulator (e.g., YIG), with long-range magnetic order and  $T_c$ . In these systems almost all magnetic moments are aligned with the field direction, resulting in  $\langle S_{\perp}^2 \rangle \ll \langle S_{\parallel}^2 \rangle$ . This situation corresponds to  $G_s \approx 0$  according to Eq. 6.13. Moreover, neglecting the effects of HMR (i.e., by setting  $\Lambda = \lambda_{\text{sd}}$ ) one finally recovers the usual SMR amplitude (see Eq. 6.2). Conversely, the HMR amplitude (Eq. 6.4) can be recovered by setting  $\mathcal{G} = 0$  (and  $G_s = 0$ ), which is equivalent to say that there is no magnetic specimen in contact with the NM capping film. In this way, these two regimes (SMR and HMR) may be envisioned as two extremes of the same theory, and intermediate situations can be easily considered within it. For instance, the simultaneous effect of SMR and HMR in a FMI/NM bilayer can be taken into consideration by setting  $G_s = 0$  in Eqs. 6.13 and 6.14.

As a final remark, it should be mentioned that the usually eluded spin-sink or effec-

tive conductance  $G_s$  acquires a precise definition within this model. It is proportional to  $\langle \mathbf{S}_\perp^2 \rangle$  and, thus, it accounts for the fact that not all local moments may be pointing in the direction of the magnetic field. Moreover, a direct evaluation of Eq. 6.8 shows that  $G_s$  is also proportional to  $1/\tau_\parallel$ , which is the longitudinal relaxation time. Consequently, the quantity  $G_s$  is related to spin-flip processes and unambiguously linked to mechanisms of magnon emission and absorption [57].

For the interpretation of our results, as stated earlier, the data was fitted considering two possible scenarios: that the magnetic surface state is i) a superparamagnet or ii) a 2D Heisenberg ferromagnet. It can be seen from Eqs. 6.13 and 6.14 that besides the spin expectation values  $\langle S_\parallel \rangle$ ,  $\langle \mathbf{S}_\perp \rangle$ , and their squares, there are additional unknown parameters to consider, namely: the spin diffusion length  $\lambda_{sd}$  and spin Hall angle  $\Theta_{SH}$  of Pt, the pre-factor  $\nu_F J_{sd}$ , and the Pt diffusion coefficient  $D$ . In this way, the fitting routine consists in calculating the spin expectation values as a function of the magnetic field at different temperatures (from 75K to 300K) according to one of the two models, and then fitting the listed quantities in order to reproduce the measured SMR curves. In addition, the temperature dependence of these quantities must be fully taken into account.

The temperature dependence of  $\Theta_{SH}$  is a topic that is discussed in detail in Section 5.1.3 from the previous Chapter. It is argued that, within the experimental evidence, the Pt spin Hall angle either decreases lightly or is almost independent of temperature [219, 222]. Specifically, recent reports [223, 224] suggest that in the intrinsic regime,  $\Theta_{SH}$  is proportional to the Pt longitudinal resistivity. Accordingly, in the fitting process, the spin Hall angle is constrained to vary with temperature as the Pt resistivity. The pre-factor  $\nu_F J_{sd}$  is considered to remain constant, since the exchange interaction between the metal  $s$  and oxide  $d$  electrons barely depends on temperature owing to the fact that this is a microscopic parameter not affected by particle statistics. In addition, the density of states at the Fermi level  $\nu_F$  should not vary significantly in the range of temperatures studied. Lastly, the number of spins per unit area  $n_s$  is also considered to be constant with temperature. As a consequence, the only parameters with a clear dependence on temperature in this fitting routine are  $\Theta_{SH}$ ,  $\lambda_{sd}$  and  $D$ , and as is discussed in the previous Chapter, the experimental evidence on the temperature dependence of  $\lambda_{sd}$  is multiple and somewhat controversial [219, 225]. However, in the intrinsic regime and within the Elliot-Yafet theory, it has been shown [223] that  $\lambda_{sd}$  is *inversely* proportional to the Pt longitudinal resistivity. As such, this specific temperature dependence is used for the fitting process <sup>5</sup>.

We start by introducing the results obtained for the superparamagnetic model. In this case, the expressions used for describing the spin expectation values are [270]

---

<sup>5</sup>The specific numerical programs responsible for all the fits presented in this Section have been developed by Dr. Carlos Frontera.

$$\langle S_{\parallel} \rangle = n\mu \left( \coth a - \frac{1}{a} \right), \quad (6.15)$$

$$\langle S_{\parallel}^2 \rangle = n\mu^2 \left( 1 + \frac{2}{a^2} - \frac{2}{a} \coth a \right), \quad (6.16)$$

$$\langle \mathbf{S}_{\perp}^2 \rangle = 2n\mu^2 \left( \frac{1}{a} \coth a - \frac{1}{a^2} \right), \quad (6.17)$$

where  $a = \mu H/kT$ ,  $\mu$  is the total magnetic moment of each cluster,  $n$  the density of clusters per unit area,  $k$  is Boltzmann's constant, and  $H$  and  $T$  the magnetic field and temperature, respectively <sup>6</sup>. It is worth noting that the parameter  $n$  is absorbed by  $n_s$  in Eq. 6.13 and always appear as a  $n_s \cdot n$  pre-factor (constant with temperature). Moreover, it is considered that  $\mu$  varies with temperature according to Bloch's  $T^{3/2}$  law [271],

$$\mu(T) = \mu(0) \left[ 1 - \left( \frac{T}{T_B} \right)^{3/2} \right], \quad (6.19)$$

being  $T_B$  the blocking temperature of the superparamagnetic clusters.

In Fig. 6.14, the fitted FDMR measurements in the  $z$  and  $y$  field directions as a function of temperature are shown. As can be observed, the fitting curves follow with great accuracy the experimental curves in the whole range of temperatures studied. Moreover, the negative MR in the  $y$  direction observed at 100K and below is also perfectly fitted within this model. It is worth mentioning that the fitting process is not free of error, as the experimental data has noise of the order of  $10^{-5}$  in units of  $\Delta\rho_L/\rho_L$ . In this way, a (fitted) vertical displacement in the experimental curves with rigid limits of  $\pm 10^{-5}$  has been introduced.

A total magnetic moment of  $31 \mu_B$  at 75K with a temperature dependence according to Bloch's  $T^{3/2}$  law (Eq. 6.19) is obtained. In addition, the fitted blocking

---

<sup>6</sup>Eq. 6.15 is the well-known Langevin equation of paramagnetism, and it was derived according to Cullity and Graham [270, p. 92]. There, the total spin in the direction of the magnetic field  $\langle S_{\parallel} \rangle$  is obtained from multiplying the number of clusters  $dn$  by the contribution  $\mu \cos \theta$  of each cluster, being  $\theta$  the angle between the magnetic moment and the magnetic field, followed by an integration over the total number of clusters, i.e.,

$$\langle S_{\parallel} \rangle = \int_0^n \mu \cos \theta dn. \quad (6.18)$$

Similarly,  $\langle S_{\parallel}^2 \rangle$  is obtained by substituting  $\mu \cos \theta$  in Eq. 6.18 by  $(\mu \cos \theta)^2$ . Likewise,  $\langle \mathbf{S}_{\perp}^2 \rangle$  can be obtained using  $(\mu \sin \theta)^2$  instead.

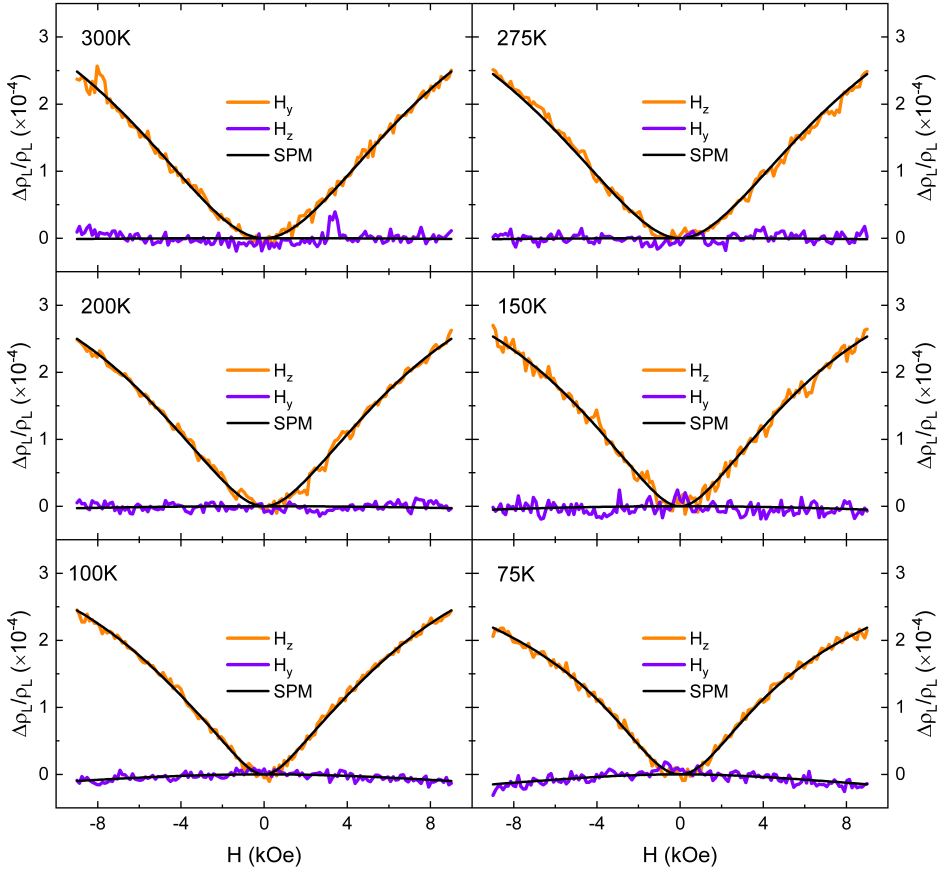


Figure 6.14: FDMR measurements with the magnetic field pointing in the  $z$  (orange) and  $y$  (violet) directions and the corresponding fits according to the superparamagnetic (SPM) model (black lines) as a function of temperature.

temperature is  $T_B = 640\text{K}$ . In Fig. 6.15, the temperature evolution of the spin diffusion length  $\lambda_{sd}$ , the diffusion coefficient  $D$ , and the spin Hall angle  $\Theta_{SH}$  is shown. As can be observed,  $D$  varies from roughly  $2.6 \times 10^{-6} \text{ m}^2 \cdot \text{s}^{-1}$  at 300K to  $3.0 \times 10^{-6} \text{ m}^2 \cdot \text{s}^{-1}$  at 75K, with a  $\approx 15\%$  variation in the whole range of temperatures studied. Likewise,  $\lambda_{sd}$  increases with decreasing temperature, ranging between 2.1 nm at 300K and 2.7 nm at 75K, whereas  $\Theta_{SH}$  changes from 3.6 % at 300K to 2.9 % at 75K. These values are in accordance with reported ones in similar systems [248, 223, 162].

Now we move on to present the fitting curves according to a 2D Heisenberg ferromagnet. This model obeys the following Hamiltonian,

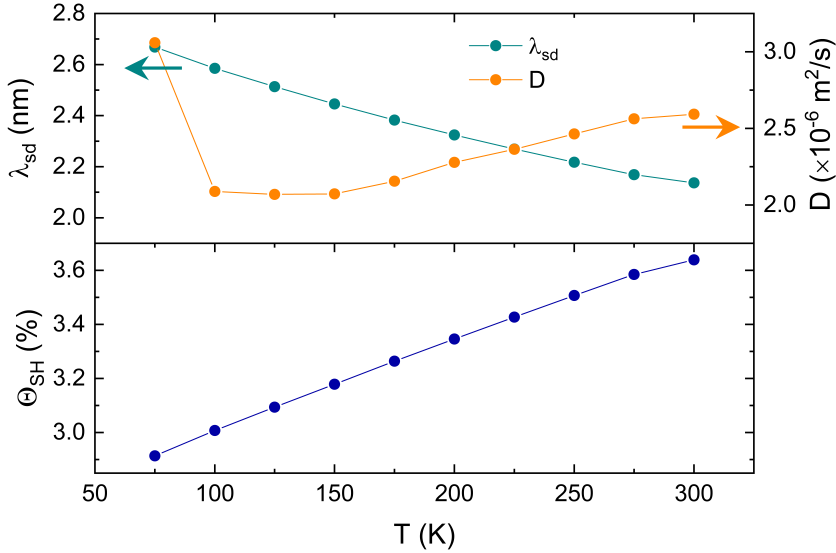


Figure 6.15: Fitted spin diffusion length  $\lambda_{sd}$ , diffusion coefficient  $D$  and spin Hall angle  $\Theta_{SH}$  of Pt and its evolution with temperature according to a superparamagnetic model.

$$\mathcal{H} = -J \sum_{\langle i,j \rangle} \mathbf{S}_i \cdot \mathbf{S}_j - \mathbf{H} \cdot \sum_{i=1}^N \mathbf{S}_i, \quad (6.20)$$

being  $J$  the exchange interaction between nearest neighbors spins  $\mathbf{S}_i$  and  $\mathbf{S}_j$ , and  $N$  the number of spins. The sum on the first term of the Hamiltonian extends over nearest neighbors, and the spins are considered to be in a surface. In this model, instead of analytical expressions, the spin expectation values were obtained by means of Montecarlo simulations. Specifically, a square lattice of  $200 \times 200$  spins has been used. The main drawback of this approach is that the fitting procedure has to be done at a fixed value of  $J$  and  $S$ . Therefore, in order to circumvent this issue, several simulations over a series of values of  $J$  and using three different values of  $S$  were performed. These  $S$  values correspond to the different valence states of Mn, i.e.,  $\text{Mn}^{+4}$  ( $S = 3/2$ ),  $\text{Mn}^{+3}$  ( $S = 2$ ), and  $\text{Mn}^{+2}$  ( $S = 5/2$ ). The resulting fitted quantities at 75K for different values of  $S$  and  $J$  are summarized in Fig. 6.16. As can be observed, the goodness of fit, which is represented by a  $\chi^2$  value <sup>7</sup> (see Fig. 6.16a),

<sup>7</sup>This quantity is defined as

$$\chi^2 = \sum [10^4 \cdot (\Delta\rho_L/\rho_L)_{\text{obs}} - 10^4 \cdot (\Delta\rho_L/\rho_L)_{\text{calc}}]^2.$$

being the first term on the right hand side the observed magnetoresistance amplitude and the second term the calculated one. In addition, the sum extends over all points along both  $y$  and  $z$  directions

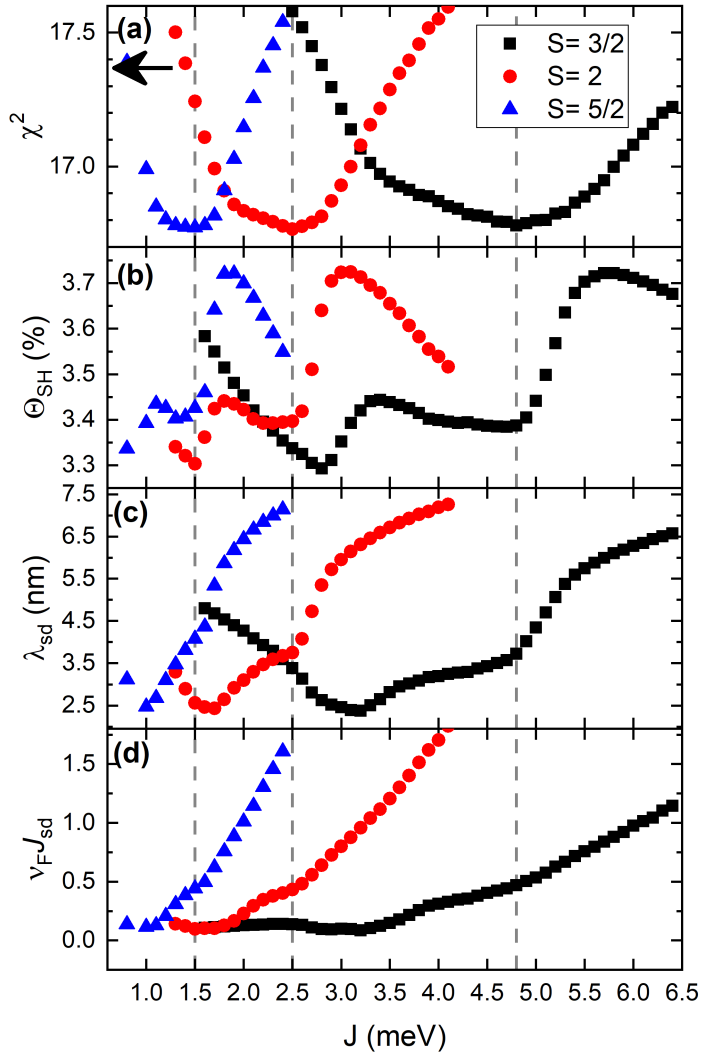


Figure 6.16: Fitted parameters at 75K as a function of the exchange constant  $J$  per each spin state  $S$ . The different panels show: the goodness of fit, represented by a  $\chi^2$  value (a); the spin Hall angle  $\Theta_{\text{SH}}$  (b); the spin diffusion length  $\lambda_{\text{sd}}$  (c); and the pre-factor  $\nu_{\text{F}} J_{\text{sd}}$  (d). The small black arrow at the top left corner of panel (a) marks the  $\chi^2$  value obtained in the superparamagnetic model.

has three distinct minima for each  $S$ . In fact, all three minima (represented by grey dashed vertical lines) are very similar. In addition, the three lowest  $\chi^2$  values are significantly better than the one obtained for the superparamagnetic model, which is

and all fitted temperatures.

represented by a black arrow at the top left corner of Fig. 6.16a.

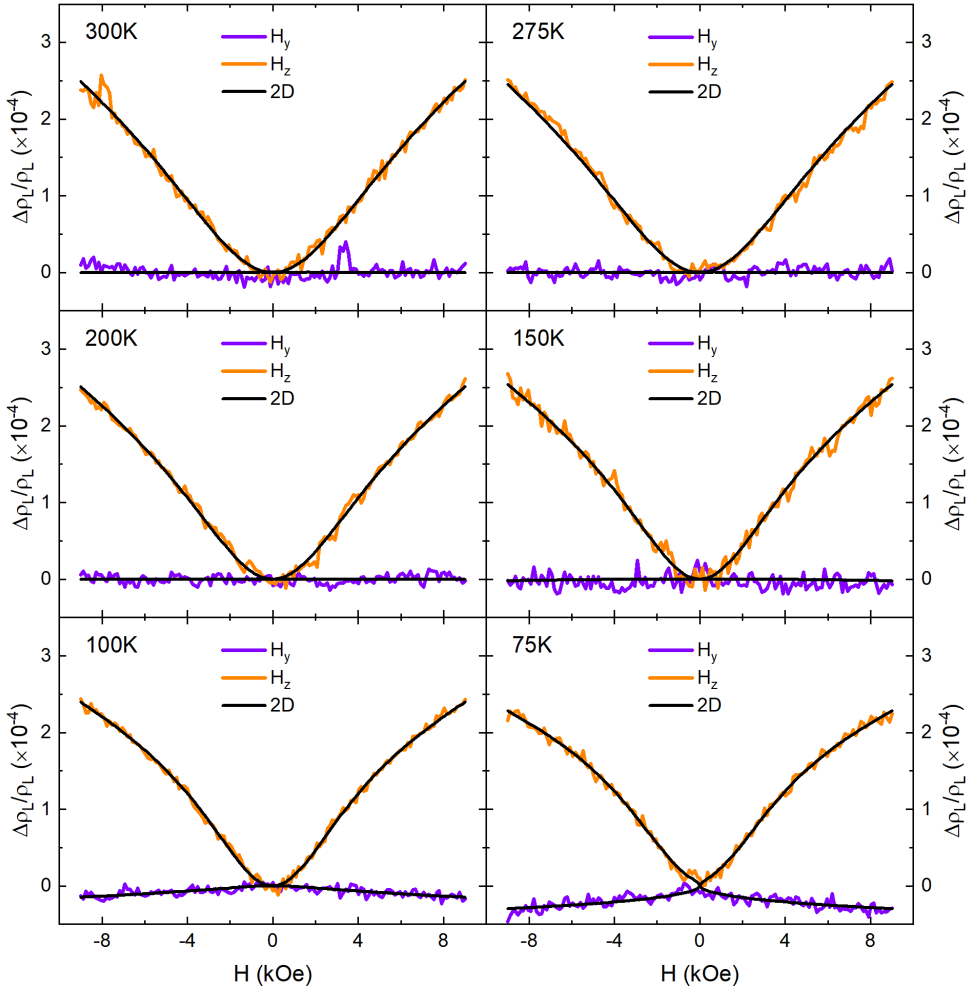


Figure 6.17: FDMR measurements with the magnetic field pointing in the  $z$  (orange) and  $y$  (violet) directions and the corresponding fits according to the 2D Heisenberg ferromagnetic (2D) model (black lines) as a function of temperature. In this case, the  $S = 2$  and  $J = 2.5$  meV values are used.

The fitted FDMR measurements in the  $z$  and  $y$  directions for the  $S = 2$  and  $J = 2.5$  meV case are shown in Fig. 6.17. As can be observed, the experimental curves are fitted with great precision in the whole range of temperatures. Moreover, the fitted  $\Theta_{SH}$ ,  $\lambda_{sd}$  and  $D$  as a function of temperature obtained in this model are shown in Fig. 6.18. In this case, the diffusion coefficient  $D$  ranges between roughly  $7 \times 10^{-6} \text{ m}^2 \cdot \text{s}^{-1}$  at 75K and  $6.6 \times 10^{-6} \text{ m}^2 \cdot \text{s}^{-1}$  at 300K, with a  $\approx 10\%$  variation in the whole



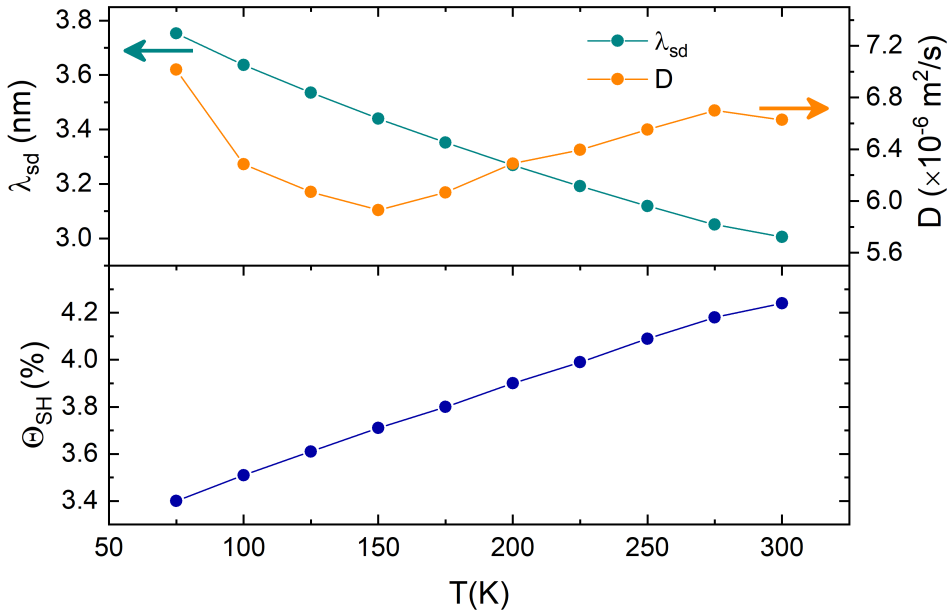


Figure 6.18: Fitted spin diffusion length  $\lambda_{sd}$ , diffusion coefficient  $D$  and spin Hall angle  $\Theta_{SH}$  of Pt and its evolution with temperature according to a 2D Heisenberg ferromagnetic model.

range of temperatures studied. Moreover, The spin diffusion length  $\lambda_{sd}$  varies from around 3.0 nm at 300K to roughly 3.8 nm at 75K, while the spin Hall angle  $\Theta_{SH}$  monotonically decreases from roughly 4.2 % at 300K to around 3.4 % at 75K. In overall, these values are consistently slightly larger than the ones found employing the superparamagnetic model (see Fig. 6.15), but are in accordance with reported values in similar systems. We can conclude that despite both models render similar results, the data is best fitted considering that the magnetic surface state of the LCMO film is a 2D Heisenberg ferromagnet.

As a final remark, it is worth comparing the  $\Theta_{SH}$  values obtained in this Section (Fig. 6.18) and those obtained in the previous Chapters. The  $\Theta_{SH}$  found in the Py/Pt system at 300K is  $1.55 \pm 0.48$  % (using  $\lambda_{sd} = 5$  nm) (see Fig. 4.21), whereas the  $\Theta_{SH}$  found in this Section at 300K is 4.2 % (and  $\lambda_{sd} = 3$  nm). This difference can be confidently attributed to the different resistivity values of Pt in each sample and is in accordance with reported values in the literature [162, 223]. Conversely, the difference between the  $\Theta_{SH}$  found in this Section and the ones found in the LMO/Pt system at 200K ( $4.5 \pm 2.4$  % using  $\lambda_{sd} = 3$  nm) and in the LSMO/Pt system at 250K ( $0.79 \pm 0.34$  % using  $\lambda_{sd} = 3$  nm) cannot be attributed to the resistivity values in each case. In Chapter 5, the spin Hall angle is determined from spin pumping experiments, while in here it is extracted from the fitting of SMR measurements,

which are strongly dependent on spin transfer torque (STT) phenomenology. Consequently, since spin pumping and STT are linked by the same physical phenomena, both methodologies should render similar results. Nevertheless, as discussed in the previous Chapter, some key parameters for the calculation of  $\Theta_{\text{SH}}$  in the LMO/Pt and LSMO/Pt systems are unknown or difficult to obtain due to extrinsic features of the samples (e.g., the difficulty to obtain a value for the spin mixing conductance; the observed lack of linearity between  $\Delta H$  and the resonance frequency, which arises from large extrinsic damping mechanisms in the samples; or the lack of knowledge regarding the frequency and temperature variation of the rf field). In conclusion, we attribute the observed difference in values to these extrinsic uncertainties and not to a methodological incompatibility of any kind. In fact, the good correspondence of values between the Py/Pt sample and the LCMO/Pt supports this interpretation.

## Summary and Conclusions

As highlighted in the introduction of this Thesis, the generation, manipulation and detection of spin currents is one of the major challenges of spintronics nowadays. In this regard, charge-spin interconversion processes play a very relevant role and having a set of materials and structures that maximize these processes is of vital importance. Moreover, it is of paramount importance to understand the fundamental physical principles on which these phenomena rely. As such, in this Thesis, the generation, manipulation, conversion, and detection of pure spin currents is probed in a wide variety of systems and structures composed by a ferromagnetic film in contact with a non-magnetic metallic capping layer. Specifically, four different ferromagnetic materials are studied: Py, LMO, LSMO, and LCMO; whereas two different non-magnetic conductors are employed: Pt and SIO. In Chapters 4 and 5, FMR spectroscopy is used for the dynamic generation of spin currents *via* spin pumping, and their subsequent detection is carried out by means of ISHE-induced voltage measurements. The archetypal bilayer Py/Pt is studied in Chapter 4, while LMO/Pt, LSMO/Pt, and LSMO/SIO are studied in Chapter 5. This last bilayer system is especially relevant in the context of this Thesis since it is the only system in which all the components are complex oxides. On the other hand, in Chapter 6, the novel spin Hall magnetoresistance is effectively measured in a bilayer system composed by the ferromagnetic insulating oxide LCMO in contact with Pt.

The common ground in all these effects is the presence of a high spin-orbit coupling (SOC) material in the system (i.e., Pt or SIO), and a magnetic film which acts as emitter or absorber of spin currents. It is in fact shown that the estimated spin Hall angle of Pt in all the systems studied is very similar whatsoever. Thus confirming that the physical mechanisms that give rise to these seemingly different phenomena are indeed the same. Moreover, it is foreseen the capability of these experimental pro-

cedures for estimating crucial spintronic figures of merit such as the aforementioned spin Hall angle, the spin diffusion length or the Gilbert damping parameter. The remaining part of this Chapter is devoted to summarize the obtained results along with the corresponding conclusions.

Chapter 4 deals with the generation of spin currents *via* spin pumping in the well-known Py/Pt bilayer system. This Chapter is divided into two main parts or sections: Section 4.1 comprises the temperature evolution of magnetization dynamics and spin pumping in Py films and Py/Pt bilayers with varying Pt thickness, while Section 4.2 deals with the spin pumping-induced spin currents and their detection through ISHE voltage measurements at room temperature. Despite the relatively wide knowledge relating these effects with Py/Pt systems, this Chapter is fundamental since it establishes the experimental foundations on which Chapter 5 is based. Moreover, it also serves as a platform for introducing very relevant topics such as magnetic relaxation and its evolution with temperature, the role of spin rectification effects in voltage measurements, or the importance of interface quality in spin-dependent transport phenomena, for instance.

In Section 4.1, the temperature dependence of the different quantities that govern magnetization dynamics is addressed. In this regard, it is inferred that the non-monotonic temperature dependence of the Gilbert damping parameter (Fig. 4.8) is mainly due to the influence of extrinsic magnetic relaxation contributions in the low-temperature regime. In addition, the lack of correlation between the Pt varying thickness and the enhancement of Gilbert damping upon Pt deposition is explained in terms of interfacial loss of spin coherence. This feature may result in the reduction or even suppression of spin current injection from the Py film into the Pt capping layer. Hence, it is proposed that this problem can be circumvented by directly measuring the ISHE transverse voltage signal across the sample generated by the spin current effectively injected into the Pt layer. ISHE is the conversion of pure spin currents into transverse charge currents. Consequently, if some spin current is being effectively injected from the Py film into the Pt layer, it may be converted to a transverse charge current and detected by electrical means. Nevertheless, despite this relative simplicity, it is well known that the spin pumping-induced voltage measured in metallic FM/NM systems may have contributions coming from the so-called spin rectification effects (SRE). These effects result from the synchronous coupling between an oscillating eddy current, induced in the FM by the rf magnetic field of the microwave, and an oscillating resistance, caused by magnetoresistance in the magnetic structure, giving place to the appearance of a dc voltage/current. In a system such as Py/Pt, the dominant SRE are anisotropic magnetoresistance (AMR) and anomalous Hall effect (AHE). The disentanglement of ISHE voltage signals from parasitic ones in spin pumping experiments is still a pending matter in the specialized community. Therefore, Section 4.2 comprises the transverse voltage measurements in Py and Py/Pt

bilayers and a novel experimental method for suppressing SRE parasitic signals in spin pumping experiments based on the geometry of the sample is proposed. Our hypothesis is that at sufficiently short sample widths ( $L$ ) along the transmission line, the circulating eddy current should be almost zero and, consequently, the SRE should vanish. On the other hand, the ISHE should not depend on the amount of current circulating in the Py film nor on the width of the film and, therefore, it should not be affected by the absence of current.

It is evidenced from the measurements regarding the transverse voltage dependence on the sample width  $L$  (see Figs. 4.17 and 4.18), that the voltage signal measured in the Py alone film is due predominantly to SRE: The measured voltage signal decreases with decreasing  $L$  until it completely vanishes below about  $L = 200 \mu\text{m}$ . Moreover, the voltage signal of the Si// Py/Pt system does also decrease with decreasing  $L$  but in this case it saturates at a positive constant value for  $L < 200 \mu\text{m}$ . Similarly, the voltage signal of an identical Si// Pt/Py bilayer with inverted stacking order decreases with decreasing  $L$  and saturates at a constant *negative* value for  $L < 200 \mu\text{m}$ , mirroring the signal of Si// Py/Pt. This inversion symmetry is in accordance with a purely ISHE-induced voltage signal considering the inversion of the spin current injection direction. Conversely, the SRE are independent of the spin current injection direction and, thus, cannot by themselves explain the observed behaviour at the smaller widths. Additionally, in order to gain insight into the behaviour of the induced current circulating in the Py layer, a numerical study of the SRE in the metallic Si// Py/Pt bilayer is performed to clarify their contribution to the measured transverse voltage signal. Three main conclusions are extracted from this numerical study: i) that the sign of the ISHE and SRE voltage signals are opposite to each other; ii) that the SRE are a combination of symmetric and antisymmetric Lorentzian curves (whilst ISHE has only symmetric contributions); and iii) that the reduction in the sample width  $L$  is accompanied by a progressive reduction of the SRE. A relevant message therein is that the detection of dc voltage in metallic FM/NM junctions under FMR conditions, regardless the symmetry presented by the signal, does not imply the detection of ISHE and/or spin pumping. The experimental methodology presented in this Chapter, thus, can be applied to any metallic FM/NM system in which SRE play a major role.

As a final remark, the spin Hall angle  $\Theta_{\text{SH}}$  of the Py/Pt bilayer is estimated from its ISHE transverse voltage curves according to Eq. 4.17. The spin diffusion length was fixed to 5 nm, according to the resistivity value of the Pt capping layer, and the obtained  $\Theta_{\text{SH}}$  equals to  $1.55 \pm 0.48 \%$  (Fig. 4.21), which is in accordance with reported values from the literature in Pt layers with similar resistivity. It is worth mentioning that future experiments could focus on the ISHE voltage evolution with temperature. For instance, at 300K, the ISHE voltage signal of Py alone films is negligible, however, self-induced ISHE or magnonic charge pumping mechanisms might arise at lower

temperatures. The experimental methodology and samples presented in this Section are thus an optimal platform for probing these elusive spintronic effects.

Now we move on to present the results obtained in Chapter 5, which deals with spin pumping and ISHE voltage measurements but employing complex oxide heterostructures. It is divided into two main sections, each related to a set of complex oxides. Section 5.1 covers the spin pumping-induced ISHE voltage measurements as a function of temperature in LMO/Pt, while Section 5.2 focuses on LSMO/Pt and LSMO/SIO bilayer systems. The complex oxide LMO was grown by means of polymer assisted deposition (a chemical deposition method), resulting in a robust ferromagnetic layer with high  $T_c$  ( $\approx 320\text{K}$ ) and saturation magnetization close to the theoretical value ( $\approx 550 \text{ emu/cm}^3$ ). Affordable chemical deposition methods are desirable because they are easier to scale up and offer the possibility to grow films over large areas at low cost while allowing an easy tuning of stoichiometry. However, there has been some concerns regarding the suitability of chemically deposited thin films for challenging applications which require microstructural quality and sharp interfaces, as in spintronics.

Prior to the measurement of spin pumping-induced ISHE voltage in LMO/Pt bilayers, however, the quality of the LMO/Pt interface was clarified. On this behalf, the STO//LMO/Pt system was analysed by means of scanning transmission electron microscopy (STEM). A sharp and defect-free LMO/Pt interface is observed, being the LMO film of excellent crystalline quality (Fig. 5.4). Nevertheless, the electron energy loss spectroscopy (EELS) analysis near the STO//LMO bottom interface shows an overlapping of Mn and Ti atoms, indicative of cationic diffusion (Fig. 5.5). It is stated that this interfacial diffusion is probably related to the high temperature used in the LMO deposition crystallization process ( $990^\circ\text{C}$ ).

The FMR characterization of the LMO film before and after the Pt deposition at 200K reveals no difference of damping whatsoever. Additionally, the expected linear dependence between the resonance linewidth  $\Delta H$  and resonance frequency  $f_{\text{res}}$  is loosely followed (see Fig. 5.13). In overall, these observations are indicative of the presence of large extrinsic magnetic relaxation contributions in the system, which can be in accordance with the Ti interdiffusion observed at the STO//LMO interface. In fact, the fitting of the curves relating  $f_{\text{res}}$  and the resonance field  $H_{\text{res}}$  according to Kittel's equation can only be achieved if a second order surface/interface magnetic anisotropy term is included. It is suggested that this term arises from the STO//LMO interface, and not from the LMO/Pt one, which is clearly more homogeneous and sharp. The effect of a large anisotropy field at this interface is the pinning of the local magnetization, resulting in an alteration of the spin precession near the interface, and giving rise to an enhancement of  $\Delta H$ . This anisotropy term is equally observed in the whole range of temperatures studied (from 280K to 100K). In addition, both Gilbert

damping and resonance linewidth (irrespective of the frequency studied) follow a non-monotonic dependence on temperature (Figs. 5.19 and 5.20, respectively), being maximum at 280K, near  $T_c$ , then decreasing down to a minimum at roughly 200K and, finally, increasing again up to 100K. This behaviour is correlated with the presence of extrinsic relaxation terms, as already reported in similar systems.

At the same time, the observation of clear transverse voltage signals consistent with ISHE in the whole range of temperatures (Fig. 5.21) indicates that the absence of enhancement of damping upon Pt deposition by no means precludes the injection of pure spin currents *via* spin pumping. All the transverse voltage signal lines observed are positive and highly symmetric (very similar to those observed for ISHE in Chapter 4), and the contributions coming from SRE in this system are expected to be scarce due to the highly resistive nature of LMO film. Additionally, thermoelectric contributions to the voltage are also neglected since the voltage measured reverses sign upon field inversion, in accordance with the symmetry of ISHE (see Fig. 5.15). As such, we are confident that the main source of voltage in these system stems from ISHE. In addition, it is observed that, in overall, the ISHE amplitude (i.e., peak value of the voltage lines) follows a non-monotonic dependence on temperature similar to a mirror image of that observed in the damping or  $\Delta H$ : it is minimal at 280K, near  $T_c$ , then increases up to a maximum at about 200K, and finally it decreases with decreasing temperature down to 100K, below which it vanishes. In order to gain insight into this dependence, the specific temperature dependence of the different parameters which give rise to the ISHE voltage (see Eq. 5.2) is analysed, and owing to the observed results and in accordance with similarly reported observations in similar systems, it is concluded that the strong reduction of the ISHE voltage signals below about 100K is mostly attributed to the increase of damping (and resonance linewidth), triggered by extrinsic relaxation mechanisms occurring in the film.

Finally, considering the spin diffusion length equal to 3 nm, the spin Hall angle  $\Theta_{\text{SH}}$  at 200K in this system was estimated (Fig. 5.26), resulting in a mean value of  $4.5 \pm 2.4$  %. In conclusion, the suitability of polymer-assisted deposited LMO epitaxial thin films for spintronic-related applications is demonstrated. Samples show excellent crystalline and interface quality, thus making LMO a promising perovskite building block for all-oxide multifunctional high frequency spintronic devices.

In the second part of this Chapter (Section 5.2) the suitability of other complex oxides for spin injectors/detectors is investigated. In a first step the performance of the perovskite oxide LSMO as spin injector are investigated in LSMO/Pt bilayers. In this regard, spin pumping-induced ISHE transverse voltage measurements in a LSMO/Pt bilayer at 250K are performed. The obtained results are quite similar to those observed in the LMO/Pt case. The spin Hall angle of Pt in LSMO/Pt bilayers is estimated to be around  $0.8 \pm 0.3$  % (Fig. 5.33) (assuming that  $\lambda_{\text{sd}} = 3$

nm, according to the estimated resistivity of the Pt layer), which is similar to that obtained in the Py/Pt system in Chapter 4. Thus, the spin injection capabilities of LSMO in contact with Pt are demonstrated. In addition, SRE and thermoelectric effects are found to be negligible, thus indicating that the main source of voltage in this systems stems from ISHE. In a second step, the study of spin injection/detection processes in an all-oxide heterostructure is addressed. A material with presumible large spin-orbit interaction, such as SIO, is introduced as spin detector. For this purpose, LSMO/SIO bilayers prepared by using RF sputtering are used. The ISHE transverse voltage signals measured in the SIO layer demonstrates both the suitability of LSMO as spin injector and SIO as spin detector.

To go a step further and to explore the potential role of the interface, two different SIO capping layers with the same thickness (9 nm) are deposited. One is deposited *In situ*, while the other one is deposited *Ex situ*. It is observed that both samples are very similar to each other in terms of magnetic properties and crystal quality. Nevertheless, there is a clear difference in the surface morphology of each film (and presumably also at the interface): The SIO film deposited *Ex situ* is flat and follows the morphology of the LSMO film underneath, whereas the one deposited *In situ* presents randomly scattered clusters of square-shaped structures on top of the LSMO surface (see Fig. 5.36). This difference is later correlated with the observation of an increased damping in the *In situ* sample. In overall, however, the magnetodynamical parameters of both samples are very similar to each other and do also present the large surface/interface anisotropy term observed in both LMO/Pt and LSMO/Pt bilayer systems. However, the transverse ISHE voltage signals in these two samples are hardly separable from noise (see Fig. 5.39).

To try to improve the signal to noise ratio, a thinner bilayer is prepared depositing the SIO layer *Ex situ*. The FMR characterization of this new bilayer reveals that it shares the same magnetodynamical properties as their thicker counterparts, including the large interface/surface anisotropy term. Regarding its surface morphology, it is flat and follows the surface of the LSMO film underneath (Fig. 5.42). The 250K ISHE voltage signal lines, however, are clearly appreciated in the whole range of frequencies and are positively-valued and highly symmetric (see Fig. 5.45), although smaller in magnitude with respect to those obtained in Pt in all the previous systems. It is further concluded that the main contribution to these voltage signals stems from ISHE, being the SRE and thermal effects negligible. Moreover, the spin Hall angle of SIO is determined to be  $\Theta_{\text{SH}} = 1.1 \pm 0.5 \%$  (Fig. 5.47), which is remarkably similar to that obtained for the well-known Py/Pt system. At the time of writing and as far as we know, this is the first clear evidence of spin pumping-induced ISHE voltage reported in a SIO capping film, thus suggesting that SIO could be a good spin-Hall material. This result may be envisioned as a first step towards the development of high-quality spin-to-charge conversion devices based on all-oxide heterostructures.



Finally, in Chapter 6, the novel spin Hall magnetoresistance (SMR) is measured in a system composed by the ferromagnetic insulator (FMI) oxide LCMO and Pt. In this case, a charge current flowing in the Pt film is converted to a spin current by means of SHE and directed towards the LCMO/Pt interface, resulting in a net spin accumulation within the Pt film. The different resistive states which result in SMR arise from the kind of interaction between the spin current spin polarization direction  $\hat{\sigma}$  and the magnetization vector  $\mathbf{M}$ : when  $\hat{\sigma} \parallel \mathbf{M}$  the spin current is reflected back to the NM layer, whereas it is completely absorbed by the FMI film when  $\hat{\sigma} \perp \mathbf{M}$  via spin transfer torque (STT). Consequently, although the experimental methodology and techniques involved in these measurements are very different from those followed in Chapters 4 and 5, the parameters and physical principles which govern all these effects are the same. It is worth recalling that spin pumping and STT are in fact reciprocal effects.

Experimentally, a series of angular-dependent (ADMR) and field-dependent (FDMR) magnetoresistance measurements were carried out as a function of temperature (above and below  $T_c$ ) for evaluating SMR in our films (see Figs. 6.7 and 6.8). It is observed, however, that the obtained results present conflicting discrepancies with conventional SMR theory. In spite of the fact that the observed angular symmetry is in accordance with SMR (thus excluding AMR from our samples), it is also detected above  $T_c$  with no reduction of amplitude. In fact, the SMR amplitude is nearly constant in the range of temperatures between 320K and  $\approx 50$ K (see Fig. 6.10). In addition to that, it is observed that it increases with increasing the magnetic field, even when the LCMO film should be saturated. Moreover, no trace of hysteresis is observed in the whole range of temperatures (Fig. 6.9) and, below  $T < 100$ K, an unexpected negative magnetoresistance is observed when the magnetization and the spin polarization direction should be parallel (i.e., full reflection situation). The detailed reasoning of these results coupled with different observations in similar systems in the literature leads us to believe that the surface magnetic state of the LCMO film is decoupled from its bulk.

This observation, which is suggested solely from the SMR measurements, is further confirmed by STEM and EELS analyses of the LCMO/Pt interface. This analysis evidences the excellent microstructural quality of the LCMO film. However, it is found that Co ions are missing in the last two atomic planes of the layer. Thus, a single perovskite  $\text{LaMnO}_3$  structure is found at the interface, magnetically decoupled from the rest of the LCMO film and with different magnetic properties. As a result, it becomes necessary to go beyond the conventional picture of FMI/NM SMR to interpret the obtained results according to the actual magnetic state of the interfacial layers. Therefore, a theoretical model based on the  $sd$  coupling between the  $s$  electrons of the NM film and localized  $d$  moments of the magnetic layer underneath is used (see Fig. 6.13). In this model, the crucial parameters which govern spin transport at the

interface (e.g., spin-mixing conductances) are expressed in terms of the  $sd$  coupling and the spin expectation values  $\langle S_{\parallel} \rangle$  and  $\langle S_{\perp} \rangle$  in the magnetic film, which ultimately depend on its specific magnetic state (see Eqs. 6.13 and 6.14). Two different models are used to fit the data, namely, that the surface magnetic state of the LCMO film behave like i) a superparamagnet, and ii) a 2D Heisenberg ferromagnet. By direct comparison and by looking at the fits rendered in each case (see Figs. 6.14 and 6.17) it is finally concluded that the 2D Heisenberg model is best suited for describing the experimental results. The fitted spin Hall angle  $\Theta_{\text{SH}}$ , which scales with temperature as the Pt resistivity  $\rho$ , varies from 3.4 % at 75K to 4.2 % at 300K, whereas the spin diffusion length varies from roughly 3 nm at 300K to about 3.8 nm at 75K, with a temperature variation according to  $1/\rho$  (see Fig. 6.18).

As a final remark, it should be noted that since interfacial LCMO layers are magnetically decoupled from the rest of the LCMO film, the strong perpendicular magnetic anisotropy of LCMO under tensile strain does not play any role on SMR measurements. In fact, no differences are observed in SMR measurements in LCMO films grown on top of LAO substrates (under compressive strain) with respect to those grown on STO substrates (under tensile strain).

# List of Publications

- Wang, H., Pomar, A., Martín-Rio, S., Frontera, C., Mestres, N., & Martínez, B. (2019). Dynamic magnetic properties and spin pumping in polymer-assisted-deposited  $\text{La}_{0.92}\text{MnO}_3$  thin films. *Journal of Materials Chemistry C*, 7(40), 12633-12640.
- Martín-Rio, S., Pomar, A., Balcells, L., Bozzo, B., Frontera, C., & Martínez, B. (2020). Temperature dependence of spin pumping and inverse spin Hall effect in permalloy/Pt bilayers. *Journal of Magnetism and Magnetic Materials*, 500, 166319.
- Martín-Rio, S., Frontera, C., Pomar, A., Balcells, L., & Martinez, B. (2022). Suppression of spin rectification effects in spin pumping experiments. *Scientific reports*, 12(1), 1-9.
- Martín-Rio, S., Pomar, A., Frontera, C., Wang, H., Manzorro, R., Magen, C., ... & Martinez, B. (2022). Spin to charge conversion in chemically deposited epitaxial  $\text{La}_{0.9}\text{MnO}_3$  thin films capped with Pt. *Journal of Materials Chemistry C*.

Currently, an article entitled *Interfacial magnetic features of  $\text{La}_2\text{CoMnO}_6/\text{Pt}$  bilayers studied by using spin-Hall magnetoresistance* has been submitted for publication and another one, related to the measurements in LSMO/Pt and LSMO/SIO bilayer systems is in preparation.



## Experimental Techniques

### A.1 Preparation of Films

#### A.1.1 Magnetron Sputtering Deposition

Excluding  $\text{La}_{0.92}\text{MnO}_3$ , which has been chemically prepared by polymer assisted deposition (PAD), all the other films presented in this Thesis (i.e., Py, Pt,  $\text{La}_{2/3}\text{Sr}_{1/3}\text{MnO}_3$ ,  $\text{SrIrO}_3$ , and  $\text{La}_2\text{CoMnO}_6$ ) have been grown by means of sputtering deposition, which belongs to the realm of physical vapour deposition techniques. Sputtering is the process by which a beam of ions is accelerated towards the surface of a solid (target material) in order to eject particles (atoms, ions, molecules, or clusters) from it. The sputtered target material, now in a gas-like phase, can condensate, nucleate, and grow as a thin film onto the so-called substrate surface. Specifically, in this Thesis we employed three different substrates, namely,  $\text{Si/SiO}_2$ ,  $\text{SrTiO}_3$ , and  $\text{LaAlO}_3$ .

Generally, the target material is placed on top of a negatively charged electrode (cathode) while the substrate acts as the positively charged anode. In the presence of gas in the chamber, a voltage bias difference between target and substrate can effectively ionize the atoms of this gas, resulting in a visible discharge glow plasma across the system. The positively charged atoms are attracted to the negatively charged target, giving place to the sputtering process. An important quantity in sputtering systems is the sputtering yield, which is defined as the mean number of atoms removed from the target surface for each incident ion [272]. In order to enhance this quantity and gain efficiency, magnetron sputtering techniques were introduced in the 1970s. The basic idea is to trap and limit the trajectories of secondary electrons

ejected from the target surface by the working gas ions using a combination of electric and magnetic fields near the surface of the target. These magnetic field lines are generated by placing a set of permanent magnets behind the target cathode. This is justified by the fact that secondary electrons removed from the target material during sputtering can effectively ionize working gas atoms nearby by scattering events, and the fact that these electrons are constrained to the target simply implies an increase of the scattering probability [273]. In Fig. A.1, a basic schematic diagram of magnetron sputtering is shown.

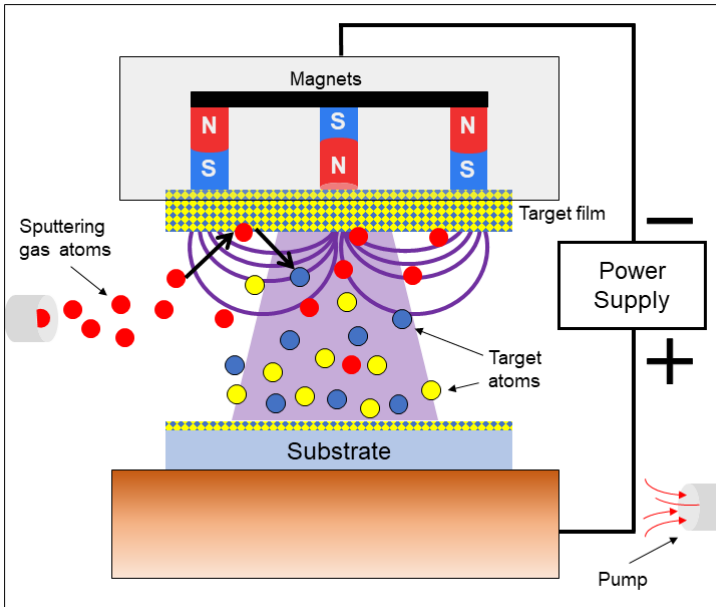


Figure A.1: Schematic diagram of the basic features of magnetron sputtering deposition technique. A discharge glow due to the voltage bias difference between target and substrate ionize the working gas atoms (red circles). Subsequently, these ions are accelerated towards the negatively charged target in order to eject particles (atoms, ions, molecules, or clusters) from it. The sputtered atoms (yellow and blue circles) are diffused across the chamber and deposited onto the substrate.

The deposition of thin films by magnetron sputtering can be controlled by adjusting the deposition conditions, which depend on a variety of parameters. These parameters include the working gas pressure, power, substrate temperature, or target-to-substrate distance. Prior to the deposition process, however, it is important to have a very low base pressure in the sputtering chamber. In our equipment, this pressure can be as low as  $10^{-6}$  Torr. This is important in order to avoid the presence of gas impurities in the chamber, which would ultimately hamper the deposition process and even chemically interact with sputtered target atoms. This is specially crucial

when growing films that are easily (and undesirable) oxidized, such as Py. Once the base pressure has been attained, the next step is to select the desired deposition temperature and working gas pressure. In this Thesis, both Py and Pt are grown at room temperature, while  $\text{La}_{2/3}\text{Sr}_{1/3}\text{MnO}_3$ ,  $\text{SrIrO}_3$ , and  $\text{La}_2\text{CoMnO}_6$  are deposited at  $900^\circ\text{C}$ . This temperature is achieved by means of a heater placed below the substrate. The deposition temperature enhances the energy of atoms at the substrate surface, thus increasing their mobility and favouring nucleation. In the case of lanthanum manganite films, a thermal treatment after deposition is also applied in order to obtain the desired chemical stoichiometry in our films. Moreover, the working gas pressure is controlled by the amount of gas allowed to flow into the chamber and the velocity of the turbomolecular pump. The specific pressure used in each film is indicated in the main text, but it generally ranges between  $10^{-3} - 10^{-1}$  Torr. In our equipment we primarily use argon, oxygen, or a 95:5 mixing of argon and hydrogen depending on the film to be deposited. Another important parameter is power, which is directly proportional to the bias voltage difference between target and substrate. In this way, an increase of voltage results in the acceleration of sputtering ions which in overall increases the deposition rate. In addition, it is worth mentioning that the bias voltage can be set as DC or AC (radiofrequency, or RF). DC bias voltage can be used in conductive targets but not in dielectrics due to charging effects. Thus, RF voltage is more convenient in the latter case. In RF the cathode remains negative due to a self-bias voltage produced by the difference in mobility between electrons and ions [274]. In our particular case, both Py and Pt are deposited in DC mode, while  $\text{La}_{2/3}\text{Sr}_{1/3}\text{MnO}_3$ ,  $\text{SrIrO}_3$ , and  $\text{La}_2\text{CoMnO}_6$  (which have significantly higher resistance) are grown in RF mode. Nowadays, magnetron sputtering has spread worldwide and applied to many different fields of academic and industrial applications, ranging from decorative coatings to functional ones, including medical applications such as orthopedic implants coatings or the coating of gold nanoparticles with different kinds of biocompatible materials for drug delivery applications, for example [273].

### A.1.2 Photolithography and Ion Milling

Lithographic processes are very relevant for the realization of the work presented in this Thesis. In Chapter 4 we used optical lithography to make the stripe-shaped and fringed patterns onto Py and Py/Pt systems (see Fig. 4.14). In Chapter 5, lithography is used as a first step towards the material removal process at the corners of the chemically growth  $\text{La}_{0.92}\text{MnO}_3$  sample (see Fig. 5.6). Finally, in Chapter 6 it is used for patterning the Hall bar on the  $\text{La}_2\text{CoMnO}_6/\text{Pt}$  system (see Fig. 6.5).

The lithographic processes shown in this Thesis are performed in the cleanroom facilities of the ICMAB-CSIC [275]. As is mentioned in the main text, the optical lithography micro-writer equipment, Micro-writer ML, is from Durham Magneto

Optics LTD, while the ion miller belongs to TSST. The combination of these two techniques allows us to imprint patterns on samples. The overall process requires a series of different steps. The first step corresponds to the deposition of a negative photoresist (Shipley s1813) on the sample surface by means of spin coating. It is called negative because it undergoes a chemical transformation upon radiation exposition. In this particular case we use UV radiation. The next step is to radiate the regions of the sample which do not belong to the desired pattern. Then, the sample is immersed into a surfactant containing developer solution which remove the exposed regions of the photoresist. At this point, the next step consists in taking the sample and placing it in the ion milling equipment, which attacks the sample surface by argon ions bombardment for a given time. Finally, the remaining photoresist can be chemically removed by a combination of acetone and ethanol. These steps are schematically presented in Fig. A.2.

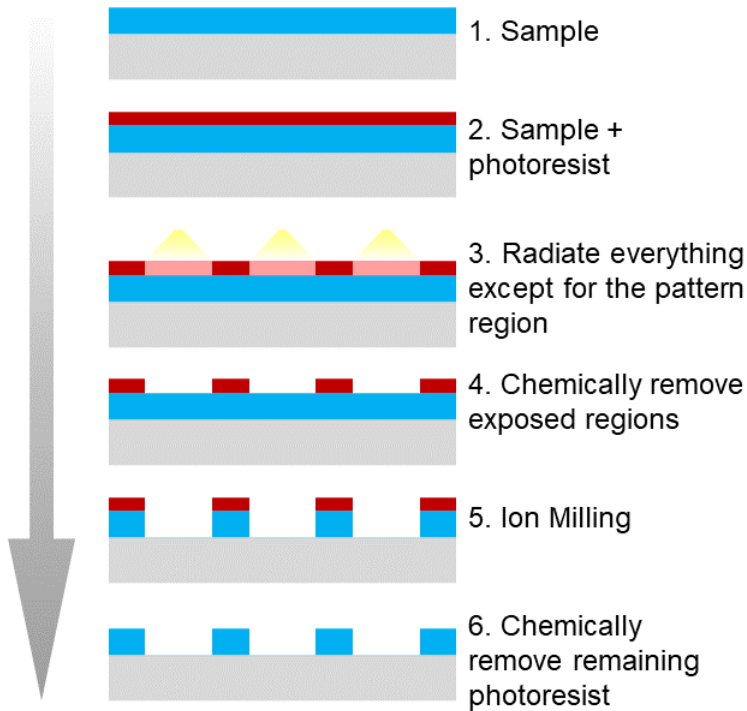


Figure A.2: Schematic diagram of the steps followed in the lithographic and ion milling processes.



## A.2 Magnetic and Transport Characterization Techniques

### A.2.1 SQUID Magnetometry

In this thesis we use Quantum Design's MPMS-XL SQUID and MPMS-3 magnetometers, which allow us to measure the magnetization dependence on both temperature and magnetic field magnitude. The temperature range of the equipment is between 4.2K and 400K and the magnetic field can be as high as  $\pm 9$  T. The magnetic field sensitivity is about  $10^{-5}$  emu, and normally the magnetization is expressed in  $\text{emu}/\text{cm}^3$ , i.e., normalized with the sample volume.

So far, the superconducting quantum interference device (SQUID) is the most accurate tool for measuring magnetization and it is used in a broad range of applications [276]. The magnetization is measured by placing the magnetic sample in so-called pickup coils or loops (see Fig. A.3a) and repeatedly moving it up and down across them. This movement induces a change of the magnetic flux through the pick-up coils due to the presence of the sample and its magnetic properties. This magnetic flux is then converted to an electric current and transferred to the input coils which, in turn, generate a magnetic flux which couples to the SQUID sensor [277]. The basic features of the SQUID sensor are shown in Fig. A.3b, and as can be observed, it is made of a superconducting ring with two Josephson junctions. When an external magnetic flux is coupled to the SQUID loop, the voltage drop across the junctions changes accordingly [278]. Of course, this external magnetic flux originates from and depends on the magnetic sample being measured. The resulting output voltage is amplified and proportional to the magnetic moment of the sample.

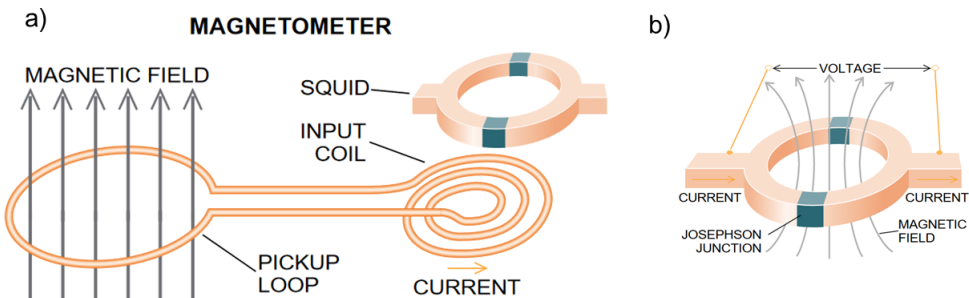


Figure A.3: a) Schematic diagram of SQUID magnetometry. b) Basics features of the SQUID. These images have been retrieved from Ref. [279].

As is mentioned at the beginning of this Section, SQUID magnetometry measures the magnetization of a sample as a function of temperature and magnetic field. The measurements as a function of temperature result in  $M(T)$  curves and are very relevant for our work since they characterize with great precision the Curie temperature of our ferromagnetic layers and the temperature evolution of the magnetization. The usual approach in this kind of measurements is to fix the magnetic field amplitude at some value high enough to saturate the magnetization of the sample. Then, the temperature is set to slowly increase from 10K to about 350K, depending on each case, and the magnetization value is recorded accordingly. Another possible approach is to perform zero-field-cooled/field-cooled (zfc/fc) curves, although it is only used in the characterization of the  $\text{La}_2\text{CoMnO}_6$  films and, in our particular case, it does not result in additional information with respect to ordinary  $M(T)$  curves. For obtaining the zfc/fc curves, the magnetization is recorded by first cooling the sample without applying any external field. Then, it is heated under the application of some magnetic field, resulting in the zfc curve. The fc curve is obtained by cooling the sample under the application of some field and then recording the magnetization when heating up the sample.

The magnetization dependence on the magnetic field amplitude results in  $M(H)$  curves or hysteresis loops. In these measurements, at a given fixed temperature, the magnetic field is swept between  $H_{\max}$  and  $-H_{\max}$  back and forth, where  $H_{\max}$  corresponds to a magnetic field value large enough to saturate the sample. The saturation magnetization and coercive field at a given temperature can be easily obtained from the hysteresis loops. This is why these kind of measurements are so important for this Thesis. Usually, the diamagnetic contribution of the substrate overlaps and dominates the signal. However, since this contribution depends linearly on the field as  $M = \chi H$ , being  $\chi < 0$  the magnetic susceptibility of the substrate, it can be easily corrected when processing the data. Moreover, a lot of information can be gathered by analyzing the shape of the hysteresis loop. For instance, the easy and hard axis or secondary magnetic phases present in the sample can be determined from it.

### A.2.2 Ferromagnetic Resonance Spectroscopy

In Chapter 3 the theory of ferromagnetic resonance is reviewed. It is shown how the resonance frequency is related to both the resonance field  $H_{\text{res}}$  and linewidth  $\Delta H$ , and how these relations allow us to extract the fundamental magnetodynamical parameters of the system. Broadband ferromagnetic resonance (FMR) spectroscopy is an experimental technique specially designed for measuring the FMR absorption curves of a given ferromagnetic specimen. The usual routine followed in this Thesis consists in fixing the rf which excites magnetic modes in the sample, while sweeping

the magnitude of the static magnetic field, resulting in a specific FMR absorption curve at each resonance frequency. In this Thesis, we use the commercial CryoFMR spectrometer from NanOsc Instruments. A schematic diagram of the experimental setup is shown in Fig. A.4a. As can be observed, an electromagnet generates the static magnetic field across the sample holder, whereas a set of Helmholtz coils generate an AC field in the same direction of the static field for lock-in detection. The rf magnetic field responsible for FMR is supplied by a coplanar waveguide (CPW), and the sample would be placed right on top of it. At resonance conditions, the sample absorbs energy from the CPW and the CPW transmission coefficient decreases accordingly. The transmission coefficient can be defined as the ratio between the incoming and transmitted signals.

While the measurement itself is made by the FMR spectrometer, the control of temperature and magnetic field in these experiments is achieved by a Quantum Design's PPMS. PPMS stands for Physical Properties Measurement System, and is a multi-probe station which, through a pinout system, allows to contact a sample electrically and carry out a series of transport measurements as a function of magnetic field, temperature and field orientation. The specific FMR probe insert for measuring the sample in the PPMS is shown in Fig. A.4b. In this figure, the set of Helmholtz coils are clearly appreciated. In addition, this sample holder has a temperature sensor different from that of the PPMS in order to have a detailed control of the temperature near the sample. The sample placed on the sample holder (which includes the CPW) is shown in Fig. A.4c. PPMS is fundamental since it allows us carry out FMR spectroscopy measurements in a wide range of temperatures (from 10K to room temperature) and magnetic fields ( $\pm 9$  T).

In order to improve the signal-to-noise ratio of the measurement, lock-in amplification is used for detecting FMR signals. Lock-in amplifiers take advantage of the time-dependence of the signals to extract them from noisy environments, and today is one of the most widely used experimental tools in physics and engineering laboratories [281]. A schematic diagram of its working principle is shown in Fig. A.5. In lock-in amplifiers, a periodic AC voltage input signal (along with the noise) is multiplied by an AC reference signal and a  $90^\circ$  phase-shifted version of the same reference signal. The multiplication of two AC signals results in the sum of two signals with frequencies equal to the sum and difference of  $f_{\text{ref}}$  and  $f_{\text{in}}$ , being the frequency of the reference and input signals, respectively. When  $f_{\text{ref}} = f_{\text{in}}$ , the multiplication results in the sum of a DC component and an AC component with frequency equal to  $2f_{\text{in}}$ . The desired DC component is further isolated from the AC component by applying a low pass filter. It is called *in-phase* or *X* component to the DC component resulting from the multiplication of the input signal with the reference signal, and *quadrature* or *Y* component to the DC component resulting from the multiplication of the input signal with the  $90^\circ$  phase-shifted version of the reference signal. The overall input

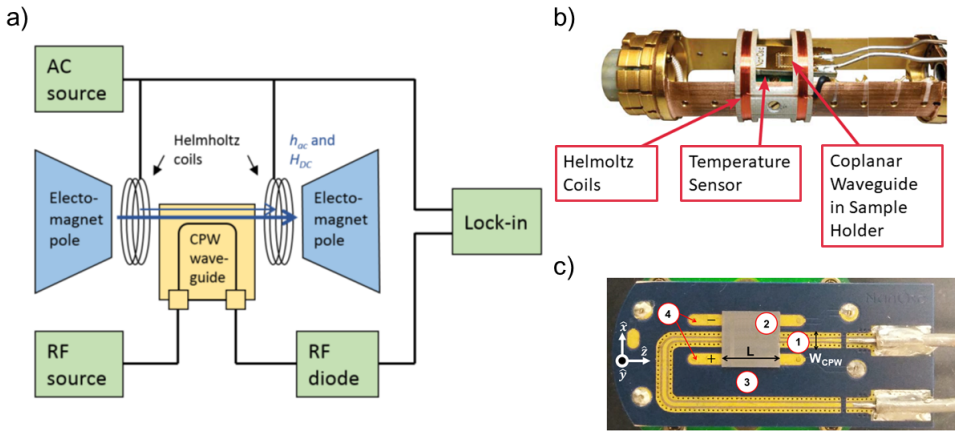


Figure A.4: a) Schematic diagram of the basic elements that compose FMR spectroscopy. This image has been retrieved from the FMR spectroscope user’s manual by NanOsc. b) Actual image of the sample holder placed in the probe insert for measuring in the PPMS. This image has been retrieved from Ref. [280]. c) Image of the sample placed on top of the sample holder’s coplanar waveguide. This is the same image as Fig. 4.9 from Chapter 4 and the numbers that appear on the image are defined in there. This sample holder is the “CPW PPMS IP ISHE” model produced by NanOsc Instruments [155].

signal amplitude  $R$  then is equal to  $\sqrt{X^2 + Y^2}$  (see Fig. A.5b). These are the basic principles of lock-in amplification.

For the lock-in FMR detection shown in Fig. A.4a, a pair of Helmholtz coils connected to an AC source are used to generate a small AC magnetic field parallel to the applied static magnetic field generated by the electromagnet. The frequency of this AC field is 490 Hz, which is very small compared to the GHz frequencies used in the experiment. The effect of this added component is the modulation of the FMR response, so that the FMR intensity  $S$  varies as  $dS/dH$ . The rf part of the output signal coming from the CPW is eliminated by using an RF diode, and the modulated response is then recovered using lock-in amplification with the AC source acting as the reference signal. In this experimental setup, due to the effect of the modulation, the FMR absorption amplitude measured is in fact the derivative of the absorption peak.

In Chapter 3, it is shown that the FMR absorption lineshape is composed by the sum of antisymmetric and symmetric lorentzian contributions. Accordingly, at a given resonance frequency, the experimental FMR absorption curve has the form:

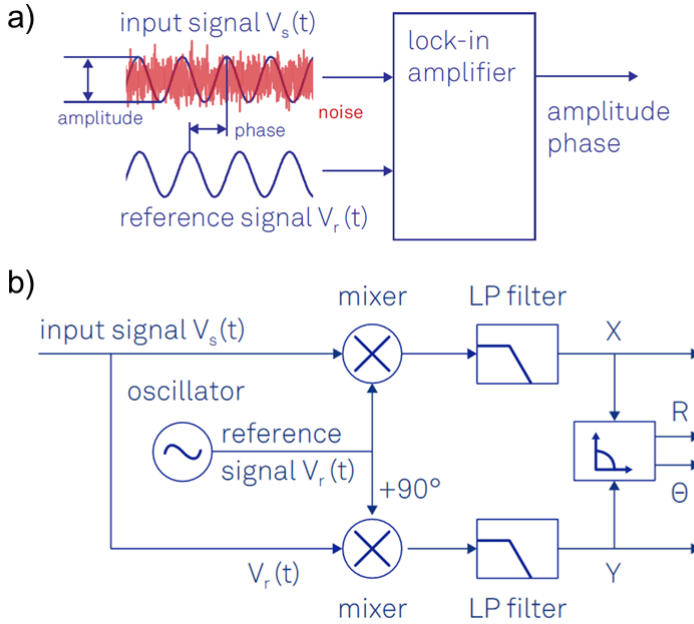


Figure A.5: a) Schematic diagram of the working principle of lock-in amplification. The input signal along with noise is combined with a reference signal of the same frequency, resulting in the amplitude ( $R$ ) and phase ( $\theta$ ) of the original input signal. b) A detailed account of the lock-in amplifier principle. The input signal is multiplied by the reference signal and a  $90^\circ$ -shifted version of this reference signal. Then, a low pass filter isolates the DC components from the AC components. At the end, the amplitude and phase of the input signal are computed as  $R = \sqrt{X^2 + Y^2}$  and  $\theta = \text{atan2}(x, y)$ , respectively. This image has been adapted from Ref. [281].

$$\frac{dS}{dH} = \frac{d}{dH} \left[ \frac{k_s \Delta H^2 + k_{as} \Delta H (H - H_{\text{res}})}{(H - H_{\text{res}})^2 + \Delta H^2} \right], \quad (\text{A.1})$$

which is the field-derivative signal of symmetric and antisymmetric lorentzian curves, and  $k_s$  and  $k_{as}$  are the symmetric and antisymmetric amplitudes, respectively, and  $H_{\text{res}}$  and  $\Delta H$  are of course the resonance field and linewidth, respectively. In addition to this, it is shown that the main magnetodynamical parameters of the system, i.e., the fundamental parameters that govern magnetization dynamics, can be deduced from the fitting of the curves relating the resonance frequency  $f_{\text{res}}$  with  $H_{\text{res}}$  and  $\Delta H$ . The equations which fit these experimental curves are Kittel's equation (see Eq. 3.11) and Eq. 3.22, from Chapter 3. It is worth noting from Eq. 3.11 that the

gyromagnetic ratio  $\gamma$  and the saturation magnetization  $M_s$  cannot be simultaneously fitted with precession. Hence, it is convenient to independently obtain the saturation magnetization value by SQUID magnetometry and then taking that value as a fixed parameter in the fitting process of FMR spectroscopy. This is especially relevant in Chapter 5, in which the interface/surface anisotropy constant  $K_2$  is relatively large.

In the context of this Thesis, besides its role as a technique for magnetic characterization, FMR spectroscopy is especially relevant due to its role in the dynamic generation of spin currents in spin pumping experiments. Spin pumping induces an increase of damping in ferromagnetic/normal metal (FM/NM) bilayers and, therefore, its effect can be measured by FMR spectroscopy. Moreover, the injected spin current in the NM can be transformed to a transverse charge current *via* inverse spin Hall effect (ISHE). This charge current will induce a voltage difference across the sample which can be detected by electrical means. In this way, an external nanovoltmeter (Keithley 2128A) is synchronized with the FMR spectrometer in order to acquire the voltage difference during a field swept. The theory of spin pumping-induced ISHE is gathered in Chapter 3. In this setup, the FMR spectra and voltage curves are probed simultaneously. A general image of the experimental setup is shown in Fig. A.6.

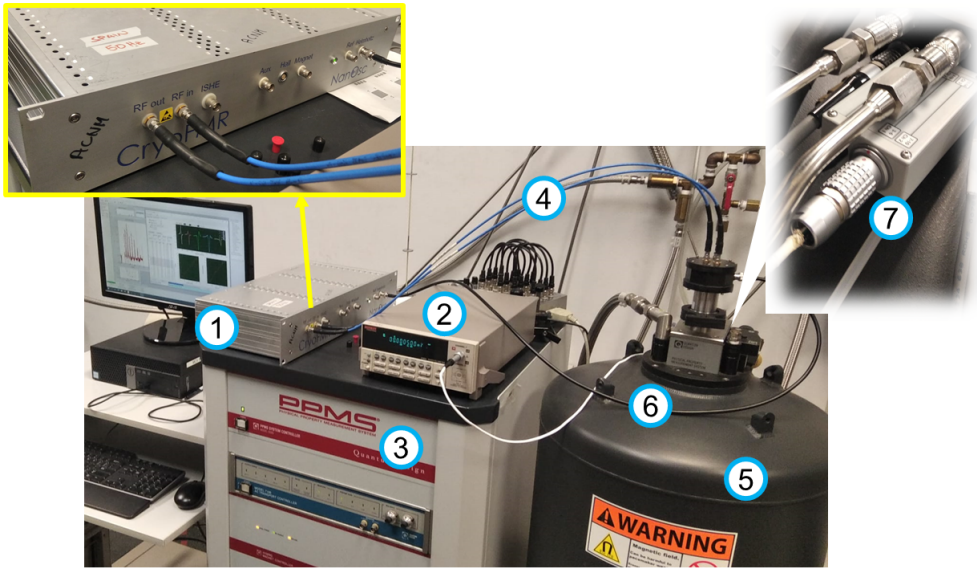


Figure A.6: Actual image of the experimental setup for measuring FMR absorption and ISHE voltage signals. The numbers stand for: (1) CryoFMR spectrometer by NanOsc. (2) Keithley 2128A nanovoltmeter. (3) PPMS multi-probe station controller. (4) Pair of coaxial cables for supplying the RF signal to the waveguide. (5) Cryogenic dewar for controlling the temperature and pressure of the measurement. (6) BNC cable to connect the Helmholtz coils to the AC source. (7) Closeup visualization of the connection between the nanovoltmeter and the PPMS, which mediates the connection with the sample holder.

### A.2.3 Transport Measurements

PPMS is also used for probing the transport properties of most of the films presented in this Thesis. The specific PPMS sample holders for these kind of measurements are the so-called rotation pucks. These pucks allow the sample to rotate with respect to the applied magnetic field direction. The spin Hall magnetoresistance measurements presented in Chapter 6 consist in a series of field-dependent (FDMR) and angular-dependent (ADMR) magnetoresistance measurements. These measurements probe the resistivity of the system with respect to the magnetic field magnitude in each of the three orthogonal directions (FDMR), and with respect to the three main rotation axes at a constant field (ADMR). The definitions of these directions and angles is shown in Fig. 6.2 from the main text, whereas the rotation pucks which enable these measurements are shown in Fig. 6.5. In that Chapter, the definitions of the normalized magnetoresistance amplitudes are:

1. ADMR:

$$\frac{\Delta\rho_L}{\rho_L} = \frac{\rho_L(\theta) - \rho_L(\theta = 0)}{\rho_L}, \quad (\text{A.2})$$

2. FDMR:

$$\frac{\Delta\rho_L}{\rho_L} = \frac{\rho_L(H) - \rho_L(H = 0)}{\rho_L}, \quad (\text{A.3})$$

where  $\rho_L = R_L w t_{Pt} / l$ , is the longitudinal resistivity at  $H = 0$ ,  $R_L$  the longitudinal resistance,  $w$  and  $l$  the width and length of the Hall bar (see Fig. 6.5),  $t_{Pt}$  the Pt film thickness in this case, and  $\theta = \alpha, \beta, \gamma$  (see Fig. 6.2). *Longitudinal* stands for the resistance measured along the current direction. In these measurements, the voltage difference is measured by the Keithley 2128A nanovoltmeter, whereas the charge current along the Hall bar is generated by a Keithley 6221 current source meter. The current has an intensity of  $60 \mu\text{A}$  and, although it is a DC current signal, each measurement voltage measurement reads

$$V_L = \frac{V_L^+ + V_L^-}{2}, \quad (\text{A.4})$$

being  $V_L^{+(-)}$  the voltage difference measured when the intensity equals  $60 \mu\text{A}$  ( $-60 \mu\text{A}$ ).



## A.3 Structural and Surface Characterization Techniques

### A.3.1 X-ray Diffraction and Reciprocal Space Maps

Nowadays, X-ray diffraction (XRD) is at the heart of the most widely used techniques for characterizing the crystal structure of materials. One of the XRD methods employed in this Thesis is that of  $\theta - 2\theta$  scans. In these measurements, the incident X-rays arrive at an angle  $\theta$  to the sample surface, whereas the detector is at an angle  $2\theta$  from the incidence. The coupled motion of the incident beam and the detector is the  $\theta - 2\theta$  scan, and the information about the crystal structure of the film is found at the positions of the diffraction peaks through Bragg's law [282],

$$2d_{hkl} \sin \theta = n\lambda, \quad (\text{A.5})$$

where  $d_{hkl}$  is the  $d$ -spacing, which corresponds to the spacing between two consecutive planes belonging to the family of planes  $(hkl)$ ,  $\lambda$  is the X-ray wavelength, and  $n$  is an integer. A geometric representation of Bragg's law is found in Fig. A.7a, whereas a schematic diagram of the experimental  $\theta - 2\theta$  scans is shown in Fig. A.7b. The  $\theta - 2\theta$  scans presented in this Thesis are performed at the X-Ray Diffraction Laboratory of ICMAB-CSIC, by using a Siemens D-5000 diffractometer.

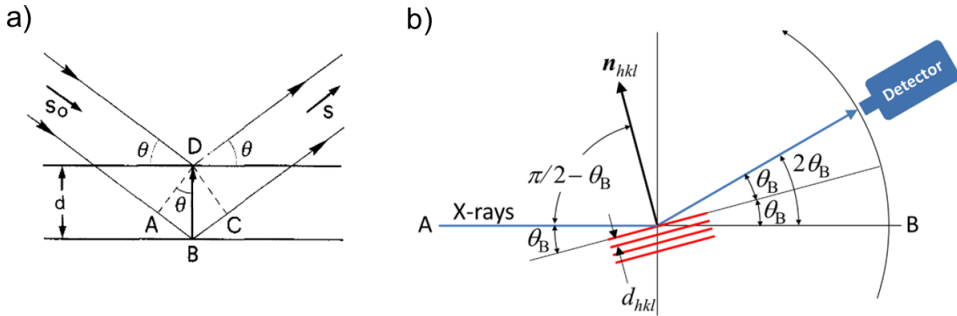


Figure A.7: a) Geometric depiction of Bragg's law: If  $\theta$  is the angle of incidence between the X-ray beams and the family of planes  $(hkl)$  of the film, then the difference in path between the waves scattered in the points  $D$  and  $B$  equals  $AB + BC = 2d \sin \theta$ . If this difference is a multiple of  $n\lambda$ , then the two waves combine themselves interfering constructively, giving rise to an observable diffraction peak. This image and explanation have been retrieved from Ref. [282]. b) Schematic diagram of the experimental setup of  $\theta - 2\theta$  scans. Note that  $\theta_B \equiv \theta$ . This image has been retrieved from Ref. [283].

Another kind of XRD diffraction analysis that is employed in this Thesis is that



of reciprocal space maps (RSM). A point in the reciprocal lattice corresponds to a family of planes in the real lattice of the crystal. Therefore, a RSM consists of a series of detailed scans around a given point in reciprocal space which result in an actual map around that point. By analyzing the shape and position of the points coming from the film or the substrate, it may be possible to determine the strain state of the film with respect to the substrate or the lattice mismatch, for instance.

### A.3.2 X-ray Reflectivity

The determination of thin film thickness in this Thesis is made mostly by means of X-ray reflectivity (XRR) measurements. XRR measures the intensity of reflected X-rays coming from grazing-incident X-ray beams. There is total reflection when the incidence angle  $\theta$  is smaller than the so-called critical angle  $\theta_c$ . Therefore, for  $\theta > \theta_c$  some of the X-rays will be reflected at the surface of film but some of them will penetrate and reflect at an inner film layer. The phase difference between interlayer reflected X-rays results in an fringe-like interference pattern as a function of  $\theta$  [284]. An schematic diagram of XRR is shown in Fig. A.8.

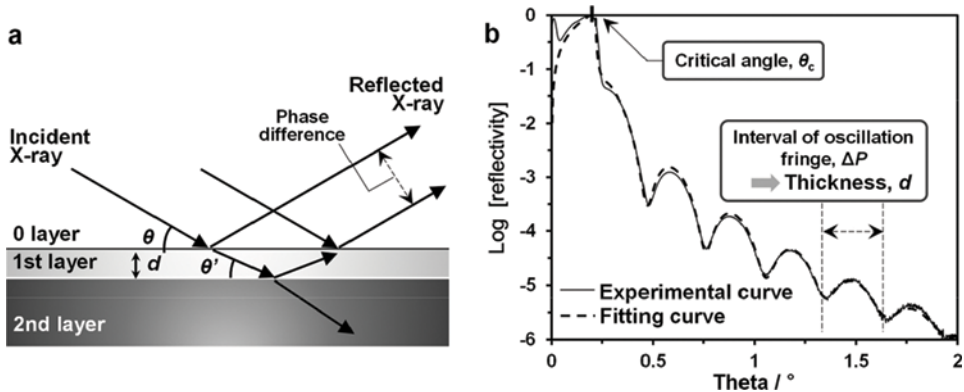


Figure A.8: a) Schematic diagram of the basic features of X-ray reflectivity (XRR) analysis. b) Representative experimental profile in XRR experiments of single thin films. The interval of oscillations is directly related to the thickness of the film. Image retrieved from Ref. [284].

XRR is widely used for determining thin film parameters such as thickness, density and surface roughness [285]. However, the film thickness alone can be directly estimated from the oscillation period of the interference pattern, i.e. [286],

$$\sin^2 \theta_i = \sin^2 \theta_c + n_i^2 \left( \frac{\lambda}{2t} \right)^2, \quad (\text{A.6})$$

where  $n_i$  is the position of the  $i$ -th oscillation minimum, and  $t$  is the film thickness. Therefore, the slope of the line relating  $\sin^2 \theta_i$  with  $n_i^2$  is directly connected to the thickness of the film. This approach is fairly valid in most of the samples presented in this Thesis. Nevertheless, it does not work very well for bilayers or multilayers with similar electron densities, such as  $\text{La}_{2/3}\text{Sr}_{1/3}\text{MnO}_3/\text{SrIrO}_3$  bilayers. In that case, the overall XRR profile is a superposition of each individual layer and a more sophisticated analysis is needed for interpreting the data. An example of this effect is observed in Fig. 5.34b from Chapter 5.

### A.3.3 Scanning Electron Microscopy

Scanning electron microscopy or SEM is employed in some of the samples in this Thesis for probing their surface morphology and composition. Instead of photons, SEM uses a focused beam of electrons for imaging. These electrons can interact with the atoms which conform the film surface and induce the emission of secondary electrons. Conversely, these electrons can also be deflected in a process called backscattering. In both cases, the electrons are collected by a detector. The emission of secondary and backscattered electrons depends strongly on the specific surface morphology of the film at that point and therefore an image of the surface of the film can be reconstructed digitally. On top of that, the emission of secondary electrons will induce the relaxation of an electron from an upper energy level to fill the hole created in the process and X-rays will be emitted. These X-rays are detected by a complementary technique called energy dispersive X-ray analysis (EDAX), and since they are fingerprints of the element which emits them, the sample composition at a specific region of the surface can be inferred as well. In Fig. A.9, a schematic representation of the three different main processes occurring in SEM imaging are shown. The SEM images presented in this Thesis have been obtained at the facilities of ICMAB-CSIC, at the Electron Microscopy Service, which owns a SEM QUANTA FEI 200 FEG-ESEM.

Another technique that is used for imaging the surface of our films, although much less relevant in the context of this Thesis, is atomic force microscopy (AFM). In AFM, a nanometric tip at the end of a microcantilever scans the surface of the sample, and the mild interaction of this tip with the sample surface allows us to map the surface morphology of the sample [288]. In this work, AFM is primarily used for characterizing the surface of  $\text{SrTiO}_3$  and  $\text{LaAlO}_3$  and, occasionally, the surface of some of the films. We have employed an Asylum Research MFP-3D from our research group at ICMAB-CSIC.

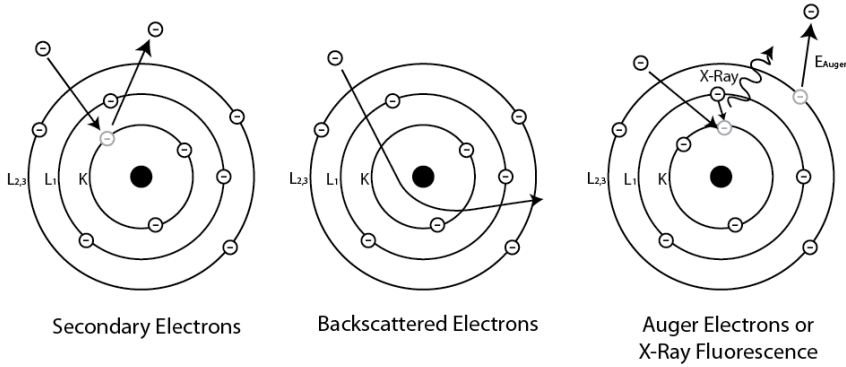


Figure A.9: Primary processes occurring in SEM, from left to right: The emission of secondary electrons, the backscattering of incident electrons, and the emission of X-rays due to relaxation from upper levels. Image retrieved from Ref. [287].

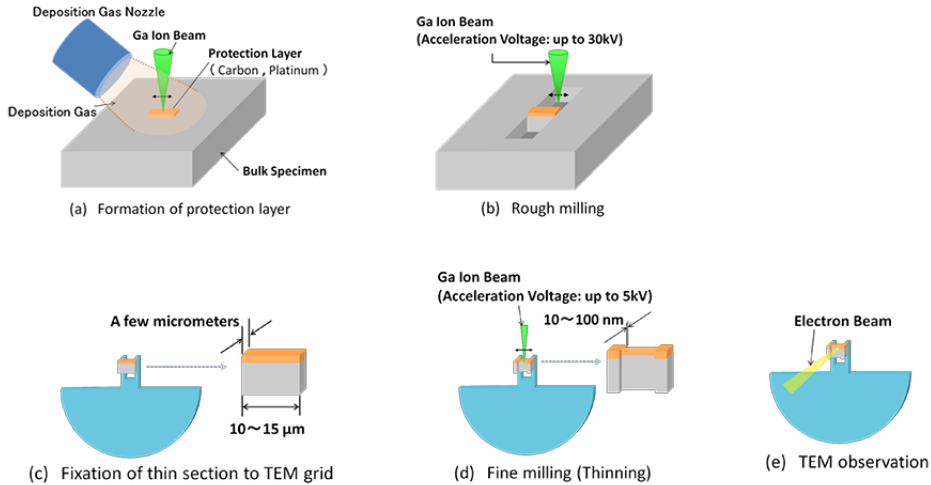


Figure A.10: Schematic diagram of the fundamental steps for the STEM sample preparation by FIB. a) Deposition of a protection layer on the target region of the film. b) Ion milling of the desired region to prepare a section of thickness of a few  $\mu\text{m}$  or less. c) The target region (i.e., the one protected before) is removed from the sample and placed in the STEM grid. d) Additional ion milling process for making the section as thin as possible (10-100 nm). e) The sample is transparent to the flow of electrons and ready to be imaged by STEM. Image retrieved from Ref. [289].

### A.3.4 Scanning Transmission Electron Microscopy

Interface quality is one of the most important features for probing spin transport phenomena across FM/NM bilayers. As such, the correct characterization of the interface in our samples is of paramount importance. In this context, scanning transmission

electron microscopy (STEM) offers an unquestionable advantage with respect to other techniques. The information regarding the local atomic structure, chemical composition, and interface quality can be obtained from STEM analysis [290]. Contrary to SEM, for example, STEM is based on the *transmission* of electrons through the sample. In this way, the region of the sample to be imaged has to be thin enough for electrons to cross it. In this Thesis, lamellas for STEM observations have been prepared by using focused ion beam (FIB) technique. This procedure allows us to obtain a thin section of the sample along a given crystallographic plane, without damaging the whole sample [289]. The necessary steps for obtaining thin cross-sectional areas for STEM imaging are shown in Fig. A.10. In addition, some of the incident electrons can undergo inelastic scattering from interactions with the electrons and atomic nuclei of the sample atoms, losing part of their energies. The experimental method for obtaining the energy-loss spectra of these inelastically scattered electrons is called electron energy-loss spectroscopy (EELS) [291]. The information about the chemical composition of the atoms in a given region of the STEM image can be inferred from EELS spectra and, thus, is very relevant for the work done in this Thesis. Figures 5.4 and 6.12 from Chapters 5 and 6, respectively, are representative examples of the power and capabilities of STEM imaging combined with EELS chemical composition analysis.

## Voltage Measurements Using Single-Stripe and Fringed Patterns: a Comparison

To prove that the voltage signal measured in a sample with multiple parallel stripes (fringed) and that measured in a single stripe are fully equivalent, a single-stripe sample of  $5 \text{ mm} \times 50 \text{ }\mu\text{m}$  and a fringed patterned one consisting of 41 parallel stripes of  $2 \text{ mm} \times 50 \text{ }\mu\text{m}$  each, were prepared. The main advantage of using a fringed pattern is that the FMR absorption curve is larger than in the single-stripe case, in which the absorption curve is noisy (strong improvement of the signal-to-noise ratio). Therefore, errors in the determination of  $\Delta H$  and  $H_{\text{res}}$  from FMR measurements are strongly reduced. Each sample is measured as stated in Chapter 4, with the CPW signal line running perpendicular to the stripes, and the voltage signal measured on both sides. The FMR absorption curves are shown in Fig. B.1. As evidenced in Fig. B.1, the FMR absorption in the fringed patterned case is nearly 40 times larger than that in the single stripe one. This difference is attributed to the fact that the FMR absorption amplitude is proportional to the quantity of material that is being excited by the CPW underneath. As a consequence, values of  $\Delta H$  and  $H_{\text{res}}$  determined by fitting the experimental curves are much more precise in the fringed patterned sample.

Furthermore, to check that both samples are equivalent and that the patterning process has not affected their magnetic properties, FMR curves from Fig. B.1 were fitted to extract  $\Delta H$  and  $H_{\text{res}}$  (see Fig. B.2). From the fitting process, in the same way as in chapter 4, the gyromagnetic ratio  $\gamma$ , saturation magnetization  $M_s$ , and Gilbert damping  $\alpha$  are determined and their values compiled in Table B.1.

The transverse voltage signal measured for each type of sample is depicted in Fig.

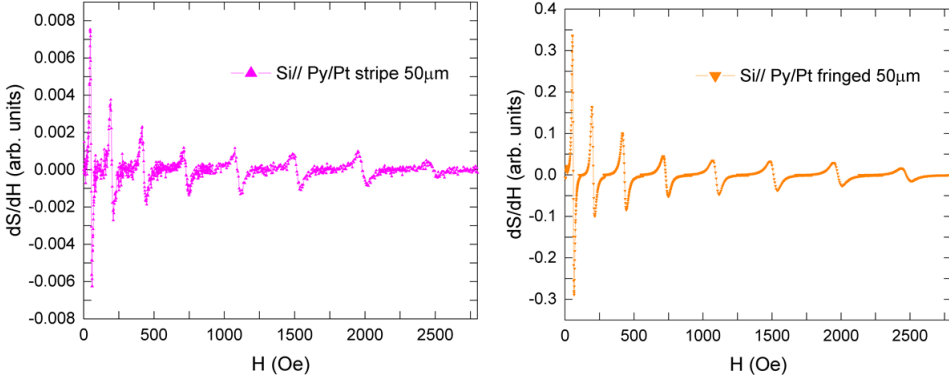


Figure B.1: Room temperature FMR absorption curves for each frequency as a function of the applied magnetic field for the single stripe sample (left), and the fringed one (right). The difference in magnitude between each other is almost 40-folds higher for the fringed patterned one, thus allowing a much more accurate evaluation of  $\Delta H$  and  $H_{\text{res}}$ .

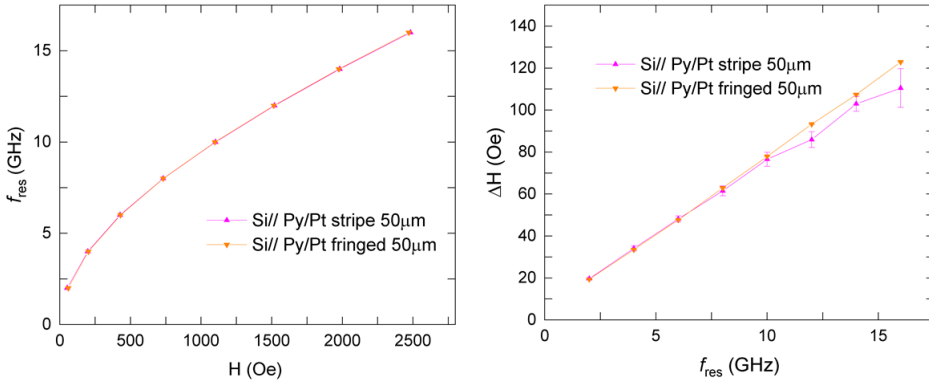


Figure B.2: Frequency dependence with respect to the resonance field (left), and FMR linewidth dependence with respect to the resonance frequency (right). Curves for both samples show a significant overlap, thus indicating that the magnetic properties of both samples are very much alike. (Room temperature).

**B.3.** The figure evidences that the two voltage curves completely overlap, having the same linewidth, resonance field, and voltage amplitude. This can be explained by the fact that the voltage in the fringed patterned sample is just the average voltage over the sample's individual stripes, i.e., that voltage is an intensive quantity. Additionally, it is observed that the voltage signal does not depend on the length of the stripe in the measurement direction since the active line of the CPW is only a few hundred

Table B.1: Magnetic parameters for the fringed and stripe samples in Fig. B.2 extracted from the fitting process.

Sample	$M_s$ (emu/cm <sup>3</sup> )	$H_4$ (Oe)	$\gamma/2\pi$ (GHz/T)	$\alpha$ ( $\times 10^{-3}$ )	$\Delta H(0)$ (Oe)
Stripe	732.11	-3.1	29.80	9.83	8.0
Fringed	748.03	-1.1	29.45	11.01	3.8

microns wide (length of the single stripe sample is 5 mm, while the multiple stripes from the fringed patterned sample is 2 mm long).

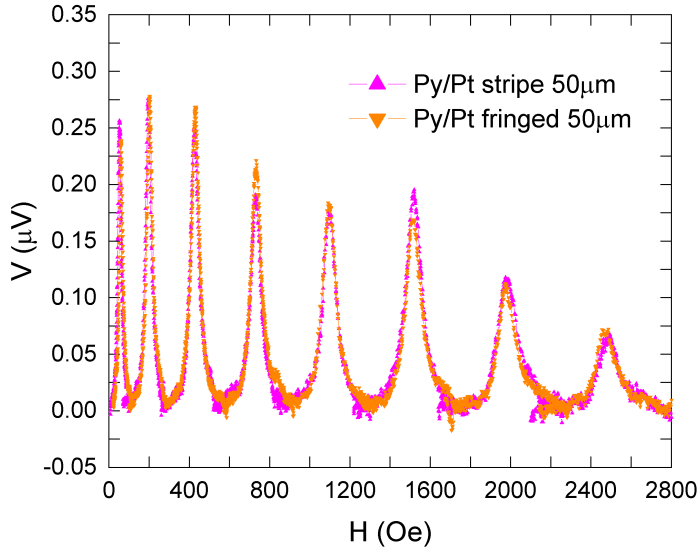


Figure B.3: Transverse voltage signal measured in the single stripe sample and fringed one at room temperature. It is evident from the figure that both voltage curves completely overlap with each other, sharing linewidth, resonance field, and voltage amplitude.





## ADMR and FDMR Measurements in Additional $\text{La}_2\text{CoMnO}_6/\text{Pt}$ Bilayers Using Different Pt Deposition Conditions

### C.1 Samples Preparation and Characterization

The experimental results presented in the main text indicate that the magnetic state of the LCMO surface is magnetically decoupled from its bulk. It is suggested that the LCMO surface modification occurs upon Pt deposition. In order to corroborate or discard this hypothesis, in this Appendix, three additional LAO// LCMO/Pt samples with different Pt deposition conditions are presented. Specifically, low deposition power and *off-axis* deposition are employed in order to evaluate the effect of Pt deposition on the LCMO surface properties. In this Section, the deposition conditions and characterization of these three additional samples are addressed. In Section C.2 their ADMR and FDMR measurements are shown and discussed. Finally, in Section C.3, the ADMR and FDMR measurements of an additional LCMO/Pt system grown on top STO (instead of LAO) are presented.

LCMO films were grown using the same deposition conditions and in the same equipment as the one from the main text. The Pt capping layers, however, were grown using different deposition conditions and, in fact, in a different equipment. The equipment that was used in this series of samples is the magnetron sputtering from BRTA CIC nanoGUNE Research Center (the ATC series AJA Sputtering System)

in Donostia-San Sebastián (Spain). In either case, this equipment and the one from our research group in Barcelona are based on the same principles and there should be no output difference between each other. Nevertheless, the main technical difference between both systems is that the sputtering from nanoGUNE has a rotational target arm which allows it to change the angle between the target and the film, i.e., it allows for *off-axis* deposition. In Fig. C.1, a schematic drawing of both of these systems is shown for comparison. It is important to note the angle  $\varphi$ , which defines the relative position between the target and the film, since it will be a relevant deposition parameter.

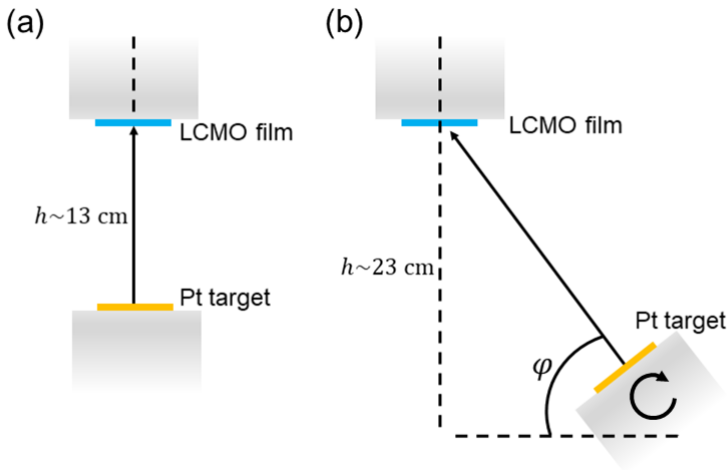


Figure C.1: Schematic drawing highlighting the technical differences between the magnetron sputtering from (a) our research group in Barcelona and (b) that from BRTA CIC nanoGUNE in Donostia-San Sebastián (Spain). The angle  $\varphi$ , which defines the relative position between the target and the film, is one of the deposition parameters to take into account.

The Pt deposition conditions of each sample are compiled in Table C.1. In this table, the Pt deposition conditions of the Pt capping layer from the main text is included for comparison. The Pt deposition conditions from sample A are the standard conditions used by the Nanodevices research group in nanoGUNE. The conditions for sample B are exactly the same but the power was decreased from 80W to 20W. Finally, the Pt from sample C uses the same deposition conditions as in A but the angle between the sample and the target was increased from  $60^\circ$  to  $75^\circ$ . In all cases, Pt was deposited at room temperature.

The magnetic characterization of each LCMO film is carried out by means of SQUID magnetometry. In Fig. C.2, the magnetization versus temperature curves,  $M(T)$ , and hysteresis loops,  $M(H)$ , of each film are shown. As can be observed, the  $T_c$  in all three

Table C.1: Pt deposition conditions of the three samples (A, B, and C) presented in this appendix as well as the ones from the Pt presented in the main text. The angle  $\varphi$  is defined in Fig. C.1.

Sample	$\varphi$ Angle (deg)	Pressure (mTorr)	Atmosphere	Power (W)
Main Text	-	5	Ar-H <sub>2</sub>	22W
A	60	3	Ar	80W
B	60	3	Ar	20W
C	75	3	Ar	80W

cases is very similar ( $\approx 255\text{K}$ ) (see Fig. C.2a), while the saturation magnetization at 10K is around 4-4.5  $\mu_B/\text{f.u.}$  (see Fig. C.2b), denoting some level of cationic disorder. The LCMO thickness of sample A has been obtained from X-ray reflectivity (XRR) measurements (see Fig. C.3a) and equals 12.2 nm. From comparison, samples B and C were assumed to have the same thickness. Moreover, the Pt capping layer thickness in each case is 5 nm according to a previous calibration process carried out by the Nanodevices group in nanoGUNE. Then, after the Pt deposition, each sample was subjected to a lithographic plus etching process in order to imprint a Hall bar identical to that described in the main text (i.e., a Hall bar for transport measurements of length  $l = 800 \mu\text{m}$  and width  $w = 100 \mu\text{m}$ ). Finally, in Fig. C.3b the longitudinal resistivity dependence on temperature of the Pt deposited in each of the samples is shown. In this case, as can be observed, samples B and C present the highest values of resistivity, up to 8 times higher than the resistivity of sample A and the one from the main text sample.

## C.2 ADMR and FDMR Measurements

We start by presenting the ADMR and FDMR measurements of sample A (i.e., the sample with the standard deposition conditions). In Fig. C.4 the ADMR and FDMR measurements are depicted. As can be observed, the results are very similar to those described in the main text. The ADMR measurements in Fig. C.4a reveal that the resistivity response is in accordance with the expected SMR/HMR symmetry. Moreover, the SMR amplitude clearly increases when increasing the magnetic field magnitude. In either case, the signal does not vanish above  $T_c$  nor decreases near it. The FDMR measurements (see C.4b) present no gap at  $H = 0$  nor reproduce the hysteretic nature of sample A magnetization (this can be deduced from the fact that regardless of the magnetic field direction, all resistivity curves are zero at exactly  $H = 0$ ). In addition to this, the negative MR in the  $H_y$  direction at 100K and 50K observed in the sample from the main text is also seen in sample A. At higher temperatures,

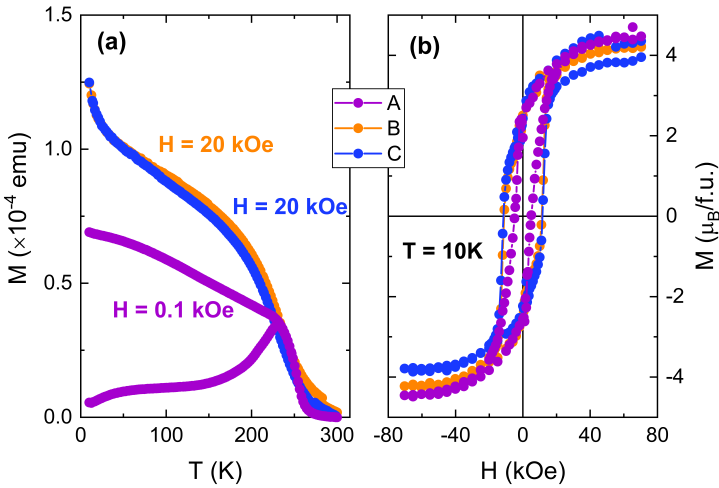


Figure C.2: (a) Magnetization *vs* temperature curves for each sample. The applied in-plane magnetic field is indicated in each case. In the case of the A sample, zero-field-cooled/field-cooled (zfc/fc) magnetization curves are shown. (b) Hysteresis loops of the samples at 10K with the magnetic field applied in the plane of the film.

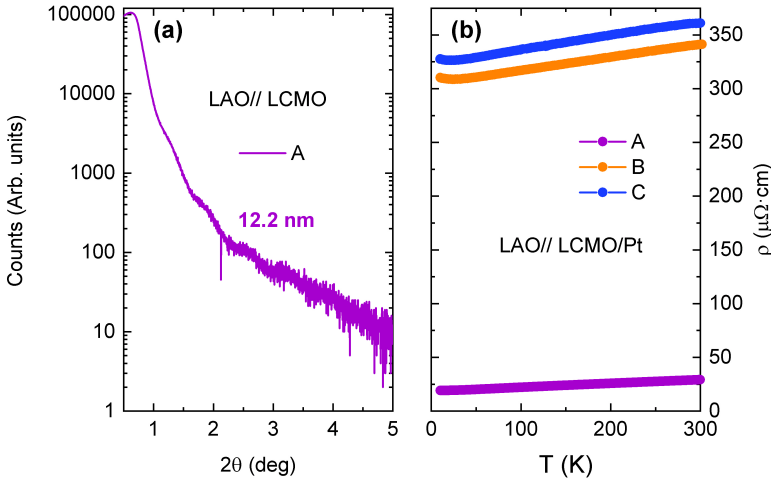


Figure C.3: (a) X-ray reflectivity (XRR) curves for the LCMO film in sample A. (b) Pt resistivity versus temperature curves for the three samples. As can be observed, the variation of growth conditions has a notorious effect on the transport properties of the Pt film.

however, the FDMR curves are in accordance with HMR phenomena. In summary, it is clearly obvious that these results are qualitatively the same as the ones obtained in the main text and, as such, it is a possibility that the Pt deposition process damages the surface of the LCMO film, inducing the formation of a magnetically decoupled

thin layer at its surface.

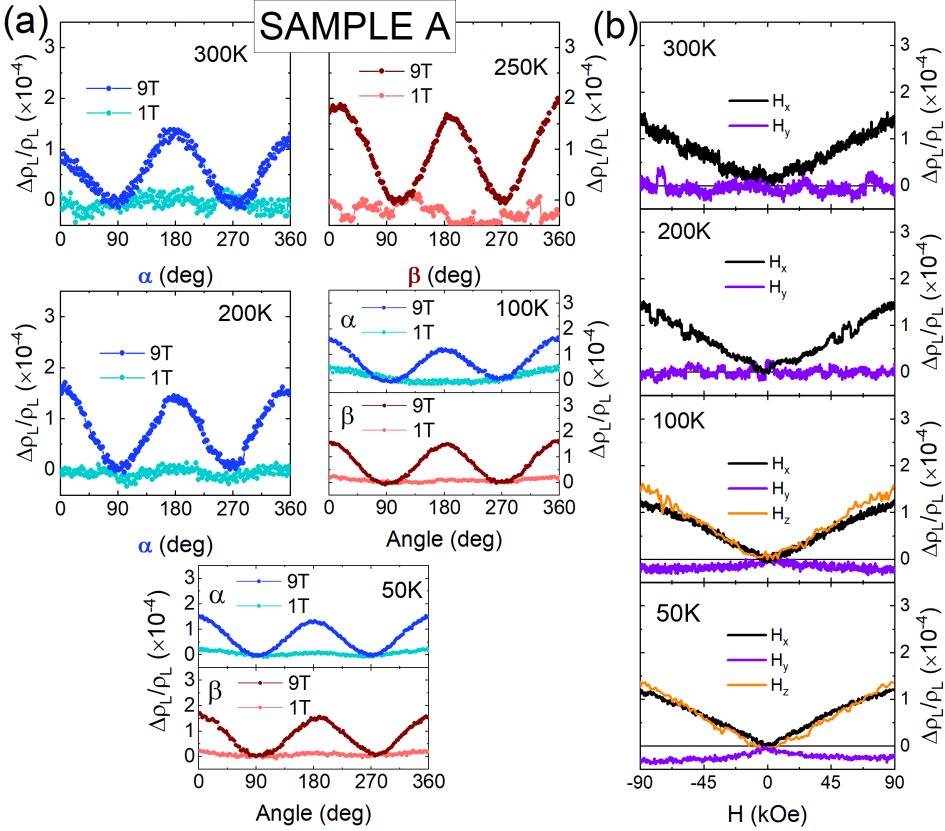


Figure C.4: (a) ADMR measurements of sample A as a function of temperature in the  $\alpha$  (blueish symbols) and  $\beta$  (reddish symbols) rotation angles from the main text. (b) FDMR measurements of sample A as a function of temperature in the three main field directions ( $x$ ,  $y$ ,  $z$ ). Both the rotation angles and magnetic field directions have been defined in Fig. 6.2 from the main text. The temperature in both setups ranges from 300K to 50K.

In order to check this hypothesis, samples B and C were fabricated using different growth conditions, i.e., lower deposition power and higher *off-axis* angle, respectively. It is important to note that the Pt deposition conditions in these samples are *softer* and have the objective of reducing the possible damage inflicted on the LCMO surface: On one hand, the Pt from sample B uses the same deposition conditions as in sample A but the power is four times smaller. On the other hand, the Pt from sample C uses the same power as in A but the Pt target is tilted at a larger  $\varphi$  angle. These measurements were performed by researchers from the Nanodevices group in nanoGUNE. In Fig. C.5, the ADMR and FDMR of samples B and C are shown. As can be observed, the ADMR measurements (see Figs. C.5a and C.5c) in both cases present the typical

SMR/HMR symmetry even above  $T_c$ , just as in sample A and the one from the main text. In addition, it is worth noticing the small SMR amplitude observed in sample C (Fig. C.5c), which corresponds to the higher off-axis angle Pt deposition. By looking at the FDMR measurements (see Figs. C.5b and C.5d), the behaviour is very different with respect to what is observed in sample A and in the one from the main text. In either case, the shared feature in all four samples is the lack of gap at  $H = 0$  and the superposition of trace and retrace FDMR measurements, which in overall is indicative of the existence of an uncoupled magnetic layer at the surface of LCMO.

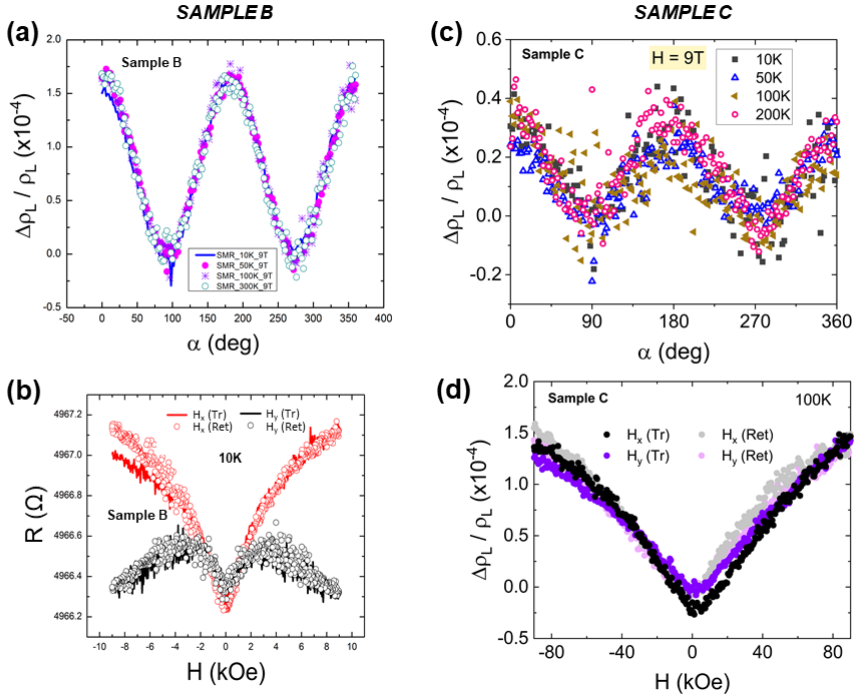


Figure C.5: (a) ADMR measurements at 9T of sample B as a function of temperature in the  $\alpha$  rotation angle (b) Trace and retrace FDMR measurements of sample B at 10K with the magnetic field pointing in the  $H_x$  and  $H_y$  directions. (c) ADMR measurements at 9T of sample C as a function of temperature in the  $\alpha$  rotation angle. (d) Trace and retrace FDMR measurements of sample C at 100K with the magnetic field pointing in the  $H_x$  and  $H_y$  directions.

In conclusion, it is shown that the three samples presented in this Appendix display similar features to the one presented in the main text, which would suggest that in all four cases there exist some sort of magnetically decoupled layer at the surface of the LCMO film. In addition, it is suspected that this layer forms during the LCMO film deposition process, i.e., *prior to the Pt deposition*. This suspicion comes from the fact that, in none of the four samples, the LCMO magnetic properties (hysteresis,  $T_c$ )

could be glimpsed. It is thus of the utmost importance to carefully study the LCMO deposition process in order to improve the SMR measurements in the LCMO/Pt system.

### C.3 SMR Measurements on $\text{La}_2\text{CoMnO}_3/\text{Pt}$ Bilayer Under Tensile Strain

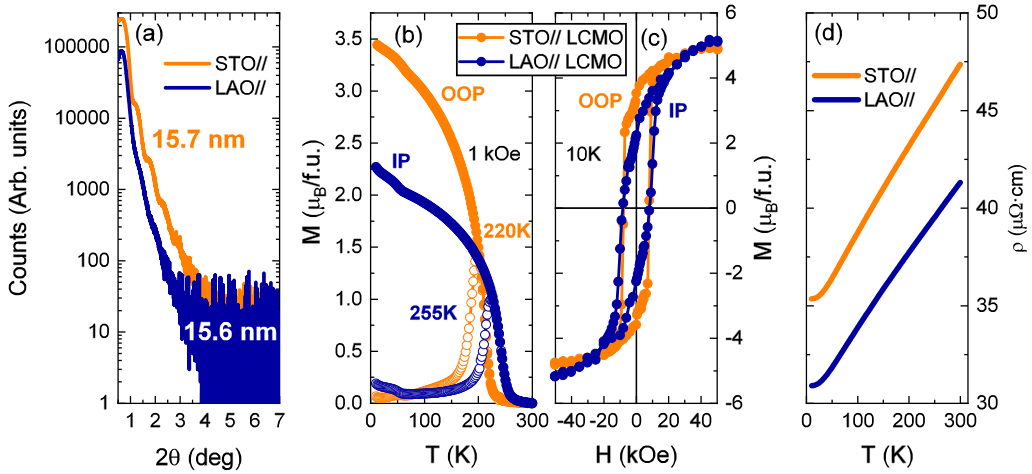


Figure C.6: (a) X-ray reflectivity curves of the LCMO film deposited on top of STO (orange) and LAO (blue) substrates. The one grown on top of LAO corresponds to the sample in the main text. (b) Temperature dependence of the magnetization of LCMO films grown on top of STO and LAO substrates, after a zero-field-cooling (empty symbols)/field-cooling (full symbols) (zfc/fc) process with an applied magnetic field of  $H = 1$  kOe. (c) Field dependence of the magnetization at  $T = 10$  K. In both cases the magnetic field is applied parallel to the easy magnetization direction, i.e., parallel to the film plane (IP) for LAO// LCMO, and perpendicular to the film plane (OOP) for STO//LCMO. (d) Longitudinal resistivity of the Pt capping layer in both LCMO/Pt bilayers as a function of temperature.

An additional LCMO thin film was deposited on top of STO using the same deposition conditions as the one from the main text. In fact, both samples were deposited simultaneously. It is known [260, 48] that LCMO thin films exhibit a large perpendicular magnetic anisotropy (PMA) when subjected to tensile strain, which can be accomplished when deposited on top of STO due to lattice mismatch. The presence of this large PMA should influence the overall SMR characteristics of the STO// LCMO/Pt system. However, in the event that there was a magnetically decoupled layer at the LCMO/Pt interface, the results observed for the LAO// LCMO/Pt system and this one should be very similar.

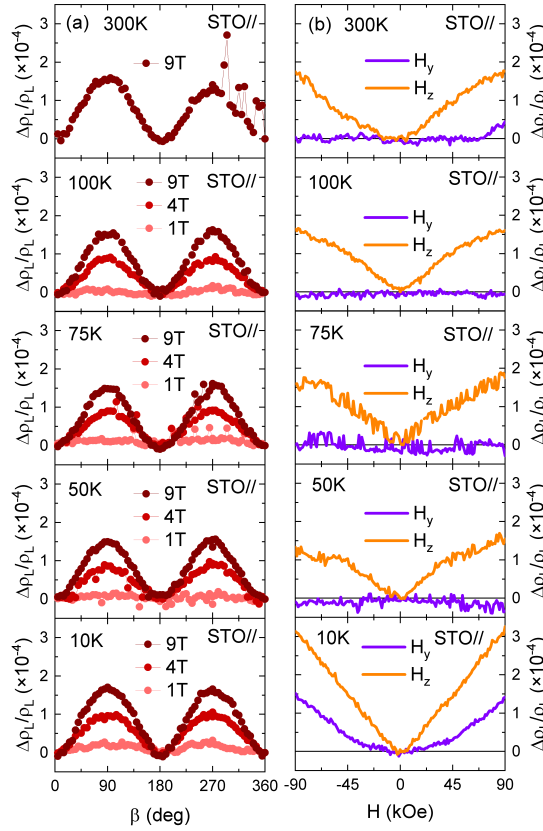


Figure C.7: (a) ADMR measurements above and below  $T_c$  in the LCMO film grown on top of STO substrate for different applied magnetic fields. As evidenced by the figure, the ADMR measurements are very similar to those in the main text irrespective to the substrate used. Thus, the strong PMA observed in STO// LCMO films does not play a relevant role on the LCMO/Pt interfacial properties. (b) FDMR measurements above and below  $T_c$  in the three perpendicular rotation planes as defined in the main text. As in (a), the very same behavior is observed for samples grown on LAO and STO substrates. The  $\beta$  rotation angle in (a) as well as the  $H_y$  and  $H_z$  field directions in (b) are defined in Fig. 6.2 from Chapter 6.

In this Section, the ADMR and FDMR measurements of this additional STO// LCMO/Pt sample are shown and compared to those obtained in the main text and this Appendix. Before that, it is mandatory to assess the equivalence between both samples. Thus, in Fig. C.6 the fundamental physical properties of each film are shown. The X-ray reflectivity curves (see Fig. C.6a) show that they indeed share the same thickness, as expected. Moreover, the magnetic characterization of both samples was carried out by SQUID magnetometry. The zero-field-cooled/field-cooled magnetization versus temperature curves as well as the magnetization hysteresis loops are shown in Figs. C.6b and C.6c, respectively. It is important to note that the



magnetic field was applied along the easy magnetization direction in each case, i.e., in-plane (IP) for LAO// LCMO and out-of-plane (OOP) for STO// LCMO. From the zfc/fc curves it can be observed that the Curie temperature  $T_c$  of the film grown on LAO (i.e., under compressive strain) is larger than that of the film grown on STO (under tensile strain). In addition, Fig. C.6c shows that both LCMO films present a similar saturation magnetization of  $M_s \approx 5 \mu_B/\text{f.u.}$  at 10K and a coercive field of  $H_C \approx 1 \text{ kOe}$ . The value of  $M_s$  is close but slightly smaller with respect to the theoretical saturation magnetization value of  $6 \mu_B/\text{f.u.}$ , suggesting that there exists still some level of B-site cationic disorder in our films. As shown in previous works from our group [48, 260], the LCMO films grown on STO substrates exhibit strong PMA. Moreover, in Fig. C.6d the longitudinal resistivities as a function of temperature of the Pt capping layers deposited in each sample are shown. The Pt deposition process was carried out by using the same deposition conditions and experimental methodology as that described in the main text. In addition, a Hall bar of  $800 \mu\text{m}$  of length and  $100 \mu\text{m}$  of width was patterned for performing the corresponding transport measurements. By direct comparison, it is observed that the resistivity of the sample grown on top of STO is slightly larger than that found in LAO, but in accordance with reported values in similar systems.

Now we move on to present the ADMR and FDMR measurements performed on the STO// LCMO/Pt sample at various temperatures above and below  $T_c$ . These results are compiled in Fig. C.7, and it can be observed that it exhibits the same angular and field dependence as that observed in the sample from the main text as well as in sample A from this Appendix (both grown on top of LAO). Conclusively, these results make evident that the LCMO uppermost layers in the LCMO/Pt bilayer exhibit the same ADMR and FDMR behavior irrespective to the substrate used. As such, we should conclude that the structural strain-induced magnetic anisotropy does not play any role in this sample. This result further supports the idea that the LCMO uppermost interfacial layers are magnetically decoupled from the rest of the film. In addition, it was also observed that ADMR and FDMR measurements were much noisier in sample grown on STO. This might be related to the difference in resistance in each case.



# Bibliography

- [1] Jairo Sinova and Igor Žutić. “New moves of the spintronics tango”. In: *Nature materials* 11.5 (2012), pp. 368–371.
- [2] SA Wolf et al. “Spintronics: a spin-based electronics vision for the future”. In: *science* 294.5546 (2001), pp. 1488–1495.
- [3] Mario Norberto Baibich et al. “Giant magnetoresistance of (001) Fe/(001) Cr magnetic superlattices”. In: *Physical review letters* 61.21 (1988), p. 2472.
- [4] Grünberg Binasch et al. “Enhanced magnetoresistance in layered magnetic structures with antiferromagnetic interlayer exchange”. In: *Physical review B* 39.7 (1989), p. 4828.
- [5] Albert Fert. “Nobel Lecture: Origin, development, and future of spintronics”. In: *Reviews of modern physics* 80.4 (2008), p. 1517.
- [6] Nevill Francis Mott. “The electrical conductivity of transition metals”. In: *Proceedings of the Royal Society of London. Series A-Mathematical and Physical Sciences* 153.880 (1936), pp. 699–717.
- [7] Claude Chappert, Albert Fert, and Frédéric Nguyen Van Dau. “The emergence of spin electronics in data storage”. In: *Nanoscience And Technology: A Collection of Reviews from Nature Journals*. World Scientific, 2010, pp. 147–157.
- [8] Atsufumi Hirohata et al. “Review on spintronics: Principles and device applications”. In: *Journal of Magnetism and Magnetic Materials* (2020), p. 166711.
- [9] Tom Coughlin. *Digital Storage Projections For 2020, Part 1*. 2019. URL: <https://www.forbes.com/sites/tomcoughlin/2019/12/21/digital-storage-projections-for-2020-part-1/>.
- [10] JE Hirsch. “Spin hall effect”. In: *Physical Review Letters* 83.9 (1999), p. 1834.
- [11] Mikhail I Dyakonov and VI Perel. “Current-induced spin orientation of electrons in semiconductors”. In: *Physics Letters A* 35.6 (1971), pp. 459–460.
- [12] Luc Berger. “Emission of spin waves by a magnetic multilayer traversed by a current”. In: *Physical Review B* 54.13 (1996), p. 9353.
- [13] John C Slonczewski et al. “Current-driven excitation of magnetic multilayers”. In: *Journal of Magnetism and Magnetic Materials* 159.1 (1996), p. L1.

- [14] Yan-Ting Chen et al. “Theory of spin Hall magnetoresistance”. In: *Physical Review B* 87.14 (2013), p. 144411.
- [15] Yaroslav Tserkovnyak, Arne Brataas, and Gerrit EW Bauer. “Enhanced Gilbert damping in thin ferromagnetic films”. In: *Physical review letters* 88.11 (2002), p. 117601.
- [16] A Brataas et al. “Spin pumping and spin transfer”. In: *Spin current* 17 (2012), pp. 87–135.
- [17] E Saitoh et al. “Conversion of spin current into charge current at room temperature: Inverse spin-Hall effect”. In: *Applied physics letters* 88.18 (2006), p. 182509.
- [18] Gerrit EW Bauer, Eiji Saitoh, and Bart J Van Wees. “Spin caloritronics”. In: *Nature materials* 11.5 (2012), pp. 391–399.
- [19] Bernhard Endres et al. “Demonstration of the spin solar cell and spin photodiode effect”. In: *Nature communications* 4.1 (2013), pp. 1–5.
- [20] SD Bader and SSP Parkin. “Spintronics”. In: *Annu. Rev. Condens. Matter Phys.* 1.1 (2010), pp. 71–88.
- [21] David Rotman. *We’re not prepared for the end of Moore’s Law*. 2020. URL: <https://www.technologyreview.com/2020/02/24/905789/were-not-prepared-for-the-end-of-moores-law/>.
- [22] Tekla S. Perry. *Forget Moore’s Law — Chipmakers Are More Worried About Heat and Power Issues*. 2019. URL: <https://spectrum.ieee.org/view-from-the-valley/semiconductors/design/power-problems-might-drive-chip-specialization>.
- [23] Pádraig Belton. *The computer chip industry has a dirty climate secret*. 2021. URL: <https://www.theguardian.com/environment/2021/sep/18/semiconductor-silicon-chips-carbon-footprint-climate>.
- [24] Udit Gupta et al. “Chasing carbon: The elusive environmental footprint of computing”. In: *2021 IEEE International Symposium on High-Performance Computer Architecture (HPCA)*. IEEE. 2021, pp. 854–867.
- [25] John Bellamy Foster. “Capitalism’s environmental crisis: is technology the answer?” In: *Monthly Review* 52.7 (2000), p. 1.
- [26] Jorge Puebla et al. “Spintronic devices for energy-efficient data storage and energy harvesting”. In: *Communications Materials* 1.1 (2020), pp. 1–9.
- [27] University of Miami. *A UM physicist proposes a longer-lasting, chemical-free ‘spin battery’*. 2022. URL: <https://climate.miami.edu/taking-electrons-for-a-spin/>.

- [28] CNRS. *Combining spintronics and quantum thermodynamics to harvest energy at room temperature*. 2019. URL: <https://phys.org/news/2019-10-combining-spintronics-quantum-thermodynamics-harvest.html>.
- [29] Bernard Dieny et al. “Opportunities and challenges for spintronics in the microelectronics industry”. In: *Nature Electronics* 3.8 (2020), pp. 446–459.
- [30] L Bruno Chandrasekar, K Gnanasekar, and M Karunakaran. “Spintronics—A mini review”. In: *Superlattices and Microstructures* 136 (2019), p. 106322.
- [31] Abhronil Sengupta and Kaushik Roy. “Neuromorphic computing enabled by physics of electron spins: Prospects and perspectives”. In: *Applied Physics Express* 11.3 (2018), p. 030101.
- [32] Igor Žutić, Jaroslav Fabian, and S Das Sarma. “Spintronics: Fundamentals and applications”. In: *Reviews of modern physics* 76.2 (2004), p. 323.
- [33] S Jin et al. “Thousandfold change in resistivity in magnetoresistive La-Ca-Mn-O films”. In: *Science* 264.5157 (1994), pp. 413–415.
- [34] R von Helmolt et al. “Giant negative magnetoresistance in perovskitelike  $\text{La}_{2/3}\text{Ba}_{1/3}\text{MnO}_x$  ferromagnetic films”. In: *Physical Review Letters* 71.14 (1993), p. 2331.
- [35] Matthias Opel. “Spintronic oxides grown by laser-MBE”. In: *Journal of physics D: Applied physics* 45.3 (2011), p. 033001.
- [36] Manuel Bibes, Javier E Villegas, and Agnes Barthelemy. “Ultrathin oxide films and interfaces for electronics and spintronics”. In: *Advances in Physics* 60.1 (2011), pp. 5–84.
- [37] Gertjan Koster, Mark Huijben, and Guus Rijnders. *Epitaxial growth of complex metal oxides*. Elsevier, 2015.
- [38] Yoshinori Tokura and Harold Y Hwang. “Complex oxides on fire”. In: *Nature materials* 7.9 (2008), pp. 694–695.
- [39] Koichi Momma and Fujio Izumi. “VESTA 3 for three-dimensional visualization of crystal, volumetric and morphology data”. In: *Journal of applied crystallography* 44.6 (2011), pp. 1272–1276.
- [40] Jochen Mannhart and Darrell G Schlom. “Oxide interfaces — an opportunity for electronics”. In: *Science* 327.5973 (2010), pp. 1607–1611.
- [41] Igor V Maznichenko et al. “Formation and tuning of 2D electron gas in perovskite heterostructures”. In: *physica status solidi (b)* 257.7 (2020), p. 1900540.
- [42] Claas Abert. “Micromagnetics and spintronics: models and numerical methods”. In: *The European Physical Journal B* 92.6 (2019), pp. 1–45.
- [43] Yurii P Ivanov and O Chubykalo-Fesenko. “Micromagnetic simulations of cylindrical magnetic nanowires”. In: *Magnetic Nano-and Microwires* (2015), pp. 423–448.

- [44] Eugene M Chudnovsky and Javier Tejada. *Lectures on Magnetism*. Rinton Press Princeton, NJ, 2006.
- [45] CAF Vaz, JAC Bland, and G Lauhoff. “Magnetism in ultrathin film structures”. In: *Reports on Progress in Physics* 71.5 (2008), p. 056501.
- [46] Gavin S Abo et al. “Definition of magnetic exchange length”. In: *IEEE Transactions on Magnetics* 49.8 (2013), pp. 4937–4939.
- [47] Michael Ziese and Martin J Thornton. *Spin electronics*. Vol. 569. Springer, 2007.
- [48] Regina Galceran et al. “Strain-induced perpendicular magnetic anisotropy in  $\text{La}_2\text{CoMnO}_{6-\varepsilon}$  thin films and its dependence on film thickness”. In: *Physical Review B* 93.14 (2016), p. 144417.
- [49] Fabrizio Porrati. “Spatially varying magnetic anisotropies in ultrathin films”. In: (2002).
- [50] Evgeny Y Tsymbal and David G Pettifor. “Perspectives of giant magnetoresistance”. In: *Solid state physics*. Vol. 56. Elsevier, 2001, pp. 113–237.
- [51] A Fert and IA Campbell. “Two-current conduction in nickel”. In: *Physical Review Letters* 21.16 (1968), p. 1190.
- [52] A Fert and IA Campbell. “Electrical resistivity of ferromagnetic nickel and iron based alloys”. In: *Journal of Physics F: Metal Physics* 6.5 (1976), p. 849.
- [53] Sadamichi Maekawa et al. *Spin current*. Oxford University Press, 2017.
- [54] T Valet and A Fert. “Theory of the perpendicular magnetoresistance in magnetic multilayers”. In: *Physical Review B* 48.10 (1993), p. 7099.
- [55] PC Van Son, H Van Kempen, and P Wyder. “Boundary resistance of the ferromagnetic-nonferromagnetic metal interface”. In: *Physical Review Letters* 58.21 (1987), p. 2271.
- [56] Michel I Dyakonov and AV Khaetskii. *Spin physics in semiconductors*. Vol. 1. Springer, 2008.
- [57] Xian-Peng Zhang, F Sebastian Bergeret, and Vitaly N Golovach. “Theory of spin hall magnetoresistance from a microscopic perspective”. In: *Nano letters* 19.9 (2019), pp. 6330–6337.
- [58] Mark Johnson and RH Silsbee. “Coupling of electronic charge and spin at a ferromagnetic-paramagnetic metal interface”. In: *Physical Review B* 37.10 (1988), p. 5312.
- [59] Xinde Tao et al. “Self-consistent determination of spin Hall angle and spin diffusion length in Pt and Pd: The role of the interface spin loss”. In: *Science advances* 4.6 (2018), eaat1670.

- [60] Y Kajiwara et al. “Transmission of electrical signals by spin-wave interconversion in a magnetic insulator”. In: *Nature* 464.7286 (2010), pp. 262–266.
- [61] Aurelien Manchon and Abderrezak Belabbes. “Spin-orbitronics at transition metal interfaces”. In: *Solid State Physics*. Vol. 68. Elsevier, 2017, pp. 1–89.
- [62] Emmanuel I Rashba. “Spin–orbit coupling and spin transport”. In: *Physica E: Low-dimensional Systems and Nanostructures* 34.1-2 (2006), pp. 31–35.
- [63] Mario Reis. *Fundamentals of magnetism*. Elsevier, 2013.
- [64] Mitchel Weissbluth. *Atoms and molecules*. Elsevier, 2012.
- [65] Frances Hellman et al. “Interface-induced phenomena in magnetism”. In: *Reviews of modern physics* 89.2 (2017), p. 025006.
- [66] Aurelien Manchon et al. “New perspectives for Rashba spin–orbit coupling”. In: *Nature materials* 14.9 (2015), pp. 871–882.
- [67] Jairo Sinova et al. “Spin hall effects”. In: *Reviews of Modern Physics* 87.4 (2015), p. 1213.
- [68] Naoto Nagaosa et al. “Anomalous hall effect”. In: *Reviews of modern physics* 82.2 (2010), p. 1539.
- [69] Yuichiro K Kato et al. “Observation of the spin Hall effect in semiconductors”. In: *science* 306.5703 (2004), pp. 1910–1913.
- [70] Charles Day. “Two groups observe the spin hall effect in semiconductors”. In: *Phys. Today* 58.2 (2005), p. 17.
- [71] Joerg Wunderlich et al. “Experimental observation of the spin-Hall effect in a two-dimensional spin-orbit coupled semiconductor system”. In: *Physical review letters* 94.4 (2005), p. 047204.
- [72] Jörg Wunderlich et al. “Spin Hall effect transistor”. In: *Science* 330.6012 (2010), pp. 1801–1804.
- [73] Saburo Takahashi and Sadamichi Maekawa. “Spin current in metals and superconductors”. In: *Journal of the Physical Society of Japan* 77.3 (2008), pp. 031009–031009.
- [74] MI Dyakonov. “Magnetoresistance due to edge spin accumulation”. In: *Physical review letters* 99.12 (2007), p. 126601.
- [75] Axel Hoffmann. “Spin Hall effects in metals”. In: *IEEE transactions on magnetics* 49.10 (2013), pp. 5172–5193.
- [76] Sergio O Valenzuela and M Tinkham. “Direct electronic measurement of the spin Hall effect”. In: *Nature* 442.7099 (2006), pp. 176–179.
- [77] Isaak D Mayergoyz, Giorgio Bertotti, and Claudio Serpico. *Nonlinear magnetization dynamics in nanosystems*. Elsevier, 2009.

- [78] LALE Landau and Evgeny Lifshitz. “On the theory of the dispersion of magnetic permeability in ferromagnetic bodies”. In: *Perspectives in Theoretical Physics*. Elsevier, 1992, pp. 51–65.
- [79] S Azzawi, AT Hindmarch, and D Atkinson. “Magnetic damping phenomena in ferromagnetic thin-films and multilayers”. In: *Journal of Physics D: Applied Physics* 50.47 (2017), p. 473001.
- [80] Thomas L Gilbert. “A phenomenological theory of damping in ferromagnetic materials”. In: *IEEE transactions on magnetics* 40.6 (2004), pp. 3443–3449.
- [81] Zhengmeng Xu, Kai Zhang, and J Li. “Disentangling intrinsic and extrinsic Gilbert damping”. In: *Physical Review B* 104.22 (2021), p. 224404.
- [82] JM Lock. “Eddy current damping in thin metallic ferromagnetic films”. In: *British Journal of Applied Physics* 17.12 (1966), p. 1645.
- [83] Ivan S Maksymov and Mikhail Kostylev. “Broadband stripline ferromagnetic resonance spectroscopy of ferromagnetic films, multilayers and nanostructures”. In: *Physica E: Low-dimensional Systems and Nanostructures* 69 (2015), pp. 253–293.
- [84] Andrii V Chumak et al. “Magnon spintronics”. In: *Nature Physics* 11.6 (2015), pp. 453–461.
- [85] Martin AW Schoen et al. “Ultra-low magnetic damping of a metallic ferromagnet”. In: *Nature Physics* 12.9 (2016), pp. 839–842.
- [86] Aidan J Lee et al. “Metallic ferromagnetic films with magnetic damping under  $1.4 \times 10^{-3}$ ”. In: *Nature communications* 8.1 (2017), pp. 1–6.
- [87] Qing Qin et al. “Ultra-low magnetic damping of perovskite  $\text{La}_{0.7}\text{Sr}_{0.3}\text{MnO}_3$  thin films”. In: *Applied Physics Letters* 110.11 (2017), p. 112401.
- [88] C Guillemard et al. “Ultralow magnetic damping in  $\text{Co}_2\text{Mn}$ -based heusler compounds: Promising materials for spintronics”. In: *Physical Review Applied* 11.6 (2019), p. 064009.
- [89] James HE Griffiths. “Anomalous high-frequency resistance of ferromagnetic metals”. In: *Nature* 158.4019 (1946), pp. 670–671.
- [90] E Zavoisky. “Spin magnetic resonance in the decimetre-wave region”. In: *J. Phys. USSR* 10 (1946), pp. 197–198.
- [91] Charles Kittel. “Ferromagnetic resonance”. In: *J. phys. radium* 12.3 (1951), pp. 291–302.
- [92] Z Celinski, KB Urquhart, and B Heinrich. “Using ferromagnetic resonance to measure the magnetic moments of ultrathin films”. In: *Journal of Magnetism and Magnetic Materials* 166.1-2 (1997), pp. 6–26.



- [93] Michael Harder, Yongsheng Gui, and Can-Ming Hu. “Electrical detection of magnetization dynamics via spin rectification effects”. In: *Physics Reports* 661 (2016), pp. 1–59.
- [94] Yin Zhang et al. “Dynamic magnetic susceptibility and electrical detection of ferromagnetic resonance”. In: *Journal of Physics: Condensed Matter* 29.9 (2017), p. 095806.
- [95] N Mecking, YS Gui, and C-M Hu. “Microwave photovoltage and photoresistance effects in ferromagnetic microstrips”. In: *Physical Review B* 76.22 (2007), p. 224430.
- [96] Arne Brataas, Yu V Nazarov, and Gerrit EW Bauer. “Spin-transport in multi-terminal normal metal-ferromagnet systems with non-collinear magnetizations”. In: *The European Physical Journal B-Condensed Matter and Complex Systems* 22.1 (2001), pp. 99–110.
- [97] Arne Brataas, Yu V Nazarov, and Gerrit EW Bauer. “Finite-element theory of transport in ferromagnet–normal metal systems”. In: *Physical Review Letters* 84.11 (2000), p. 2481.
- [98] Arne Brataas, Gerrit EW Bauer, and Paul J Kelly. “Non-collinear magneto-electronics”. In: *Physics Reports* 427.4 (2006), pp. 157–255.
- [99] Juan Manuel Gómez Pérez. *Spin transport in magnetic insulator/heavy metal heterostructures*. Euskal Herriko Unibertsitatea, 2020.
- [100] FK Dejene et al. “Control of spin current by a magnetic YIG substrate in NiFe/Al nonlocal spin valves”. In: *Physical Review B* 91.10 (2015), p. 100404.
- [101] Koichi Oyanagi et al. “Paramagnetic spin Hall magnetoresistance”. In: *Physical Review B* 104.13 (2021), p. 134428.
- [102] A Ghosh et al. “Penetration depth of transverse spin current in ultrathin ferromagnets”. In: *Physical review letters* 109.12 (2012), p. 127202.
- [103] Jianwei Zhang et al. “Identification of transverse spin currents in noncollinear magnetic structures”. In: *Physical review letters* 93.25 (2004), p. 256602.
- [104] Tomohiro Taniguchi et al. “Determination of penetration depth of transverse spin current in ferromagnetic metals by spin pumping”. In: *Applied physics express* 1.3 (2008), p. 031302.
- [105] Mark D Stiles and A Zangwill. “Anatomy of spin-transfer torque”. In: *Physical Review B* 66.1 (2002), p. 014407.
- [106] Daniel C Ralph and Mark D Stiles. “Spin transfer torques”. In: *Journal of Magnetism and Magnetic Materials* 320.7 (2008), pp. 1190–1216.
- [107] Yaroslav Tserkovnyak et al. “Nonlocal magnetization dynamics in ferromagnetic heterostructures”. In: *Reviews of Modern Physics* 77.4 (2005), p. 1375.

- [108] András Jánossy and P Monod. “Spin waves for single electrons in paramagnetic metals”. In: *Physical Review Letters* 37.10 (1976), p. 612.
- [109] RH Silsbee, A Janossy, and P Monod. “Coupling between ferromagnetic and conduction-spin-resonance modes at a ferromagnetic—normal-metal interface”. In: *Physical Review B* 19.9 (1979), p. 4382.
- [110] Dahai Wei et al. “Spin Hall voltages from ac and dc spin currents”. In: *Nature communications* 5.1 (2014), pp. 1–6.
- [111] Yaroslav Tserkovnyak, Arne Brataas, and Gerrit EW Bauer. “Spin pumping and magnetization dynamics in metallic multilayers”. In: *Physical Review B* 66.22 (2002), p. 224403.
- [112] Ryo Iguchi and Eiji Saitoh. “Measurement of spin pumping voltage separated from extrinsic microwave effects”. In: *Journal of the Physical Society of Japan* 86.1 (2017), p. 011003.
- [113] O Mosendz et al. “Quantifying spin Hall angles from spin pumping: Experiments and theory”. In: *Physical review letters* 104.4 (2010), p. 046601.
- [114] O Mosendz et al. “Detection and quantification of inverse spin Hall effect from spin pumping in permalloy/normal metal bilayers”. In: *Physical Review B* 82.21 (2010), p. 214403.
- [115] Kai Chen and Shufeng Zhang. “Spin pumping in the presence of spin-orbit coupling”. In: *Physical review letters* 114.12 (2015), p. 126602.
- [116] Kazuya Ando et al. “Inverse spin-Hall effect induced by spin pumping in metallic system”. In: *Journal of applied physics* 109.10 (2011), p. 103913.
- [117] Nils Kuhlmann, Andreas Vogel, and Guido Meier. “Magnetization dynamics and cone angle precession in permalloy rectangles”. In: *Physical Review B* 85.1 (2012), p. 014410.
- [118] MV Costache et al. “Electrical detection of spin pumping: dc voltage generated by ferromagnetic resonance at ferromagnet/nonmagnet contact”. In: *Physical Review B* 78.6 (2008), p. 064423.
- [119] P Yu et al. “Curie temperatures of fcc and bcc nickel and permalloy: Supercell and Green’s function methods”. In: *Physical Review B* 77.5 (2008), p. 054431.
- [120] Michael Farle. “Ferromagnetic resonance of ultrathin metallic layers”. In: *Reports on progress in physics* 61.7 (1998), p. 755.
- [121] PE Tannenwald and MH Seavey Jr. “Ferromagnetic resonance in thin films of permalloy”. In: *Physical Review* 105.2 (1957), p. 377.
- [122] JP Nibarger et al. “Variation of magnetization and the Landé  $g$  factor with thickness in Ni–Fe films”. In: *Applied physics letters* 83.1 (2003), pp. 93–95.

- [123] Ales Hrabec et al. “Spin-orbit interaction enhancement in permalloy thin films by Pt doping”. In: *Physical Review B* 93.1 (2016), p. 014432.
- [124] Justin M Shaw et al. “Precise determination of the spectroscopic  $g$ -factor by use of broadband ferromagnetic resonance spectroscopy”. In: *Journal of Applied Physics* 114.24 (2013), p. 243906.
- [125] Yuelel Zhao et al. “Experimental investigation of temperature-dependent Gilbert damping in permalloy thin films”. In: *Scientific reports* 6.1 (2016), pp. 1–8.
- [126] Anton A Starikov et al. “Unified first-principles study of Gilbert damping, spin-flip diffusion, and resistivity in transition metal alloys”. In: *Physical review letters* 105.23 (2010), p. 236601.
- [127] C Luo et al. “Enhancement of magnetization damping coefficient of permalloy thin films with dilute Nd dopants”. In: *Physical Review B* 89.18 (2014), p. 184412.
- [128] Qinfang Zhang, Shin-ichi Hikino, and Seiji Yunoki. “First-principles study of the spin-mixing conductance in Pt/Ni<sub>81</sub>Fe<sub>19</sub> junctions”. In: *Applied Physics Letters* 99.17 (2011), p. 172105.
- [129] W Platow et al. “Correlations between ferromagnetic-resonance linewidths and sample quality in the study of metallic ultrathin films”. In: *Physical Review B* 58.9 (1998), p. 5611.
- [130] S Ingvarsson et al. “Role of electron scattering in the magnetization relaxation of thin Ni<sub>81</sub>Fe<sub>19</sub> films”. In: *Physical Review B* 66.21 (2002), p. 214416.
- [131] G Counil et al. “Temperature dependences of the resistivity and the ferromagnetic resonance linewidth in permalloy thin films”. In: *IEEE transactions on magnetics* 42.10 (2006), pp. 3323–3325.
- [132] JF Sierra et al. “Interface and temperature dependent magnetic properties in permalloy thin films and tunnel junction structures”. In: *Journal of nanoscience and nanotechnology* 11.9 (2011), pp. 7653–7664.
- [133] L Berger. “Effect of interfaces on Gilbert damping and ferromagnetic resonance linewidth in magnetic multilayers”. In: *Journal of Applied Physics* 90.9 (2001), pp. 4632–4638.
- [134] B Heinrich, DJ Meredith, and JF Cochran. “Wave number and temperature dependent Landau-Lifshitz damping in nickel”. In: *Journal of Applied Physics* 50.B11 (1979), pp. 7726–7728.
- [135] J Cochran and B Heinrich. “Microwave transmission through ferromagnetic metals”. In: *IEEE Transactions on Magnetics* 16.5 (1980), pp. 660–665.

- [136] Keith Gilmore, Yves U Idzerda, and Mark D Stiles. “Spin-orbit precession damping in transition metal ferromagnets”. In: *Journal of Applied Physics* 103.7 (2008), p. 07D303.
- [137] V Kambersk. “On ferromagnetic resonance damping in metals”. In: *Czechoslovak Journal of Physics B* 26.12 (1976), pp. 1366–1383.
- [138] J Kuneš and V Kambersk. “First-principles investigation of the damping of fast magnetization precession in ferromagnetic 3d metals”. In: *Physical Review B* 65.21 (2002), p. 212411.
- [139] Yajun Wei, Shin Liang Chin, and Peter Svedlindh. “On the frequency and field linewidth conversion of ferromagnetic resonance spectra”. In: *Journal of Physics D: Applied Physics* 48.33 (2015), p. 335005.
- [140] J-C Rojas-Sánchez et al. “Spin pumping and inverse spin Hall effect in platinum: the essential role of spin-memory loss at metallic interfaces”. In: *Physical review letters* 112.10 (2014), p. 106602.
- [141] J-C Rojas-Sánchez et al. “Spin pumping and inverse spin Hall effect in Platinum and other 5d metals: The essential role of spin-memory loss and spin-current discontinuities at interfaces”. In: *Proc. of SPIE Vol.* Vol. 9167, pp. 916729–1.
- [142] Weifeng Zhang et al. “Role of transparency of platinum–ferromagnet interfaces in determining the intrinsic magnitude of the spin Hall effect”. In: *Nature Physics* 11.6 (2015), pp. 496–502.
- [143] Z Feng et al. “Spin Hall angle quantification from spin pumping and microwave photoresistance”. In: *Physical Review B* 85.21 (2012), p. 214423.
- [144] Sergi Martín-Rio et al. “Temperature dependence of spin pumping and inverse spin Hall effect in permalloy/Pt bilayers”. In: *Journal of Magnetism and Magnetic Materials* 500 (2020), p. 166319.
- [145] M Harder et al. “Analysis of the line shape of electrically detected ferromagnetic resonance”. In: *Physical Review B* 84.5 (2011), p. 054423.
- [146] Paul Noël et al. “Negligible thermal contributions to the spin pumping signal in ferromagnetic metal–platinum bilayers”. In: *Journal of Applied Physics* 127.16 (2020), p. 163907.
- [147] BF Miao et al. “Inverse spin Hall effect in a ferromagnetic metal”. In: *Physical review letters* 111.6 (2013), p. 066602.
- [148] Kazuya Ando et al. “Angular dependence of inverse spin–Hall effect induced by spin pumping investigated in a Ni<sub>81</sub>Fe<sub>19</sub>/Pt thin film”. In: *Physical Review B* 78.1 (2008), p. 014413.

- [149] Lin Chen, Fumihiko Matsukura, and Hideo Ohno. “Direct-current voltages in (Ga, Mn) As structures induced by ferromagnetic resonance”. In: *Nature communications* 4.1 (2013), pp. 1–6.
- [150] A Azevedo et al. “Spin pumping and anisotropic magnetoresistance voltages in magnetic bilayers: Theory and experiment”. In: *Physical review B* 83.14 (2011), p. 144402.
- [151] Lihui Bai et al. “Universal method for separating spin pumping from spin rectification voltage of ferromagnetic resonance”. In: *Physical review letters* 111.21 (2013), p. 217602.
- [152] Hiroyasu Nakayama et al. “Geometry dependence on inverse spin Hall effect induced by spin pumping in Ni<sub>81</sub>Fe<sub>19</sub>/Pt films”. In: *Physical Review B* 85.14 (2012), p. 144408.
- [153] Wenxu Zhang et al. “Separating inverse spin Hall voltage and spin rectification voltage by inverting spin injection direction”. In: *Applied Physics Letters* 108.10 (2016), p. 102405.
- [154] Sang-Il Kim et al. “Stacking order dependence of inverse spin Hall effect and anomalous Hall effect in spin pumping experiments”. In: *Journal of Applied Physics* 117.17 (2015), p. 17D901.
- [155] NanOsc Instruments. *Wave Guides*. 2021. URL: <http://www.nanosc.se/wave-guides-cpws.html>.
- [156] Ayaka Tsukahara et al. “Self-induced inverse spin Hall effect in permalloy at room temperature”. In: *Physical Review B* 89.23 (2014), p. 235317.
- [157] O Gladii et al. “Self-induced inverse spin Hall effect in ferromagnets: Demonstration through nonmonotonic temperature dependence in permalloy”. In: *Physical Review B* 100.17 (2019), p. 174409.
- [158] Kazunari Kanagawa, Yoshio Teki, and Eiji Shikoh. “Self-induced inverse spin-Hall effect in an iron and a cobalt single-layer films themselves under the ferromagnetic resonance”. In: *AIP Advances* 8.5 (2018), p. 055910.
- [159] Chiara Ciccarelli et al. “Magnonic charge pumping via spin-orbit coupling”. In: *Nature nanotechnology* 10.1 (2015), pp. 50–54.
- [160] A Azevedo et al. “Electrical detection of ferromagnetic resonance in single layers of permalloy: Evidence of magnonic charge pumping”. In: *Physical Review B* 92.2 (2015), p. 024402.
- [161] Biswajit Sahoo et al. “Spin pumping and inverse spin Hall effect in iridium oxide”. In: *Advanced Quantum Technologies* 4.9 (2021), p. 2000146.
- [162] Yi Wang et al. “Determination of intrinsic spin Hall angle in Pt”. In: *Applied Physics Letters* 105.15 (2014), p. 152412.

- [163] Luqiao Liu, RA Buhrman, and DC Ralph. “Review and analysis of measurements of the spin Hall effect in platinum”. In: *arXiv preprint arXiv:1111.3702* (2011).
- [164] Martin Wahler et al. “Inverse spin Hall effect in a complex ferromagnetic oxide heterostructure”. In: *Scientific reports* 6.1 (2016), pp. 1–7.
- [165] Purbasha Sharangi et al. “Spin pumping and inverse spin Hall effect in CoFeB/C<sub>60</sub> bilayers”. In: *arXiv preprint arXiv:2106.06829* (2021).
- [166] Braj Bhusan Singh et al. “High Spin to Charge Conversion Efficiency in Electron Beam-Evaporated Topological Insulator Bi<sub>2</sub>Se<sub>3</sub>”. In: *ACS Applied Materials & Interfaces* 12.47 (2020), pp. 53409–53415.
- [167] Vincent Vlaminck et al. “Dependence of spin-pumping spin Hall effect measurements on layer thicknesses and stacking order”. In: *Physical Review B* 88.6 (2013), p. 064414.
- [168] E Van de Riet and F Roozeboom. “Ferromagnetic resonance and eddy currents in high-permeable thin films”. In: *Journal of applied physics* 81.1 (1997), pp. 350–354.
- [169] Ivan S Maksymov and Mikhail Kostylev. “Microwave eddy-current shielding effect in metallic films and periodic nanostructures of sub-skin-depth thicknesses and its impact on stripline ferromagnetic resonance spectroscopy”. In: *Journal of Applied Physics* 116.17 (2014), p. 173905.
- [170] Zhuonan Lin and Mikhail Kostylev. “A rigorous two-dimensional model for the stripline ferromagnetic resonance response of metallic ferromagnetic films”. In: *Journal of Applied Physics* 117.5 (2015), p. 053908.
- [171] Mikhail Kostylev. “Coupling of microwave magnetic dynamics in thin ferromagnetic films to stripline transducers in the geometry of the broadband stripline ferromagnetic resonance”. In: *Journal of Applied Physics* 119.1 (2016), p. 013901.
- [172] Mikhail Kostylev et al. “Microwave magnetic dynamics in ferromagnetic metallic nanostructures lacking inversion symmetry”. In: *Journal of Applied Physics* 119.10 (2016), p. 103903.
- [173] Rihan Hai and Mikhail Kostylev. “Theoretical study of the stripline ferromagnetic resonance response of metallic ferromagnetic films based on an analytical model”. In: *Spin*. Vol. 6. 04. World Scientific. 2016, p. 1640015.
- [174] Shyam Balaji and Mikhail Kostylev. “A two dimensional analytical model for the study of ferromagnetic resonance responses of single and multilayer films”. In: *Journal of Applied Physics* 121.12 (2017), p. 123906.

- [175] Matthieu Bailleul. “Shielding of the electromagnetic field of a coplanar waveguide by a metal film: Implications for broadband ferromagnetic resonance measurements”. In: *Applied Physics Letters* 103.19 (2013), p. 192405.
- [176] Ognyan Kounchev. *Multivariate polysplines: applications to numerical and wavelet analysis*. Academic Press, 2001.
- [177] T McGuire and RL Potter. “Anisotropic magnetoresistance in ferromagnetic 3d alloys”. In: *IEEE Transactions on Magnetism* 11.4 (1975), pp. 1018–1038.
- [178] YQ Zhang et al. “Anomalous Hall effect in epitaxial permalloy thin films”. In: *Journal of Applied Physics* 114.16 (2013), p. 163714.
- [179] Yasutomo Omori et al. “Relation between spin Hall effect and anomalous Hall effect in 3d ferromagnetic metals”. In: *Physical Review B* 99.1 (2019), p. 014403.
- [180] Eric W. Weisstein. *Convolution Theorem*. 2021. URL: <https://mathworld.wolfram.com/ConvolutionTheorem.html>.
- [181] Eric W. Weisstein. *Modified Bessel Function of the Second Kind*. 2021. URL: <https://mathworld.wolfram.com/ModifiedBesselFunctionoftheSecondKind.html>.
- [182] José Manuel Vila-Fungueiriño et al. “Polymer assisted deposition of epitaxial oxide thin films”. In: *Journal of Materials Chemistry C* 6.15 (2018), pp. 3834–3844.
- [183] JM Vila-Fungueiriño et al. “Thermodynamic conditions during growth determine the magnetic anisotropy in epitaxial thin-films of  $\text{La}_{0.7}\text{Sr}_{0.3}\text{MnO}_3$ ”. In: *Journal of Physics D: Applied Physics* 49.31 (2016), p. 315001.
- [184] QX Jia et al. “Polymer-assisted deposition of metal-oxide films”. In: *nature materials* 3.8 (2004), pp. 529–532.
- [185] José Manuel Vila-Fungueiriño et al. “Interface magnetic coupling in epitaxial bilayers of  $\text{La}_{0.92}\text{MnO}_3/\text{LaCoO}_3$  prepared by polymer-assisted deposition”. In: *Chemistry of Materials* 26.3 (2014), pp. 1480–1484.
- [186] GF Zou et al. “Polymer-assisted-deposition: a chemical solution route for a wide range of materials”. In: *Chemical Society Reviews* 42.2 (2013), pp. 439–449.
- [187] José Manuel Vila-Fungueiriño et al. “Room-temperature ferromagnetism in thin films of  $\text{LaMnO}_3$  deposited by a chemical method over large areas”. In: *ACS applied materials & interfaces* 7.9 (2015), pp. 5410–5414.
- [188] Hailin Wang et al. “Spontaneous cationic ordering in chemical-solution-grown  $\text{La}_2\text{CoMnO}_3$  double perovskite thin films”. In: *NPG Asia Materials* 11.1 (2019), pp. 1–8.

- [189] J Töpfer and JB Goodenough. “LaMnO<sub>3+δ</sub> Revisited”. In: *Journal of Solid State Chemistry* 130.1 (1997), pp. 117–128.
- [190] Jaume Roqueta et al. “Strain-engineered ferromagnetism in LaMnO<sub>3</sub> thin films”. In: *Crystal Growth & Design* 15.11 (2015), pp. 5332–5337.
- [191] Hailin Wang et al. “Dynamic magnetic properties and spin pumping in polymer-assisted-deposited La<sub>0.92</sub>MnO<sub>3</sub> thin films”. In: *Journal of Materials Chemistry C* 7.40 (2019), pp. 12633–12640.
- [192] Felip Sandiumenge et al. “Competing misfit relaxation mechanisms in epitaxial correlated oxides”. In: *Physical review letters* 110.10 (2013), p. 107206.
- [193] Wang Hailin. “Epitaxial growth of complex functional oxide thin films by green and sustainable chemical solution methods”. In: (2020).
- [194] J Mannhar and A Herrnberger. “The interface is still the device”. In: *Nat. Mater.* 11 (2012), p. 91.
- [195] Masashi Watanabe, Eiji Okunishi, and Kazuo Ishizuka. “Analysis of spectrum-imaging datasets in atomic-resolution electron microscopy”. In: *Microscopy and Analysis-UK* 135 (2009), p. 5.
- [196] Pavel Potapov and Axel Lubk. “Optimal principal component analysis of STEM XEDS spectrum images”. In: *Advanced structural and chemical imaging* 5.1 (2019), pp. 1–21.
- [197] M Farle et al. “Higher-order magnetic anisotropies and the nature of the spin-reorientation transition in face-centered-tetragonal Ni (001)/Cu (001)”. In: *Physical Review B* 55.6 (1997), p. 3708.
- [198] Justin M Shaw, Hans T Nembach, and Thomas J Silva. “Measurement of orbital asymmetry and strain in Co<sub>90</sub>Fe<sub>10</sub>/Ni multilayers and alloys: Origins of perpendicular anisotropy”. In: *Physical Review B* 87.5 (2013), p. 054416.
- [199] Rodrigo Arias and DL Mills. “Extrinsic contributions to the ferromagnetic resonance response of ultrathin films”. In: *Physical review B* 60.10 (1999), p. 7395.
- [200] Robert D McMichael and Pavol Krivosik. “Classical model of extrinsic ferromagnetic resonance linewidth in ultrathin films”. In: *IEEE transactions on magnetics* 40.1 (2004), pp. 2–11.
- [201] Kh Zakeri et al. “Spin dynamics in ferromagnets: Gilbert damping and two-magnon scattering”. In: *Physical Review B* 76.10 (2007), p. 104416.
- [202] Martin AW Schoen et al. “Radiative damping in waveguide-based ferromagnetic resonance measured via analysis of perpendicular standing spin waves in sputtered permalloy films”. In: *Physical Review B* 92.18 (2015), p. 184417.



- [203] Robert D McMichael, DJ Twisselmann, and Andrew Kunz. “Localized ferromagnetic resonance in inhomogeneous thin films”. In: *Physical review letters* 90.22 (2003), p. 227601.
- [204] William K Peria et al. “Magnetoelastic Gilbert damping in magnetostrictive  $\text{Fe}_{0.7}\text{Ga}_{0.3}$  thin films”. In: *Physical Review B* 103.22 (2021), p. L220403.
- [205] William K Peria et al. “Interplay of large two-magnon ferromagnetic resonance linewidths and low Gilbert damping in Heusler thin films”. In: *Physical Review B* 101.13 (2020), p. 134430.
- [206] Timothy Allen Peterson. “Electrical, Microwave, and Thermoelectric Studies of Epitaxial Heusler Compound-Based Thin Films”. PhD thesis. University of Minnesota, 2018.
- [207] Mikhail Kostylev et al. “Magnetization pinning in conducting films demonstrated using broadband ferromagnetic resonance”. In: *Journal of Applied Physics* 108.10 (2010), p. 103914.
- [208] Jun Cheng et al. “Quantitative estimation of thermoelectric contributions in spin pumping signals through microwave photoresistance measurements”. In: *Physical Review B* 103.1 (2021), p. 014415.
- [209] Vincent Castel et al. “Frequency and power dependence of spin-current emission by spin pumping in a thin-film YIG/Pt system”. In: *Physical Review B* 86.13 (2012), p. 134419.
- [210] Mohamed Belmeguenai et al. “Structural, static and dynamic magnetic properties of  $\text{Co}_2\text{MnGe}$  thin films on a sapphire a-plane substrate”. In: *Journal of Applied Physics* 108.6 (2010), p. 063926.
- [211] Åsmund Monsen et al. “Thickness dependence of dynamic and static magnetic properties of pulsed laser deposited  $\text{La}_{0.7}\text{Sr}_{0.3}\text{MnO}_3$  films on  $\text{SrTiO}_3$  (001)”. In: *Journal of magnetism and magnetic materials* 369 (2014), pp. 197–204.
- [212] M Cabero et al. “Modified magnetic anisotropy at  $\text{LaCoO}_3/\text{La}_{0.7}\text{Sr}_{0.3}\text{MnO}_3$  interfaces”. In: *APL Materials* 5.9 (2017), p. 096104.
- [213] Victor Haspot et al. “Temperature dependence of the Gilbert damping of  $\text{La}_{0.7}\text{Sr}_{0.3}\text{MnO}_3$  thin films”. In: *Physical Review Materials* 6.2 (2022), p. 024406.
- [214] VA Atsarkin et al. “Temperature dependence of pure spin current and spin-mixing conductance in the ferromagnetic—normal metal structure”. In: *Journal of Physics D: Applied Physics* 51.24 (2018), p. 245002.
- [215] VA Atsarkin, VV Demidov, and TA Shaikhulov. “Influence of Magnetization on the Spin Pumping Efficiency in a Ferromagnet–Normal Metal Bilayer Structure”. In: *Journal of Experimental and Theoretical Physics* 130.2 (2020), pp. 228–234.

- [216] Ei Shigematsu et al. “Significant reduction in spin pumping efficiency in a platinum/yttrium iron garnet bilayer at low temperature”. In: *Applied Physics Express* 9.5 (2016), p. 053002.
- [217] PE Seiden. “Ferrimagnetic resonance relaxation in rare-earth iron garnets”. In: *Physical review* 133.3A (1964), A728.
- [218] CL Jermain et al. “Increased low-temperature damping in yttrium iron garnet thin films”. In: *Physical Review B* 95.17 (2017), p. 174411.
- [219] SR Marmion et al. “Temperature dependence of spin Hall magnetoresistance in thin YIG/Pt films”. In: *Physical Review B* 89.22 (2014), p. 220404.
- [220] KS Das et al. “Temperature dependence of the effective spin-mixing conductance probed with lateral non-local spin valves”. In: *Applied Physics Letters* 114.7 (2019), p. 072405.
- [221] Sibylle Meyer et al. “Temperature dependent spin transport properties of platinum inferred from spin Hall magnetoresistance measurements”. In: *Applied Physics Letters* 104.24 (2014), p. 242411.
- [222] Miren Isasa et al. “Temperature dependence of spin diffusion length and spin Hall angle in Au and Pt”. In: *Physical Review B* 91.2 (2015), p. 024402.
- [223] Edurne Sagasta et al. “Tuning the spin Hall effect of Pt from the moderately dirty to the superclean regime”. In: *Physical Review B* 94.6 (2016), p. 060412.
- [224] Minh-Hai Nguyen, DC Ralph, and RA Buhrman. “Spin torque study of the spin Hall conductivity and spin diffusion length in platinum thin films with varying resistivity”. In: *Physical review letters* 116.12 (2016), p. 126601.
- [225] T Kimura, T Sato, and Y Otani. “Temperature evolution of spin relaxation in a NiFe/Cu lateral spin valve”. In: *Physical review letters* 100.6 (2008), p. 066602.
- [226] Annamária Kiss, Lénard Szolnoki, and Ferenc Simon. “The Elliott-Yafet theory of spin relaxation generalized for large spin-orbit coupling”. In: *Scientific reports* 6.1 (2016), pp. 1–10.
- [227] Kazuya Harii et al. “Frequency dependence of spin pumping in Pt/Y<sub>3</sub>Fe<sub>5</sub>O<sub>12</sub> film”. In: *Journal of applied physics* 109.11 (2011).
- [228] Braj Bhusan Singh and Subhankar Bedanta. “Large spin Hall angle and spin-mixing conductance in the highly resistive antiferromagnet Mn<sub>2</sub>Au”. In: *Physical Review Applied* 13.4 (2020), p. 044020.
- [229] Harold Y Hwang et al. “Emergent phenomena at oxide interfaces”. In: *Nature materials* 11.2 (2012), pp. 103–113.
- [230] Joerg Heber. “Materials science: Enter the oxides”. In: *Nature News* 459.7243 (2009), pp. 28–30.

- [231] Mariona Coll et al. “Towards oxide electronics: a roadmap”. In: *Applied surface science* 482 (2019), pp. 1–93.
- [232] Adarsh S Patri et al. “Theory of large intrinsic spin Hall effect in iridate semimetals”. In: *Scientific reports* 8.1 (2018), pp. 1–10.
- [233] Ibtissem Benguetat-El Mokhtari et al. “Spin Pumping and Magnetic Anisotropy in  $\text{La}_{2/3}\text{Sr}_{1/3}\text{MnO}_3/\text{Pt}$  Systems”. In: *physica status solidi (b)* 257.12 (2020), p. 2000265.
- [234] GY Luo et al. “Spin Pumping Induced Inverse Spin-Hall Effects in  $\text{La}_{0.7}\text{Sr}_{0.3}\text{MnO}_3/\text{Platinum}$  Bilayer Film”. In: *IEEE transactions on magnetics* 48.11 (2012), pp. 3958–3960.
- [235] Han Kyu Lee et al. “Magnetic anisotropy, damping, and interfacial spin transport in Pt/LSMO bilayers”. In: *AIP Advances* 6.5 (2016), p. 055212.
- [236] Satoru Emori et al. “Spin transport and dynamics in all-oxide perovskite  $\text{La}_{2/3}\text{Sr}_{1/3}\text{MnO}_3/\text{SrRuO}_3$  bilayers probed by ferromagnetic resonance”. In: *Physical Review B* 94.22 (2016), p. 224423.
- [237] Christoph Hauser et al. “Enhancement of spin mixing conductance in  $\text{La}_{0.7}\text{Sr}_{0.3}\text{MnO}_3/\text{LaNiO}_3/\text{SrRuO}_3$  heterostructures”. In: *physica status solidi (b)* 257.7 (2020), p. 1900606.
- [238] Haoliang Liu et al. “Studies of spin related processes in fullerene  $\text{C}_{60}$  devices”. In: *Journal of Materials Chemistry C* 6.14 (2018), pp. 3621–3627.
- [239] Hailong Wang et al. “Large spin-orbit torque observed in epitaxial  $\text{SrIrO}_3$  thin films”. In: *Applied Physics Letters* 114.23 (2019), p. 232406.
- [240] Tianxiang Nan et al. “Anisotropic spin-orbit torque generation in epitaxial  $\text{SrIrO}_3$  by symmetry design”. In: *Proceedings of the National Academy of Sciences* 116.33 (2019), pp. 16186–16191.
- [241] TA Shaikhulov et al. “Spin current and magnetic measurements in heterostructure  $\text{SrIrO}_3/\text{La}_{0.7}\text{Sr}_{0.3}\text{MnO}_3$ ”. In: *Journal of Physics: Conference Series*. Vol. 1389. 1. IOP Publishing. 2019, p. 012079.
- [242] S Crossley et al. “All-oxide ferromagnetic resonance and spin pumping with  $\text{SrIrO}_3$ ”. In: *Physical Review B* 100.11 (2019), p. 115163.
- [243] A Khapikov et al. “Magnetic domains and twin structure of the  $\text{La}_{0.7}\text{Sr}_{0.3}\text{MnO}_3$  single crystal”. In: *Applied Physics Letters* 77.15 (2000), pp. 2376–2378.
- [244] U Gebhardt et al. “Formation and Thickness Evolution of Periodic Twin Domains in Manganite Films Grown on  $\text{SrTiO}_3$  (001) Substrates”. In: *Physical review letters* 98.9 (2007), p. 096101.
- [245] GY Luo et al. “Spin pump and probe in lanthanum strontium manganite/platinum bilayers”. In: *Scientific Reports* 7.1 (2017), pp. 1–9.

- [246] Dominik Kriegner, Eugen Wintersberger, and Julian Stangl. “xrayutilities: a versatile tool for reciprocal space conversion of scattering data recorded with linear and area detectors”. In: *Journal of Applied Crystallography* 46.4 (2013), pp. 1162–1170.
- [247] Mara Strungaru et al. “Model of magnetic damping and anisotropy at elevated temperatures: Application to granular FePt films”. In: *Physical Review Applied* 14.1 (2020), p. 014077.
- [248] Saül Vélez et al. “Hanle magnetoresistance in thin metal films with strong spin-orbit coupling”. In: *Physical review letters* 116.1 (2016), p. 016603.
- [249] Matthias Althammer et al. “Quantitative study of the spin Hall magnetoresistance in ferromagnetic insulator/normal metal hybrids”. In: *Physical Review B* 87.22 (2013), p. 224401.
- [250] Saül Vélez et al. “Competing effects at Pt/YIG interfaces: Spin Hall magnetoresistance, magnon excitations, and magnetic frustration”. In: *Physical Review B* 94.17 (2016), p. 174405.
- [251] Juan M Gomez-Perez et al. “Synthetic antiferromagnetic coupling between ultrathin insulating garnets”. In: *Physical Review Applied* 10.4 (2018), p. 044046.
- [252] Saül Vélez et al. “Spin Hall magnetoresistance in a low-dimensional Heisenberg ferromagnet”. In: *Physical Review B* 100.18 (2019), p. 180401.
- [253] Miren Isasa et al. “Spin Hall Magnetoresistance as a Probe for Surface Magnetization in Pt/CoFe<sub>2</sub>O<sub>4</sub> Bilayers”. In: *Physical Review Applied* 6.3 (2016), p. 034007.
- [254] Hua Wang et al. “Antiferromagnetic anisotropy determination by spin Hall magnetoresistance”. In: *Journal of Applied Physics* 122.8 (2017), p. 083907.
- [255] RI Dass and JB Goodenough. “Multiple magnetic phases of La<sub>2</sub>CoMnO<sub>6-δ</sub> (0 < δ < 0.05)”. In: *Physical Review B* 67.1 (2003), p. 014401.
- [256] Laura López Mir et al. *Transport phenomena and magnetism in nanostructures of lanthanum manganitebased oxide thin films*. Universitat Autònoma de Barcelona, 2018.
- [257] Regina Galceran Vercher et al. *Spin-dependent transport in oxide-based tunnel junctions*. Universitat Autònoma de Barcelona, 2015.
- [258] HZ Guo et al. “Effect of oxygen concentration on the magnetic properties of La<sub>2</sub>CoMnO<sub>6</sub> thin films”. In: *Applied Physics Letters* 91.20 (2007), p. 202509.
- [259] AJ Barón-González et al. “Effect of cation disorder on structural, magnetic and dielectric properties of La<sub>2</sub>MnCoO<sub>6</sub> double perovskite”. In: *Journal of physics: Condensed matter* 23.49 (2011), p. 496003.

- [260] Laura López-Mir et al. “Magnetic anisotropy and valence states in  $\text{La}_2\text{Co}_{1-x}\text{Mn}_{1+x}\text{O}_6$  ( $x \approx 0.23$ ) thin films studied by x-ray absorption spectroscopy techniques”. In: *Physical Review B* 95.22 (2017), p. 224434.
- [261] L López-Mir et al. “Anisotropic sensor and memory device with a ferromagnetic tunnel barrier as the only magnetic element”. In: *Scientific reports* 8.1 (2018), pp. 1–10.
- [262] Quantum Design. *Physical Property Measurement System*. Aug. 2019. URL: <https://www.qdusa.com/products/ppms.html>.
- [263] Mathias Weiler et al. “Experimental test of the spin mixing interface conductivity concept”. In: *Physical review letters* 111.17 (2013), p. 176601.
- [264] H Wu et al. “Hanle magnetoresistance: The role of edge spin accumulation and interfacial spin current”. In: *Physical Review B* 94.17 (2016), p. 174407.
- [265] Cheng Gong et al. “Discovery of intrinsic ferromagnetism in two-dimensional van der Waals crystals”. In: *Nature* 546.7657 (2017), pp. 265–269.
- [266] N David Mermin and Herbert Wagner. “Absence of ferromagnetism or anti-ferromagnetism in one-or two-dimensional isotropic Heisenberg models”. In: *Physical Review Letters* 17.22 (1966), p. 1133.
- [267] Patrick Bruno. “Absence of spontaneous magnetic order at nonzero temperature in one-and two-dimensional Heisenberg and XY systems with long-range interactions”. In: *Physical Review Letters* 87.13 (2001), p. 137203.
- [268] Juan M Gomez-Perez et al. “Strong interfacial exchange field in a heavy metal/ferromagnetic insulator system determined by spin Hall magnetoresistance”. In: *Nano Letters* 20.9 (2020), pp. 6815–6823.
- [269] Sara Catalano et al. “Spin Hall magnetoresistance effect from a disordered interface”. In: *ACS Applied Materials & Interfaces* (2022).
- [270] Bernard Dennis Cullity and Chad D Graham. *Introduction to magnetic materials*. John Wiley & Sons, 2011.
- [271] Felix Bloch. “Zur theorie des ferromagnetismus”. In: *Zeitschrift für Physik* 61.3 (1930), pp. 206–219.
- [272] Daniel Lundin, Jon Tomas Gudmundsson, and Tiberiu Minea. *High Power Impulse Magnetron Sputtering: Fundamentals, Technologies, Challenges and Applications*. Elsevier, 2019.
- [273] Manuel Braun. “Magnetron sputtering technique”. In: *Handbook of manufacturing engineering technology*. Springer (2015), pp. 2929–2957.
- [274] Witold Gulbiński. “Deposition of Thin Films by Sputtering”. In: *Chemical Physics of Thin Film Deposition Processes for Micro-and Nano-Technologies*. Springer, 2002, pp. 309–333.

- [275] ICMAB-CSIC. *Nanoquim Platform*. 2022. URL: <https://services.icmab.es/nanoquim/>.
- [276] John Clarke and Alex I Braginski. *The SQUID handbook: Applications of SQUIDs and SQUID systems*. John Wiley & Sons, 2006.
- [277] Quantum Design. *SQUID Application Note 1052-202A: Coupling Magnetic Signals to a SQUID Amplifier*. 2001. URL: <https://qdusa.com/siteDocs/appNotes/1052-202.pdf>.
- [278] RL Fagaly. “Superconducting quantum interference device instruments and applications”. In: *Review of scientific instruments* 77.10 (2006), p. 101101.
- [279] John Clarke. “SQUIDs”. In: *Scientific American* 271.2 (1994), pp. 46–53.
- [280] Quantum Design. *Broadband FMR Spectrometers*. 2020. URL: [https://qd-europe.com/fileadmin/Mediapool/products/magnetometers/pdf/Broadband-FMR\\_spectrometer.pdf](https://qd-europe.com/fileadmin/Mediapool/products/magnetometers/pdf/Broadband-FMR_spectrometer.pdf).
- [281] Zurich Instruments. *Principles of lock-in detection and the state of the art*. 2016. URL: [https://www.zhinst.com/sites/default/files/documents/2020-06/zi\\_whitepaper\\_principles\\_of\\_lock-in\\_detection.pdf](https://www.zhinst.com/sites/default/files/documents/2020-06/zi_whitepaper_principles_of_lock-in_detection.pdf).
- [282] Carmelo Giacovazzo et al. *Fundamentals of crystallography*. Vol. 7. Oxford University Press Oxford, 2002.
- [283] Hideo Toraya. “Introduction to X-ray analysis using the diffraction method”. In: *Rigaku J* 32.2 (2016), pp. 35–43.
- [284] Shigesaburo Ogawa and Isao Takahashi. “Glass Transition of Ultrathin Sugar Films Probed by X-Ray Reflectivity”. In: *Carbohydrate*. IntechOpen, 2017.
- [285] Miho Yasaka et al. “X-ray thin-film measurement techniques”. In: *The Rigaku Journal* 26.2 (2010), pp. 1–9.
- [286] TC Huang, R Gilles, and G Will. “Thin-film thickness and density determination from X-ray reflectivity data using a conventional power diffractometer”. In: *Thin Solid Films* 230.2 (1993), pp. 99–101.
- [287] Matthew P Dewar. “Characterization and evaluation of aged 20Cr32Ni1Nb stainless steels”. In: (2013).
- [288] Memed Duman et al. “Atomic Force Microscopy (AFM) for Topography and Recognition Imaging at Single Molecule Level”. In: *Encyclopedia of Biophysics*. Ed. by Gordon C. K. Roberts. Berlin, Heidelberg: Springer Berlin Heidelberg, 2013, pp. 102–112. ISBN: 978-3-642-16712-6. DOI: [10.1007/978-3-642-16712-6\\_496](https://doi.org/10.1007/978-3-642-16712-6_496). URL: [https://doi.org/10.1007/978-3-642-16712-6\\_496](https://doi.org/10.1007/978-3-642-16712-6_496).
- [289] JEOL Ltd. *Focused ion-beam milling*. 2018. URL: [https://www.jeol.co.jp/en/words/emterms/search\\_result.html?keyword=focused%20ion-beam%20milling](https://www.jeol.co.jp/en/words/emterms/search_result.html?keyword=focused%20ion-beam%20milling).

- [290] ND Browning et al. “Scanning transmission electron microscopy: an experimental tool for atomic scale interface science”. In: *Reviews on Advanced Materials Science(Russia)* 1.1 (2000), pp. 1–26.
- [291] JEOL Ltd. *Electron energy-loss spectroscopy*. 2021. URL: [https://www.jeol.co.jp/en/words/emterms/search\\_result.html?keyword=EELS](https://www.jeol.co.jp/en/words/emterms/search_result.html?keyword=EELS).